Photocatalytic Water Reduction Systems Based on Iridium and Non-Noble Metal Complexes

---

Maike Tünnermann

September, 2018

Paderborn University

Department of Chemistry
Inorganic Chemistry
Bauer Group

Photocatalytic Water Reduction Systems Based on Iridium and Non-Noble Metal Complexes

Maike Tünnermann

A thesis submitted in partial fulfillment
of the requirements for the degree
"Doctor rerum naturalium"
in the
Faculty of Science
Department of Chemistry
at the Paderborn University

1. Reviewer Prof. Dr. Matthias Bauer
Department of Chemistry
Paderborn University

2. Reviewer PD Dr. Hans Egold
Department of Chemistry
Paderborn University

Supervisor Prof. Dr. Matthias Bauer

September, 2018

Maike Tünnermann

Photocatalytic Water Reduction Systems Based on Iridium and Non-Noble Metal Complexes

PhD Thesis, September, 2018
Reviewers: Prof. Dr. Matthias Bauer and PD Dr. Hans Egold
Supervisor: Prof. Dr. Matthias Bauer

Paderborn University
Bauer Group
Inorganic Chemistry
Department of Chemistry
Warburger Str. 100
33098 Paderborn

One never notices
what has been done;
one can only see
what remains to be done.
— **Marie Curie**

Abstract

Humankind is, triggered by their increasing energy demand and the emerging scarcity of fossil energy carriers, facing a serious energy crisis. Moreover, the extensive burning of fossil fuels for more than 200 years has induced escalating climate changes that must be stopped or at least mitigated.

One promising but at this time rarely researched method is the evolution of hydrogen from water under the application of molecular systems, and solar irradiation. This process is known as photocatalytic water reduction. There are two competing approaches, which also exhibit many similarities: the two- and one-component approach. All systems are composed of a photosensitizer (PS) that is excited by solar irradiation and afterward capable of donating an electron. A catalyst (CAT) that accepts that electron and reduces protons to hydrogen. To restart the catalytic cycle a sacrificial reductant (SR) is required, which provides the photosensitizer with electrons and gets therefore oxidized. The difference between these two contrary approaches is based on the connection between PS and CAT. The two-component system contains no connection between the two building blocks and the electron has to be transferred through the reaction medium from the PS to the CAT. The electron transfer is therefore diffusion-dependent. In contrast to that the one-component system features a structural organization of PS and CAT in the form of a bridging ligand or linker. This results in a directional electron transfer within the molecular scaffold. Hence, both systems show fundamental differences regarding the electron transfer, but their individual components are very similar. Nowadays, the individual components are mostly based on noble metals like platinum, palladium, ruthenium or iridium.[1–7] Besides their high activity, these systems are unpreferable due to the scarcity of noble metals entails a high price.

The aims of this thesis are to develop one- and two-component systems that do not require noble catalysts, but support non-noble catalysts to move a big step forward to a more sustainable energy production. One additional task is the development of bridging ligands, which show an efficient electron transfer.

This thesis describes the development and test of eight new iridium photosensitizers in the photocatalytic water reduction in combination with a cobalt CAT as two-

component system. The challenging task was the design and synthesis of a completely new ligand structure. It was also possible to synthesize two iridium-cobalt one-component systems and evaluate their hydrogen evolution potential under photocatalytic conditions. Based on the photocatalytic results and taking account of spectroscopic and electrochemical properties, a structure-activity correlation was derived. The systems showed the high potential of non-noble catalyst building blocks for the hydrogen evolution, and additionally, they provide many development potentials for the future.

Kurzfassung

Die Menschheit bewegt sich mit ihrem immer stärker ansteigendem Energiekonsum und der gleichzeitigen Verknappung der fossilen Energieträger einer Energiekrise entgegen. Zusätzlich stehen wir vor der Herausforderung, die Klimaerwärmung und ihre Folgen, die auch durch unseren Umgang mit fossilen Brennstoffen hervorgerufen wurden, zu stoppen um somit noch größere Schäden zu vermeiden.

Eine vielversprechende, aber momentan noch recht unerforschte Methode, stellt dabei die Erzeugung von Wasserstoff aus Wasser mithilfe von molekularen Systemen unter der Nutzung von Sonnenlicht dar. Dieser Prozess wird als photokatalytische Wasserreduktion bezeichnet. Dabei gibt es zwei miteinander in Konkurrenz stehende Ansätze, die trotzdem viele Gemeinsamkeiten aufweisen: Den Ein- und Mehrkomponentenansatz. Alle Systeme benötigen einen Photosensibilisator (PS), der durch Sonnenlicht in einen angeregten Zustand versetzt wird und somit in der Lage ist ein Elektron abzugeben. Das Elektron wird von einem Katalysator (KAT) aufgenommen, an dem aus Protonen durch Reduktion Wasserstoff entsteht. Um den katalytischen Zyklus von vorne zu beginnen ist es notwendig eine dritte Komponente hinzuzufügen, das Opferreduktanz (OR). Dieses stellt seine Elektronen dem Photosensibilisator zur Verfügung und wird dabei selbst oxidiert. Der Unterschied der beiden Ansätze liegt in der Verbindung zwischen PS und KAT. Während bei den Zwei- oder Mehrkomponentensystemen keine Verknüpfung der beiden Bausteine PS und KAT vorliegt und das Elektron vom PS zum KAT durch das Reaktionsmedium diffundieren muss, wird bei den Einkomponentensystemen eine strukturelle Organisation durch die Einführung eines Brückenliganden vorgenommen der PS und KAT direkt miteinander verknüpft. Das Elektron kann hierbei direkt innerhalb des Molekülgerüstes übertragen werden. Die beiden Systeme unterscheiden sich damit grundlegend, was die Art des Elektronentransfers angeht, jedoch nicht was die einzelnen Komponenten betrifft. Heutzutage werden für die einzelnen Bausteine hauptsächlich edle Metalle wie Platin, Palladium, Rhenium, Ruthenium oder Iridium verwendet.[1–7] Neben der hohen Aktivität dieser Systeme sind sie jedoch mit dem großen Nachteil belastet, dass durch die Seltenheit der edlen Metalle sie gleichzeitig einen hohen Kostenaufwand mit sich bringen.

Die zentralen Bausteine dieser Dissertation waren die Entwicklung von Ein- und Zweikomponentensystemen die auf edle Katalysatoren verzichten und mit dem Einbau von unedlen Metallen einen weiteren, signifikanten Schritt in Richtung nachhaltiger Energieproduktion machen. Zusätzlich stand die Entwicklung eines elektronentransfereffizienten Brückenliganden im Fokus.

Im Zuge der Arbeit wurden acht neue Iridium Photosensibilisatoren systematisch entwickelt und in der photokatalytischen Wasserreduktion in Kombination mit einem Cobaltkatalysator als Mehrkomponentensystem getestet. Eine besondere Herausforderung bestand dabei in der Synthese eines komplett neuen Liganden-gerüstes. Ebenfalls war es möglich zwei Iridium-Cobalt Einkomponentensysteme zu synthetisieren und diese ebenfalls unter photokatalytischen Bedingungen zu erforschen. Basierend auf diesen Ergebnissen wurde unter Berücksichtigung von spektroskopischen, elektrochemischen und photokatalytischen Ergebnissen eine Struktur-Aktivitäts-Beziehung für diese Systeme abgeleitet. Die Systeme zeigen sehr gut das Potenzial von unedlen, nicht fossilen, Bausteinen zur Wasserstofferzeugung und bieten für die Zukunft noch hohe Weiterentwicklungsmöglichkeiten.

Acknowledgement

First, I would like to thank my supervisor, Prof. Dr. Matthias Bauer, for giving me the opportunity to work on such an exciting and promising topic. Also, I want to thank him for providing my work with everything necessary to obtain good results and his advice on research questions. My second thanks is dedicated to the Deutsche Bundesstiftung Umwelt for giving me the financial support I needed for three years, which enabled me to focus on my thesis and not on financial issues. I also would like to thank PD Dr. Hans Egold for being my second reviewer. For the whole course of my studies, my bachelor's and master's thesis, and the PhD thesis you were very helpful, and NMR questions that bother me for days are answered by you in less than a minute.

I am also very grateful for the whole analytic team who make my life much more straightforward: Hans Egold, Karin Stolte and Andrea Harbarth for the NMR measurements. Maria Busse and Christiane Gloger for the elemental analyses. Ulrich Flörke for the X-ray diffraction analyses. Rodica Kaup, Mariola Zukowski, Adam Neuba and Heinz Weber for the mass analyses. Mr. Weber, thank you for the help with difficult analyses and traveling advice, for sharing your life experiences with us, providing us with chocolate, and for many enjoyable conversations.

Next, I'd like to thank my bachelor's students and my student assistants, Johann Plaschke, Simon Friesen, Salvador Martinez and finally, Pia Rehsies. It was nice to have you by my side, working for me, observing how your techniques evolve, and having fun in the lab with me. Thank you!

Since I am already on the topic fun in the lab, I am so grateful that I have colleagues and also friends like my working group. In particular, I want to mention Yannik, Patrick, Roland, Kai, Voicu and Steffen, and of course my girls Hatice and Regina. I don't want to miss the time with you. You make the hard times so much more comfortable, and the pleasant times even more pleasant. I hope our friendship will last a long time.

The last sentences are dedicated to my family. Mama, Papa, thank you for your constant support from the beginning to the present. Without you, it wouldn't be possible for me to achieve this career path.

And now, Jan, you have been my companion for over eleven years. I am sure your support and belief in my abilities pushed me to higher limits. Since we both chose the academic career, it was possible for us to share similar problems, challenges, and successes. Thank you! I am excited about what the future holds for us.

Compound List

Building Blocks for Two-Component Systems

Ligands

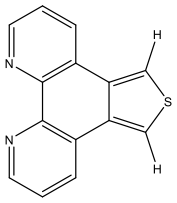	**L2**
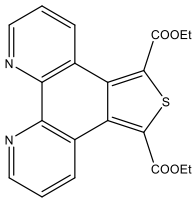	**L3**
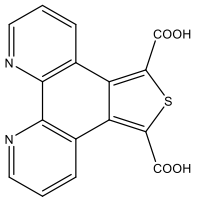	**L4**
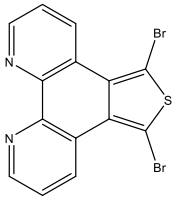	**L5**
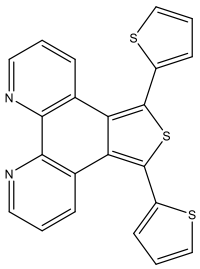	**L6**

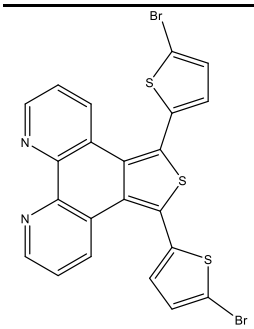	**L7**
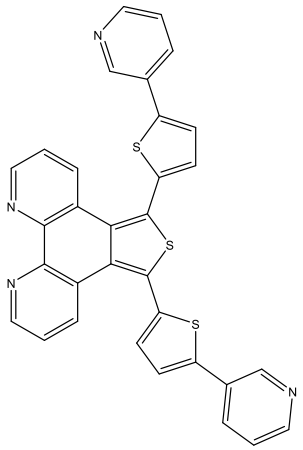	**L8**
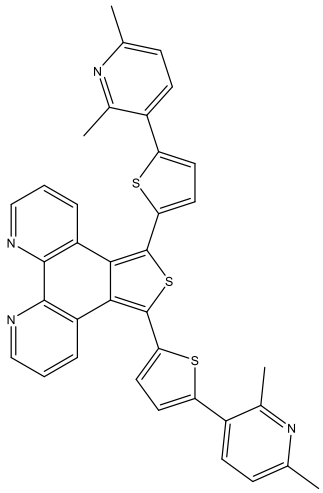	**L9**
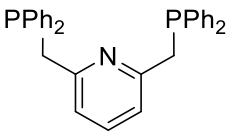	**21**

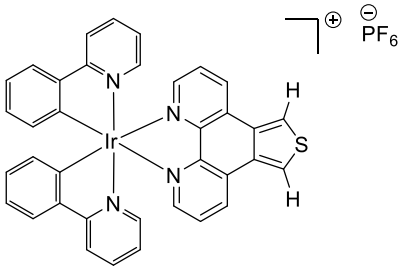

PS2

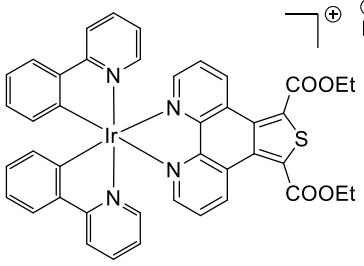

PS3

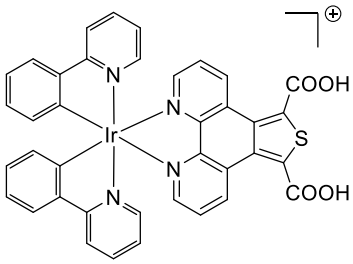

PS4

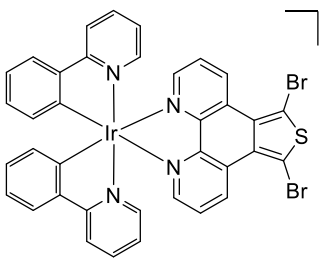

PS5

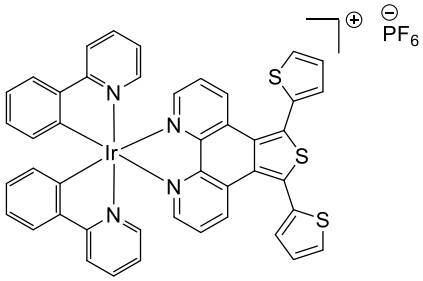

PS6

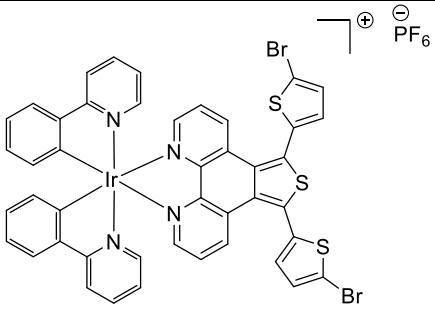

PS7

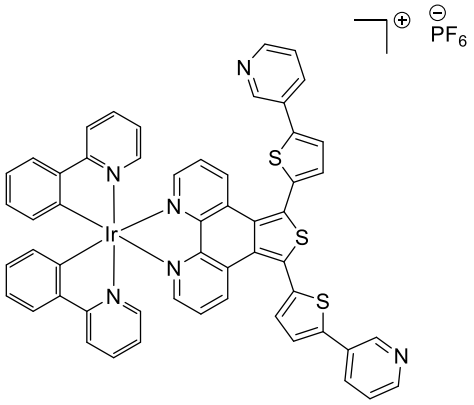

PS8/Irth

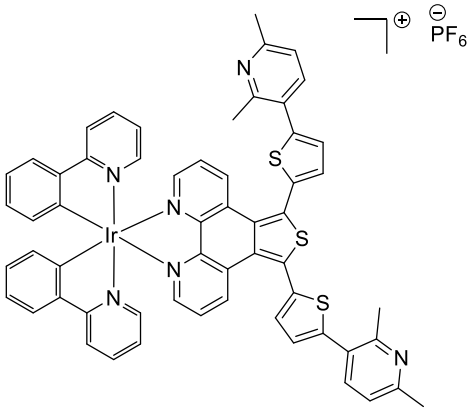

PS9

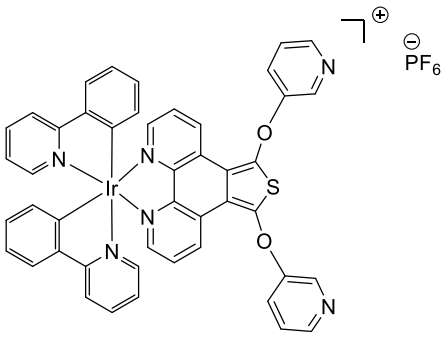

IrO

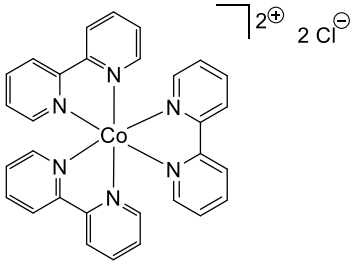	**Co1**
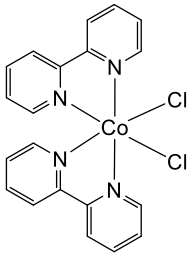	**Co2**
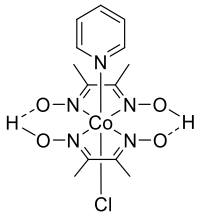	**Co3**
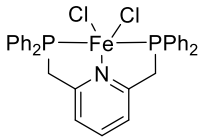	**Fe1**
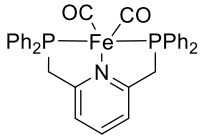	**Fe2**

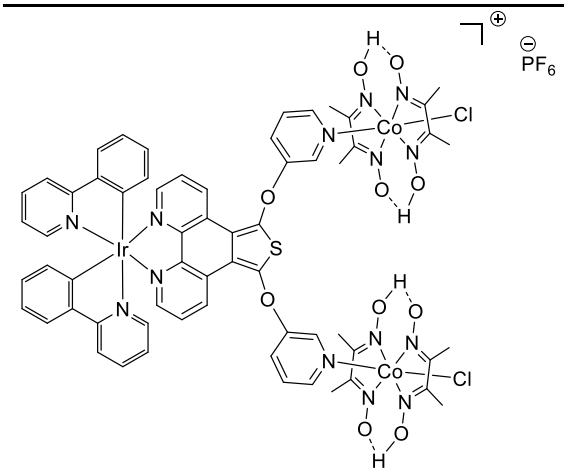

IrOCo

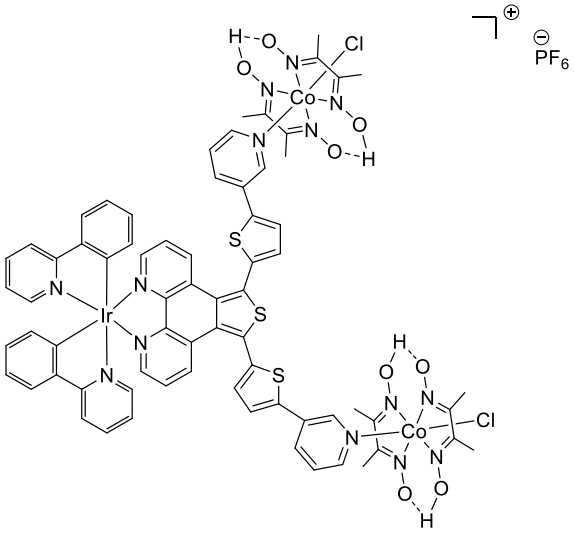

IrthCo

Nomenclature

δ	Chemical shift
τ	Excited state lifetime
bs	Broad singlet
CAT	Water reduction catalyst
CI	Chemical Ionization
CV	Cyclic Voltammogram
d	Doublet
DBU	Deutsche Bundesstiftung Umwelt
dd	Double doublet
DME	Dimethoxyethane
$dmgBF_2$	Difluoroboryl-dimethylglyoxime
dmgh	Dimethylglyoxime
dppp	1,3-Bis(diphenylphosphino)propane
EI	Electron Ionization
eV	Electron Volt
FT-IR	Fourier Transform Infrared Spectroscopy
IEA	International Energy Agency
LC	Ligand Centered
LEEC	Light Emitting Electrochemical Cells
LL'CT	Ligand to- Ligand' Charge Transfer
LLCT	Ligand to Ligand Charge Transfer
LMCT	Ligand to metal Charge Transfer

MLCT	Metal to Ligand Charge Transfer
ML’CT	Metal to Ligand’ Charge Transfer
NBS	N-Bromosuccinimide
OECD	Organization for Economic Cooperation and Development
OLED	Organic Light Emitting Diode
PEM	Polymer Electrolyte Membrane
ppm	Parts per million
ppy	Phenylpyridine
PS	Photosensitizer
PS*	Excited photosensitizer
PV	Photovoltaic
q	Quartet
s	Singlet
sept	Septet
SR	Sacrificial reductant
t	Triplet
TBAN	Tetrabutylammonium nitrate
TCSPC	Time-Correlated Single Photon Counting
TMS	Tetramethylsilane

Contents

1 Introduction

> *There is no energy crisis, only a crisis of ignorance.*
>
> **— Richard Buckminster Fuller**

1.1 Motivation and Problem Statement

A basic understanding of the indispensable development of an emission-free, hydrogen-based society will be outlined in this chapter. Fossil fuel deposits are highly limited. This problem is becoming even more prominent as densely populated countries like China and India are becoming more and more industrialized. Projections assume a complete depletion of fossil reserves within the next 100 years (according to BP statistics) if all fossil stocks are accessible. This is the first main argument for a fossil-free economy, which uses hydrogen instead of fossil fuels as emission-free energy carrier.

The second main argument is closely related to the use of fossil fuels: Climate change. Humankind cannot use fossil fuels for another 100 years. Through the combustion of fossil fuels, CO_2 emissions increase. CO_2 is responsible for global warming and climate change. The molecule functions as a heat-trap and prevents heat from leaving the earth's surface. CO_2 is not the only greenhouse gas, but it is the most abundant, and, therefore, its reduction is the most prominent target. The urgent need to mitigate greenhouse gases is a central issue for all countries in the world. Therefore, global warming was discussed at the 2015 United Nations Climate Change Conference in Paris. All countries agreed to reduce the emission of greenhouse gases, especially CO_2. This shall limit the global warming level to less than 2 °C compared to the pre-industrial levels. In 2016, the global average temperature exceeded that of pre-industrial times by 1 °C.[8] In 2017, DBU environmental award winner (2015) Johan Rockström published a roadmap for decarbonization in Science.[9] He pointed out that the maximum overall emission to reach the goals of the Paris Agreement is 700 Gt CO_2 until 2100. The maximum emission must be reached in 2020, and afterward, the CO_2 emission must be halved every decade. Additionally, the subsequent development of methods to remove atmospheric CO_2 is necessary.[9]

Sadly, America's 45th President Donald Trump decided at the time of this writing to leave the Paris Agreement, and the USA will not further adopt measures to stop climate change. Nonetheless, some individual states and huge US companies will further participate in achieving the climate change goals of the Paris Agreement.

Nowadays, in Germany, emission-free, renewable energy sources are mostly based on solar and wind energy, while hydropower accounts for only a small proportion. The utilization of solar energy refers to photovoltaic (PV) systems. Typically, small PV installations are found on the roofs of private houses or factories and not power plants as often used in large deserts with intense solar radiation over many hours. Wind energy is captured by wind turbines, which have shaped the landscape in Germany significantly for the last 20 years in large onshore or offshore wind parks. Both methods are, in principle, good candidates to stop global warming since they emit no CO_2 when producing electricity. Unfortunately, all these methods of electricity production are not stable. They are called fluctuating methods, which are strongly dependent on the energy suppliers, wind and solar energy. This is a huge problem because temporary storing and release of energy to balance the grid is not possible with the existing infrastructure.

A new and promising but also rarely researched method that utilizes solar energy is photocatalytic hydrogen production. Solar energy is used to split water into hydrogen and oxygen. Here, solar energy is not converted into electricity as in PV systems. Instead, it is converted into chemical energy and stored as hydrogen. With hydrogen as the storage medium, the fluctuation problem can be avoided. In times when solar radiation is not available, the chemical energy is reconverted to electricity.

The storage of energy in hydrogen is possible and even already used, but it is not without problems. Hydrogen is a highly volatile gas, and well-insulated tanks are needed to prevent the loss of this compound. The storage of gaseous hydrogen also requires large tanks, which makes it unattractive for use in mobile applications like cars. The storage of liquid hydrogen is possible, but it is problematic due to the requirement for high-pressure storage tanks. Therefore, new methods are under investigation to store hydrogen more efficiently and more safely, for example, in other chemical compounds like formic acid.[10,11] Nowadays, the hydrogen economy is no alternative to conventional fossil fuels, or solar or wind energy. This is mainly due to the absence of a comprehensive hydrogen distribution infrastructure like hydrogen gas stations or pipelines.

Nevertheless, hydrogen production by photocatalysis is by no means a fully developed method. In a sense, hydrogen evolution is an apt term. Beyond its actual meaning, it reminds us that concepts, technologies, and applications are still evolving.

Now at an early stage, research must provide the variability on which subsequent selection in fundamental and applied research can act to isolate and further improve the most promising methods. Hopefully, it will not take geological time for practical approaches to evolve.

This thesis contributes to this long-term endeavor, providing new starting points for a hopefully fruitful future hydrogen economy that will counteract the emerging energy crisis and climate change.

1.2 Thesis Structure

This thesis is subdivided in nine individual chapters. **Chapter 1** presents the problems as well as the motivation that led to the choice of subject for this thesis. **Chapter 2** deals with the most fundamental, theoretical background which helps to understand the results presented in this thesis. Additionally, the examples will help to fit the results in the scientific context.

Chapter 3 outlines the concrete aims of this thesis. The synthesis of two-component systems based on iridium photosensitizers with new diimine ligands and non-noble iron and cobalt complexes as catalysts are the focus of **Chapter 4**. In the next chapter, **Chapter 5**, the water splitting results of the previously described two-component systems will be presented. Beyond that, the results will be analyzed with regard to the spectroscopic and electrochemical properties of the individual building blocks. While the two chapters previously deal with the development and testing of two-component systems, the focus of **Chapter 6** is now on the synthesis of iridium-cobalt one-component systems. **Chapter 7** describes the evaluation of the synthesized one-component systems in the phototalaytic proton reduction and connect the electrochemical and spectroscopic properties to the photocatalytic activity. The results of this whole thesis are summarized in **Chapter 8**. The most important findings will be highlighted again. A short part in this chapter is also dedicated to future directions in this research area. The last chapter, **Chapter 9**, contains experimental procedures and analyses of the synthesized compounds.

2 Background

> *Because we are now running out of gas and oil, we must prepare quickly for a third change, to strict conservation and to the use of coal and permanent renewable energy sources, like solar power.*
>
> **— Jimmy Carter**

2.1 Energy Problems, Climate Change and Renewable Energy Sources

The combustion of fossil fuels is a highly problematic issue as briefly mentioned in the introduction. In 2015, global CO_2 emissions from fuel combustion reached 32.3 Gt CO_2, which is comparable to the 2014 level. The countries, which are mainly responsible for these emissions are China (28 %), the United States (15 %), the European Union (10 %), and India (6 %) and the energy demand of humanity is growing more and more, which is connected to a growing population in India and China while subsequent "industrialization" of these countries occurs. However, the feedstock of fossil fuels is limited, and the increasing demand for energy will be covered for a maximum of 100 years before the reserves are exhausted.[12]

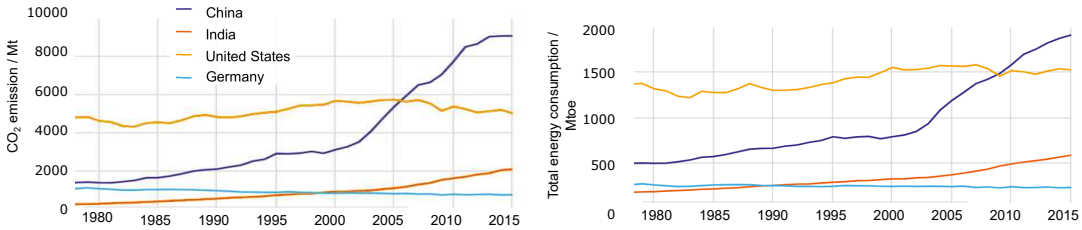

Figure 2.1: CO_2 emission and total energy consumption of China, India, the United States and Germany. Mtoe= million tonnes of oil equivalent.[13]

Figure 2.1 shows the CO_2 emissions of China, India, the US and Germany since 1970. While the emissions of the US are constantly high with approximately 5000 Mt CO_2 per year, the CO_2 emissions of China explosively growth after 2000 and now,

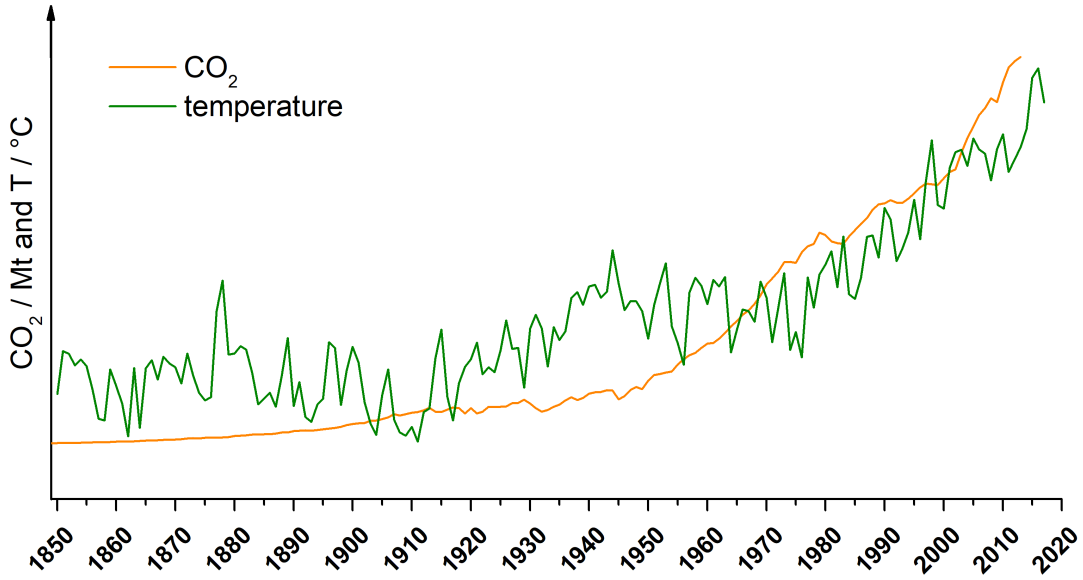

Figure 2.2: CO_2 and temperature evolution since the beginning of the industrialization.[20,21]

they emit nearly twice as much as the US. This explosive growth could also be expected for India, but this date lies in the future. Germany only minor contributes to the CO_2 emissions and shows already a small decrease in the CO_2 emissions. The figure shows also that the correlation between energy consumption and emissions is significant. This makes clear that the most energy is provided by fossil fuels and not renewable energy sources.

This increased demand of energy, associated with increased emissions, results inevitably in global warming. Skeptics claim that the Humankind does not cause the global warming. They argue that in earth´s history there were warm periods, like nowadays, and glacial periods, but statistics show that this claim is not true: Figure 2.2 shows the CO_2 evolution with a persistent growth after the beginning of the industrial age in 1770, which was started with the invention of the steam engine by James Watt.[14] This new method utilized fossil fuels and changed the geochemistry of our planet. At about the same time, the global warming of our planet started, which is also displayed in Figure 2.2. For many years, the consequences of a higher earth temperature were underestimated. Nowadays, nearly every person on earth gets in contact with the various consequences of climate change. The first point is melting ice and glaciers that raises the sea level. Many coastal megacities like Shanghai, Jarkata or Mumbai will be in danger if this process is still ongoing.[15] In Europe, the city Venice could be one of the first victims of a rising sea level.[16] However, it is not only the rising sea level but also the threats of storms, floods, heat waves, and droughts increased, too. Some publications show a correlation of climate change with the risk of occurrence of these extreme weather conditions.[17–19]

The so-called "freak weather" is not only a threat to human life, but it also affects the lives of animals and nature. Through climate change, the natural habits of many animals were shrunk or wholly vanished. Usually, animals could assimilate to changes in their environments, but the rate at which the climate change occurs is too high to adjust. A symbol for the climate change is the polar bear, whose habit becomes smaller and smaller by the melting ice. On the other side, in Australia, there are also animals which are threatened by habit loss like the yellow-footed rock-wallaby or the golden-shouldered parrot.[8] Also, sea dwellers are affected. The higher earth temperature leads to higher adsorption of CO_2 by the seas. This again results in an acidification of the oceans, which makes the seas to a habit, in which many fishes and plants are unviable. This affects again the humanity, especially coastal cities which are dependent on the fishing industry. Another example, which is frequently mentioned related to the consequences of climate change, is the great barrier reef. The corals tend to bleach in a more acidified medium, and they are not prepared for environmental changes like higher temperatures.[8] Therefore, decreasing biodiversity of animals and plants will be one of the greatest disadvantages of global warming.

After this enumeration of many aspects of the climate change caused by the combustion of fossil fuels, it should be clear that the rejection of fossil fuels is unavoidable to stop the negative changes. Therefore, significant efforts are directed toward the development of renewable energy sources that emits no CO_2. Renewable energy sources like biomass will not be discussed here, because they only hit the aspect of the limited feedstock of fossil fuels and not the thereby caused CO_2 emissions.

In Germany, as already mentioned in the introduction, the renewable and sustainable energy sources focus on hydropower, wind and solar energy. Figure 2.3 shows the evolution of the individual methods since 1990. While hydropower has a constant amount to the overall energy production, the amount solar energy rises since 2007, but from 2015 the amount stagnates. For wind energy it is different. The proportion on the overall energy production rises since the turn of the millennium and contributes most significantly to the renewable energy sources.

The renewable energy sources might stop the global warming, but they have one huge disadvantage. They are inextricably linked to environmental conditions, and therefore, they are referred to as fluctuating methods. This means the production of energy fluctuates over one day and night period, but also over the whole year with different seasons. For a constant energy supply, like it is necessary for a balanced grid, this is not a suitable method. In the long term, these methods are only attractive, if it is possible to develop suitable storage devices. A second aspect, which can be called fluctuating is the location of the production site. Colossal wind parks were built in the northern see in offshore parks or PV systems in desert solar parks, which

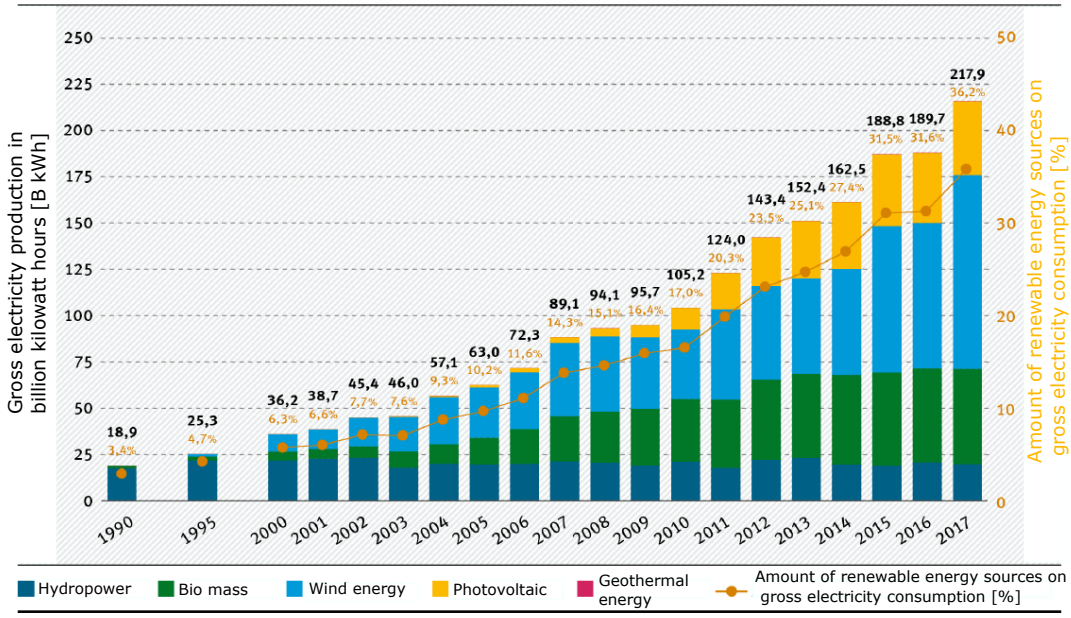

Figure 2.3: Evolution of renewable energy production in Germany. Source: Workgroup Erneuerbare Energien-Statistik (AGEE-Stat).[22]

guarantee intense solar irradiation. To provide many households with this energy, a grid expansion to these power parks is at this time not existing, but necessary to use this energy.

The working principle of a wind turbine is simple. The blades of a wind turbine begin to rotate by capturing the motion energy of wind. A generator produces then electricity through the rotation of the blades like a dynamo of a bicycle.[23] For PV systems, the working principle is not so easy to understand because it involves a more specified knowledge. PV systems are based on semiconductor materials and consist of different layers usually based on silicon. The layers are doped with different materials to create opposite charges and therefore an electric field. One layer is doped with phosphorus due to the higher number of valence electrons (five) compared to silicon (four). This leads to a negative charge of the layer, which is called p-type layer. The second layer is doped with boron due to a smaller number of valence electrons (three), which creates a positively charged layer. The electron vacancies are called holes due to the missing of electrons compared to pure silicon or p-type layers. The layer with the holes is called n-type. Between these two layers, a depletion zone is located, which divides electrons and holes from each other. Through the solar irradiation, an electron of the p-layer is ejected when a photon hits it. Now, there is a hole in the p-layer. The released electron is incorporated in the n-layer. When both layers are connected *via* a metallic wire, the electrons which are incorporated in the n-layer flow back to the p-layer and the holes back to the n-layer. This means a current is produced.[24]

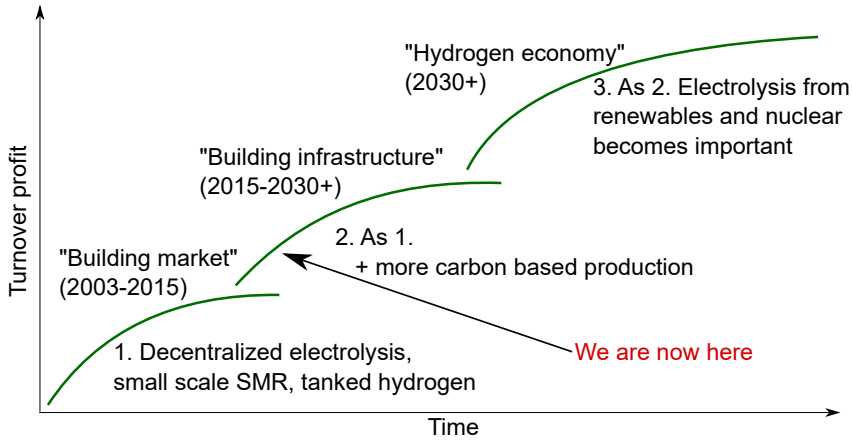

Figure 2.4: Development of a hydrogen infrastructure during the next 20 years.[25] Graphic was modified from original.

Another possibility for the renewable energy production, which was not further discussed until now, is the implementation of a hydrogen economy to use this instead of fossil fuels. Hydrogen has a double or three times higher energy density referred to the mass of fossil fuels with 120 MJ per kg. But if the density is based on the volume, it is reversed. The fossil fuels have a four or five times higher energy density (31 MJ/L–41.5 MJ/L) compared to hydrogen (2 MJ/L–8.5 MJ/L). In this cases, it is of minor importance if the hydrogen is a liquid or a gas,[26] but this is the main handicap of hydrogen as a fuel in mobile applications. To achieve the same distance with a hydrogen-driven vehicle, it is necessary to store the hydrogen under extreme pressure or as a liquid, which requires very low temperatures. Whereas when hydrogen is used in static applications, it is possible to use pipelines and this is not a problem. It is also possible to utilize already existing pipelines for the distribution of hydrogen.

It is necessary to develop production and storage methods for hydrogen to achieve and guarantee a reliable hydrogen economy. At this time, it is not possible to use hydrogen as an energy carrier due to the missing infrastructure and storage possibilities. There are different constitutions, which elaborate timetables to achieve a hydrogen economy. Figure 2.4 shows the timetable published by HYDRO and distributed by the International Energy Agency (IEA), an autonomic unit of the OECD. Unfortunately, they focus on a hydrogen production which is mostly based on fossil resources. Therefore, the production of hydrogen leads automatically to an additional release of carbon dioxide. However, nowadays it is not possible to produce hydrogen only from renewable, sustainable energy sources. According to the IEA, the current time is the research and development phase. First examples of hydrogen-driven vehicles were tested, for example, an airplane, developed by the German aerospace center, which uses hydrogen instead of kerosene or a hydrogen train which connects the German cities Frankfurt and Wiesbaden.[27,28]

2.2 Hydrogen Production

In the 1920's, hydrogen was produced by electrolysis and then shifted toward fossil production ways.[29] In 2010, 96 % of hydrogen was produced from fossil fuels. The primarily used process is steam reforming.[30,31] The process utilizes carbon-based energy sources and water to generate hydrogen. The process is divided into two key steps. The first process is an endothermic reaction. Fossil fuels like hydrocarbons or alcohols and steam react in contact with a heterogeneous nickel catalyst to carbon monoxide and hydrogen. The obtained gas mixture is called synthesis gas. The reaction is depicted in Equation 2.1. Inside the steam reactor, the gases react at 750 °C–1000 °C with a pressure of 15 bar–25 bar.

$$\mathrm{C}_n\mathrm{H}_m + n\,\mathrm{H_2O_{(g)}} \rightleftharpoons n\,\mathrm{CO_{(g)}} + (\mathrm{n} + 0.5\,\mathrm{m})\,\mathrm{H}_{2(g)} \mid \quad \Delta H = 206.2 kJ/mol \tag{2.1}$$

The process gases are passed into a second reactor, the shift reactor. Here, additional steam is added to decrease the overall amount of carbon monoxide and produce more hydrogen. This reaction takes place at 200 °C–300 °C and is in contrast to the first step an exothermic reaction (2.2). After the gases passed through the shift reactor, the hydrogen gas is purified in the last step by adsorption.

$$\mathrm{CO} + \mathrm{H_2O_{(g)}} \rightleftharpoons \mathrm{CO}_{2(g)} + \mathrm{H}_{2(g)} \mid \quad \Delta H = -41.2 kJ/mol \tag{2.2}$$

The energy conversion efficiency is up to 70 %. Two side reactions must be mentioned, which occur during the reforming process. In the first reaction, the produced hydrogen reacts with carbon monoxide to methane and reduces the overall yield of synthesis gas. This reaction is called methanation. The second reaction is called Boudouard reaction. Carbon monoxide decomposes to carbon dioxide and carbon.

Another possibility for the hydrogen production is the partial oxidation of natural gas, coal or oil. The carbon source is mixed with oxygen. The oxygen is supplied in deficiency to the carbon source to prevent the total combustion. The coasts of this process are determined by the use of pure, expensive oxygen.[32] The reaction is exemplified by the partial oxidation of methanol in Equation 2.3.

$$2\,\mathrm{CH_3OH} + \mathrm{O_2(g)} \longrightarrow 2\,\mathrm{CO}_{2(g)} + 2\,\mathrm{H}_{2(g)} \tag{2.3}$$

There are various forward-looking methods to generate hydrogen from one of the most abundant substances: water. The most developed method in this area is water

electrolysis with alkaline or PEM cells (Equation 2.4). The former was developed in the early 1920s. The latter was developed 40 years later in 1960.

$$2\,H_2O \xrightarrow{\text{electricity}} 2\,H_2 + O_2 \tag{2.4}$$

In an alkaline electrolysis cell, KOH is used as an electrolyte. The two half-cells are separated by a diaphragm, which is permeable to hydroxide ions and water molecules. The diaphragm has although the function to keep the evolved gases apart from each other for safety and efficiency reasons, but unfortunately, this membrane is not entirely non-permeable for hydrogen and oxygen gases.[33] In an alkaline cell, the electrode on which hydroxide ions are oxidized to oxygen and water is called anode. The anode is mostly produced from metals like nickel, cobalt or iron. The other electrode, on which water is consumed to form hydrogen and hydroxide ions is called cathode. The cathode is composed of nickel and carbon. In a PEM cell, no additional electrolyte is required like it is necessary for alkaline cells. The half cells are separated by a polymer electrolyte membrane or proton exchange membrane (PEM). The name already implies that this membrane is only permeable to protons and not for gases. At the anode, water is oxidized to oxygen and protons. The protons pass through the membrane to the cathode at which hydrogen is evolved. The electrodes are produced from noble metal. While the anode is composed of iridium, the cathode is made up of platinum. At this time, the PEM is not competitive with the alkaline cell. First, the costs of a PEM cell are too high due to the noble metal electrodes and second, no stack option is available at this time. Stacks are necessary for the industrial production of hydrogen *via* PEM electrolysis to make it competitive with alkaline cells.[29,34]

Through the efficiency of nature, it is only logical to harness natural resources. This field is called photobiological hydrogen production or water biophotolysis. Microalgae and cyanobacteria are capable of producing energy-rich carbon substances and oxygen. They obtain the energy that is required for this process from the sunlight and this process is known as photosynthesis. In a second process, microalgae can produce hydrogen from water. The catalyst for this reaction is a hydrogenase enzyme. One necessary condition to evolve hydrogen with microalgae is an anaerobic environment. If the process is not oxygen-free, the efficiency of hydrogen production drops due to toxic effects of oxygen on the enzymes.[35] Since the conditions are difficult to simulate, *e.g.* anaerobic conditions, nitrogen balance, light energy, a scale up and therefore a long-term solution for hydrogen generation was not successful with this method.[36] Besides the water biophotolysis, the organic biophotolysis is also a method for hydrogen production which should be mentioned here. Organic molecules are converted into water and carbon dioxide with enzymes. With this

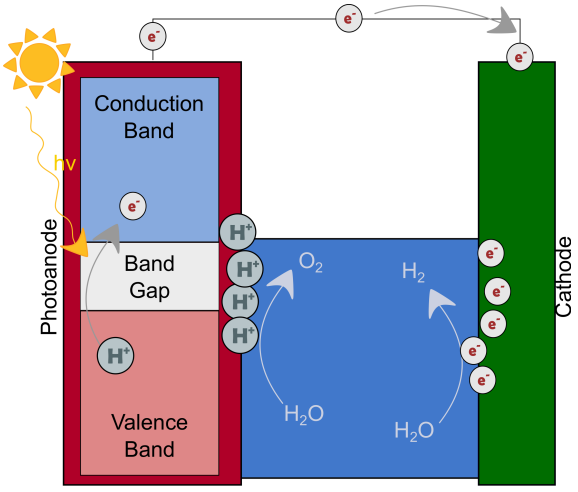

Figure 2.5: Schematic representation of a PEC cell consisting of a semiconductor and an electrolysis cell.[41] Graphic was modified from original.

significant disadvantage due to the need for emission reduction, the process is not further discussed here.[37,38]

An entirely different scientific research focuses on the development of photo-electrochemical cells (PEC) as shown in Figure 2.5. These cells are described as a light-absorbing semiconductor that is connected to an electrolysis unit. Through irradiation with sunlight either electricity or hydrogen is produced.[39] The solar irradiation generates holes and electrons within the photoanode (semiconductor). The electrons are transferred to the cathode *via* an external wire. At the cathode, water is split into hydrogen, while on the surface of the photoanode oxygen is evolved.[40] The major challenge for this method is the development of suitable materials for the process. The requirements of such electrode materials and process technologies relate to two areas. On the one side, high efficiency and hence, performance is essential, and on the other side, non-corrosive materials which lead to longevity due to the constant contact with water. If these major points are overcome, the PEC is a highly attractive commercial method for hydrogen and electricity formation.[25]

The last method to evolve hydrogen from water is explained in the next section. Similar to the PEC cells, the photocatalytic water splitting utilizes the solar irradiation, but now molecular systems are used to produce hydrogen from water instead of a semiconductor and an electrode.

2.3 Photocatalytic Homogeneous Water Splitting

It is essential to understand the thermodynamics of water conversion to understand the development of catalytic light-driven water splitting systems. The reaction is

an uphill process with a free Gibbs energy ΔG° of 237 kJ per mole as shown in Equation 2.5.[42] This corresponds to an energy barrier of 1.23 eV, which have to be overcome by irradiation with wavelengths shorter than 1000 nm.[43] Since the sun supplies suitable radiation for this process, it is a logical and attractive way to use solar energy.

The energy-demanding reaction is the water oxidation, which requires energy of 1.23 eV and therefore, this is the crucial reaction to realize the overall water splitting.[44]

$$2\,\mathrm{H_2O} \longrightarrow 2\,\mathrm{H_2} + \mathrm{O_2} \mid \qquad 474kJ \tag{2.5}$$

$$Oxidation : 2\,\mathrm{H_2O} \longrightarrow 4\,\mathrm{H^+} + 4\,\mathrm{e^-} + \mathrm{O_2} \tag{2.6}$$

$$Reduction : 4\,\mathrm{H^+} + 4\,\mathrm{e^-} \longrightarrow 2\,\mathrm{H_2} \tag{2.7}$$

Despite the Equations 2.5–2.7 appear to be trivial, the understanding of the mechanisms responsible for the overall water splitting with molecular systems is lacking. To change this deficiency, the half reactions of water oxidation (2.6) and reduction (2.7) are investigated separately. Moreover, only when an adequate knowledge of the half reactions is obtained, the reactions should be combined to the overall water splitting reaction. As long as they are investigated separately, both reactions need an additional reagent which donates or accepts electrons due to the missing of the second half-cell reaction. In water reduction, this additional reagent is called sacrificial reductant (SR), which donates electrons. In water oxidation, the reagent is called sacrificial oxidant (SO), and this compound accepts electrons that were released by the oxidation of OH^- to O_2.

The molecular, homogeneous systems are based on two different approaches that are shown in Figure 2.6. Both methods use identical components, but they are still different. First, there was the two- or multi-component approach, which was based on the combination of individual components to evolve hydrogen. All systems contain a photosensitizer (PS), which is capable of absorbing sunlight and generating an excited state (PS*). The second essential component is the water reduction catalyst (CAT) on which the reduction of protons to hydrogen takes place. A third component, which can be omitted in many multi-component systems, is an electron relay. By excitation of the PS, the PS* is capable of donating an electron directly to the catalyst or in some cases to the electron relay, which afterward donates this electron to the catalyst. If an electron relay is necessary depends on the applied system and

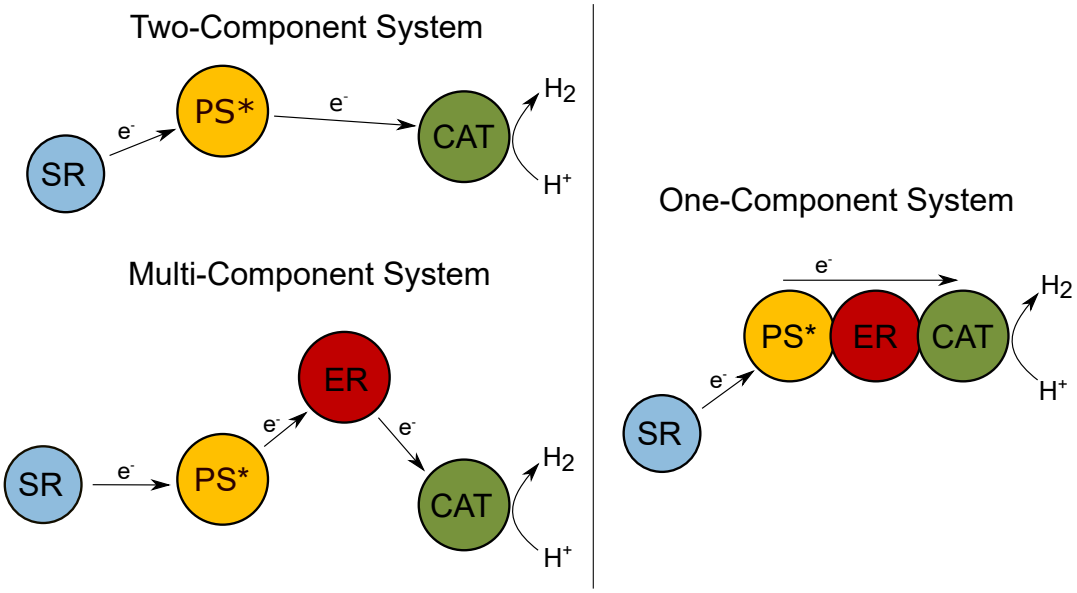

Figure 2.6: Schematic representation of two- or multi-component system and an one-component system. PS* is the excited photosensitizer, ER is the electron relay or bridge, CAT water reduction catalyst and SR the sacrificial reductant.

properties of PS and CAT, *e.g.*, the redox potentials.[45–47] The CAT has to pass two cycles for the evolution of one molecule hydrogen.

The one-component approach is constructed of identical components. Historically, not sure if a development which goes on for only 40 years should be called so, the one-component systems were invented later and they are a further development of the multi-component-systems.[48–50] One might think a further development is undoubtedly more efficient for the hydrogen evolution, but the systems and processes are complex and this make such a general statement illegitimate.[51–53] As diverse as the systems are the notations of this approach: Some call them one-component systems, some supramolecular devices or assemblies and still other call them dyads or triads.[51,54–56] However, back to the differences between one- and two-component systems. As before mentioned, the one-component system contains the identical components as the two-component system. But these components are connected to each other by a linker or bridging ligand. This structural organization of the separate units results in a different electron transfer within the one-component system. While the electron transfer of a two-component system is diffusion dependent and determined by the applied concentrations of components, temperature and viscosity of the solvent, the one-component system uses an intramolecular electron transfer.[57,58] This makes parameter like component concentrations or solvent viscosity irrelevant. However, one-component systems are highly influenced by the linker that connects the PS and the CAT. Up to now, it remains unclear, if a conjugated system, aromatic or non-aromatic, an alkyl chain, an amide or ester is the most efficient electron transfer building block.

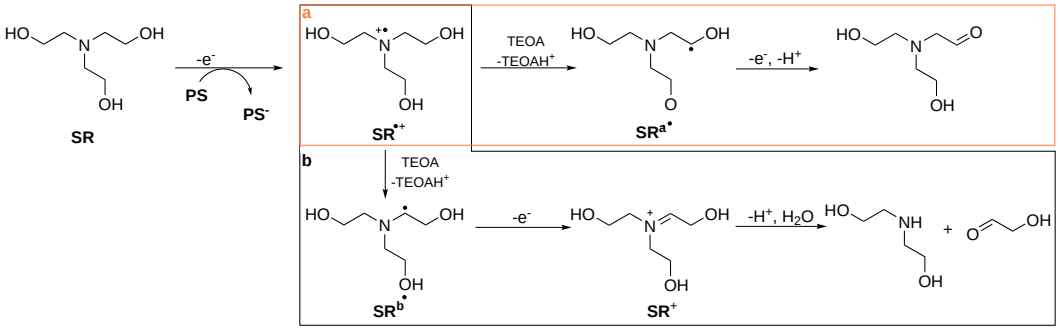

Scheme 2.1: Degradation of TEOA after the donation of an electron during photocatalytic proton reduction without water (route a) or in the presence of water (route b).[62]

2.3.1 Sacrificial Reductant

Sacrificial reductants (SRs) must be used in every water reduction system. A sacrificial reductant donates an electron to the photosensitizer to guarantee a restart of the catalytic cycle. They are mostly used with high excess due to the consumption and subsequent degradation of the SR after the electron donation. Typically used SRs are triethanolamine (TEOA), triethylamine (TEA), ascorbic acid, dimethylamine (DMA) or ethylenediaminetetraacetic acid (EDTA).[45,46,59–61] It is also important that the SR does not degrade automatically in the applied system and it is necessary that the SR does not interfere with the catalyst or solvent. Otherwise, recombination processes between PS and SR and CAT and SR could occur.[62] The degradation process of TEOA induced by the e^- transfer is shown in Scheme 2.1. In the first step after the donation of the electron to the PS, a positively charged aminyl radical $\mathbf{SR}^{\cdot+}$is formed. This is a good oxidant and promotes the unwanted back electron transfer: In case of reductive quenching back electron transfer from PS^- and for the oxidative quenching back electron transfer from CAT^-. Through deprotonation of this radical by TEOA, a carbon-centered radical is formed ($\mathbf{SR}^{a\cdot}/\mathbf{SR}^{b\cdot}$). This new radical has a high reductive power and therefore, reduces the PS or mediates the electron transfer between PS and CAT.[63] This process is called dark electron transfer because no irradiation with light is necessary for this step. In a water-free environment, the degradation stops with this step (route a). In the presence of water, the degradation goes on an stops with hydroxyethanal and a secondary amine (route b). The degradation of TEA proceeds *via* a similar mechanism.[64,65]

If the excited state PS* accepts the electron from the SR and donates the electron afterward to the CAT, this is called reductive quenching. However, there is a second process where the PS* gets first oxidized by the CAT and afterward reduced by TEOA to restart the cycle for the hydrogen evolution. This second process is referred to as oxidative quenching. Both mechanisms are shown in Figure 2.7.[47] It is essential that the quenching process proceeds with high efficiency. The efficiency of

quenching is determined *via* quenching experiments and subsequent generation of a Stern-Volmer-Plot.

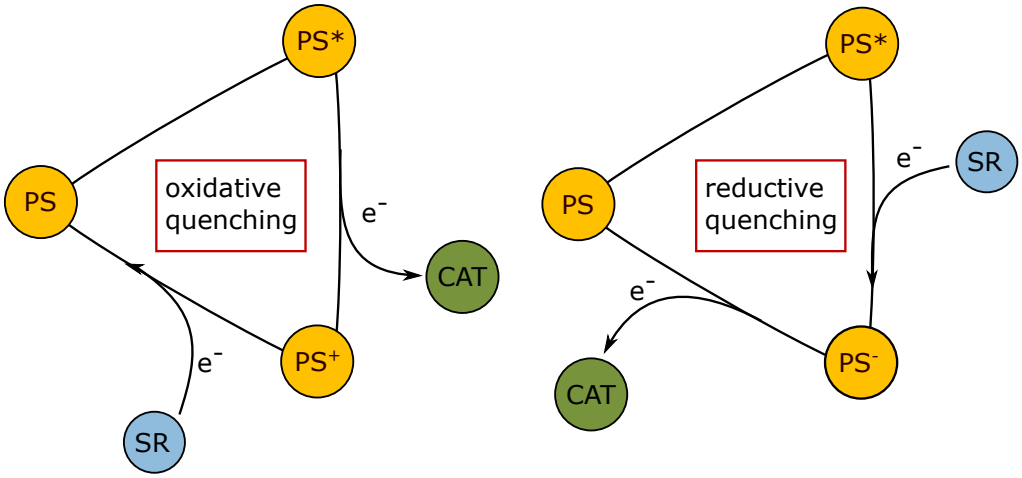

Figure 2.7: Quenching pathways for an excited state photosensitizer. Both mechanisms involve all three components.

There are two different mechanisms which can be distinguished for quenching processes: the dynamic and static quenching. In case of dynamic quenching, the excited molecule (PS*) returns to the ground state (PS) by collision with a quencher Q and therefore the excitation energy is transferred from the excited photosensitizer to the quencher. The Stern-Volmer equation for dynamic quenching is shown in Equation 2.8.[66,67]

$$\frac{I_0}{I} = \frac{\tau_0}{\tau} = 1 + k_q \cdot \tau_0 \cdot c(Q) = 1 + K_{SV} \cdot c(Q) \tag{2.8}$$

I_0 is the emission intensity in the absence of a quencher, whereas I is the emission intensity while a quencher is present. τ_0 is the lifetime of the excited state in the absence of a quencher, whereas τ refers to the excited state lifetime in the presence of a quencher. k_q is the bimolecular quenching rate constant [$M^{-1} \cdot s^{-1}$] and provides information about the efficiency of the quenching process. Ideally, k_q has the same magnitude as the diffusion rate constant k_{diff} and is consequentially a diffusion-controlled process.[68] Both parameters, τ and k_q are summarized in K_{SV}, which is called Stern-Volmer constant. And last, c(Q) is the concentration of the quencher molecule.[69] The Stern-Volmer equation is derived from the excited state lifetime. Without a quencher, the excited state lifetime τ_0 is influenced by fluorescence and non-radiative decays.

$$\tau_0 = \frac{1}{k_f + k_{nr}} \tag{2.9}$$

In the presence of a quencher, the excited state lifetime τ is reduced by the amount of a quencher $k_q c(Q)$.

$$\tau = \frac{1}{k_f + k_{nr} + k_q c(Q)} \tag{2.10}$$

By plotting $\frac{I_0}{I}$ or $\frac{\tau_0}{\tau}$ against the quencher concentration, a linear graph is obtained. The rise of the experimental temperature results in a steeper graph. In contrast, a less steep graph by a rise of the temperature is a result of static quenching. Opposed to the dynamic quenching, in static quenching no energy transfer occurs by collision of the excited molecule with the quencher. In this case, the fluorescence vanishes by the formation of a radiation-free adduct (FQ) composed of the excited state molecule F and the quencher Q.[67] The resulting Stern-Volmer equation is given in Equation 2.11.[70]

$$\frac{I_0}{I} = 1 + \frac{FQ}{F \cdot Q} \cdot c(Q) = 1 + K_a \cdot c(Q) \tag{2.11}$$

Both, dynamic and static quenching, are extreme cases and it is also possible that a mixture of both processes occurs. Consequently, the Stern-Volmer equation for a mixed quenching is composed of both individual Stern-Volmer equations:

$$\frac{I_0}{I} = (1 + K_{SV} \cdot c(Q)) \cdot (1 + K_a \cdot c(Q)) \tag{2.12}$$

For the dynamic quenching process, a linear graph is obtained by plotting $\frac{I_0}{I}$ against the quencher concentration. If the mixed process is present, an upward graph is obtained for this plot and for the plot $\frac{\tau_0}{\tau}$ against the quencher concentration a linear graph is obtained. In contrast, for static quenching, this plot would result in a straight line with slope zero.[70]

2.3.2 Photosensitizer

Iridium has the atomic number 77 and is located in the 9th group of the periodic table. The electronic configuration is $[Xe]4f^{14}5d^{7}6s^{2}$. The metal was discovered in 1804 by Smithon Tennant as an impurity in crude platinum. Iridium or in classical Greek ιριοειδης means colorful like a rainbow. Tennant chose this name due to the high variety of colors obtained with iridium compounds.[71] Iridium compounds could possess a huge number of formal oxidation states from -I to +IX. Ir^{+IX} is the highest oxidation state of an element reported yet. It was found in 2014 as $[IrO_4]^+$ by the group of Mingfei Zhou.[72] The most common oxidation state is +I and +III. In Ir^{+III} compounds, which should be considered here because the PS is an Ir^{+III}

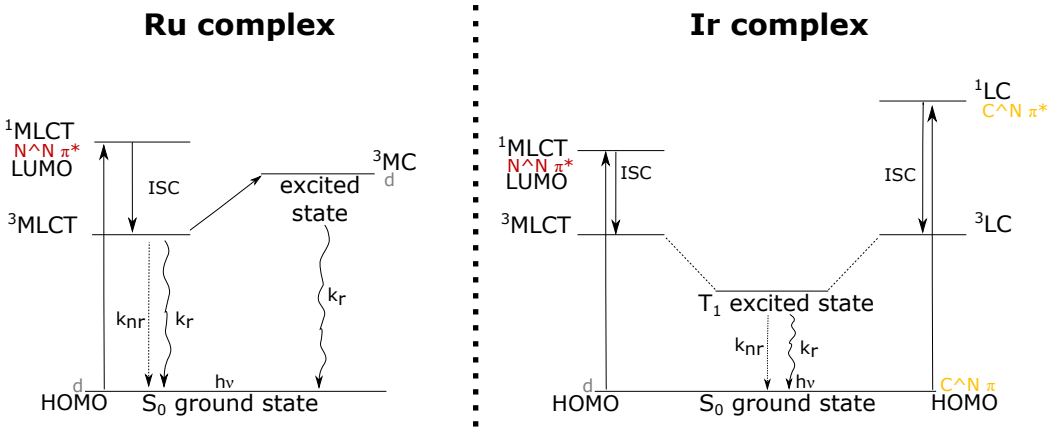

Figure 2.8: Jablonksi diagrams of $[Ru(N^{\wedge}N)_3]^{2+}$ (left) and $[Ir(N^{\wedge}N)_2((C^{\wedge}N)]^{+}$ (right) complex.[98–101]

complex, the electronic configuration is $5d^6$. They are mostly sixfold coordinated and show an octahedral arranged.[71]

Iridium complexes are widely used in many different fields like catalysis,[73–75] bioimaging,[76–78] OLEDs[79,80] or LEECs[81]. For most of these applications, they take advantage of the photophysical properties of iridium complexes. In photocatalytic water splitting they are used as catalysts in water oxidation[82–85] or as photosensitizers in water reduction.[4,86–88] The first time that an iridium complex was used as a photosensitizer (PS) was in 1979 by Lehn and Sauvage.[89] They chose $[Ir(bpy)_3]^{+}$ as PS in a system with TEOA as SR and K_2PtCl_4 as CAT. Nearly 30 years ago, they already showed the ability of iridium complexes to act as photosensitizers, but they also postulate that iridium complexes could never compete with rhodium complexes in photocatalytic water reduction experiments. This forecast was proven wrong. Iridium complexes were the preferred PS over many years and still are due to their superior photophysical properties and the high tunability through ligand modifications.[43,60,86,90–95] Before iridium complexes were even tested as photosensitizers ruthenium complexes were used instead, but compared to the iridium PSs their photophysical properties are static and could not be adjusted as desired.[5,45,96,97] Therefore, iridium complexes mostly replaced the ruthenium PS in photocatalytic applications.

Figure 2.8 shows two Jablonski diagrams of a ruthenium (II) tris(diimine) complex and an iridium (III) complex with two cyclometalating and one diimine ligands. The excited states of both complexes are composed differently. While the excited state of a ruthenium complex is only influenced by the MLCT state, the excited state of an iridium complex shows a mixed character of MLCT and LC transitions.[102] The distinctive feature is that the MLCT transitions only occur on the neutral diimine ligand and the metal center, while the LC transitions are mainly located on the cyclometalating ligands. This explains the tunability of the photophysical properties

of iridium complexes. The excited state can be influenced by first, modifying the N^N ligand and therefore the MLCT state and second, modifying the C^N ligand and consequently the LC state. The impact of MLCT and LC transitions on the excited state is flexible and can change from iridium complex to complex, which makes a prediction of the exact excited state composition and properties difficult.[99,103]

This theory can also be considered from another view. DFT calculations show that the HOMO of a Ru(II) complex is entirely located on the ruthenium center, whereas the HOMO of an Ir(III) complex is located on the C^N ligand and the metal center. On the other side, the LUMO of a ruthenium complex is entirely composed of a N^N ligand-centered state, and in contrast to that, the LUMO of an iridium complex is almost entirely located on the N^N ligand.[100,101] Therefore emission spectra of iridium complexes are quite interesting because they give some indication of the excited state composition. If the LC character strongly influences the excited state of an iridium complex, a vibronic structure is observable in the emission spectrum, whereas broad and featureless emission bands are typical for a primarily MLCT composed excited state.[104,105]

As already described before the HOMO and LUMO can be tuned by modifications on the C^N and N^N ligand. Certainly, the redox potentials are also influenced by the choice of the ligand. The first reduction process is equivalent to the excitation of an electron into the LUMO of a complex. Therefore the reduction potential is strongly affected by the N^N ligand. The oxidation potential of the Ir^{III+}/Ir^{IV+} couple is also strongly influenced by the character of the C^N ligand.[99,106] Using the redox potentials, another key parameter could be determined to understand the photophysical behavior of iridium photosensitizers: The excited state potential could be calculated using the ground state potentials obtained from CV measurements and the emission energy obtained from the emission spectrum.[107] This will be discussed later in more detail in Chapter 4.3.4.

The group of Bernhard incorporated the theoretical background and synthesized a huge library of iridium complexes.[103,106,108] In Figure 2.9, a set of different cyclometalating and neutral ligands are shown, which were synthesized by Bernhard's group.[60] They were combined with each other to result in the following complexes: $[Ir(ppy)_2bpy]^+$, $[Ir(Fmppy)_2bpy]^+$, $[Ir(Fmppy)_2dpbpy]^+$, $[Ir(ppy)_2dpbpy]^+$ and $[Ir(ppy)_2phen]^+$. With this five examples, the before described influences can be illustrated. The cyclometalating ligand should be considered first. Therefore $[Ir(ppy)_2bpy]^+$ and $[Ir(Fmppy)_2bpy]^+$ were compared to each other. As described, the HOMO of iridium complexes is completely localized on the C^N ligand. By the introduction of a fluorine substituent on the phenyl ring as an electron-withdrawing group, the electron density is pulled away from the metal center. Therefore, the metal d orbitals are stabilized, which is equivalent to a stabilized HOMO. Hence, the

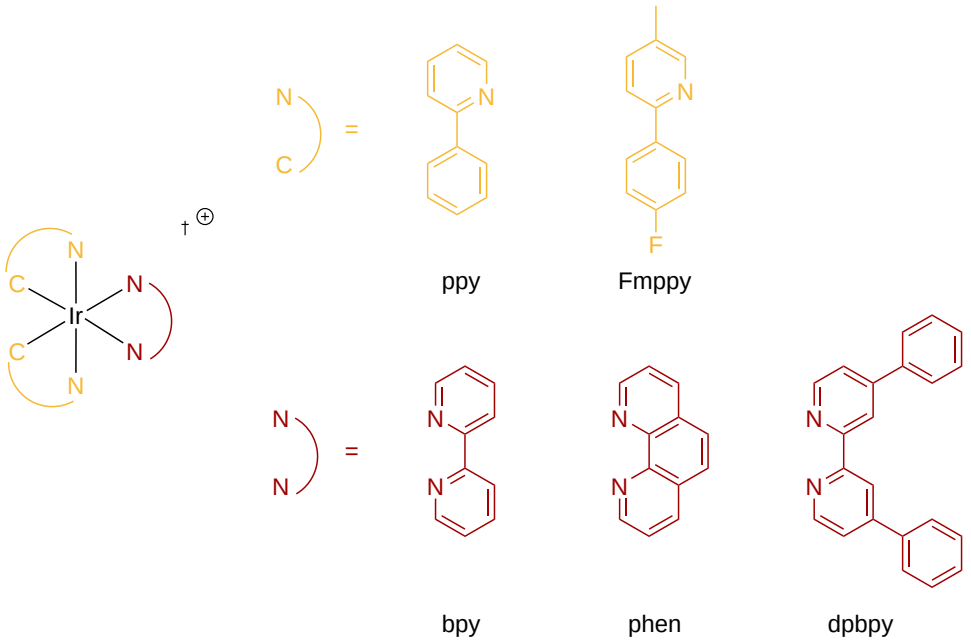

Figure 2.9: Iridium complexes with two different cyclometalating and three neutral ancillary ligands designed by Bernhard's group.[60]

oxidation of the iridium is more difficult in this case.[106] It is reflected by a 130 mV increased oxidation potential from 1.25 V to 1.38 V. The excited state lifetime τ is also increased by a factor of 2.5 from 390 ns in the ppy complex to 1049 ns in the Fmppy iridium complex.

Now, the N^N ligand should be considered and therefore the LUMO properties. By changing bpy to phen as the neutral ligand, no significant changes in the reduction potential are observed. However, when the extended bipyridine system (dpbpy) is used, the reduction potential is shifted from -1.42 V to a less negative potential of -1.38 V and consequently, the LUMO of this complex is lowered by a stabilization of the π^* orbitals compared to the bpy complex.[104] A combination of both modifications on the C^N and N^N ligand is represented in $[Ir(Fmppy)_2dpbpy]^+$. This complex has the highest oxidation and reduction potential and the longest excited state lifetime of all five complexes. By a more extreme modification of both ligands, the photo- and electrochemical properties could be shifted more. The composition of the excited state could also remarkably change by a ligand exchange to a more substantial contribution of either the LC or the MLCT state.[109]

The first part of this section focused on the photo- and electrochemical properties of iridium photosensitizers. Now, the electron transfer of an iridium complex in a water splitting system should be discussed in more detail. Despite the redox potentials of the iridium photosensitizers were already considered above, they should be again discussed here under the electron transfer aspect.

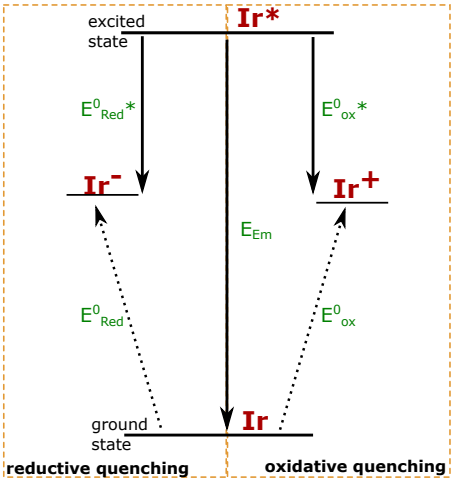

Figure 2.10: General ground and excited state diagram involving the potentials of an iridium complex that are obtained from CV data and calculated with the Hess law.[107,110,111]

Therefore, some knowledge of the processes that involve a photosensitizer during water reduction is necessary. The photosensitizer in a water reduction system could be quenched *via* an oxidative or a reductive pathway. The reductive pathway occurs when the excited state photosensitizer is quenched by the sacrificial reductant (SR) *via* a donation of an electron to the photosensitizer. Opposed to that, oxidative quenching occurs when the excited photosensitizer gives an electron to the catalyst and is therefore oxidized. Both pathways proceed *via* the degradation of the excited state. Thus, the knowledge of the redox potentials of the catalyst, sacrificial reductant and the excited photosensitizer is essential. The excited state potential of the PS is estimated by using Hess´s law of heat summation. The required equations are given in 2.13 and 2.14.

$$E_{Ox}^{0\ *} = E_{Ox}^{0} - E_{Em} \tag{2.13}$$

$$E_{Red}^{0\ *} = E_{Red}^{0} + E_{Em} \tag{2.14}$$

The parameter E_{Em} is obtained from the maximum of the emission spectrum and E_{Red}^{0}/E_{Ox}^{0} are taken from the ground state potentials of the CV analysis.[107,110,111] Figure 2.10 elucidates the coherences given by the Hess law.

The calculations will be shown here for $[Ir(Fmppy)_2dpbpy]^+$ as an example. The reduction potential of the ground state for this iridium complex is -1.35 V (*vs.* SCE), the oxidation potential is 1.36 V and the energy of the emission maxima is 2.2 eV (564 nm). This results in an excited state oxidation potential $E_{Ox}^{0\ *}$ of -0.84 V (*vs.* SCE). This potential is important for the oxidative quenching pathway and will be compared to the redox potential of the CAT, for example, $PyCo(dmgH)_2Cl$ with -1.22 V. The excited state oxidation potential of $[Ir(Fmppy)_2dpbpy]^+$ is unfavorable for an oxidative quenching process. For the excited state reduction potential $E_{Red}^{0\ *}$

a value of 0.85 V (*vs.* SCE) is obtained, which must be compared to the potential of the sacrificial reductant, for example, TEA.[60] The potential of TEA is 0.69 V (*vs.* SCE). The comparison of the redox potentials of PS* and the SR shows that the reductive quenching is favorable for a system with this iridium complex, TEA as SR and $PyCo(dmgH)_2Cl$ as CAT.[112]

Another factor that must be taken into account when photocatalytic water splitting is discussed is the excited state lifetime of the photosensitizer. Systems with a long-lived charge-separated state are desirable because of the long duration of diffusion-dependent electron transfer. However, this long-lived state, which is in general favorable, also has a few disadvantages. Through the extended length of the excited state, recombination processes and hence, deactivation and decomposition of the PS became likelier.[88,113] In contrast, too short lifetimes make an electron transfer to the PS* or from the PS* to the catalyst unlikely. A larger LC character of the excited state results mostly in a prolonged excited state lifetime. For example, $[Ir(ppy)_2bpy]^+$ and $[Ir(Fmppy)_2bpy]^+$ exhibited lifetimes τ of 390 ns and 1049 ns. This small variation on the CˆN ligand yielded in an increased excited state lifetime and therefore in a larger contribution of the LC state to the mixed excited state.[60] The water splitting results support the theoretical considerations and a TON of 920 was achieved for the Fmppy iridium complex and a TON of 800 for the ppy iridium complex.

The electron transfer can also be influenced by the connection of PS and CAT. Through a non-covalent or covalent bond, the electron transfer from the PS to the CAT can be influenced. In the last years, different methods were developed and tested to generate linked systems. For example with vinyl groups on the NˆN ligand. With this modification, it was possible to adsorb the photosensitizer on a colloidal platinum catalyst, which enhanced the catalytic activity significantly.[114,115] Another approach utilized cyano groups on the NˆN ligand for a non-covalent linkage to colloidal platinum. To ensure that the cyano groups were adsorbed on the platinum surface, they also tested a molecular rhenium catalyst that is known as a homogeneous catalyst and should not show this behavior. With this modifications, a reduced hydrogen evolution was achieved. Interestingly, these systems exhibited low excited state lifetimes that should, in general, reduce the catalytic activity, but the advantages of the cyano group overcame this disadvantage.[116]

At the end of the photocatalytic experiments, most iridium photosensitizers degrade. The typical degradation mechanism is shown in the Scheme 2.2. The diimine ligand dissociates from the iridium complex through irradiation and is replaced by solvent molecules. This degradation process is more prominent in coordinating solvents like acetonitrile. The dissociation is caused by the population of the anti-bonding π^* orbital of the diimine ligand. The iridium complex that is formed by the

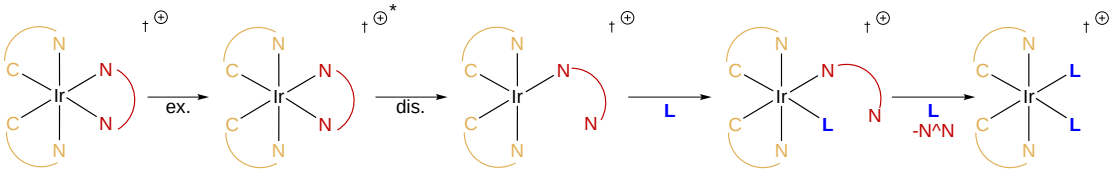

Scheme 2.2: Degradation of an iridium photosensitizer triggered by the irradiation with light. ex.= excitation, dis.= dissociation.[88]

coordination of two solvent molecules is inactive in photocatalytic water reduction experiments, which finally result in no further hydrogen evolution.[88]

2.3.3 Catalyst

The general molecular formula of cobaloximes is $Co(dmgH)_2(B)X$, where B is a base and X an anion. Cobaloximes were first reported in 1907 by Tschugaeff. He named this substances "Kobaltiake" and discovered first the ammonia derivatives with the general structure $Co(dmgH)_2NH_3X$. One year later he also reported the pyridine derivatives of $Co(dmgH)_2PyX$.[117] The trivial name cobaloxime was established by Schrauzer and Kohnle in 1964 and refers to the cobalt-dimethylglyoximato unit ($Co(dmgH)_2$). They introduced cobaloximes as a model compound for cobalamines like vitamin B_{12} or coenzyme B_{12}. Cobalamines are natural structures that are coordinated by five nitrogen atoms, whereby four of the nitrogens are square planar coordinated, and one nitrogen is axially bound. Schrauzer and Kohnle assumed that cobaloximes are suitable and easy accessible model compounds due to the obvious similarity of these two structures.[118] Through the sp^2 hybridization of the nitrogen atoms of the cobaloximes, they are known as stable complexes. In 1968 Schrauzer first described the influence of the pH on the present cobalt species. He also reported the formation of a cobalt(III) hydride based on the conversion of a Co(I) species. This was an important observation, which will be later relevant for photocatalytic water reduction experiments conducted with cobaloximes as catalysts.[119]

The general structure of cobaloximes is shown in Figure 2.11. The cobalt is coordinated to two bidentate anions of dimethylglyoxime, called dimethylglyoximato ($dmgH_2$). The coordination of the bidentate ligands is square planar, and a base and an anion occupy the axial positions. As mentioned before, cobaloximes are prone to pH changes, which is important to understand the mechanisms and conditions when they are used as catalysts in water reduction experiments. Under acidic conditions protonated base, dimethylglyoxime and cobalt salts are formed. Whereas, when basic conditions prevail, derivatives of $Co(dmgH)_2$ are formed.[120]

In 1978, Chao and Espenson investigated the mechanism of hydrogen evolution based on the formation of a Co(III) hydride. They reported that depending on the

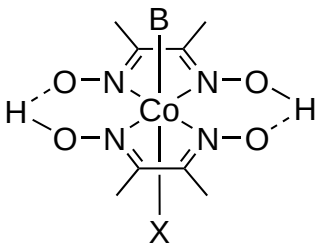

Figure 2.11: General structure of a cobaloxime. B is referred to a base and X to an anion.

applied system (hydride concentration and pH), a homolytic or heterolytic pathway is possible for the H_2 generation. Homo- and heterolytic refers here to the cleavage of the cobalt hydride bond. If two Co(III)H are required for the evolution of one molecule hydrogen, as depicted in Equation 2.15, it is called homolytic.[121]

$$2\,\mathrm{Co}^{(+\mathrm{III})}\mathrm{H} \longrightarrow 2\,\mathrm{Co}^{(+\mathrm{II})} + \mathrm{H}_2 \tag{2.15}$$

On the other hand, if hydrogen is evolved under the application of one Co(III)H and a proton, it is called heterolytic cleavage (see equation 2.16).

$$\mathrm{Co}^{(+\mathrm{III})}\mathrm{H} + \mathrm{H}^+ \longrightarrow \mathrm{Co}^{(+\mathrm{III})} + \mathrm{H}_2 \tag{2.16}$$

Years later, another mechanism was postulated that involves a reduction of a Co(III)H to a Co(II)H and hydrogen is released *via* the heterolytic mechanism (Equation 2.17 and 2.18).[122,123]

$$\mathrm{Co}^{(+\mathrm{III})}\mathrm{H} + \mathrm{e}^- \longrightarrow \mathrm{Co}^{(+\mathrm{II})}\mathrm{H} \tag{2.17}$$

$$\mathrm{Co}^{(+\mathrm{II})}\mathrm{H} + \mathrm{H}^+ \longrightarrow \mathrm{Co}^{(+\mathrm{II})} + \mathrm{H}_2 \tag{2.18}$$

The first time, that a cobaloxime was used as a water reduction catalyst was in 1983 by Lehn *et al.* They used $[\mathrm{Ru(bpy)_3}]^{2+}$ as photosensitizer with $\mathrm{Co(dmgH)_2(OH)_2}$ as catalyst in DMF at a pH of 8.8.[48] Afterward many research, photochemical and electrochemical, was focused on the optimization of the catalyst itself and the catalytic environment.[122,124–126]

2.4 Supramolecular Devices

Cobaloximes were also tested in supramolecular arrangements as catalysts, which are characterized by a connection between the photosensitizer and the catalyst. This results in an intramolecular electron transfer instead of an intermolecular transfer between the individual components. As photosensitizers ruthenium and iridium complexes, porphyrins or organic dyes were used, whereas the cobaloxime contained the BF_2- or OH-bridged glyoximes as ligands.

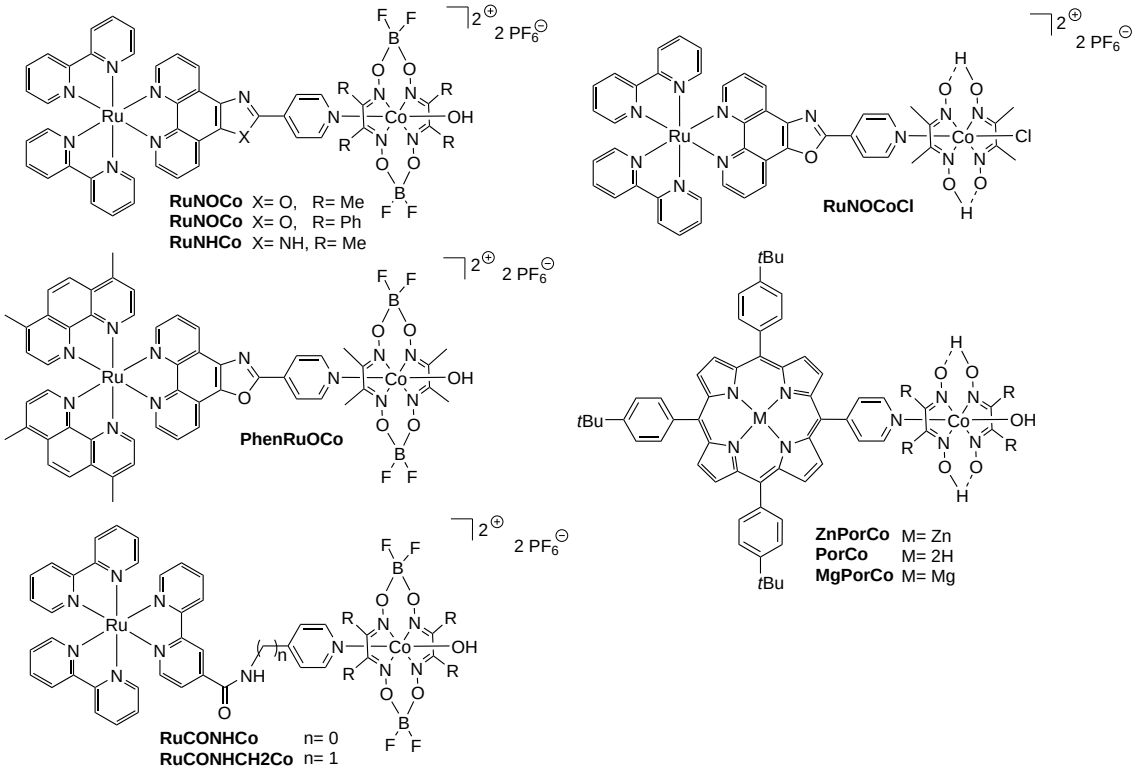

Figure 2.12: Supramolecular systems based on a cobaloxime catalyst and varying photosensitizer units for photocatalytic hydrogen generation.[53,127–129]

Figure 2.12 shows a selection of supramolecular cobalt systems. The only systems, which are identical except of a modification within the cobalt catalyst are **RuNOCo** and **RuNOCoCl**. Therefore, only this two Ru-Co-systems were compared with regard to the catalyst unit. In **RuNOCoCl** the BF_2-bridge is replaced by OH-groups on the glyoxime ligand. Additionally, the axial hydroxyl ligand is replaced by a chloride. This modifications resulted in a reduced TON_{Cat} of 17 when **RuNOCoCl** is used in the light-driven hydrogen evolution experiments. In contrast, **RuNOCo** achieved under identical conditions a twice as high TON_{Cat} of 32. The increased activity of the BF_2-bridged system is a consequence of the two modifications. The BF_2-cobaloxime provides higher stability and tolerance against hydrolysis and hydrogenation, and the initial Co^{2+} state of **RuNOCo** is also more easily reducible, which finally results in an enhanced hydrogen evolution.[53] However, the other eight examples should also be considered, even if they were modified either on the photosensitizer or the linker building block. Therefore, **RuNOCo** and **PhenRuOCo** were compared to each other due to different cyclometalating ligands of the PS building block. By an exchange from bipyridine to dimethylphenanthroline the TON_{Cat} was reduced from 60 to 9.[53,127] Finally, the activity of **RuNOCo**, **PhenRuOCo**, **RuCONHCo** and **RuCONHCH2Co** were compared due to the same experimental conditions during the photocatalytic hydrogen evolution experiments. As before already mentioned, **RuNOCo** has a TON_{Cat} of 60, and **PhenRuOCo** a TON_{Cat} of 9. The systems con-

taining an amide functionality on the linker unit (**RuCONHCo**, **RuCONHCH2Co**) are also interesting. The minor modification generated by insertion of a CH_2 group (**RuCONHCH2Co**) results in an increased TON_{Cat} of 48 compared to the system without CH_2 (**RuCONHCo**) and a TON_{Cat} of 38. The authors postulate a back electron transfer in the conjugated system **RuCONHCo**, which led to a slightly reduced hydrogen evolution.[128]

To sum up, even small modifications in the supramolecular assembly can change the activity of these systems drastically and up to this point, the experimental conditions are not taken into account in this discussion. However, at least an impression of the complexity of this linked systems is given.

An example of a dyad with another non-precious cobalt catalyst was reported in 2010 by the group of Sakai.[56] They produced four different iridium-cobalt molecules, which are distinguished by the bridging ligand. All four systems are shown in Figure 2.13. The synthetic strategy was different from other reported supramolecular devices. They choose an *in situ* self-assembly approach, which utilizes an iridium complex with a N^N ligand that can be coordinated by cobalt chloride *in situ*. In a photocatalytic hydrogen evolution experiment, the dyad with **L1** as bridging ligand reached the highest TON_{Cat} of 5.2. The system with **L3** ended up with a TON_{Cat} of 3.9 and **IrL4Co** with a TON_{Cat} of 2.5. Unfortunately, they did not test **L2** under identical conditions. Sakai's group also used systems where one of the components were neglected but none of these systems produced hydrogen. They also tested the analogously two-component-system composed of $[Ir(ppy)_2(bpy)]^+$ as photosensitizer and $[Co(bpy)_3]^{2+}$ as catalyst. This system reached under identical conditions in a hydrogen evolution experiment a TON_{Cat} of 2.4. Hence, in this case, the self-assembled Ir-Co system with **L1** as ligand is a more effective water reduction system as the corresponding two-component system. Despite the systematic variation of the bridging ligand with an alkyl or alkyne chain or a hydroxy group on the alkyl chain, they did not discuss the activity of the different systems regarding the nature of the bridging ligand. This is an interesting aspect which is lacking for this system up to now.

In literature, three different systems are known, consisting of an iridium photosensitizer and a cobaloxime reduction catalyst. The three dyads are shown in Figure 2.14. The first system (**IrOxaOCo**) was synthesized in 2008 by Fihri and Fontecave.[127] The iridium PS is composed of two cyclometalating and one neutral ligand. The neutral phenanthroline molecule is connected *via* an oxazole to a pyridine, which is the ligand for the cobalt catalyst. They choose difluoroboryl groups as residuals on the cobaloxime, which provides higher stability as hydroxyl groups.[130] This dyad was tested in a photocatalytic hydrogen evolution experiment with acetone as solvent, TEA as sacrificial donor and Et_3NHBF_4 as proton source. The concentration

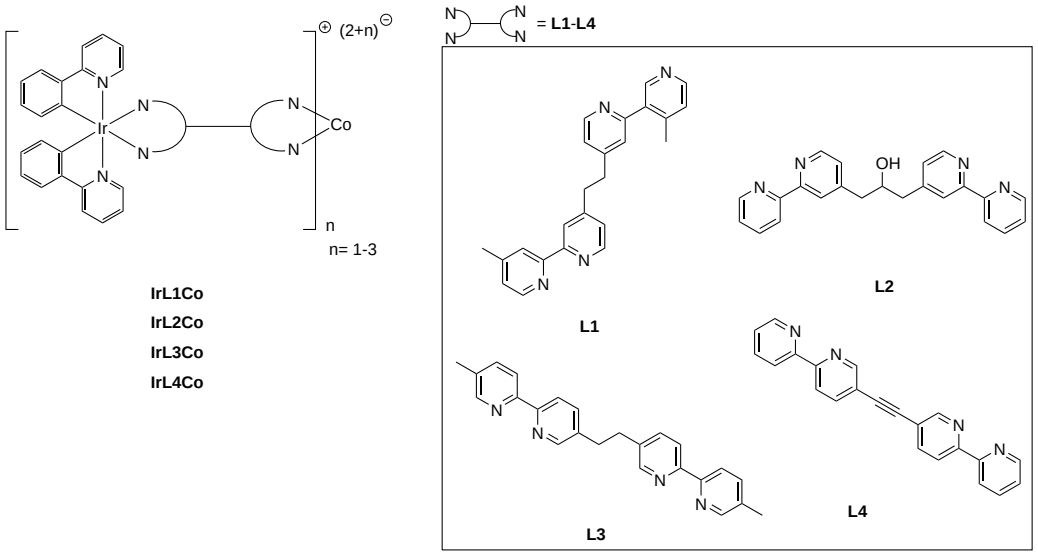

Figure 2.13: Self-assembly approach of an iridium precursor complex with Co^{2+} reported by Sakai *et al.* in 2010.[56]

of the dyad was 0.55 mM. Under these conditions and irradiation with a 150 W mercury lamp with a cut-off filter (λ >380 nm), they achieved a TON_{Cat} of 210 based on the cobalt center.

The second dyad (**IrterpyCo**) was published in 2016 by the Elias group.[131] In contrast to the first described dyad, they choose a tridentate ligand for the iridium photosensitizer. Additionally, they used hydroxyl groups on the glyoxime ligand. They tested the dyad under irradiation with a LED at a wavelength of 452 nm with a sample concentration of 0.1 mM and acetonitrile as solvent, TEOA as sacrificial donor and HBF_4 as proton source. This dyad exhibit a TON_{CAT} of 112.

The third dyad (**IrpicCo**), shown on the right side of Figure 2.14, is composed of an iridium complex with two phenylisochinoline ligands. The neutral ligand is a terpyridine, whereby two nitrogens are connected to the iridium, and the third nitrogen is bound to the cobalt complex. The cobaloxime unit is the same as in the second system. The Elias group tested this new system under similar conditions as the second one.[132] They used the same components, but different concentrations and a green LED with a wavelength of 523 nm were used for the irradiation. The achieved TON was slightly higher as for the previously described system with a value of 125 based on the cobalt center.

These three dyads, which are the only literature known iridium-cobaloxime systems, showed the ability for the light-driven hydrogen generation, but not in an aqueous medium. All systems used an acid as proton source. The change to water as proton source led to an extreme drop in activity or, even worse, no hydrogen evolution was observed. One explanation is that the pH was so drastically changed due to

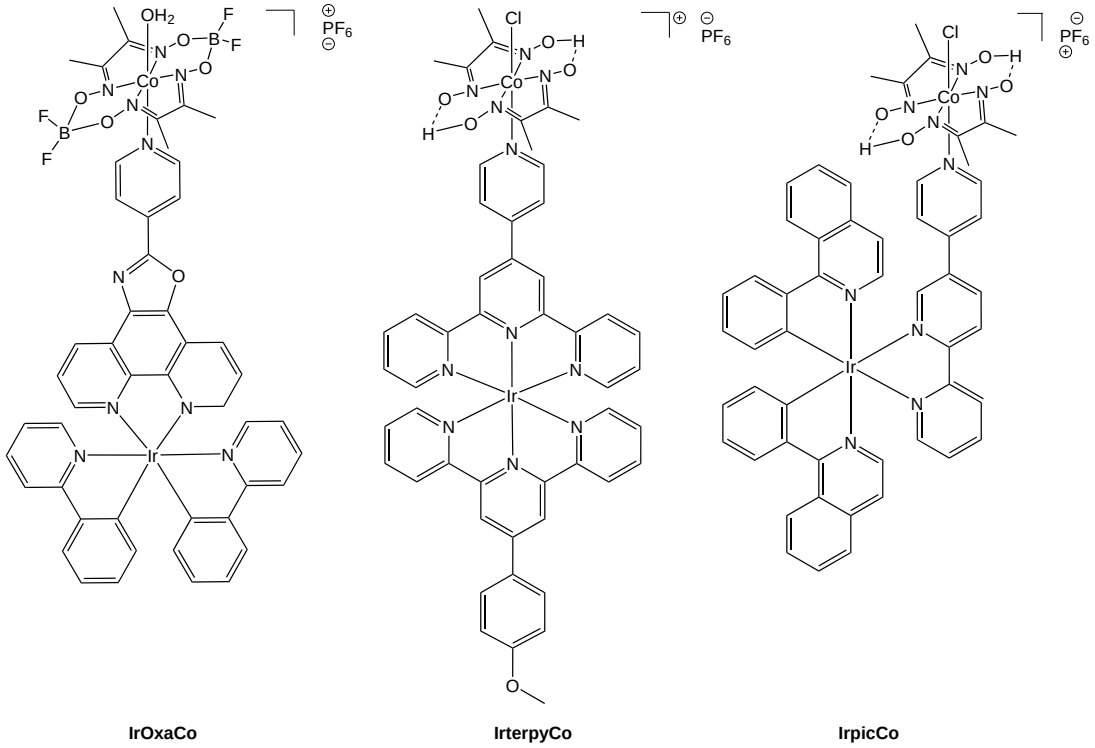

Figure 2.14: Supramolecular iridium-cobalt systems for photocatalytic hydrogen generation.[127,131,132]

the exchange of the proton source that the systems were no longer active. It is also possible, that the pyridine-cobalt coordination dissociated, which led to a reduced activity.[56,133,134]

The first part of this section showed some supramolecular systems that were at least partly composed of non-noble metals, but most molecules that were reported in literature were completely based on noble metals.[45,135–137] A well-investigated dyad is a ruthenium-palladium system, which was first published in 2006 by Rau *et al.*[1] The structure of **RuPd1** is shown in Figure 2.15. First experiments showed that all components were essential for the evolution of hydrogen. They successively eliminated the individual components to examine if the dyad works only with all components or if the ruthenium or palladium part can be neglected. In the photocatalytic water reduction catalysis, this system achieved a TON_{Cat} of 56 in a 29 h experiment. Interestingly, the introduction of a bromine substituent on the phenanthroline in 3,8-position (see Figure 2.15; **RuPd2**) led to an increase of the hydrogen evolution by a TON_{Cat} of 238.[138] The Rau group also exchanged the catalytic active palladium center by platinum. This results in a decreased TON_{Cat} of only 7. This drop of activity was at first glance unexpected due to the similar spectroscopic properties of both systems, but they figured out that the palladium catalyst forms *in situ* colloidal palladium particles, which are responsible for the

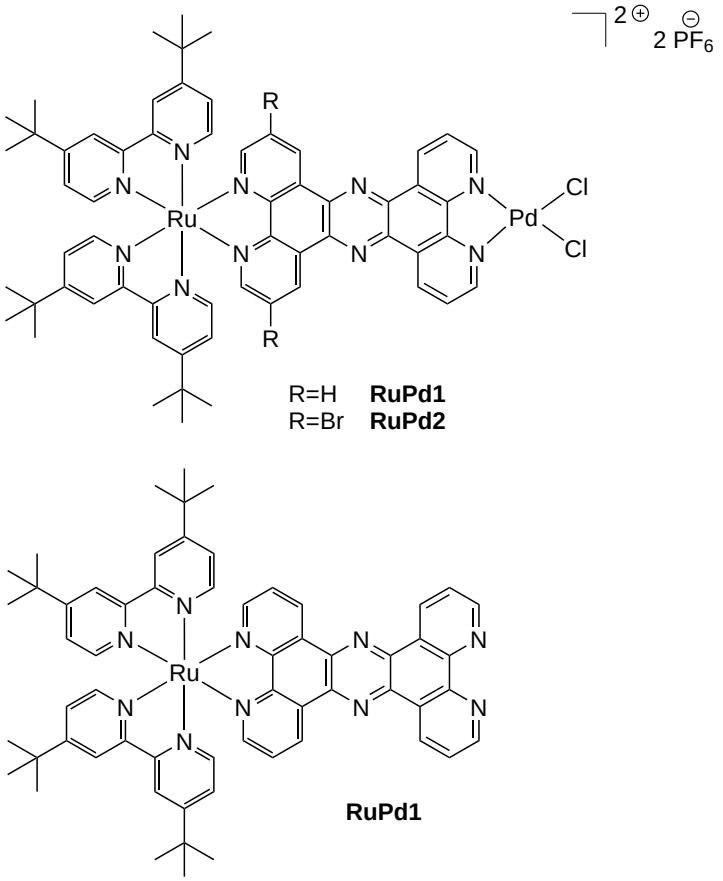

Figure 2.15: Top: Ru-Pd based one-component systems designed by Rau *et al.* in 2006 and 2011 and the analog two-component system (bottom).[1,138]

hydrogen evolution. In contrast to that, the platinum is stably coordinated and no colloids are formed during the reaction.[139]

They revisited the Ru-Pd system **RuPd1** and the analog two-component system **Ru1** to investigate the electron transfer for the competitive approaches. They showed that the electron transfer within the two-component system needs 40 times longer compared to the one-component system. While the e^- transfer from the PS to the bridging ligand was similar in both systems (0.8 ps *vs.* 1.2 ps), the transfer within the ligand differed strongly from each other. The dyad needed only 5 ps, and in contrast to that, the two-component system required 240 ps for the same process. This study ascertains beyond doubts the positive impact of a direct connection between the PS and the CAT *via* a bridge on the electron transfer.[58]

3 Thesis Aims

This thesis focuses on the construction of new molecular systems for the photocatalytic hydrogen production. The photosensitizer unit will be represented by iridium complexes, and the catalyst part will be synthesized from non-noble metals. With these modifications, a crucial step forward toward a more sustainable energy production *via* photocatalytic water reduction will be made.

The thesis is divided into two separate parts that share some characteristics: The first part tackles the design, synthesis, and characterization of various iridium and non-noble complexes. The iridium complexes will then be introduced as photosensitizers and the non-noble complexes as catalysts into the photocatalytic water splitting reactions to evaluate their ability to evolve hydrogen as two-component system. The iridium complex design deals with new, highly active systems that should be suitable to act as photosensitizer due to their photo- and electrochemical properties with the general structure $[Ir(C\hat{}N)_2(N\hat{}N)]^+$. The efforts are directed to the alteration of the (N^N) ligands to work out a structure–activity correlation. Figure 3.1 shows a representation of the planned two-component systems and the different diimine ligands of the iridium complexes. The thiophene rings on the N^N ligand were

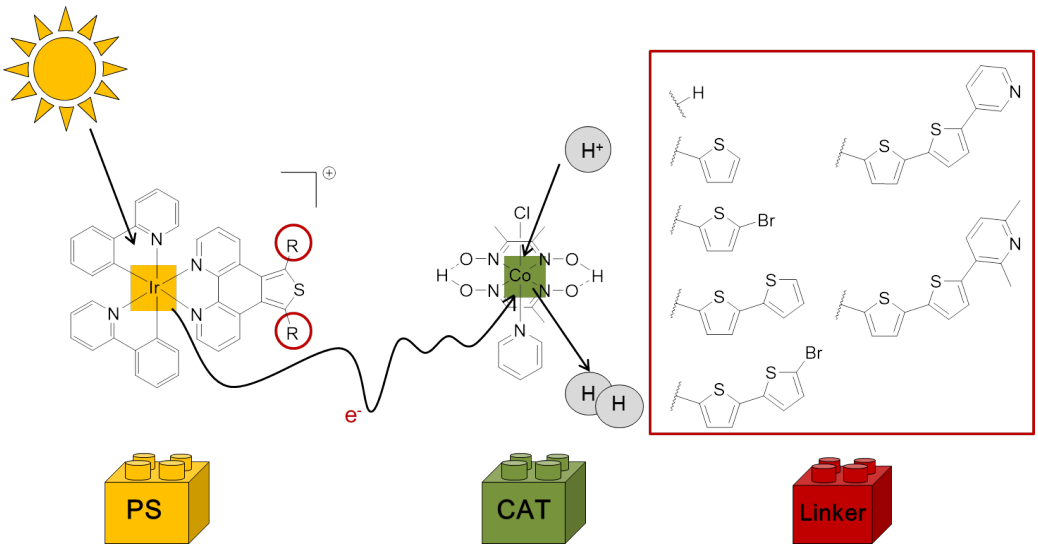

Figure 3.1: Schematic representation of the iridium-cobalt systems that will be synthesized for this thesis and tested in the photocatalytic hydrogen evolution. After the excitation of the PS with solar radiation the electron is transferred to the CAT, where hydrogen is evolved.

chosen due to their superior electron transfer ability in semiconductors and, until now, no molecular systems have been reported that use iridium-thiophene complexes and evaluate the photocatalytic activity concerning the ligand structure.[140–144] The hypothesis is that the fully conjugated thiophene system will support a coplanar arrangement that will enhance the necessary electron transfer from the PSs to the CAT.[145–148] The catalyst synthesis is more established than the iridium photosensitizer procedure. Molecules known from the literature will be tested in combination with the new iridium PS in the photocatalytic water reduction.

The second part of this thesis focuses on the design, synthesis, characterization, and evaluation of the photocatalytic activity in proton reduction experiments of iridium-cobalt one-component systems that provide an additional connection between the individual building blocks. Figure 3.2 depicts the general structure of an iridium-cobalt one-component system that should be synthesized during this thesis. Parallel to the structure–activity correlation described in the first part of this thesis for the iridium photosensitizers, the second part deals with the bridge that connects PS and CAT. The C^N ligands of the iridium complexes will stay unchanged, and only the linking unit of the diimine ligand is varied. Either a conjugated or a non-conjugated bridge connects the PS with the catalytic center so that the differences in photocatalytic proton reduction can be associated to the bridge.

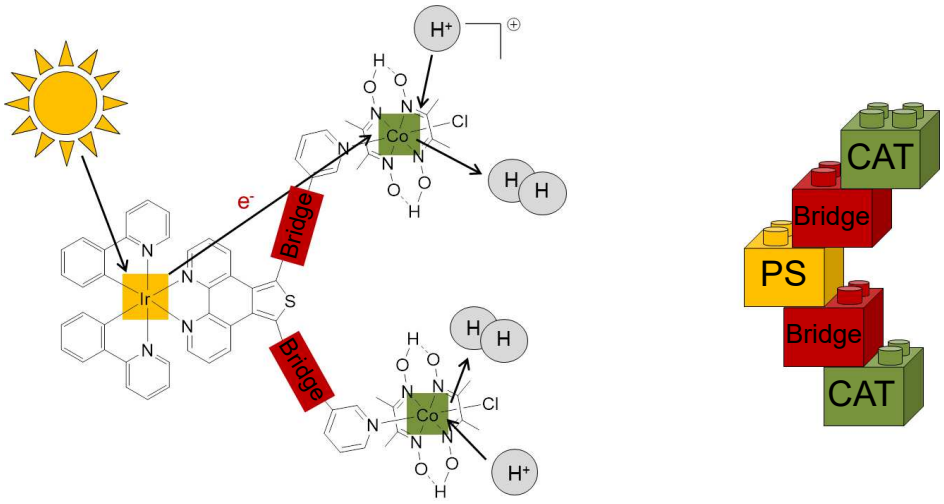

Figure 3.2: Schematic representation of the iridium-cobalt one-component systems that should be synthesized for this thesis. The electron, which is donated after the excitation of the PS with solar radiation, is transferred *via* an intramolecular pathway to the cobalt CAT, where hydrogen is evolved after two cycles.

Finally, the two-component and the one-component approach are compared to each other to make a statement, whether the system composed of individual building blocks or the connected version or PS and CAT is more efficient as a hydrogen-evolving system. This system might be further refined towards a fossil fuels avoiding society.

4 Synthesis and Characterization of Two-Component Systems

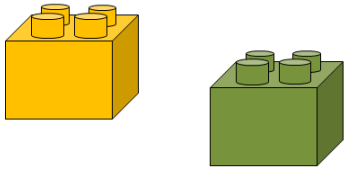

4.1 Synthetic Strategy

This part is divided into two individual issues: The first part focuses on the synthesis of two-component systems, starting with the ligand syntheses and the synthesis of nine different iridium complexes that will be characterized afterward. Additionally, different non-noble metal complexes will be synthesized and also characterized. In the second part, the iridium compounds will be used as photosensitizers in photocatalytic water reduction experiments and the non-noble complexes as catalysts.

The general synthetic procedures for the ligands of the iridium complexes are shown in Scheme 4.1. The first ligand is a simple 1,10-phenanthroline, which will be used as ligand for the reference complex **PS1**. The preparation of the new developed ligands and complexes will start with the synthesis of a dicarboxylic acid. Initially, only three reactions are necessary to obtain the ligand for complex **PS4**. The ring-closing reaction to the thiophene with dicarboxylic acid functionalities is a modified Hinsberg-thiophene synthesis. Starting with the dicarboxylic acid **L4**, it is possible to synthesize three other ligands. The first one, ligand **L2**, can be synthesized through heating of **L4**, which will result in the decarboxylation. The second ligand, **L3**, is an ethyl ester that is obtained by a simple esterification of **L4**. The preparation of **PS5** will be realized by bromination of the dicarboxylic acids with NBS. Based on the dibromine compound, further ligands will be synthesized. Starting with an extended thiophene ligand that will be obtained through a C-C cross-coupling reaction with two additional thiophene rings to obtain **PS6**. This ligand will be brominated to isolate the diimine ligand **L7**. The procedure, which was chosen for the ligand of **PS6** will be transferred to this extended system, but this time a C-C cross-coupling reaction will be conducted with a pyridine instead of additional thiophene rings. This will lead to the ligand of **PS8**. The cross-coupling will be repeated with a pyridine containing two methyl groups in 2,6-position to isolate the ligand for **PS9**.

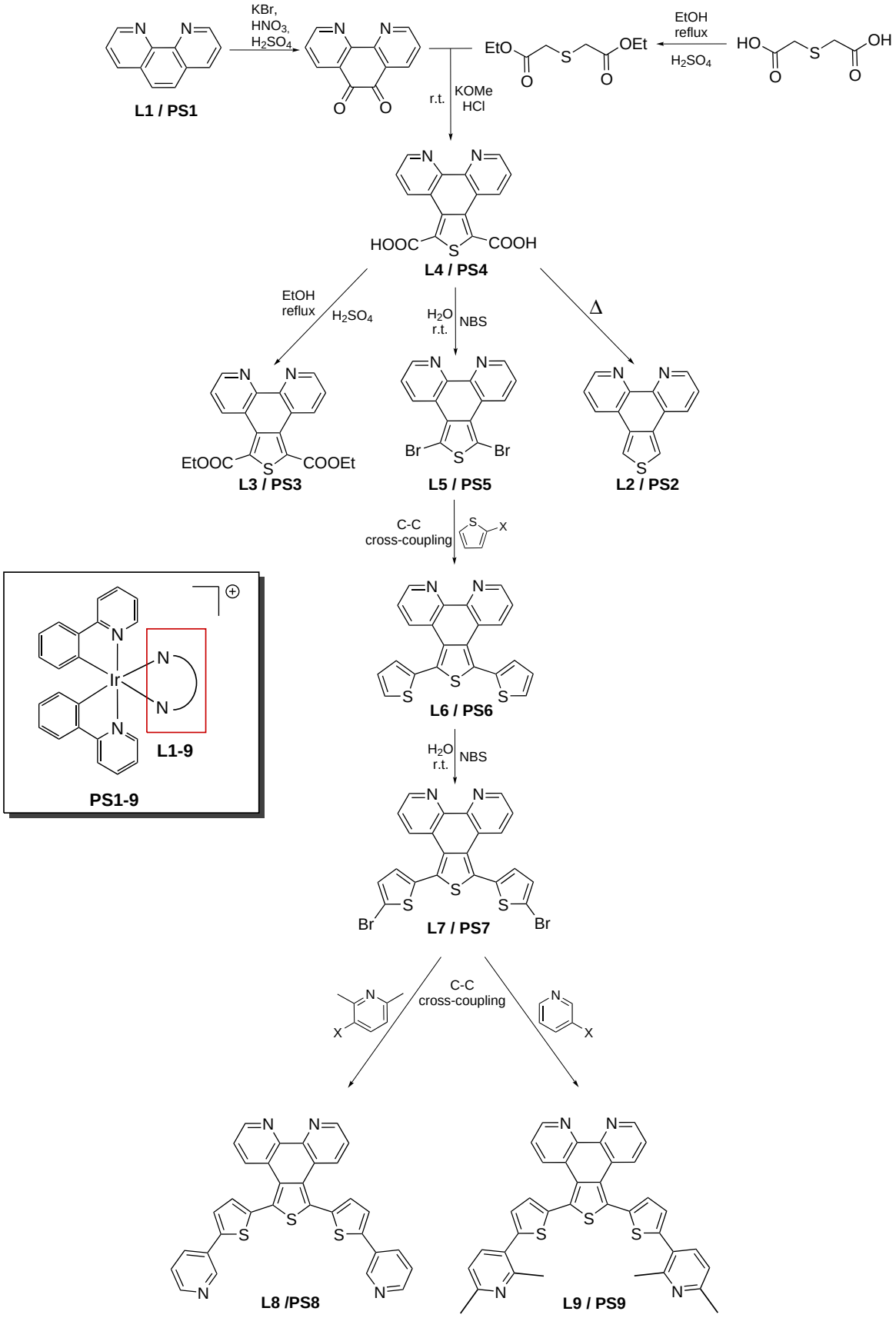

Scheme 4.1: Synthetic strategy for the ligands **L1–L9** and the corresponding photosensitizers **PS1–PS9**.

4.2 Ligands

4.2.1 Synthesis and Characterization

The synthesized ligands were all composed of the same scaffold. The basic idea was the synthesis of a coplanar ligand to generate iridium complexes with an improved electron transfer from the photosensitizer to the water reduction catalyst.[145–148] This was accomplished by the reaction of 1,10-phenanthroline-5,6-dione **1** with diethyl-2,2'-thiodiacetate **2**. It was the first time that a 1,10-phenanthroline with a fused thiophene was obtained. The reaction was developed based on the Hinsberg-thiophene synthesis as shown in Scheme 4.2. The original procedure recommended the application of NaO*t*Bu for the deprotonation of **2** to obtain the thiophene unit.[149] However, this procedure did not yield the desired product. Instead of the Hinsberg product **L4**, 1,10-phenanthroline-5,6-diol was obtained. The structure was identified by NMR, shown in Figure 4.1, and by mass spectrometry.

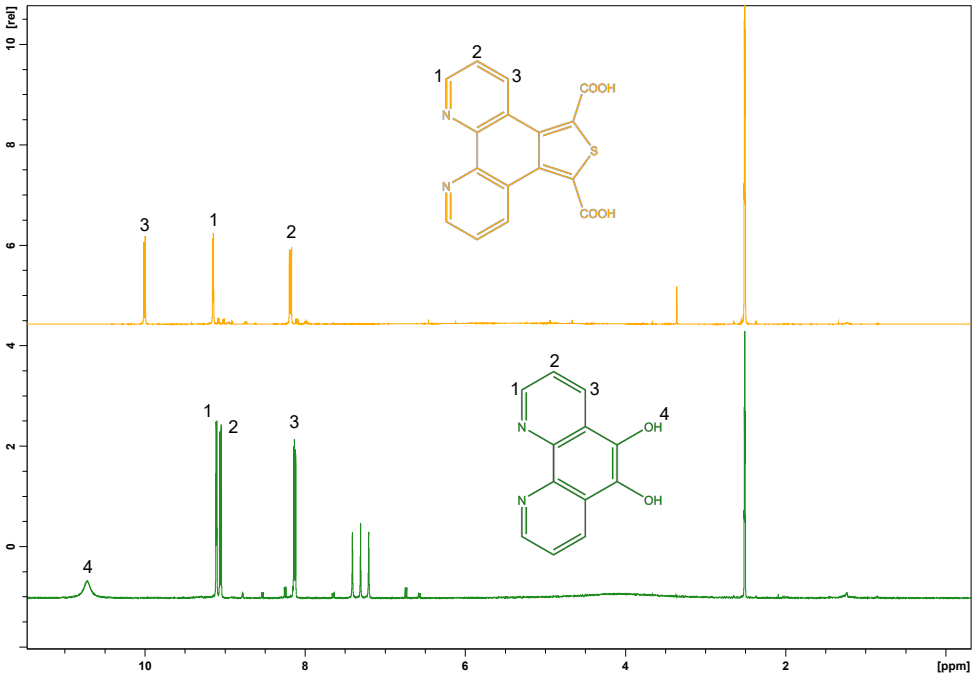

Figure 4.1: ^{1}H NMR spectra of 1,10-phenanthroline-5,6-diol and **L4** recorded in DMSO d_6. The NMR data corresponded with the mass spectra and led to the identification of the 1,10-phenanthroline-5,6-diol (bottom) and the Hinsberg product **L4** (top).

To identify the right reaction conditions a screening with different reaction parameters was conducted. The examined parameters were: nature of the used solvent,

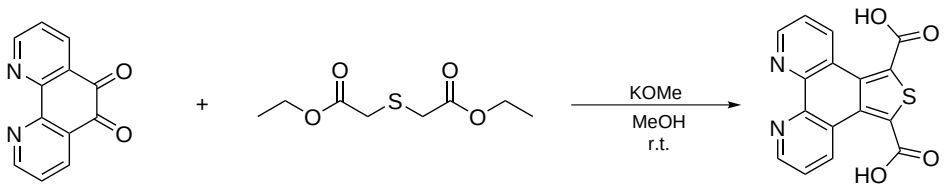

1 81 % **2** 85 % **L4** 96 %

Scheme 4.2: Synthesis of **L4** beginning with 1,10-phenanthroline-5,6-dione **1** and diethyl-2,2'-thiodiacetate **2**.

Table 4.1: Parameter screening for a successful Hinsberg-thiophene synthesis.

Entry	Solvent				Base					
	*t*BuOH	MeOH	EtOH	KO*t*Bu	NaO*t*Bu	KOMe	1^{st}	2^{nd}	Addition at 0 °C	Isolated Yield [%]
1	x			x			x			1.7
2	x			x				x		-
3		x		x				x		18.4
4	x			x				x	x	-
5	x				x			x	x	-
6		x		x				x	x	31.7
7			x	x				x	x	27.2
8		x				x	x		x	91.5
9		x				x		x	x	96.1

1^{st}: Base was added first to the reaction vessel. 2^{nd}: Base was added last to the reaction vessel.

reaction temperature, base and the order of reagent addition to the rest of the reaction mixture. The summarized results of the screening are shown in Table 4.1. Due to the screening, it was possible to highlight two major parameters for the successful synthesis of **L4**: First, the use of MeOH as solvent instead of *t*BuOH led to an increased yield of 16 % (Entry 1 and 3). The second parameter had a higher influence on the overall yield. The initial base, KO*t*Bu, was replaced by KOMe. This enhanced the yield to 91 %. The order of the reagent addition, whether the base was added to the suspended reagents or conversely to the reaction vessel was of minor influence for the successful synthesis and led only to a five percent increase in yield. Finally, the screening resulted in satisfying 96 % of the desired product **L4**. This new scaffold represented the starting material for a series of new ligands as depicted in Figure 4.3. The synthesis will be presented on the next pages.

The second ligand was prepared starting with a conversion of **L4** to generate the decarboxylated Hinsberg product **L2**. In a first attempt, it was tried to decarboxylate **L4** with KOH in ethylene glycol. Unfortunately, this led not to the desired product. In a second experiment, **L4** was stirred in quinoline with copper powder, which also yielded an unknown, unwanted product that was not further analyzed. The desired product **L2** was obtained by a neat reaction during which the dicarboxylic acid **L4**

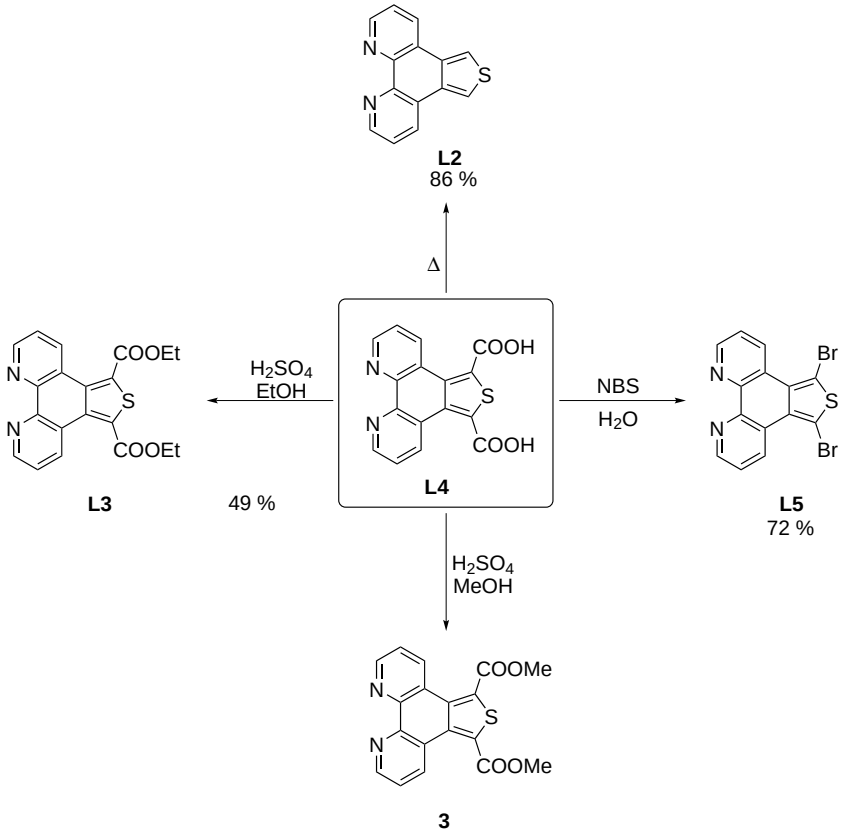

Scheme 4.3: Synthesis of four different ligands. All starting with the conversion of the dicarboxylic acid **L4**.

was heated under vacuum with the application of a cold finger. This resulted in the desired product, which sublimated as a yellow solid on the cold finger.

The third molecule, which was synthesized, was the diethyl ester of the dicarboxylic acid **L4**. Therefore, **L4** was refluxed for four days in ethanol with a catalytic amount of sulfuric acid. The diethyl ester **L3** was formed selectively and no traces of the monoethyl ester, which is a possible product too, was found. Due to this straightforward synthesis, the dimethyl ester **3** was synthesized under the application of the same conditions, but methanol was used instead of ethanol as solvent. The molecules, **L3** and **3**, exhibit a negative mesomeric effect. To obtain a ligand with a positive mesomeric effect another ligand was chosen additionally.

The dicarboxylic acids of **L4** were substituted by bromine, and therefore, the electronic properties of the scaffold were changed, which resulted in a positive mesomeric effect. The bromination of the Hinsberg compound **L4** was achieved by conversion with NBS. The low solubility of the dicarboxylic acid in common organic solvents like $CHCl_3$ or CH_2Cl_2, which are typically used for the bromination with NBS forced us to try other solvents. After many solvents, it was tried to use water as solvent for this synthesis, but even here the solubility was low, but higher compared to

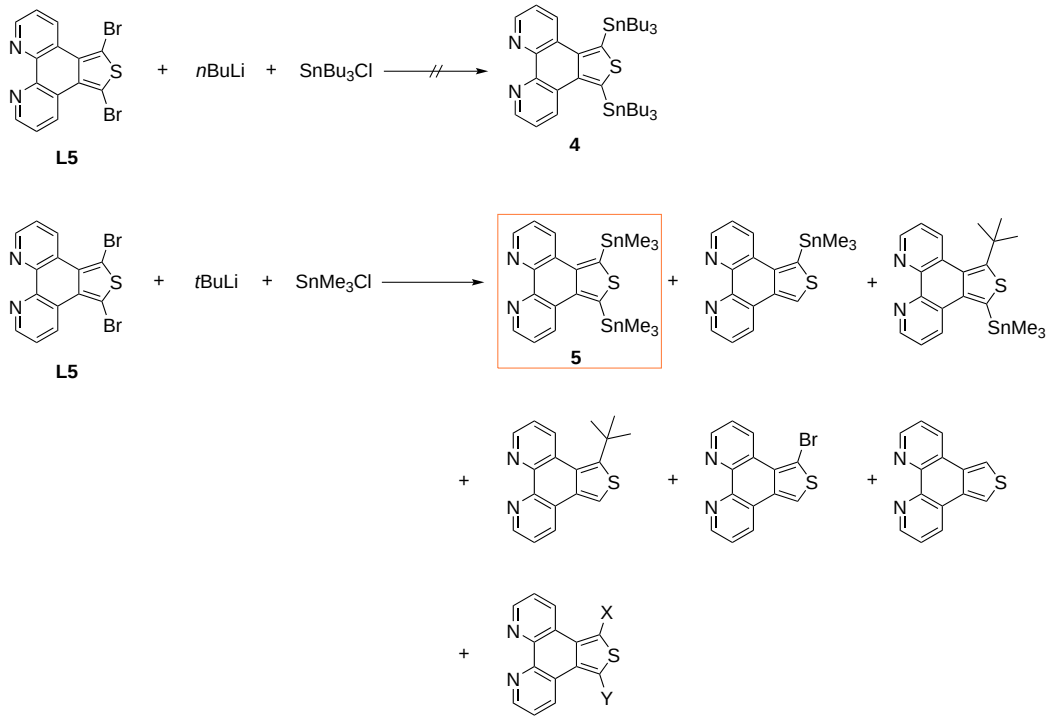

Scheme 4.4: Synthetic approaches to obtain an organotin reagent starting by conversion of **L5** with two different organotin chlorides.

other solvents. Hence, water was used as solvent and the reaction was conducted as suspension. Fortunately, the isolated substance was the desired product in an acceptable yield of 72 %. Although the choice of solvent was not intentional, it was an excellent achievement according to the fifth rule of green chemistry. This rule implies the use of safer solvents. It is also desirable to avoid the use of organic solvents and the production of chemical waste.[150]

Based on **L5**, it was tried to synthesize an organotin reagent. The synthetic approaches are shown in Scheme 4.4. The organotin reagent was chosen to introduce it into a Stille coupling with 2-bromothiophene to obtain the extended ligand structure of **L6**, but this turned out to be a challenging task. During the first experiments, the desired product **4** was tried to synthesize by conversion of **L5** with *n*BuLi and $SnBu_3Cl$. Unfortunately, only the reagent was isolated after the workup. Therefore, the tin precursor was changed to the more reactive $SnMe_3Cl$ and also the more reactive *t*BuLi was used during the synthesis due to the low reactivity of **L5**. Indeed, this resulted in the desired product **5**, but also in a high variety of side products, some of which were identified by mass spectrometry and are also depicted in Scheme 4.4. They consist of mono-, di- or mixed-substituted thiophene structures of hydrogen, bromo, trimethyltin or *tert*-butyl groups. Attempts to isolate and purify the tin compound **5** failed, which is not completely a surprise due to the high similarity and the large number of side products. Finally, this strategy did not produce the next product for a successful continuation of the synthetic pathway.

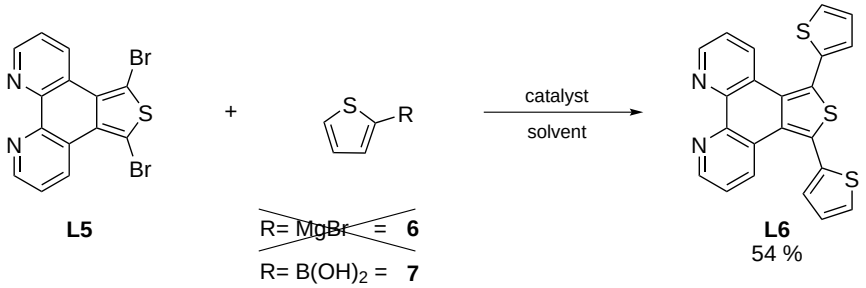

Scheme 4.5: C-C cross-coupling of **L5** with 2-thienylmagnesium bromide **6** or 2-thienylboronic acid **7** to obtain **L6**.

Through the not satisfactory synthesis of the tin reagent, it was necessary to obtain another organometallic compound for the cross-coupling reaction. Therefore, **L5** was applied to a conversion with *n*BuLi and $B(OMe)_3$. This resulted in identical problems as the approach with the organotin reagents. Consequently, a new strategy was developed to synthesize the desired product **L6**.

In this new developed approach, the functionalities of the reagents were switched. This possessed two major advantages: First, the rather non-reactive ligand **L5** does not need not be converted to another species and second, the thiophene-based organometallic reagents were commercial available. Two examples for the new synthesis route are shown in Scheme 4.5. The first attempts involved a Kumada coupling, which should generate a C-C coupling of **L5** with a thiophene grignard reagent. Therefore, a solution of 2-thienylmagnesium bromide **6** was conducted to a synthesis with **L5**. First, $Ni(dppp)Cl_2$ was used as catalyst for the cross-coupling reaction, which did not yield the desired product (see Table 4.2, Entry 1 and 2).

For this reason, a screening was performed to obtain the extended thiophene structure **L6**. The results of this experimental series are summarized in Table 4.2. It should be mentioned that none of the realized Kumada couplings resulted in the desired product (Entry 1–5). Unfortunately, no identification of the products was possible by NMR or mass spectrometry. The iron-catalyzed cross-coupling (Entry 4 and 5) led to the homo-coupling of 2-thienylmagnesium bromide. The 2,2'-bithiophene was identified by NMR and mass spectrometry. After the Kumada coupling a number of Suzuki couplings were conducted but first, 2-thienylboronic acid **7** was synthesized based on a literature procedure with a yield of 65 %.[151] The conversion of the boronic acid **7** with **L5** in a Suzuki coupling resulted in the first attempt in the desired ligand **L6** with a yield of nearly 39 %. $Pd(PPh_3)_4$ was used as catalyst (Entry 7) and water with DME as solvent mixture for the reaction. It was tried to enhance the yield by an extension of the reaction time (Entry 8), which led not to the expected result and the yield was reduced to 21.7 %. When the solvent was changed to DMF, it resulted in a further reduction of the yield to 14.6 %, but a tripling of the reaction time with an additional change of the base from Na_2CO_3 to K_3PO_4 increased the

Table 4.2: Reaction condition screening for the C-C cross-coupling of **L5** with an organometallic reagent (2-Thio**R**) to obtain the product **L6**. The reaction is shown in Scheme 4.5.

Entry	R		Solvent					Catalyst					Base				
	MgBr	$B(OH)_2$	THF	Et_2O	DME	H_2O	DMF	$Ni(dppp)Cl_2$	$Fe(acac)_3$	$Pd(PPh_3)_4$	$Pd(ac)_2$	$Pd(dppf)Cl_2$	Na_2CO_3	K_3PO_4	Time [h]	Isolated Yield [%]
1	x			x				x							21	-
2	x		x					x							68	-
3	x		x									x			2	-
4	x			x					x						24	-
5	x		x						x						72	-
6		x			x	x					x			x	21	-
7		x			x	x				x			x		22.5	38.8
8		x			x	x				x			x		40.5	21.7
9		x					x			x				x	62	14.6
10		x					x			x				x	142	54.3

yield of **L6** to 54.3 % (Entry 10), which was an acceptable result to realize the next reaction step.

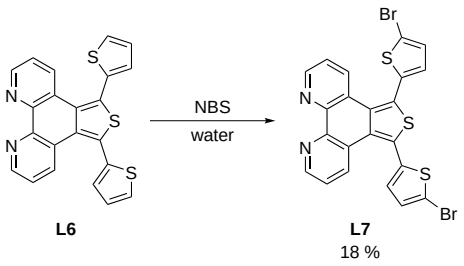

Scheme 4.6: Bromination of **L6** with NBS in water.

The bromination of **L6**, depicted in Scheme 4.6 was conducted as described before for the synthesis of **L5** with water as solvent and NBS as bromine source, but the yield of this reaction was only 18 %. An extension of the reaction time did not result an enhanced yield of **L7**. Due to the small number of hydrogens in the scaffold of **L7** it was more difficult to assign the signals of the quaternary carbon atoms in the ^{13}C NMR spectrum. Figure 4.2 shows the ^{13}C NMR and the dept135 spectra of **L7**. The quaternary carbon peaks are marked by arrows and assigned by symbols. The assignment was made with 2D spectra like HMBC and HMQC.

Since one goal of this thesis was the synthesis of bimetallic complexes, an additional donor functionality atom for the coordination of a second metal must be introduced into the ligand scaffold. In addition to the 1,10-phenanthroline, pyridine was chosen as the second ligand to guarantee the selective coordination of iridium to the phenanthroline and iron or cobalt to the pyridine. To obtain this last extension of the ligand scaffold, it was again necessary to carry out a C-C cross-coupling with **L7** and an organotin pyridine. Alternatively, **L7** should be converted first into a boronic acid

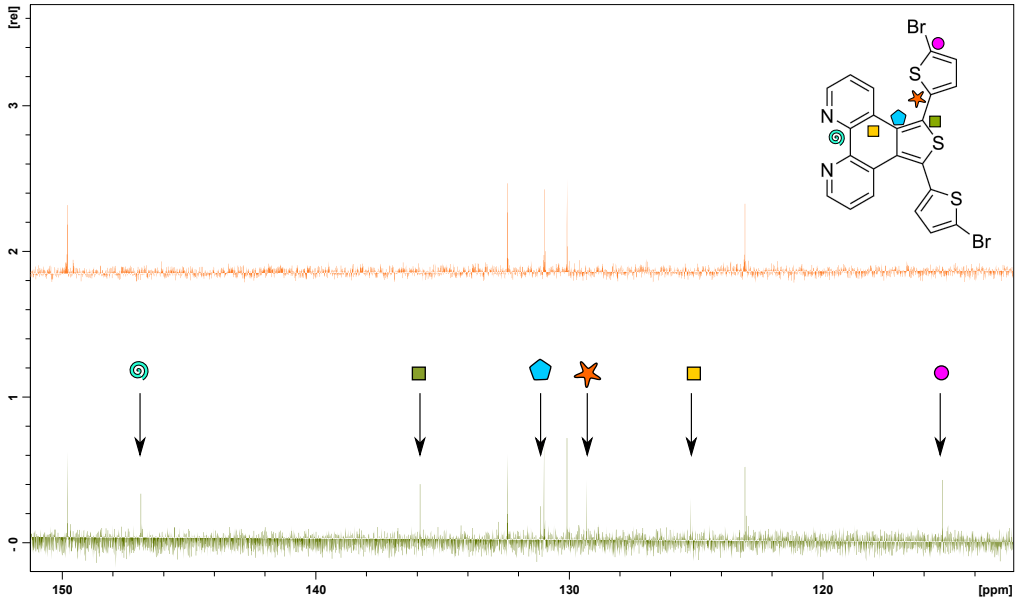

Figure 4.2: ^{13}C NMR (green) and dept135 (orange) spectra of **L7** measured in $CDCl_3$. The quaternary carbons are marked by arrows and symbols.

or an organotin reagent to submit this to a cross-coupling with **11**. Both approaches are depicted in Scheme 4.7. Unfortunately, neither the first technique nor the second produced the target ligand **12**.

Hence, another approach was developed to obtain the target molecule. Until now, it was tried to synthesize the ligand structure starting from the phenanthroline side. Therefore, the strategy was changed and the target molecule should be build up from the pyridine side. It was planned to connect the pyridine first to the thiophene, and afterward, this new molecule should be bound to the fused thiophene-phenanthroline unit. It should be mentioned here, that this new strategy utilized *meta* substituted pyridines instead of the *para* substituted pyridine that was used for the phenanthroline-side-strategy. The different pyridines are shown in Scheme 4.7 and Scheme 4.8. The *meta* substituted pyridine was chosen due to a more easier accessibility of this new structure. For the first synthesis, 3-bromo-2,6-dimethyl-pyridine **13**, a commercially available chemical, was applied to a cross-coupling reaction with 2-thienylboronic acid **7**. Unfortunately, this resulted again in the reagents and no conversion was observed. Consequently, the 2-thienylboronic acid was replaced by the corresponding tin compound, 2-(tributylstannyl)thiophene **14**. With this reagents, $Pd(PPh_3)_4$ as catalyst and a mixture of DMF and toluene, is was possible to isolate the desired product **15** as depicted in Scheme 4.8.

To conduct the next cross-coupling reaction on the synthesis route to obtain the target molecule with two different coordination sides, **15** was converted first into the bromo and afterward to the tin compound. The reactions are shown in Scheme 4.8. The

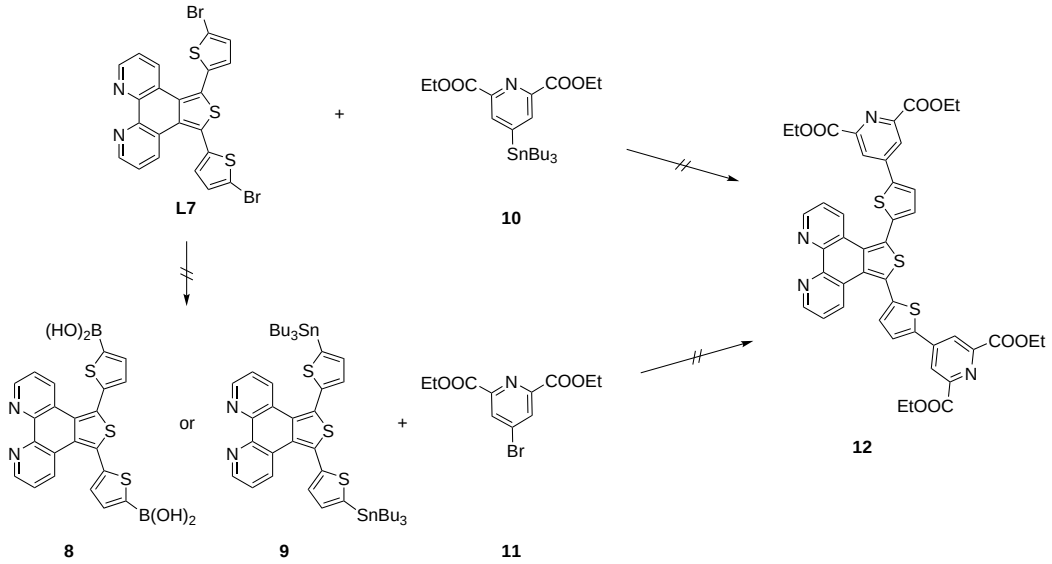

Scheme 4.7: Preparative cross-coupling attempts for the synthesis of the target molecule **12**.

bromination was conducted, as described before, with NBS, but this time chloroform and acetic acid were used as solvents. The reaction yielded quantitative the product **16** with a yield of 99.8 %.

A standard procedure was used for the synthesis of the tin reagent. **16** was dissolved in THF, and *n*BuLi was added. The successful dehalogenation was observed by a color change of the solution from yellow to red. Afterward, the tin precursor $SnBu_3Cl$ was added, which resulted in the desired product **17** with a yield of 82 %.

This tin reagent **17** was applied to the next cross-coupling reaction with **L5**. Different reactions with varying solvent ratios and catalysts were tested again. Finally, a setup

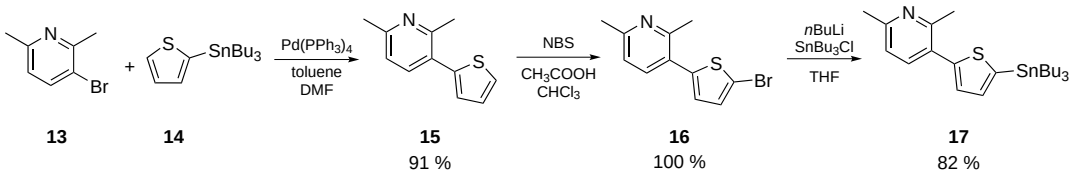

Scheme 4.8: Synthesis route starting with **13** and **14** to finally isolate **17** as starting material for a further cross-coupling reaction.

was successful which resulted in the precipitation of the pure product **L9**. It used a mixture of toluene and DMF as solvent and $Pd(PPh_3)_4$ as catalyst. The precipitation of the product was a major advantage due to the problematic and time-consuming workup of phenanthroline-based molecules. The ratio of the solvents DMF and toluene seemed to play a crucial role in this synthesis. When the ratio of 1:4 (DMF:toluene) was slightly changed, both, purification grade and yield, decreased drastically. The target molecule was completely characterized by NMR spectroscopy,

mass spectrometry, elemental analysis and the X-ray crystal structure. The further conversions of **L9** will be described in Chapter 4.3 and 6 since it is one ligand for a bimetallic system.

By summarizing the synthetic route of **L9**, only the first two steps to synthesize the reagents for the Hinsberg-thiophene synthesis were literature known. All other reactions were conducted for the first time and none of the molecules were reported in the literature until now. The reaction route consisted of eight individual steps, whereby two brominations and two C-C cross-coupling reactions were carried out. All reactions can be clustered into two linear synthesis routes, starting from the phenanthroline or the pyridine side. Based on the second synthesis route, which was presented last, the overall yield for **L9** was 51.3 %.

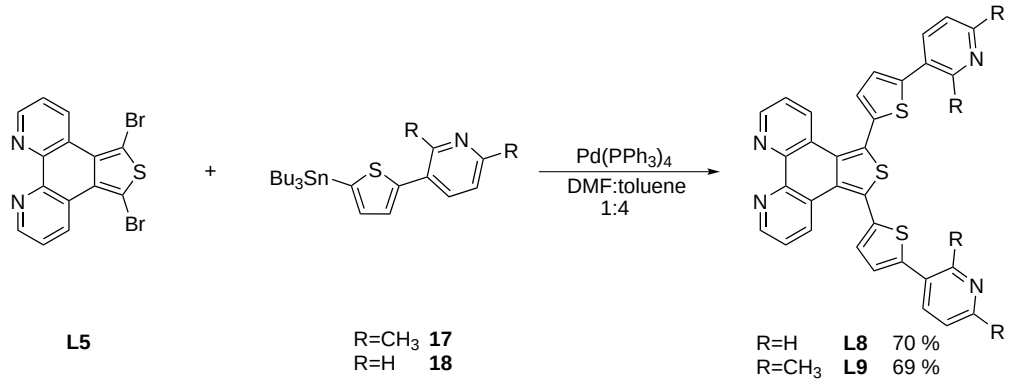

Scheme 4.9: Cross-coupling reaction to prepare the ligand, which possesses two spatial independent coordination possibilities for different metals. Both molecules were synthesized in an eight-step synthesis route.

The synthesis of a bimetallic system with the above-described linker **L9**, iridium and cobalt or iron failed. Details of this issue will be discussed later in Chapter 6. Therefore, a modification of **L9** was necessary to explore the possibility to synthesize a bimetallic system. Hence, the structure of **L9** was slightly modified. Now, the linker was synthesized without the methyl groups in 2,6-position of the pyridine. Fortunately, the synthesis route of **L9** was adapted to the new molecule **L8**. The final ligand is shown in Scheme 4.9 as **L8**. Equally to **L9**, the overall yield was calculated. In contrast to the previous presented molecule, the overall yield was only 40.9 %. The lower overall yield of **L8** was not an inconclusive result: The first route to obtain **L9** was more improved, and screenings were conducted to ascertain suitable reaction conditions. For the second molecule, the reaction procedures were only transferred and not further optimized. Nevertheless, it is an adequate overall yield for such a large molecule like **L8**. Further conversions of **L8** will be described in Chapter 4.3 and 6.

4.2.2 Crystal Structures

It was possible to isolate crystals suitable for X-ray structure analysis of **L5**, **L6**, **L7** and **L9**. The yellow crystals of ligand **L5** were grown by slow diffusion of THF into a concentrated solution of **L5** in $CHCl_3$. Four molecules of **L5** occupy the asymmetric unit of a monoclinic cell. **L6**, with an extension of two thiophene rings on the fused 1,10-phenanthroline-thiophene scaffold, also crystallizes in a monoclinic cell as pale yellow prisms. They were obtained by slow diffusion of Et_2O into $CHCl_3$. The orange prisms of **L7** were also obtained by slow diffusion of Et_2O into $CHCl_3$. As noticed before for the other two crystal structures, four ligand molecules are occupying the monoclinic cell. The last yellow crystals of **L9** were grown by slow diffusion of Et_2O into a solution of **L9** in $CHCl_3$. As for every other molecule, four ligand molecules occupy one monoclinic cell.

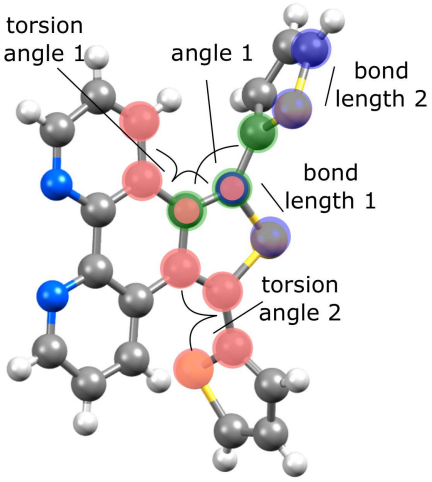

Figure 4.3: Label of bond lengths, angle and torsion angles for the presented ligand crystal structures.

Figure 4.3 illustrates the designations of different bond lengths and angles, which are valid for all crystal structures. The torsion angles 1 and 2 will be of importance in this discussion since a planar ligand structure should be synthesized for an improved electron transfer within the bimetallic dyads. A few selected bond lengths and angles are summarized in Table 4.3 and will be discussed in this section.

The C-S bond lengths (bond length 1 and 2) in all thiophene rings are between 1.711(5) Å–1.741(5) Å. These lengths are in the typical range for C-S bonds in thiophene rings.[152,153] Bond length 2 is elongated in **L6** (1.728(2) Å) and **L7** (1.736(5) Å/ 1.741(5) Å), while for **L9**, the molecule with the adjacent pyridine rings, the C-S bonds of the outer thiophene rings are shortened (1.716(6) Å).

The angle (angle 1) between the fused and the extended thiophene rings is widened in **L6**, **L7**, and **L9**. In other, similar crystal structures, this angle is approximately 128 °, whereas in the crystal structures of **L6**, **L7**, and **L9** the angles range between 131 °–132 °.[152–154] It is possible that the outer thiophene rings are forced to a wider angle and consequently to a larger distance with reference to the phenanthroline through the connection of the fused thiophene to the bulky phenanthroline.

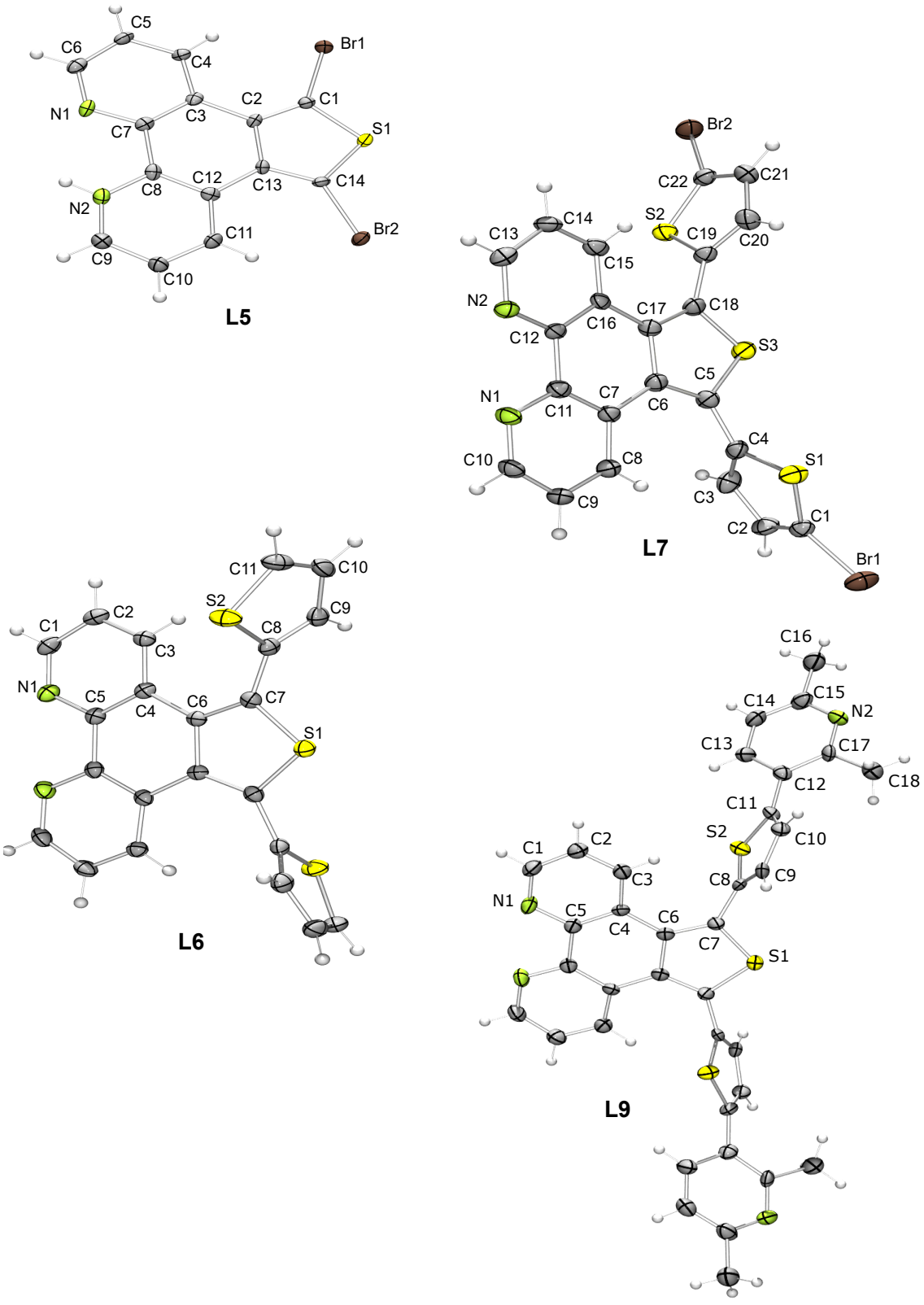

Figure 4.4: ORTEP plot with anisotropic displacement ellipsoids drawn at the 50 % probability level for **L5**, **L6**, **L7**, and **L9**. All crystals suitable for X-ray diffraction analysis were grown by slow diffusion of ether solvents.

Table 4.3: Selected bond lengths and angles of the ligand crystal structures **L5**, **L6**, **L7**, and **L9**. The corresponding crystal structures are shown in Figure 4.4.

	L5	**L6**	**L7**	**L9**
Crystal system	monoclinic	monoclinic	monoclinic	monoclinic
Space group	Cc	C 2c	P 21/c	C 2/c
bond length 1 [Å]	1.714(5)/ 1.717(5)	1.717(2)	1.711(5)/1.712(5)	1.720(6)
bond length 2 [Å]	-	1.728(2)	1.736(5)/1.741(5)	1.716(6)
angle 1[°]	-	132.2(2)	131.1(4)/131.6(5)	131.1(5)
torsion angle 1* [°]	0. 13/ 1.44	4.66	4.00/4.06	3.18
torsion angle 2* [°]	-	75.08	75.75/ 94.04	71.82

*torsion angles were measured in mercury

As described in Chapter 3, a coplanar ligand should be synthesized to obtain an optimized electron transfer from the photosensitizer to the catalyst in a supramolecular assembly. Therefore, the torsion angles of the fused thiophene-phenanthroline unit (torsion angle 1) and the adjacent thiophene rings (torsion angle 2) are essential for this discussion. The angles will be later compared to the angles of the synthesized iridium complexes in Chapter 4.3.2. The crystal structures of **L5** and **L7** contain no mirror plane; consequently two different torsion angles are measured. Torsion angle 1 is measured on the one side with 0.13 ° in **L5** (see Figure 4.4; C1-C2-C3-C4) and on the other side of the same thiophene the angle is 1.44 ° (see Figure 4.4; C11-C12-C13-C14). Hence, the structure is slightly distorted around the thiophene-phenanthroline connection, but the planar structure is nearly perfect for the smallest of all ligands. Due to the existing mirror plane of **L6**, only one torsion angle 1 is determined with 4.66 °. This molecule, with an extended thiophene ring, exists only in an undistorted arrangement around the phenanthroline-thiophene unit. Torsion angle 2 is measured for the adjacent thiophene rings with 75.08 °. For the bromine extended system **L7**, torsion angle 2 is on the first side very similar to **L6** with 75.75 ° (see Figure 4.4; C16-C17-C18-S2). On the other side, the angle possesses a value of 94.04 ° (see Figure 4.4; C6-C5-C4-S1), which is nearly perpendicular. Torsion angle 1 exhibits a value of 4.00 °, which is also slightly twisted out of the plane. The last molecule contains a mirror plane like **L6**. The mirror plane of **L9** passes through the middle of the N^N-unit of 1,10-phenanthroline and the sulfur of the fused thiophene. Torsion angle 1 is determined with 3.18 °. Again, as for **L6** and **L7**, the thiophene is twisted out of the plane. For torsion angle 2, a value of 71.82 ° is measured, which is again far away from a planar arrangement.

At this point, it can be summarized that torsion angle 1 of the phenanthroline-thiophene units indicates a twist out of the plane, which is enhanced by the introduction of additional thiophene rings in **L6**, **L7** and **L9** to avoid steric tensions. Torsion angle 2, between the adjacent thiophene rings, is far away from zero degrees and therefore, the ligand is far away from a coplanar arrangement. Because this is a

critical condition for an optimized electron transfer, this issue will be discussed later in Chapter 4.3.2 after the coordination of the ligands to the iridium centers.

4.2.3 UV-Vis Spectroscopy

All ligands that will be introduced to the complex syntheses were also characterized by UV-Vis spectroscopy. The UV-Vis spectra of **L1–L9** were recorded in CH_2Cl_2 with a concentration of $2.5 \cdot 10^{-5}$ M at room temperature. The spectra are shown in Figure 4.5.

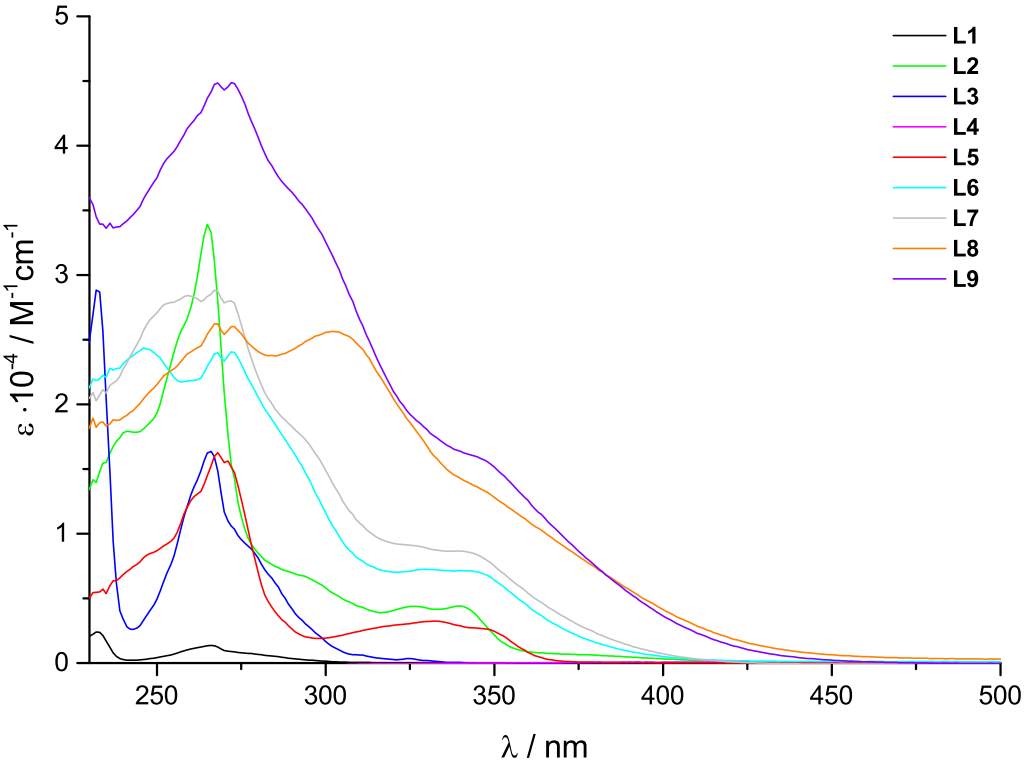

Figure 4.5: UV-Vis spectra of all ligands, which were used in the iridium photosensitizer syntheses. The spectra were recorded in CH_2Cl_2 at room temperature.

All spectra show a similar shape with comparable absorption signals. The most prominent absorption peak is located around 265 nm. The signals are of narrow shape for the ligands with only one extension-sphere (**L1–L5**). The extended systems with a minimum of two additional thiophene groups (**L6**-**L9**) show a broadened signal at around 260 nm with a second absorption that appears nearby the first absorption band (~268 nm). The more extended systems display also a larger extinction coefficient ($\epsilon >$ 20000 M^{-1} cm^{-1}), whereas the pyridine containing systems (**L8**/**L9**) exhibit again larger extinction coefficients ($\epsilon >$ 25000 M^{-1} cm^{-1}) by tendency as the molecules that are only prolonged by a second thiophene sphere (**L6**/**L7**). This is the consequence of a larger π system of these ligands. The extension

Table 4.4: UV-Vis absorption bands and extinction coefficients of **L1–L3**, and **L5–L9** measured in CH_2Cl_2.

Ligand	λ_{abs} (ϵ) [nm] (M^{-1} cm^{-1})
L1	233 (2382), 266 (1359), 277 (733), 298 (177)
L2	240 (17792), 255 (24875), 265 (33922), 294 (6697), 325 (4377), 340 (4410),
L3	232 (28834), 266 (16368), 279 (8453), 286 (5884), 311 (611), 325 (342)
L5	247 (834), 261 (12873), 268 (16266), 333 (3232), 349 (2448)
L6	247 (24932), 267 (23900), 272 (24061), 290 (16460), 330 (7254), 344 (7082)
L7	250 (27088), 259 (28423), 267 (28839), 272 (27989), 294 (17289), 326 (9087), 343 (8549)
L8	260 (24068), 267 (26210), 272 (26022), 304 (25600), 327 (17890), 347 (13309), 443 (801)
L9	252 (38642), 268 (44509), 273 (44810), 295 (34733), 347 (15561), 443 (359)

L4 was not soluble in common organic solvents and is therefore not listed in this table

of the ligand framework also leads to a red-shifted absorption behavior, while the effect is even more pronounced in the pyridine containing ligands.

After this superficial consideration of the absorption spectra, we now take a closer look on the ligand transitions. Therefore, **L1** and **L2** were chosen as exemplary ligands and TD-DFT calculations were done to compare the theoretical data with the experimental spectra. The resulting spectra are shown in Figure 4.7. In general, only $\pi \rightarrow \pi^*$ and n $\rightarrow \pi^*$ transitions were observed in the investigated regions. Starting with the reference substance **L1**, the first intense signal at ~250 nm is assigned to a spin-allowed $\pi \rightarrow \pi^*$ transition. The involved orbitals depicted in Figure 4.6 are the HOMO-2 and HOMO, LUMO, LUMO+1 and LUMO+2. This is in agreement with previous literature reports.[155]

The absorption bands at 295 nm are also calculated as $\pi \rightarrow \pi^*$ transitions that are very similar to the involved absorption processes at 250 nm. With a very weak signal at 320 nm, a n $\rightarrow \pi^*$ transition is observed. The participating ground state orbital is located on the nitrogen atoms of the 1,10-phenanthroline (HOMO-3). For **L2**, the $\pi \rightarrow \pi^*$ transition is also located at 265 nm. A series of other typical $\pi \rightarrow \pi^*$ transitions are observed in both, the experimental and the calculated spectra, in the range of 240 nm–280 nm. The absorption bands are strongly red-shifted for **L2** compared to **L1**, which might be a result of a larger π system in **L2**. Interestingly, the HOMO that is involved in the appearance of the absorption band at 338 nm, is delocalized over the complete ligand, whereas the LUMO is solely located on the 1,10-phenanthroline unit. The n $\rightarrow \pi^*$ transition, which was already observed for **L1**

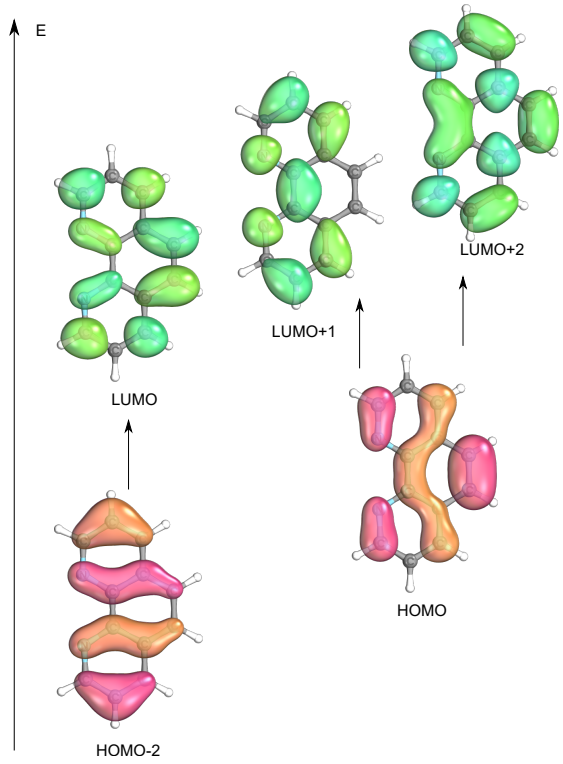

Figure 4.6: Donor (pink/orange) and acceptor (green/turquoise) orbitals involved in the absorption band at 250 nm for **L1**.

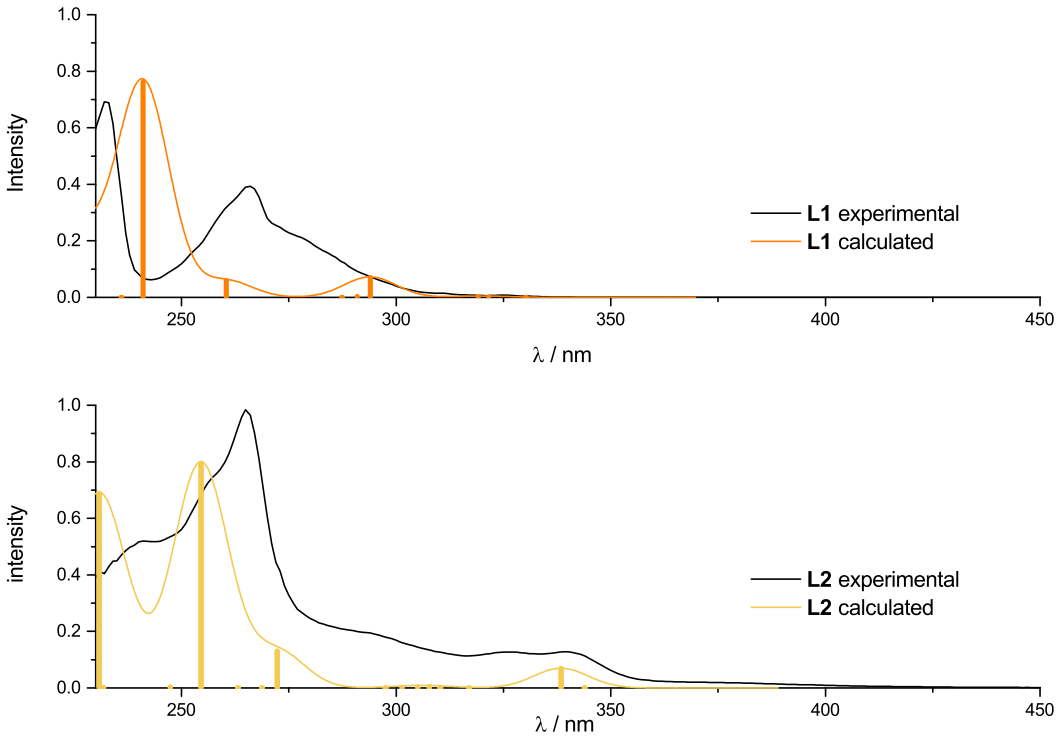

Figure 4.7: Experimental and theoretical UV-Vis data of **L1** and **L2**. The data were calculated with TD-DFT methods.

is located at 308 nm. Opposed to the previous observations is this signal blue-shifted compared to **L1** with 320 nm. The last absorption band is assigned to $\pi \rightarrow \pi^*$ and n $\rightarrow \pi^*$ transitions, but here, the n $\rightarrow \pi^*$ transition involves the thiophene sulfur, and after the excitation, the π electrons are only delocalized on the 1,10-phenanthroline part.

4.3 Photosensitizer

4.3.1 Syntheses and Characterization

The completely new 1,10-phenanthroline-based ligands **L2**–**L9** were introduced into a straightforward complex synthesis to obtain an iridium complex with the general structure $[Ir(C\hat{}N)_2(N\hat{}N)]^+$. Phenylpyridine (ppy) was chosen as cyclometalating (C^N) ligand and was not modified for any of the following nine photosensitizers. The phenanthroline-based ligands, which were described in the previous sections were introduced as N^N ligands. This heteroleptic iridium complexes are in general arranged in the *trans* configuration regarding the phenylpyridine nitrogen atoms.[156] By deciding to only change the N^N ligand, solely the LUMO energy is influenced in this complexes. This was discussed in detail in Chapter 2.3.2, which shows a localization of the LUMO on the diimine ligands, while the HOMO is mostly localized on the ppy-ligand and the iridium center.[99,103–105] DFT calculations show that this is also valid for the iridium complexes presented here. This should be kept in mind for the following discussion of the photophysical properties.

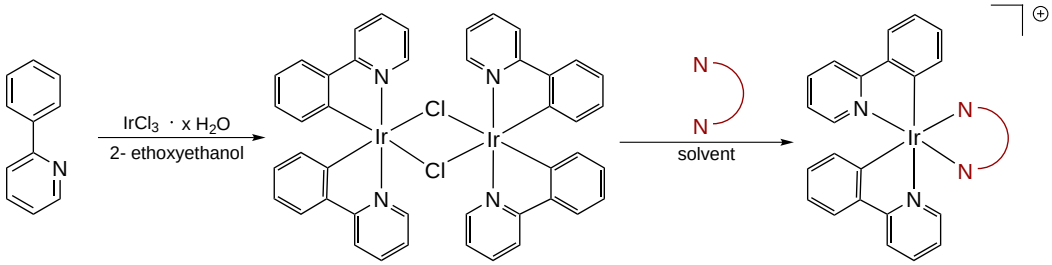

Scheme 4.10: Iridium photosensitizers with $IrCl_3$ as starting material and μ-$[Ir(ppy)_2Cl]_2$ as precursor for all iridium complexes synthesized in this thesis.

In a first step, an iridium precursor, a μ-chloro-bridged iridium dimer was prepared in a conversion of iridium trichloride with phenylpyridine (see Scheme 4.10). The ligands **L1**–**L9** and **IrDimer** were brought together in a second reaction to obtain the final iridium photosensitizers **PS1**–**PS9**, which are displayed in Figure 4.8. Finally, an anion exchange was conducted with NH_4PF_6 to obtain the hexafluorophosphate salt, instead of the chloride complex. In general, the complexes were purified by column chromatography with MeCN and saturated KNO_3 solution. Interestingly, the synthesis of the phenanthroline-thiophene-methyl ester complex with **3** as N^N ligand failed, whereas the comparable ethyl ester complex **PS3** was successfully synthesized. The methyl ester complex synthesis resulted in the mono-methyl ester complex. The

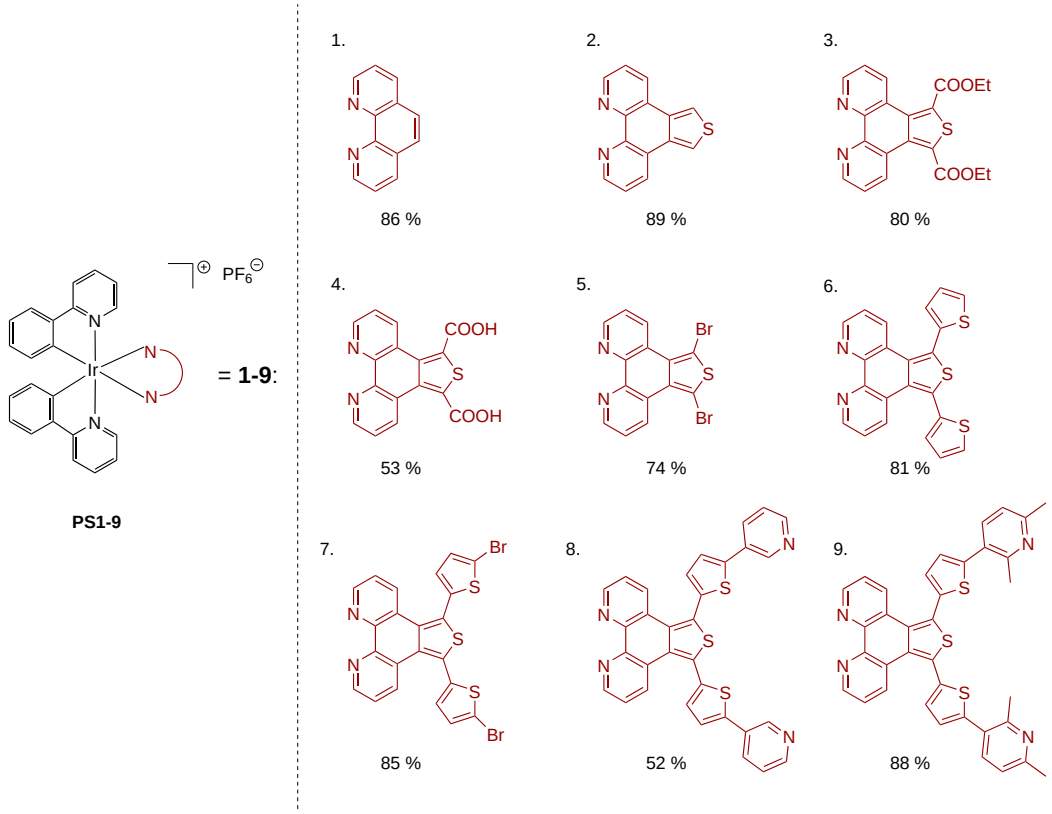

Figure 4.8: Nine different iridium photosensitizers with varying N^N ligands. Abbreviations for the ligands are: 1.**PS1**, 2. **PS2**, 3.**PS3**, 4. **PS4**, 5. **PS5**, 6. **PS6**, 7. **PS7**, 8. **PS8**, and 9. **PS9**.

second methyl ester was decarboxylated and therefore this complex was excluded from the further discussion. All iridium complexes were characterized by elemental analysis, mass spectrometry, NMR, IR, UV-Vis and fluorescence spectroscopy. All mass spectra show the molecular peak of the cation. For the extended complexes **PS7**, **PS8**, and **PS9**, the doubly charged ion was also detected.

Figure 4.9 shows the ^{1}H NMR spectrum of **PS3** as an example for all iridium photosensitizers synthesized for this thesis. The spectrum was recorded in CD_2Cl_2. In general, the NMR spectra of the synthesized iridium compounds display several multiplets, which is not surprising for large molecules like these photosensitizers. Four proton signals, which exist for all photosensitizers, should be emphasized here. First, a doublet of doublets at 6.39 ppm, which is marked in the spectrum with a red pentagon. Compared to the pure 2-phenylpyridine this signal is shifted strongly upfield from 8.08 ppm to 6.39 ppm.[157] In 2-phenylpyridine, it is a typical proton signal for an aromatic substance, whereas in the iridium complexes the signal has more like an alkene character. This is the result of a formal anionic character of the phenylpyridine caused by the complexation to the iridium. The second signal, which should be mentioned is also a signal of the phenylpyridine ligand, but this time it is located on the pyridine adjacent to the nitrogen (marked

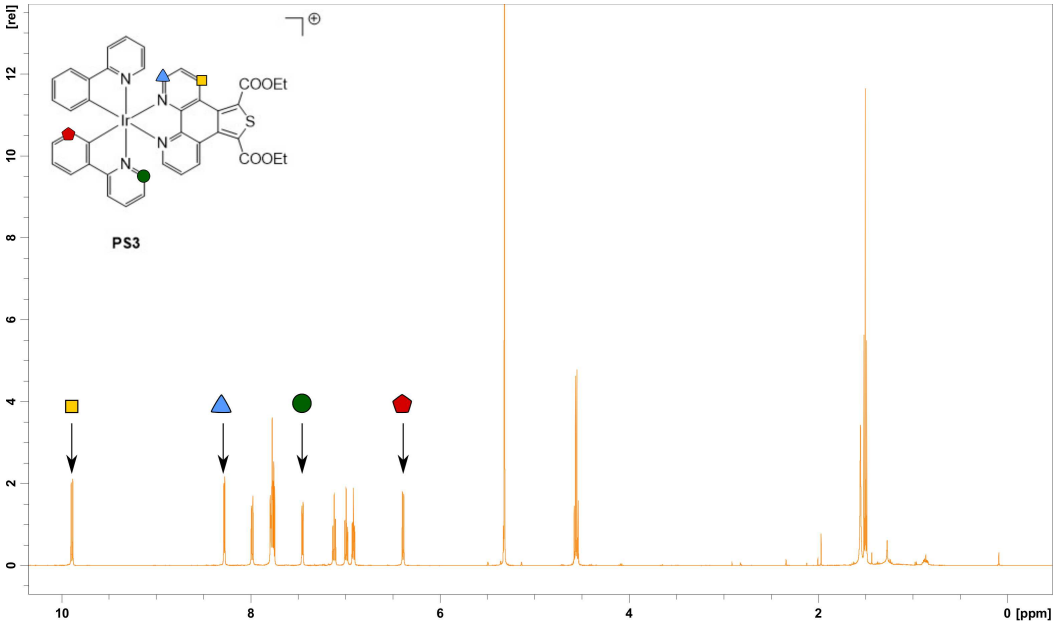

Figure 4.9: Exemplary ^{1}H NMR spectrum of **PS3** for all photosensitizers recorded in CD_2Cl_2.

with a green circle). Identically to the before discussed signal, this doublet of doublet of doublets at 7.45 ppm is also shifted upfield compared to the free phenylpyridine (8.71 ppm). This is caused by the dative bond of the nitrogen to iridium and the electron-withdrawing effect of the pyridine nitrogen. The last two signals that will be emphasized belong to the protons, which are in *para* position to the phenanthroline nitrogen (marked with a yellow square), and the proton adjacent to the same nitrogen labeled with a blue triangle. By coordination of the ligand to the iridium these two signals were inverted in their chemical shifts. While the blue-triangle-proton peak is located at 9.01 ppm for the ligand, in the complex this signal is found at 8.28 ppm. In contrast, the yellow-square-proton peak was found at 9.44 ppm for **L3** and in the complex, this signal is located at 9.89 ppm. This is interesting since the proton, which is marked with the green circle shows a contrary chemical shift (compared to the blue triangle). The strong downfield shift of the proton labeled with the yellow square might occur due to mesomeric structures or a strong ring current.

Next, we take a look on the IR spectra of the iridium complexes. Figure 4.10 shows a selection of IR spectra of the synthesized compounds **PS2**–**PS4**, **PS6**, and **PS8** and a few key signals will be highlighted. First, the P-F vibrations of the PF_6 anions are located at nearly 830 cm^{-1} for all photosensitizers.[158] The aromatic C-H stretch vibrations are visible in the range of 2845 cm^{-1}–3085 cm^{-1} as medium intense signals.[159] Other peaks, which are valid for all complexes are difficult to assign due to the great number of signals. The vibrations of the ester groups of **PS3** are located at 1709 cm^{-1} and 1229 cm^{-1}. **PS4**, the iridium complex with the dicarboxylic acid groups on the N^N ligand displays the typical absorption signals for a carboxylic

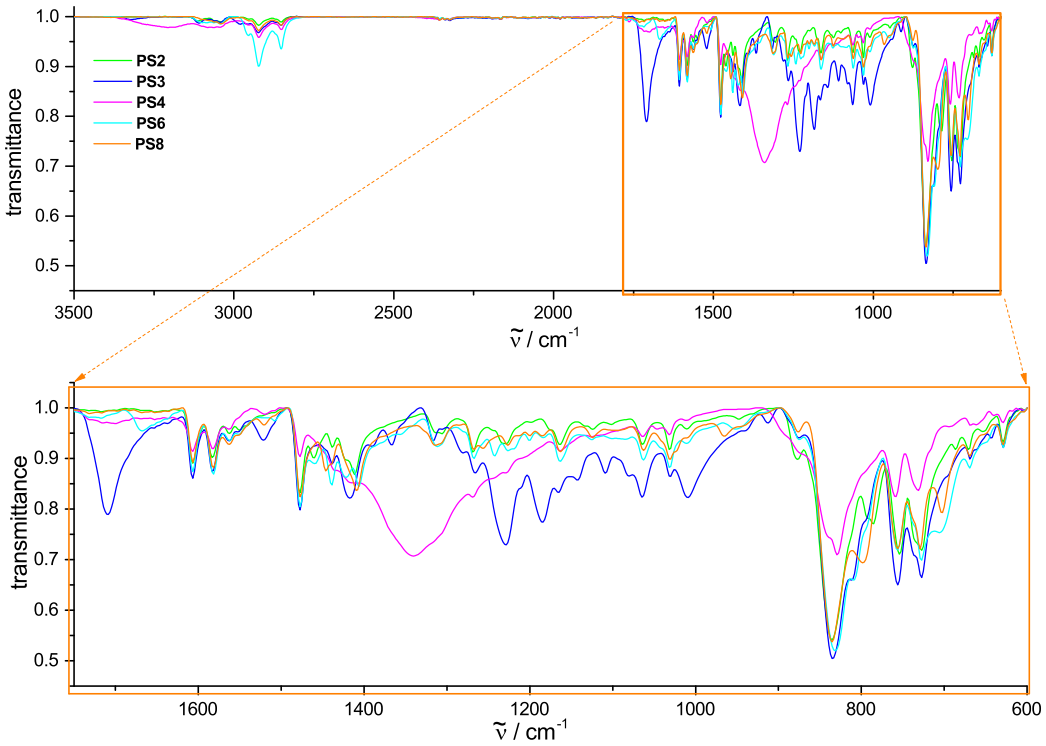

Figure 4.10: Solid state ATR spectra of five selected iridium complexes: **PS2**–**PS4**, **PS6** and **PS8**.

acid at 1338 cm^{-1} (C-O stretch), 1705 cm^{-1} (C=O) and 3222 cm^{-1} (O-H stretch), whereby the first and last peak is extremely broadened.

4.3.2 Crystal Structures

Crystals suitable for X-ray structure analysis were grown by slow diffusion of Et_2O into concentrated solutions of **PS2** and **PS5** in CH_2Cl_2. Acetone was used instead of CH_2Cl_2 for the crystal growth of **PS6**. It was not possible to obtain crystals suitable for X-ray diffraction structure analysis of the remaining complexes. The most important crystal structure data, selected bond lengths and angles for the complexes are listed in Table 4.5. The designations are equivalent to those from Chapter 4.2.2 in which the ligand crystal structures were discussed.

A feature of **PS2** is the *cis* arrangement of the phenylpyridine units. In general, the nitrogens of the phenylpyridines are oriented *trans* to each other as shown for **PS5** and **PS6**. Only a few examples are given in the literature with a *cis* conformation.[160–164] The comparison of the bond lengths of the Ir-N and Ir-C bonds in iridium complexes with the general structure $[Ir(ppy)_2(N\hat{}N)]^+$ revealed average bond lengths for the Ir-N bonds of 2.040 Å, while the average Ir-C bonds are shorter with lengths of 1.950 Å–2.030 Å.[165,166] Due to the poor quality of the **PS2** crystals, which were used

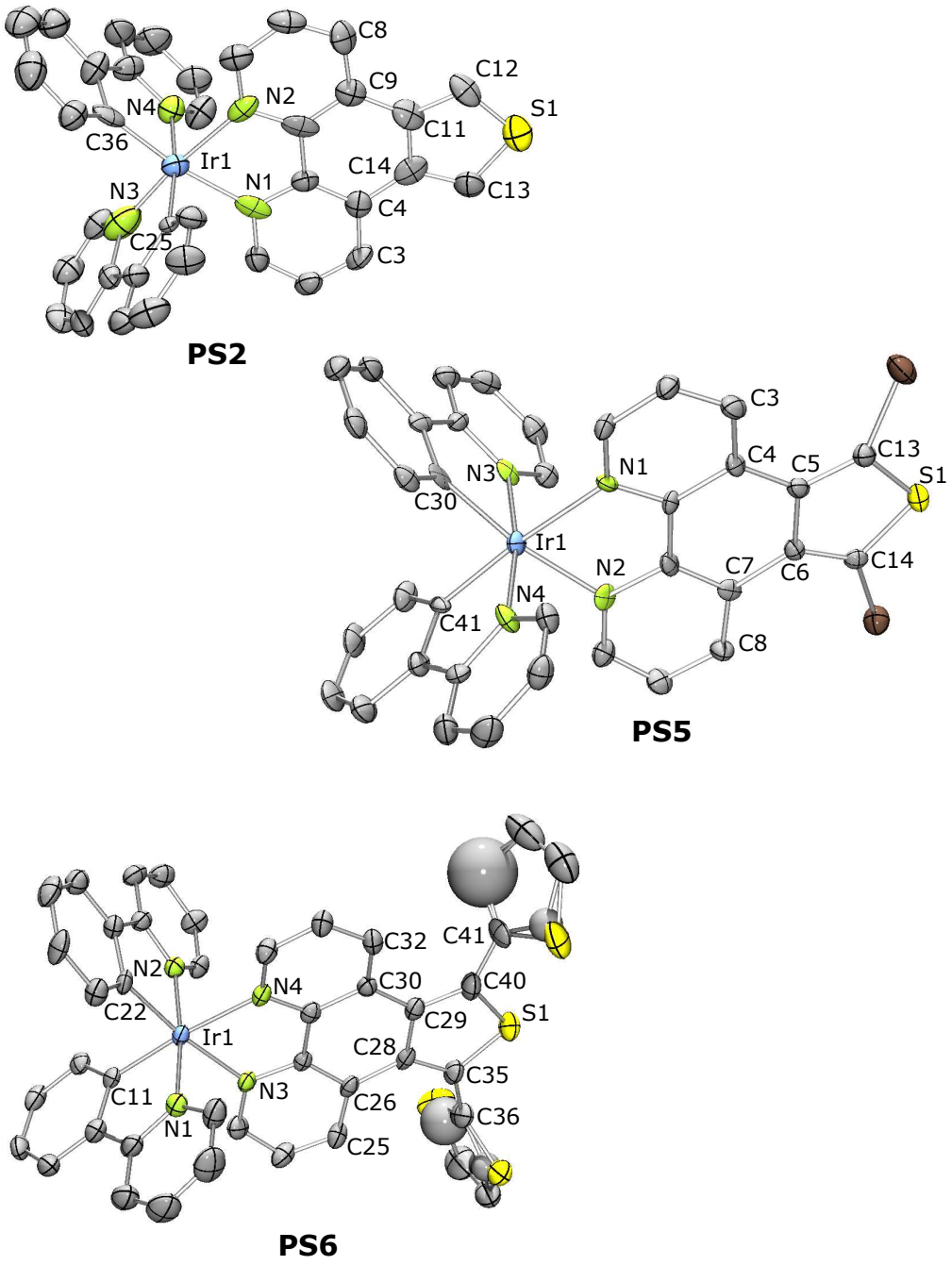

Figure 4.11: ORTEP plot with atomic numbering of **PS2**, **PS5**, and **PS6** drawn at 50 % probability level. All crystals suitable for X-ray diffraction analysis were grown by slow ether diffusion. The PF_6 anions and the hydrogen atoms were omitted for clarity.

Table 4.5: Selected bond lengths and angles of the crystal structures **PS2**, **PS5** and **PS6**. The corresponding structures are shown in Figure 4.11. The designations for the angles and bonds are shown in Figure 4.3 in Chapter 4.2.2.

	PS2	**PS5**	**PS6**
Crystal system	Triclinic	Orthorhombic	Monoclinic
Space group	P -1	P2(1)2(1)2(1)	P2(1)/n
bond length 1 [Å]	1.669(14)/1.672(14)	1.699(6)/ 1.706(6)	1.706(5)/1.711(5)
bond length 2 [Å]	-	-	1.683(8)/1.700(7)
			1.665(8)/1.720(6)[a]
angle [°]	-	-	131.3(4)/130.8(4)[a]
torsion angle 1 [°][b]	0.66/2.46	-9.78 /8.20	7.27/-9.12
torsion angle 2 [°][b]	-	-	68.08/112.03[a]
			76.63/105.11[a]

a) two bond lengths, angles or torsion angles are given for one thiophene due to a disorder of the sulfur atoms over two positions
b) torsion angles were measured in mercury

for the crystal structure analysis, it is possible that on one phenylpyridine the nitrogen and a carbon atom are interchanged and **PS2** also exhibits a *trans* conformation as expected for iridium complexes of this type. The data for **PS2** support this theory with bond lengths for Ir-N(3) of 1.954(15) Å and for Ir-C(25) of 2.029(11) Å (see Figure 4.11). The atoms seem to be interchanged by comparing the Ir-N and Ir-C lengths to the average lengths of the Ir-N and Ir-C bonds. Unfortunately, it was not possible to grow these crystals again for a second crystal structure analysis to assure the *cis* conformation.

In the previous paragraph, the Ir-N bond lengths were already briefly mentioned in the discussion. Now, the Ir-N bond lengths of the cyclometalating and the neutral, ancillary ligand will be considered. The Ir-N bonds are shorter for the C^N ligands compared to the Ir-N bonds between the iridium and the diimine ligands. The Ir-N_{ppy} bond lengths are 1.954 Å–2.059 Å long, while the Ir-$N_{diimine}$ bond lengths are between 2.102 Å–2.148 Å with the assumption that the crystal structure of **PS2** is correct. These different bond lengths are the result of the *trans* influence of the carbon donors on the C^N ligand and, in line with the expectations as it was already reported for many other iridium complexes.[76,80,165–167]

The bite angles of the diimine ligands (N-Ir-N) are smaller than the bite angles of the phenylpyridine ligands (N-Ir-C). The diimine angles range between 76.61 °–77.33 °, while the ppy angles range between 79.80 °–80.88 °. The bite angles are in accordance with other crystal structures, which also consist of two ppy ligands and one phenanthroline derivative as diimine ligand.[168–170]

Chapter 4.2.2 already covered the torsion angles of the phenanthroline-thiophene derivatives due to a preferable coplanar arrangement of the whole ligand structure to obtain an improved electron transfer within the photosensitizers and later, within the dyads. Now, it will be discussed again to clarify, if the coordination to the iridium changed some of these properties and arrangements. Since only crystal structure pairs of two ligand/complex combinations (**L5**/**PS5** and **L6**/**PS6**) are obtained only they will be considered. The designations stay unchanged to that one assigned in Chapter 4.2.2 in Figure 4.3. Torsion angle 1 of **L5** was 0.13 °/1.44 ° (each angle measured on opposite sides of the thiophene), which is a nearly planar arrangement. Through coordination to the iridium this torsion angle is increased to 8.20 ° and -9.78 °in **PS5**. The different algebraic signs imply a twist around the C-C bond of the fused thiophene out of the plane to the foreground and, on the other side, to the background. However, for this ligand-complex pair, a coordination to iridium results in the opposite effect as it is preferred. Torsion angle 1 of **L6** was 4.66 ° , while for **PS6** the same torsion angle is increased to 7.26 ° and -9.12 °. The result is comparable with the before discussed system: Through coordination to iridium torsion angle 1 is increased and also a twist against each other of the fused carbon-thiophene chain occurs. While the torsion angles of **PS5** and **PS6** are larger than five degrees, the torsion angle of **PS2** is -0.22 ° and 2.45 °. This is the smallest torsion angle for all three crystal structures, which can be explained by the missing of any substituent on the fused thiophene ring like in **PS5** the bromine atoms or in **PS6** the additional thiophene rings. Hence, it is logical that torsion angle 1 is larger for **PS6** compared to **PS5** because the additional thiophene rings occupy more space than the bromine atoms. The crystal structures are also compared to a similar structure with regard to the torsion angle. The compound is very similar to **PS2**, but instead of the thiophene, this iridium complex has a fused pyrrole on the backbone.[170] This model complex also has two phenylpyridines as cyclometalating ligands. The general structure of this complex is $[Ir(ppy)_2(phen\text{-}pyrrole)]^+$. Hence, it is a suitable reference complex. Torsion angle 1 of this complex is -0.96 °/-3.96 ° and therefore, they are in the same range as the torsion angles of the here reported crystal structures and even very close to **PS2**. Unlike the three structures, the pyrrole-containing complex is just distorted in one direction while the three complexes show an additional twist around the C-C bond of the fused thiophene out of the plane.

Torsion angle 2, which is only present in **L6** and **PS6** considers the twist of the extended thiophene rings out of the phenanthroline-thiophene plane. For **L6**, a torsion angle of 75.08 ° was measured. A disorder in **PS6** of the sulfur atoms of the outer thiophene rings over four positions makes the measurement of torsion angle 2 more difficult. This disorder of the terminal thiophene rings is not at all a result of poor-quality crystals rather than the result of a not unusual 180 ° rotation of the C-C bond that connects the inner and outer thiophene rings (C(35)-C(36), C(40)-C(41); see Figure 4.11).[152,153] However, the torsion angle changed through

the coordination of to the iridium to -68.08 ° and 76.63 °. Nevertheless, due to the pre-existing orientation out of the plane in **L6**, it can be summarized that the coordination to the iridium has no large influence on the distortion of the outer thiophene rings.

Concerning the hypothesis that a thiophene chain builds a coplanar structure to achieve an improved electron transfer, these structures do not support this theory. If this molecular scaffold builds a coplanar arrangement in the final supramolecular assembly can only be disclosed when a crystal structure of a dyad will be obtained, and the theory will be confirmed or disproved.

4.3.3 Spectroscopy

UV-Vis Spectroscopy

The photosensitizers **PS1–PS9** were characterized by steady-state absorption spectroscopy. This method is a standard analysis procedure to gain a deeper understanding of the photophysical properties. All spectra were recorded with samples prepared in CH_2Cl_2 with a concentration of approximately $2.5 \cdot 10^{-5}$ M. The photosensitizer absorption spectra are shown in Figure 4.12. The corresponding absorption peaks and molar absorption coefficients for **PS1–PS9** are given in Table 4.6. All peak assignments were made by comparison with the ligand spectra and TD-DFT calculations.

The shape of the individual spectra is typical for organometallic compounds. All complexes show strong absorption in the UV region ($\epsilon >$ 50000 $M^{-1} \cdot cm^{-1}$) and weaker absorption in the visible region. Beyond 400 nm only minor absorption is detected ($\epsilon <$ 10000 $M^{-1} \cdot cm^{-1}$). The iridium complexes display good agreement with the ligand spectra (see Chapter 4.2.3). By comparison of the ligands with the corresponding iridium complexes, the complex absorption spectra show a redshift due to an enlarged π system. Considering only the photosensitizers, **PS8** and **PS9** show the largest redshift and molar absorption coefficient due to the largest π system of the ancillary ligand, while **PS6** and **PS7**, which also have an extended π system, are nearly indistinguishable from the small photosensitizers (**PS1–PS5**).

In more detail, the iridium complexes can be divided into two classes, if only the absorptions around 250 nm–300 nm are considered. This are the absorption bands with the highest intensity in the spectra. The complexes **PS1–PS4** show one broad absorption band around 270 nm. This absorption band is assigned to an intraligand $\pi \rightarrow \pi^*$ transfer (LC) on the phenylpyridine ligand as shown in Figure 4.13 for **PS2**.

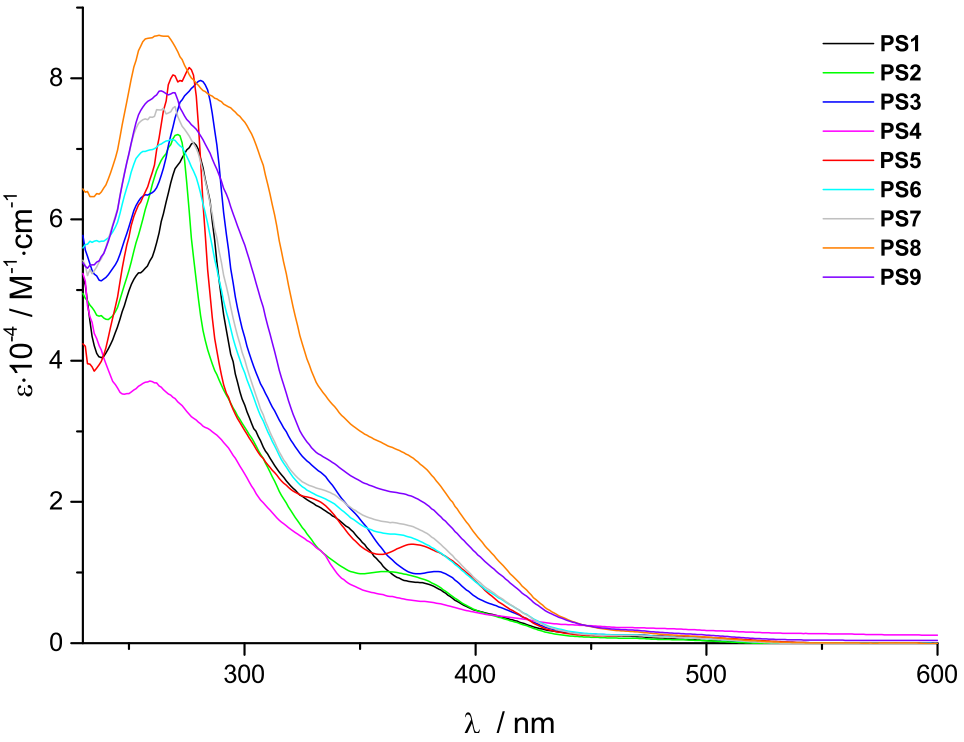

Figure 4.12: UV-Vis spectra of all synthesized iridium photosensitizers measured in deaerated CH_2Cl_2 at 25 °C.

The photosensitizers **PS5**–**PS9** display a double peak structure at approximately 260 nm that is also assigned to an intraligand $\pi \rightarrow \pi^*$ charge transfer process (L'C) on the ancillary N^N ligand. L refers to the cyclometalating phenylpyridine ligand, while L' refers to the ancillary diimine ligand. The associated energy diagram is shown in Figure 4.14. The ancillary ligand-centered $\pi \rightarrow \pi^*$ transitions (L'C) are observed around 335 nm–375 nm for all iridium complexes. **PS1** is an exception with a blue-shifted L'C transition at 293 nm, but this might be due to the different ligand structure of the reference complex. At higher wavelengths only phenylpyridine ligand-centered (LC) and metal-to-ligand-charge-transfer (MLCT) processes are observed. The intensity of the absorption bands are characteristically low as expected for MLCT processes. Three examples of MLCT processes are displayed in Figure 4.15. The figure shows no pure MLCT transitions due to the mixed excited state character of iridium complexes. The HOMO is composed of ppy ligand and iridium centered orbitals, whereas the LUMO is almost localized on the diimine ligands. Additional to the HOMOs (pink/orange orbitals) and LUMOs (green/turquoise orbitals) of **PS2**, **PS7**, and **PS9** the figure illustrates the differences between ligand and iridium complex absorption spectra. For **PS1**-**PS5**, the onset of MLCT transitions can clearly be attributed to a wavelength starting at 400 nm (Figure 4.15, top). The extended ligands **L6** and **L7** show a redshift for the π to π^* transition. Hence, the MLCT absorption range is shortened for the complexes (Figure 4.15, middle). The results of **L8**/**PS8** and **L9**/**PS9** are in accordance with the previous made observations

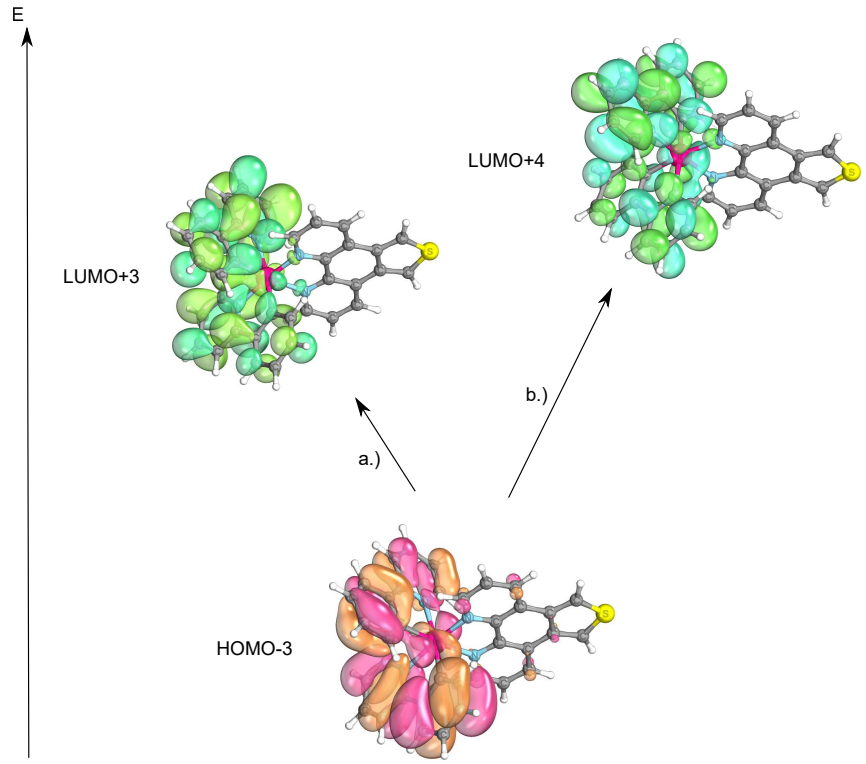

Figure 4.13: Molecular orbitals for **PS2**. a) LC transition on the phenylpyridine ligand from HOMO-3 (pink/orange) to a.) LUMO+3 b.) LUMO+4 (green/turquoise) at 270 nm.

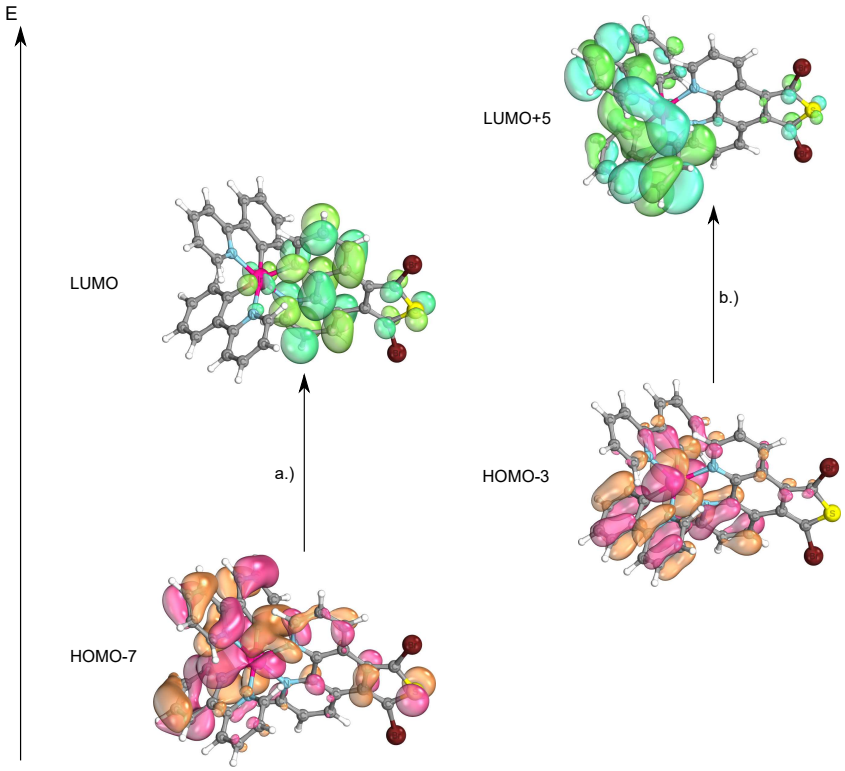

Figure 4.14: Representation of the donor (pink/orange) and acceptor (green/turquoise) orbitals responsible for the absorption at 279 nm in **PS5** a.) LL'CT from HOMO-7 to the LUMO, b.) LC transition from HOMO-3 to LUMO+5.

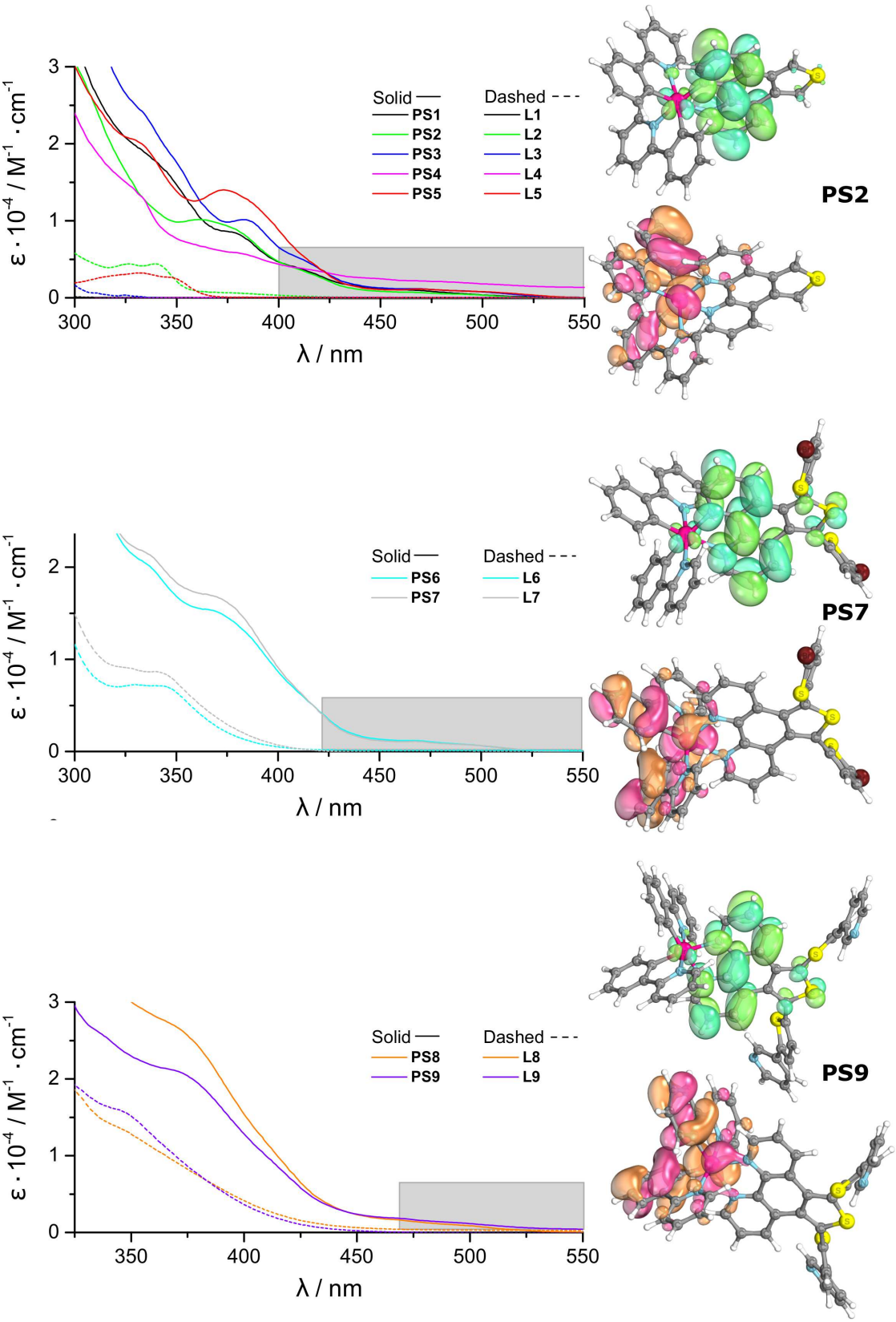

Figure 4.15: Absorption spectra of all synthesized ligands (dashed lines) and iridium complexes (solid lines) with focus on the MLCT transitions (grey rectangle). The right side show the donor (pink/orange) and acceptor (green/turquoise) orbitals for the MLCT process for **PS2**, **PS7** and **PS9**.

(bottom of Figure 4.15). The $\pi \rightarrow \pi^*$ transition is again red-shifted, which results in a superposition of LC and MLCT processes up to 475 nm for **PS8** and **PS9**.

Finally, special attention is directed to the composition of the acceptor orbital of **PS9**. The LUMO involves only the phenanthroline and the fused thiophene part, while the extended thiophenes and pyridines are not involved in this state. This might be of interest for the discussion of the corresponding bimetallic iridium-cobalt system, which will be discussed in Chapter 6.3.1 due to the desired directional electron transfer from the iridium photosensitizer to the cobalt catalyst during the photocatalysis.

Fluorescence Spectroscopy

For a complete characterization of the synthesized iridium photosensitizers, they were submitted to fluorescence spectroscopy. All samples were prepared with a concentration of approximately $2.5 \cdot 10^{-5}$ M measured in CH_2Cl_2. Prior to use, all dissolved samples were applied to at least four freeze-pump-thaw cycles to guarantee an oxygen-free environment

Figure 4.16: Photograph of all synthesized iridium complexes dissolved in CH_2Cl_2 under irradiation with UV light. From left to right: **PS2**, **PS4**, **PS3**, **PS5**, **PS6**, **PS7**, **PS8**, and **PS9**.

Figure 4.16 shows a photograph of the synthesized iridium complexes under UV irradiation. It illustrates really good the different emission efficiencies of the synthesized photosensitizers. The molecule size is increased from left to right from **PS2** to **PS9**, which correlates with a decreased emission ability. The picture shows also a redshift in emission for the first four complexes.

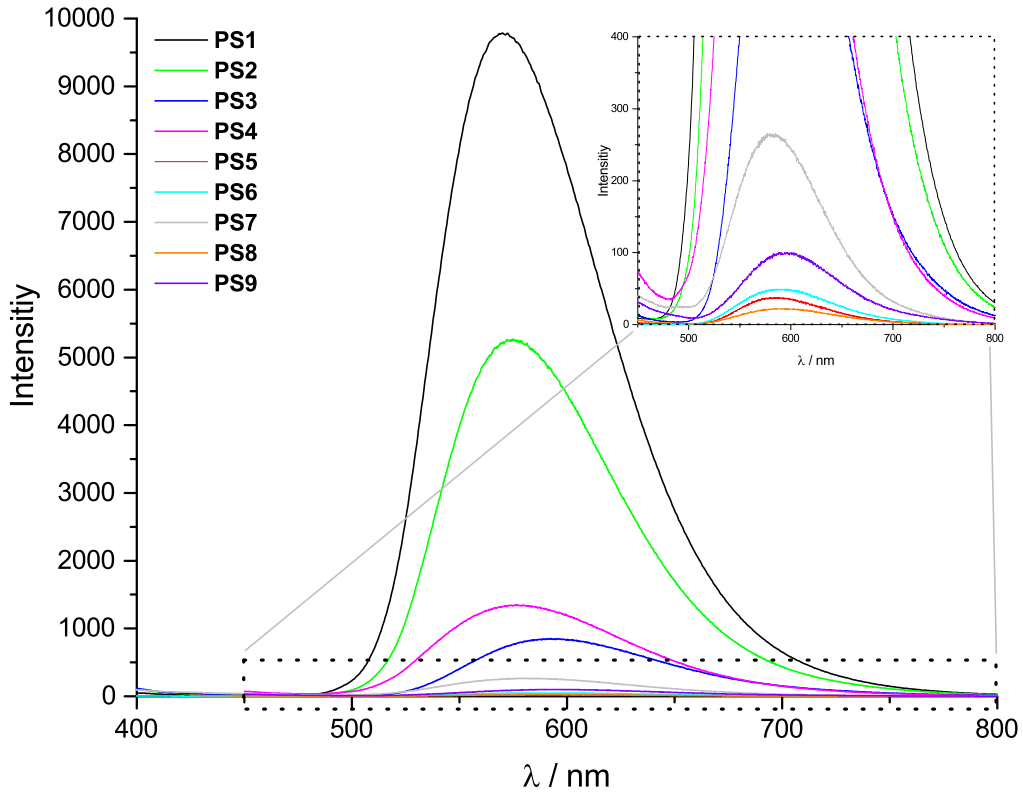

Figure 4.17: Unnormalized fluorescence spectra of **PS1**–**PS9** measured at an excitation wavelength of 260 nm in oxygen-free CH_2Cl_2 at 25 °C.

As well as the picture already showed, there is a huge emission difference for the individual iridium photosensitizers. For a direct comparison of the complexes, the unnormalized emission spectra, which were recorded at an excitation wavelength of 260 nm, are plotted in a single graph (Figure 4.17). The reference complex **PS1** shows the greatest emission at this wavelength. With half of the intensity of **PS1**, the second most emissive complex is **PS2**, which posses the smallest diimine ligand. The photograph already revealed visually that **PS2** shows the highest emission of the newly developed iridium complexes. Only two other iridium complexes exhibit also strong emission, **PS3** and **PS4**. After this four strong-emitting complexes there is a drop in emission for the other five iridium complexes. This might be a result of an increased amount of non-radiative decay pathways due to a larger ligand structure of the diimine unit.[87,171]

This visually made observations are also confirmed by the calculated quantum yield ϕ. In general, the fluorescence quantum yield is the number of absorbed photons in relation to the number of photos emitted by fluorescence. ϕ gives the probability for the deactivation of an excited state by fluorescence, rather than possible deactivation processes through non-radiative radiation. An expression for the quantum yield is given in Equation 4.1:

$$\phi = \frac{k_r}{k_{nr} + k_r} \tag{4.1}$$

Table 4.6: Summarized photophysical properties of **PS1**–**PS9** measured in CH_2Cl_2 at 25 ° C.

PS	λ_{abs} (ϵ) [nm] (M^{-1} cm^{-1})	λ_{em}^{a} [nm]	τ^{b} [ns]	ϕ^{c} [%]
1	253 (52016), 278 (70901), 342 (17129), 378 (8484), 413 (3578), 465 (1008)	570	234	14.0
2	264 (68361),271 (72042), 303 (29060), 365 (10060), 414 (3298), 498 (408)	575	155	11.9
3	257 (63490), 280 (79685), 384 (10141), 412 (4798), 468 (1178), 496 (825)	593	201	1.56
4	256 (37123), 286 (29959), 328 (14375), 382 (5735), 479 (2097)	577	-	0.85
5	253 (61244), 269 (80450), 276 (81528), 332 (20145), 374 (13943), 469 (1130), 505 (748)	584	167	0.08
6	254 (69071), 269 (71270), 336 (20258), 366 (15401), 474 (1079), 495 (724)	590	277	0.11
7	256 (74117), 269 (75774), 335 (21601), 375 (16205), 410 (6567), 468 (1083), 500 (637)	582	365	0.07
8	256 (85154), 265 (85949), 296 (75211), 370 (26786), 413 (10609), 468 (1652), 499 (898)	588	211	0.06
9	255 (75440), 263 (78171), 270 (77950), 280 (71832), 337 (25798), 370 (21054), 470 (1811), 498 (898)	595	523	0.02

a) λ_{ex} was set to 260 nm
b) excited state lifetimes were determined with TCSPC
c) $[Ir(ppy)_2(phen)]PF_6$ was used as reference substance (ϕ= 14.0 %), measured in degassed CH_2Cl_2.[172]

Since the quantum yield is a value that cannot be directly measured, it was necessary to calculate ϕ from the emission data under application of Equation 4.2.

$$\phi_x = \phi_{Std} \cdot \frac{A_{Std}}{A_x} \cdot \frac{F_x}{F_{Std}} \cdot \frac{{\eta_x}^2}{{\eta_{Std}}^2} \tag{4.2}$$

Here, the index x refers to the unknown substance and Std to the standard or reference substance. A is the absorbance at the excitation wavelength. The absorbance should be below 0.05 to avoid inner filter effects and guarantee the validity of the Lambert-Beer law.[173] F is the area under the emission peak, which is recorded at the excitation wavelength and η is the refractive index of the used solvent. If standard and sample are measured in the same solvent, this parameter could be neglected.[174] $[Ir(ppy)_2phen]PF_6$ was chosen as reference substance with ϕ= 14 % in degassed CH_2Cl_2.[102] The quantum yield of this complex was determined multiple times before. For example ϕ= 12.11 % in degassed MeCN with $[Ir(ppy)_2bpy]Cl$ as standard,[103] ϕ= 11.86 % in MeCN with $[Ir(ppy)_2bpy]Cl$ as reference[60] or ϕ= 7 % in degassed CH_2Cl_2 using coumarin as reference.[175] The different quantum yields of $[Ir(ppy)_2phen]PF_6$ already show, that ϕ is dependent on the standard used for the

determination. The excitation wavelength for this experiments was set to 450 nm for **PS2**–**PS9**.

The highest quantum yield of 11.9 % is obtained for **PS2**. The quantum yields of the carboxyl-containing complexes **PS3** and **PS4** are much lower compared to **PS2** with 1.56 % and 0.85 %. The other complexes exhibit extreme weak emission, which is reflected by low quantum yields. These complexes have a ϕ below 0.1 %. According to the definition of the fluorescence quantum yield, which was given above, this means, that these complexes returned to the ground state after the excitation with non-radiative radiation.

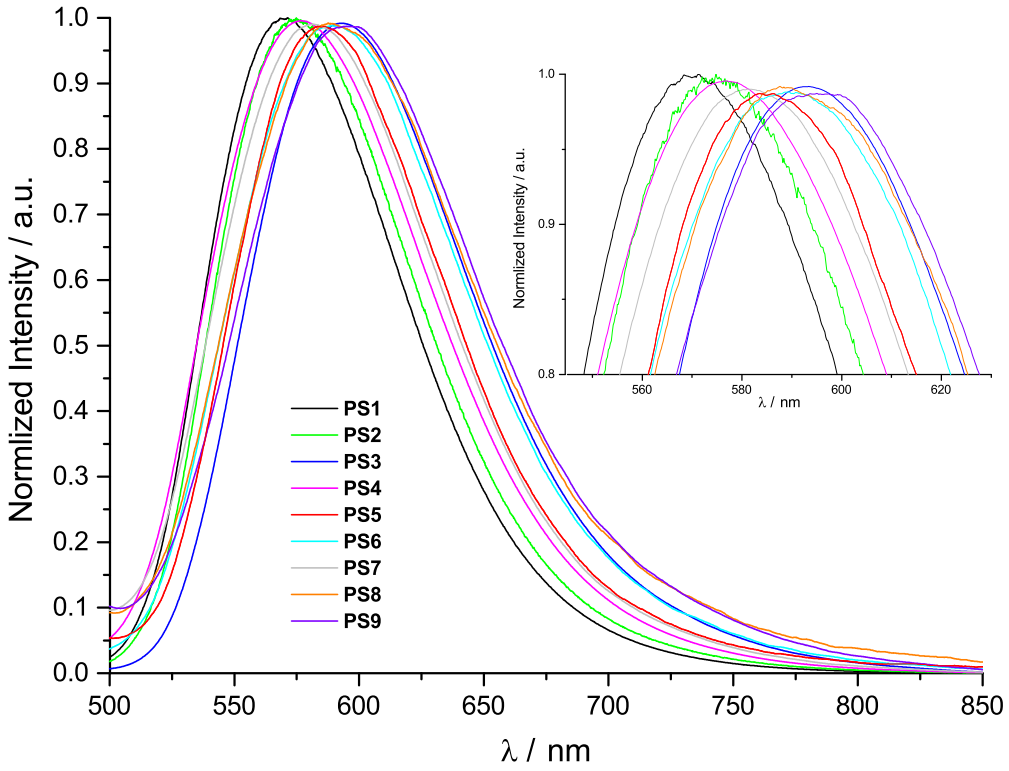

Figure 4.18: Normalized fluorescence spectra of **PS1**–**PS9** measured at an excitation wavelength of 260 nm in deaerated CH_2Cl_2 at 25 °C.

The normalized fluorescence spectra of **PS1**–**PS9** are shown in Figure 4.18. The complex with the shortest emission maximum of λ_{em} = 570 nm is **PS1**. With slightly higher energies, the emissions of **PS2** (λ_{em} = 575 nm) and **PS4** (λ_{em} = 577 nm) are detected. It seems like the carboxylate group has only minor influences on the emission maximum of the photosensitizer **PS4**, whereas the ethyl ester groups of **PS3** lead to a stronger redshift with an emission maximum located at 593 nm. It also seems like the ester groups essentially affect the LUMO, which is located on the N^N ligand and therefore the HOMO-LUMO gap. With an increasing diimine system, the emission is red-shifted compared to **PS1**. This was already observed for the absorption spectra and now confirmed with the emission data. The exact emission wavelengths are listed in Table 4.6.

Besides the standard characterization methods, all iridium complexes were also characterized by TCSPC emission lifetime determination. The knowledge about the excited state lifetimes is essential to evaluate if an electron transfer is possible within the interval during which the photosensitizer is excited. The excited state lifetime of a photosensitizer must be as long as possible to guarantee an electron transfer from the PS to the catalyst, but this time must also be as short as possible to prevent recombination processes with the SR or the CAT, depending on if the reductive or oxidative quenching mechanism is present. Therefore, it is an important method to understand the photocatalytic water splitting results under application of these iridium complexes.

For the sample preparation, all samples were deaerated by at least four freeze-pump-thaw-cycles. Afterward, the emission maxima were taken from the already reported fluorescence spectra. The knowledge of the emission maxima is necessary to obtain an adequate result of the lifetime determination. Every sample was irradiated with a 374 nm LASER diode and the investigated range lay between 30 ps and 10 μs. Also, a minimum of 10000 counts was collected for every sample to guarantee a suitable result. Figure 4.19 shows a typical decay of an iridium photosensitizer. For each lifetime determination, a prompt and a decay must be measured. The prompt might be understood as a blank value, which is essential for the data analysis. The decay shows a typical exponential decrease like it is typical for iridium photosensitizers.[81,165] The shoulder or bump around 1000 channels indicated the presence of an additional species with a different excited state lifetime. The equation, which is used by the data analysis program DAS6 is given in Equation 4.3 and 4.4. A refers here to the background offset, B is a pre-exponential factor that relates to how much of an emitting species is present in the sample and τ is the lifetime. The emission lifetime which is reported here is τ_{av}.[176]

$$F(t) = A + \sum_{i=1}^{i} B_i + exp(-\frac{t}{\tau_i}) \tag{4.3}$$

$$\tau_{av} = \sum_{i=1}^{n} B_i \tau_i \tag{4.4}$$

The calculated emission lifetimes of **PS1–PS9** are summarized in Table 4.6. All photosensitizers are unknown up to this point. Therefore, a direct comparison with already characterized iridium complexes is difficult. However, it will be tried to connect this results to already known systems. Slight deviations are possible and comprehensible due to different solvents used for emission lifetime determinations. For this measurements, CH_2Cl_2 was used as solvent, but most analyses reported in the literature are

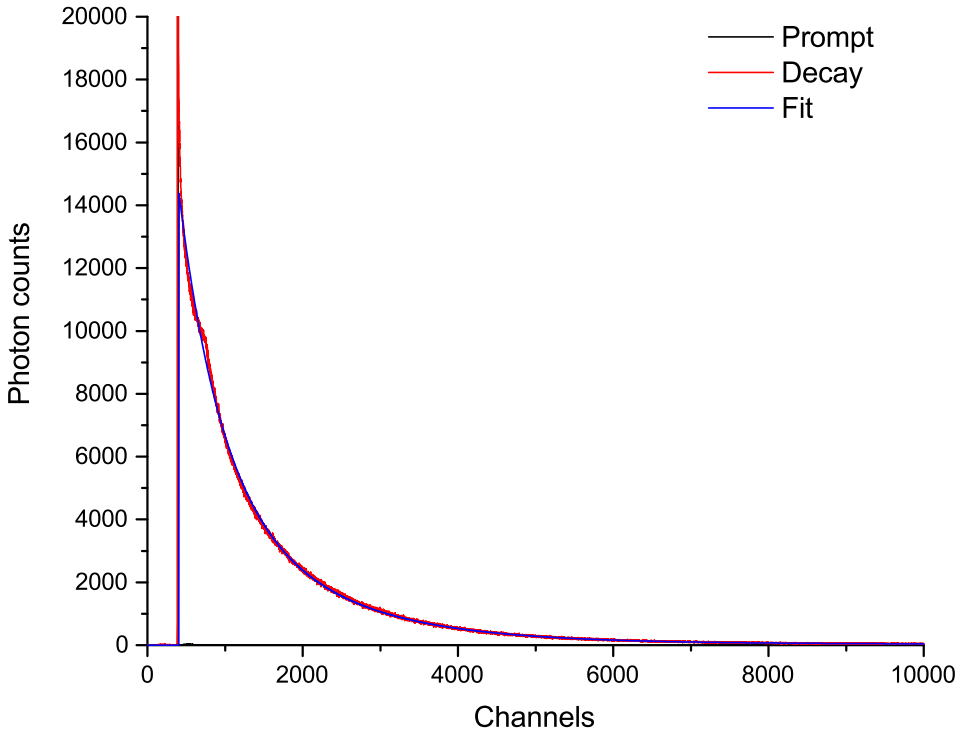

Figure 4.19: Example for a TCSPC emission lifetime determination of **PS9**. τ was calculated with a three exponential fit and a lifetime of 523 ns.

conducted in MeCN. Furthermore, typically, emission lifetimes cover a huge range from the nanosecond to the high microsecond range, and they depend strongly on the method used for the emission lifetime determination.[4,60,86,87,92,103,115,177–180] In 2004, the Bernhard group synthesized a series of new iridium complexes with various bipyridine and phenanthroline derivatives as N^N ligands, which were all characterized by emission lifetime measurements.[103] Only one result should be discussed here: They determined the emission lifetime of $[Ir(ppy)_2phen]^+$ (**PS1**) as a reference complex with a τ of 877 ns. In comparison to the lifetime determined here for the same complex (τ= 234 ns), their lifetime is much longer. Whereas the group of Murakami Iha published an emission lifetime for **PS1**, which is quite similar to that one reported here with τ= 360 μs.[179] A third and last value should also be mentioned here reported by the Zhao group. They determined the lifetime with 770 ns for the complex.[180] The three examples show the large influences of solvents, which device is used for the data acquisition, what method is used for the analysis and most important if the sample is measured under oxygen-free conditions.[103,179,180]

The comparison of **PS2** (τ= 155 ns) with **PS5** (τ= 167 ns) and **PS6** (τ= 277 ns) with **PS7** (τ= 365 ns) reveals that the introduction of a bromine substituent on the diimine ligand results in a prolonged emission lifetime. Even stronger is the effect

that is observed for **PS4**. It was not possible to determine the excited state lifetime with our device due to a τ that is longer than 10 μs. The higher emission lifetimes might be a result of the electron withdrawing effects of the substituents, which results in an enhanced ability of the iridium complexes to maintain in the excited state. A tendency shows a correlation between the emission maxima and the excited state lifetimes for all iridium photosensitizers; With a lower energetic emission wavelength, the excited state lifetime is prolonged, except for **PS8** (τ= 211 ns), which exhibited a relatively short excited state lifetime. In general, the excited state lifetime is prolonged in the order **PS2** < **PS5** < **PS8** < **PS6** < **PS7** < **PS9**.

4.3.4 Cyclic Voltammetry

After the spectroscopic characterization of the iridium photosensitizers, they were also characterized by electrochemistry. Therefore, the redox potentials were determined with cyclic voltammetry (CV). Samples with a concentration of 1 mM were prepared and the CVs were recorded in prior to use degassed MeCN at 25 °C with tetrabutylammonium nitrate (TBAN) as supporting analyte. All peaks were quoted relative to the ferrocene/ferrocenium (Fc/Fc^{+}) couple, and a three-electrode arrangement was used consisting of a Pt working electrode, an $Ag/Ag(NO)_3$ reference electrode and a Pt wire as counter electrode.

The CV data of **PS1–PS9** are displayed in Figure 4.20. The spectra of the investigated complexes exhibit all a high variety of oxidation and moreover reduction processes. The oxidations are mainly present for metal-centered orbitals, whereas the reduction processes solely occur on the ligands.

The signals at 0.86 V–0.89 V are assigned to the oxidation of the iridium center (Ir^{+III}/Ir^{+IV}). These signals show typically a reversible or quasi-reversible behavior.[166,181–183] They are in accordance with previous reported oxidation potentials for iridium complexes.[4,51,184–186] In general, the oxidation peaks are associated with the HOMO, while the diimine reduction processes are associated with the LUMO.[106] The most positive potentials are measured for one of the largest iridium complexes **PS8**. This result is unexpected due to the considerable distance of the pyridine groups to the iridium center. Moreover, the diimine ligands should not influence the HOMO energy of the iridium complex. However, this process that is formally assigned to the iridium oxidation is just minor influenced by the variation of the neutral ligand. The second oxidation, which was not observed for every photosensitizer, is more positive with potentials around 1.20 V. This oxidation is assigned to a thiophene-based process and is only visible for **PS6**, **PS7**, and **PS8**.[187] The square wave spectrum of **PS9** also shows this oxidation process, but in the CV the thiophene-based and iridium-centered oxidation signals seem to superimpose

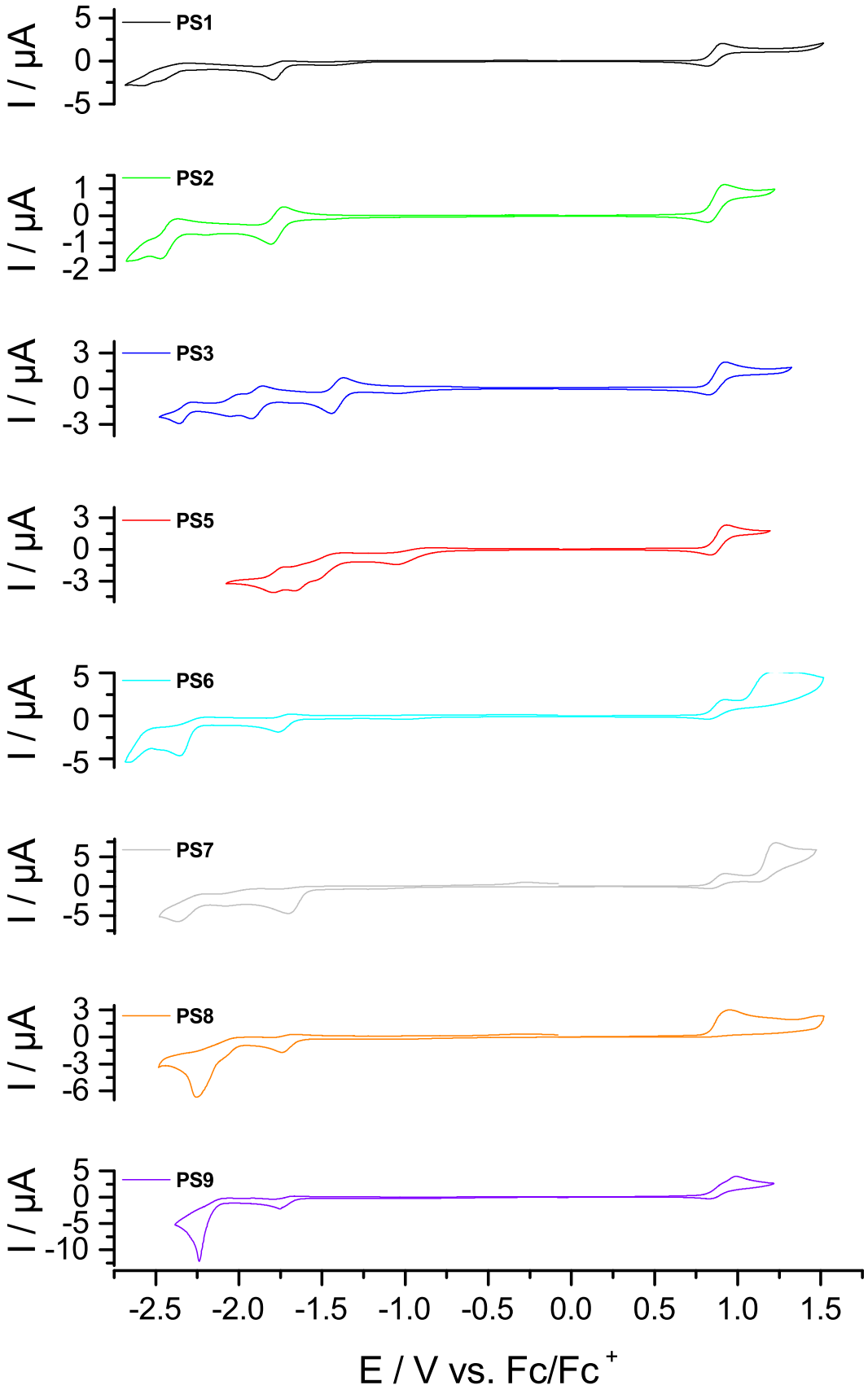

Figure 4.20: CV of eight heteroleptic iridium complexes measured in MeCN with TBAN as supporting analyte. All peaks are quoted relative to the ferrocene/ferrocenium(Fc/Fc^{+}) couple.

Table 4.7: Redox potentials (*vs.* Fc/Fc^+) of **PS1**–**PS9** in degassed CH_3CN at 25 °C.

PS	E_{Ox} [V] (Δ E [mV])		E_{Red} [V] (ΔE [mV])				ΔE [V][c]
1		0.86 (95)		-1.76 (71)		-2.37 (112)	2.62
2		0.87 (103)		-1.77 (81)		-2.42 (105)	2.64
3		0.88 (100)	-1.41 (73)	-1.89 (68)	-2.03 (41)	-2.32 (78)	2.29
5		0.88 (97)	-1.47 (129)	-1.67[b]	-1.76 (56)		2.35
6	1.23[a]	0.87 (110)		-1.72 (76)		-2.29 (136)	2.59
7	1.18 (120)	0.88 (96)		-1.66 (80)	-1.99 (171)	-2.29 (154)	2.58
8	1.20[a]	0.89 (133)		-1.70 (75)	-2.04 (107)	-2.25[b]	2.59
9		0.86 (68)		-1.72 (71)		-2.24[b]	2.58

a) $E_{p,c}$ b) $E_{p,a}$ c) $\Delta E = E_{Ox,min} - E_{Red,max}$

on each other, and the thiophene-based oxidation potential cannot be determined properly. Therefore, this potential is not listed in Table 4.7 for **PS9**. The results indicate that the oxidation occurs at the terminal thiophene rings, which are present in **PS6**–**PS9**, due to missing oxidation peaks for the iridium complexes **PS2**–**PS5**. They also possess the fused thiophene ring, but this ring is not involved in the oxidation process.

The assignment of the reduction potentials is more complicated due to a rich voltammetric pattern for the reductions associated with the cyclometalating phenylpyridine and the neutral diimine ligands. All reduction processes between -1.43 V and -2.04 V are assigned to processes present on the phenanthroline derivatives. **PS1**–**PS9** show a reversible reduction at -1.66 V–-1.89 V, which is assigned to a phenanthroline based reduction.[172] The potential of **PS3** is shifted significantly toward a more cathodic current by 120 mV compared to **PS2** with a potential of -1.77 V to -1.89 V, which might be a result of the electron-withdrawing ester groups in **PS3**. The electron density on the phenanthroline part is reduced, which lead to a lowering of the LUMO energy.[99] Hence, with the HOMO as an iridium-centered orbital with contributions from the CˆN ligand, and the LUMO as a diimine-localized orbital, the energy gap between HOMO and LUMO is assigned to the difference between the first oxidation and reduction wave.[106] The energy differences are also given in Table 4.7. Interestingly, the bromine containing photosensitizer **PS5** shows the opposite effect. Both iridium complexes exhibit a different mesomeric behavior. The ester groups has a negative mesomeric effect, and therefore the electron density within the complex is reduced. In contrast to this, the bromide atoms pushes their electrons into the system and increase the electron density. The same effect is observed for the extended iridium complexes **PS6** and **PS7**. The potential is shifted by 60 mV from -1.72 V to -1.66 V through the introduction of the bromine atoms. The reduction of the phenylpyridine ligand is known to occur at more negative potentials as discussed until now. Usually, they are present at potentials more negative than -2.3 V *vs.* Fc.[172,181,188] Therefore, the reduction waves between -2.24 V–-2.42 V are assigned to a phenylpyridine-based reductions.

4.4 Catalysts

4.4.1 Iron Catalysts

During this thesis, different types of water reduction catalysts were synthesized and tested in photocatalytic water splitting experiments. One focus laid on the synthesis of an iron catalyst. In 2011, Beller *et al.* tested a series of phosphine and phosphite ligands in combination with $Fe_3(CO)_{12}$ as water reduction catalysts.[59] The efficiencies for these systems were the highest reported in literature until now for an iron-phosphine system. Inspired by these results, a pincer complex was chosen that seems a promising candidate for competitive results.

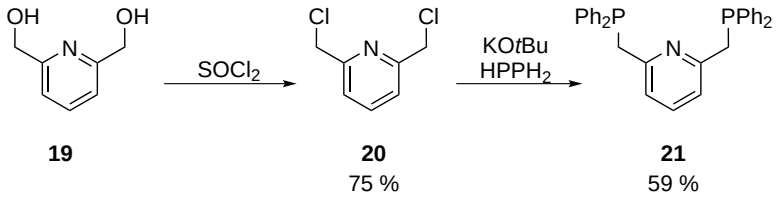

Figure 4.21: Synthetic route from 2,6-Bis(hydroxymethyl)pyridine **19** to 2,6-bis(diphenylphosphanyl)methylpyridine **21**.

The results presented here for the catalysts **Fe1** and **Fe2** were obtained in cooperation with Pia Rehsies as part of a bachelors thesis.[189] The final PNP pincer ligand was synthesized in a two-step reaction. First, pyridine-2,6-dimethanol **19** was converted with $SOCl_2$ to the pyridine dichloride **20**. The product was isolated with a yield of 74.5 %. The dichloride was afterward brought to reaction with KO*t*Bu and $HPPh_2$ to isolate the desired ligand **21** for the iron complexes **Fe1** and **Fe2**. Since the syntheses of these two products were already literature known, the characterization will not be further discussed here.

The first iron catalyst **Fe1** was isolated after the conversion of the pincer ligand **21** with $FeCl_2$. The second iron catalyst **Fe2** was generated with two different

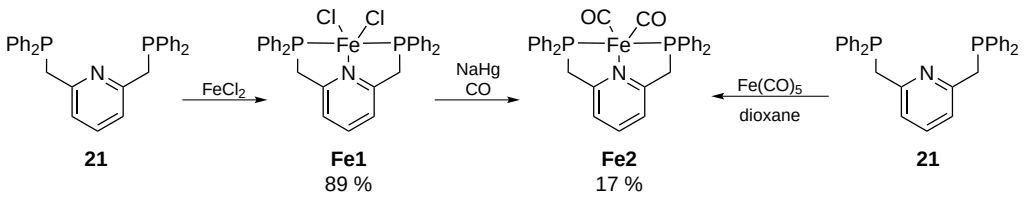

Figure 4.22: Two different synthesis strategies to obtain two different iron catalysts **Fe1** and **Fe2** from **21**.

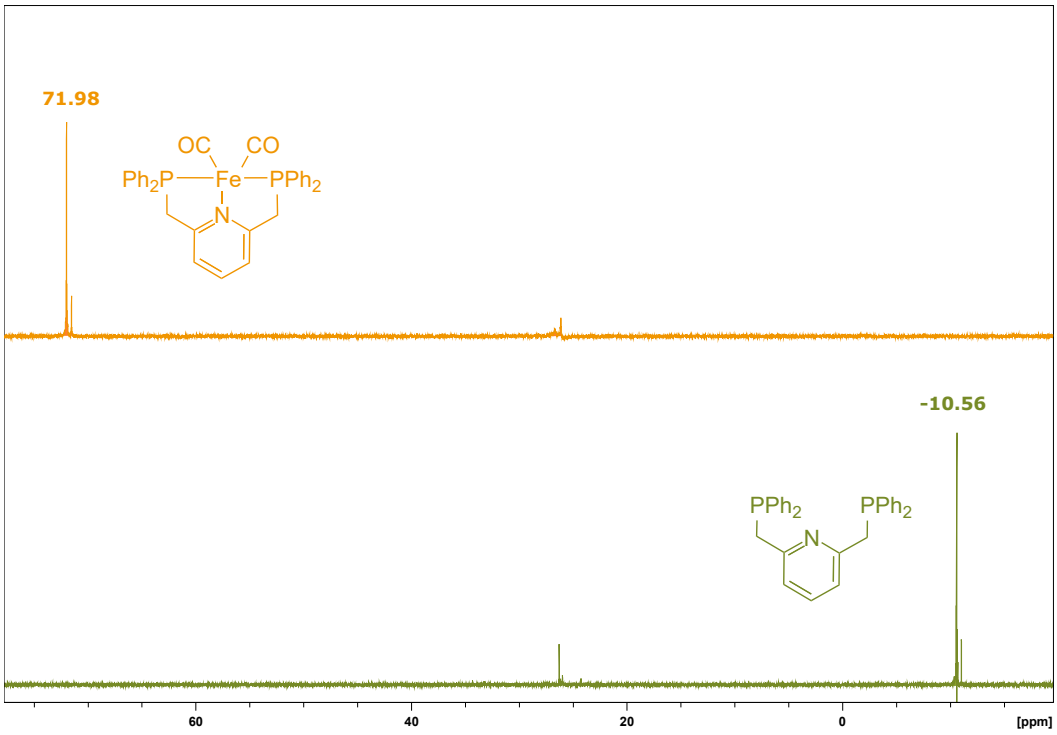

Figure 4.23: ^{31}P NMR spectra of free PNP ligand **21** (green) and Fe(PNP)(CO)$_2$ **Fe2** (orange) in C_6D_6.

reactions. The first synthesis used Fe(PNP)Cl$_2$ with NaHg$_x$ and CO gas. **Fe1** and NaHg$_x$ was submitted to a Schlenk flask and stirred for a while. Afterward CO gas was bubbled through the reaction solution. During this time the color of the reaction mixture changed from yellow to purple, which indicates a conversion of the reagents. The solution was filtered through celite, and the solvent was removed to obtain a black solid. The ^{1}H spectrum of the complex was significantly broadened due to paramagnetic impurities and no analysis was possible. The ^{31}P NMR shows a lowfield shift of the uncoordinated PNP ligand from -10.56 ppm to 71.98 ppm, which also indicates a successful synthesis of the desired product. Both spectra, ligand and complex, are depicted in Figure 4.23. The second method was conducted with the free pincer ligand **22** and iron pentacarbonyl in dioxane. The mixture was stirred for more than 72 h and after filtration a dark red solid was isolated, which was also identified as the product **Fe2**. The characterization of **Fe2** *via* mass spectrometry was also difficult due to the easy loss of CO ligands during the measurements. Therefore, no mass peak was found in these spectra.

To ensure the synthesis of **Fe2**, an IR spectrum was recorded and a DFT-based IR spectrum was calculated. The spectra were plotted in one graph and the result is shown in Figure 4.24. Both spectra display identical, very intense signals for the carbonyl ligands. The asymmetric vibration is found at 1944 cm^{-1} (cal: 1914 cm^{-1}) and the symmetric vibration at 1904 cm^{-1} (cal: 1881 cm^{-1}). At this moment this

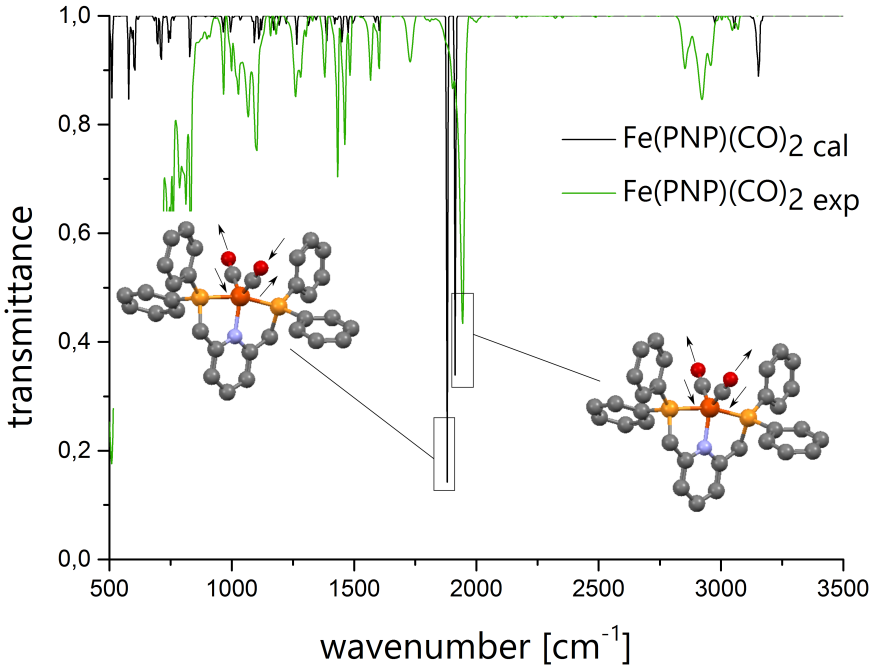

Figure 4.24: Calculated and experimental IR spectra of Fe(PNP)$(CO)_2$. The left structure shows the asymmetric vibrations of the carbonyl ligand in **Fe2**. The right structure shows the symmetric vibration of the CO ligand in **Fe2**.

analysis was found to be sufficient to ensure the synthesis of the carbonyl-based iron pincer complex.

After the successful conversion of the PNP ligand to the desired iron catalyst **Fe2**, the pyridine pincer ligand was additionally introduced into a reaction with the precursor iridium complex. It should be tested, if the coordination of **21** to the iron precursor is a selective process and no iridium will be introduced into the pincer when iridium is also available as possible coordination metal. For the eventual synthesis of a supramolecular iridium-iron system, it is essential that selective coordination of the final ligand to the two different metals is possible. The reactions were monitored *via* mass spectrometry (Figure 4.25 and 4.26). Figure 4.25 shows the reaction of the precursor iridium dimer complex $[Ir(ppy)_2Cl]_2$ with the PNP pincer ligand **21**. Unfortunately, the iridium was incorporated into the pyridine pincer, and an iridium complex with a mass of 976.25 m/z was formed, which was identified as $[Ir(ppy)_2(PNP)]$. Besides the mass peak, the spectrum shows several other signals that are assigned to species that occur during the measurement. Due to the sensitivity of phosphor to get oxidized, the spectrum also shows the signals of the singly oxidized product as well as the doubly oxidized species.

Since the first reaction showed that the PNP pincer is also attractive for a coordination to iridium a second reaction was conducted with an additional reagent. Besides the iridium precursor and the pincer reagent, the diimine ligand 1,10-phenanthroline that should be more favored to be coordinated by the iridium was introduced to the reaction mixture.

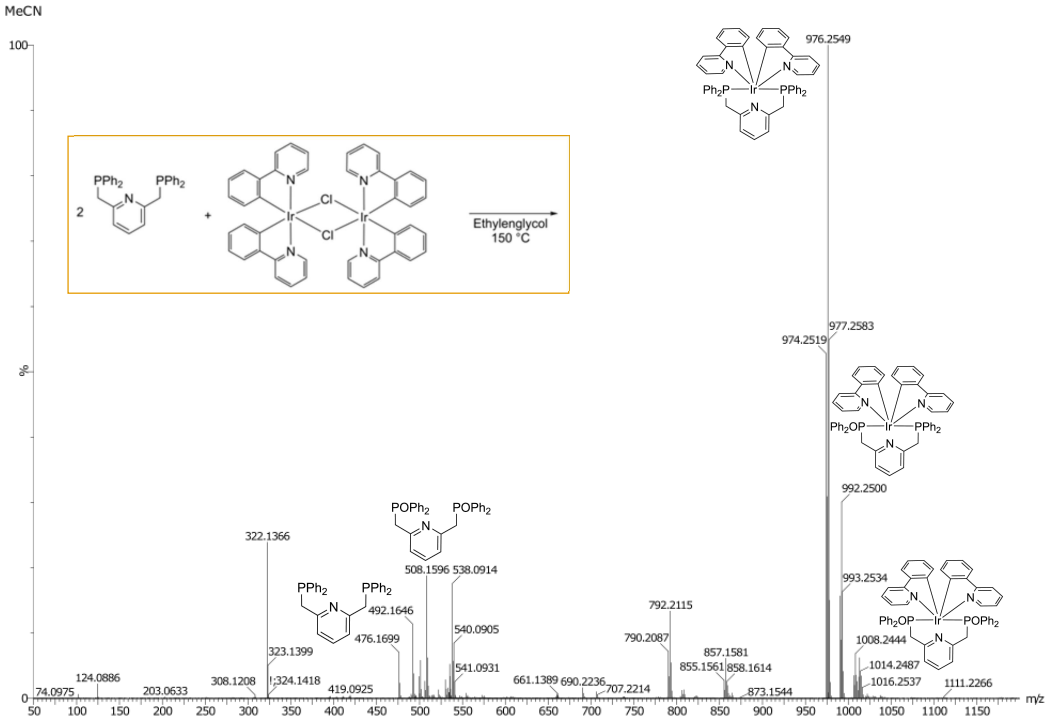

Figure 4.25: ESI(pos)-MS spectrum of the reaction of $[Ir(ppy)_2(Cl)]_2$ with the PNP pincer ligand.

The mass spectrum of this reaction is shown in Figure 4.26. Unfortunately, this spectrum also shows the mass peak of $[Ir(ppy)_2(PNP)]$ that was already found in the previous experiment. But the spectrum shows the signal for the desired $[Ir(ppy)_2(phen)]^+$ complex, too. Even if it is not possible to give a statement about the amounts of the individual components with the analysis of the mass spectrum, it is obvious that active, competitive reactions proceed on the coordination of the pyridine pincer. This is challenging due to an upcoming non-selective synthesis of a supramolecular Ir-Fe system. Hence, it is necessary to protect the PNP unit on the pyridine when the ligand is brought to reaction with the iridium precursor to prevent the undesired incorporation of the iridium into the pincer ligand. One possibility is the protection of the phosphine groups with a borane.[190,191] After the successful synthesis of the desired iridium complex, the phosphine-borane adduct can be deprotected to enable the PNP ligand to be coordinated to the iron center. This protection procedure would have another advantage because the phosphine groups were also protected against oxidation.

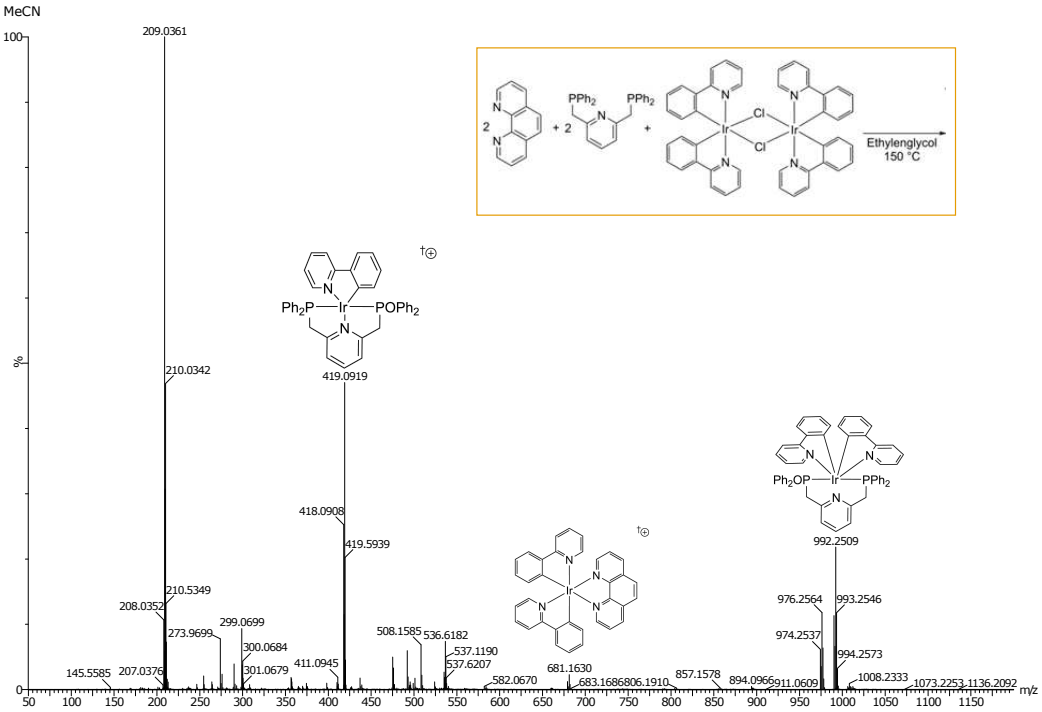

Figure 4.26: ESI(pos)-MS spectrum of the reaction of $[Ir(ppy)_2(Cl)]_2$ with the PNP pincer ligand and 1,10-phenanthroline.

4.4.2 Cobalt Catalyst

In addition to the iron systems, two different cobalt complexes were also synthesized for the application as water reduction catalysts in two-component systems. $[Co(bpy)_3]^{2+}$ **Co1** was the first synthesized catalyst. This catalyst was already used in photocatalytic water reduction experiments.[60,106,192] Although the reaction was already reported in the literature, the synthesis was not as easy as expected. Two different solvents, MeOH and EtOH, were used for the reaction and, depending on the solvent the desired catalyst or another, undesired complex was produced (Figure 4.27). For the synthesis with ethanol as solvent, a complex structure of $[Co(bpy_2)Cl_2]$ **Co2** was obtained. The crystal structure is shown in Figure 4.30. Instead of the third bipyridine ligand, this one has two coordinated chloride ligands. Under similar conditions, but this time with methanol as solvent, the desired cobalt complex $[Co(bpy)_3]^{2+}$ **Co1** was obtained. It was possible to isolate crystals suitable for X-ray diffraction analysis for this structure, too. The ORTEP plot of **Co1** is also shown in Figure 4.30. The changes in the reaction conditions led to a completely different result, which was triggered by a change of the reaction temperature and not as initially thought by a solvent change. While the methanol reaction, which led to **Co1**, was stirred at 40 °C, the ethanol reaction was refluxed during the reaction time. The higher temperature leads to thermal decomposition of the initially desired complex **Co1** and forms the structure of **Co2**.[193] Strangely, the group of Bernhard

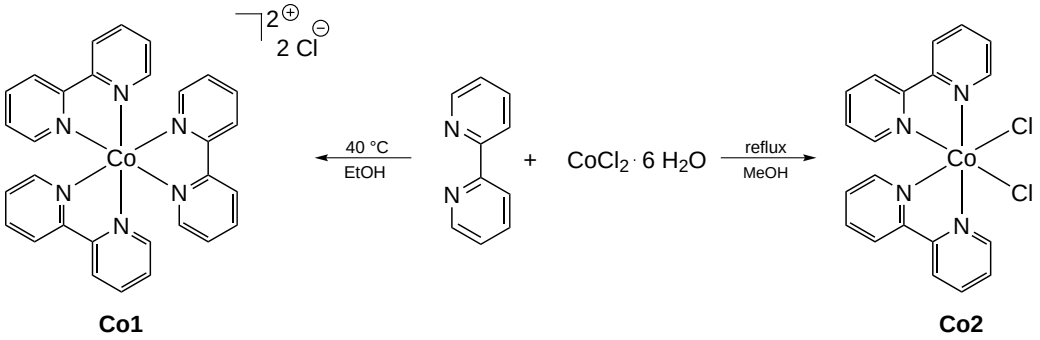

Figure 4.27: Synthesis of **Co1** and **Co2**. The formation of the respective product depends on the reaction conditions.

reported they used $[Co(bpy)_3]Cl_2$ as water reduction catalyst, but they carried out the synthesis that leads to **Co2**. Since they published no analysis data for this structure, it stays unclear up to this point if they really used $[Co(bpy)_3]Cl_2$ or maybe $Co(bpy)_2Cl_2$.[60,106]

As second cobalt catalyst, $PyCo(dmgH)_2Cl$ **Co3**, an already known cobaloxime was also synthesized. The procedure was a straightforward two-step synthesis, which is shown in Figure 4.28.[68,194] During the first step, $CoCl_2 \cdot 6\ H_2O$ and dimethylglyoxime was stirred in acetone, which resulted in a violet suspension. The product **Co3-1** precipitated as dark crystals that were finally filtered off. This dark-green product was applied to a synthesis with TEA in methanol with subsequent addition of pyridine, which resulted again in a precipitation of a solid. The yield of the final product **Co3** was 71.2 %. The first cobalt intermediate **Co3-1** was only roughly

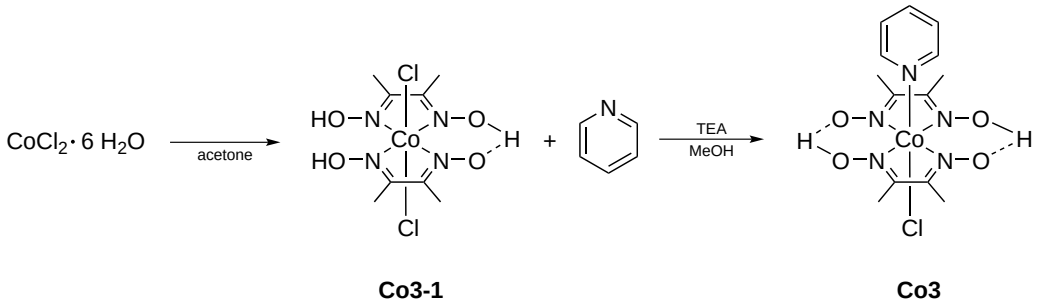

Figure 4.28: Two-step synthesis route for the dimethylglyoxime-based cobalt catalyst.

characterized due to a minor solubility in organic solvents, only a ^1H NMR spectrum was recorded in DMSO d_6. The ^1H spectrum shows just two signals that are assigned to the methyl groups and the broad signal around 5 ppm to the hydroxyl groups of the dimethylglyoxime.

The final product **Co3** exhibited again a good solubility in common organic solvents and were therefore fully characterized by standard procedures. Figure 4.29 shows the ESI-MS spectrum of **Co3** recorded in acetonitrile. The spectrum shows that the

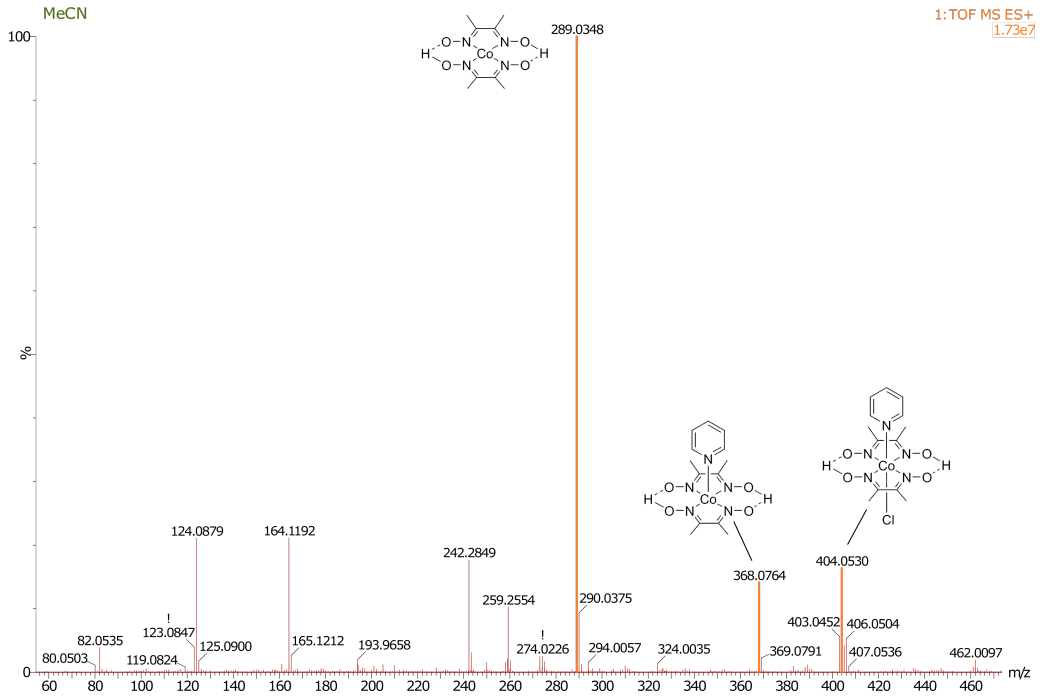

Figure 4.29: ESI(pos)-MS spectrum of **Co3** measured in MeCN.

most stable fragment is based on the cobalt-dimethylglyoxime fragment, while **Co3** gets fragmented during the measurement. The axially bound pyridine and chloride ligands are more weakly coordinated compared to the bidentate dimethylglyoxime ligands of the cobalt complex.

Crystal Structures

The crystal structure of **Co1** was obtained after an anion exchange to hexafluorophosphate. Afterward the solid was dissolved in CH_2Cl_2 and submitted to ether diffusion with THF to obtain crystals as yellow prisms. The red crystals of **Co2** was obtained by ether diffusion of Et_2O into a concentrated **Co2** solution made of ethanol.

Both Co(II) structures show a distorted six-fold coordinated octahedral arrangement. **Co1** crystallizes in the space group P 31, while **Co2** in the space group P2(1)/c. The structures of **Co1** and **Co2** were already reported in literature, but with other anions or crystallized solvent molecules.[193,195–197] A few selected bond lengths and angles are summarized in Table 4.8. Interestingly, the bite angle of Cl-Co-Cl in **Co2** is quite similar, but wider with an angle of 98.54(2) ° to that one reported in 1986 by Krämer and Strähle with 97.9(1) °. Although it is the same structure, the deviation of the bite angle to that one reported by Dayalan *et al.* with 92.22(5) ° is more significant.[193,197] This different angles might be an effect of packing caused by the solvent molecules (EtOH *vs.* (CH_2Cl_2 or H_2O). The Co-Cl bond lengths

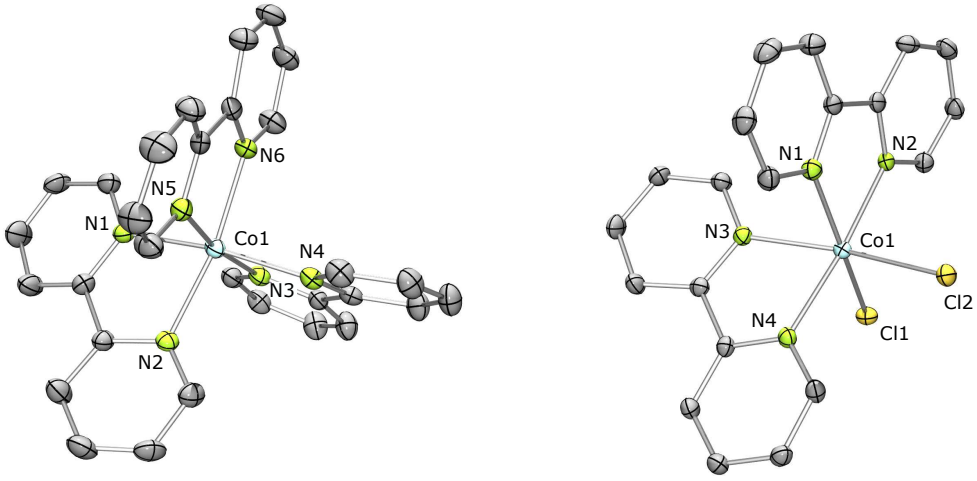

Co1 **Co2**

Figure 4.30: X-ray structure of **Co1** and **Co2**. Hydrogens, anions and solvent molecules were omitted for clarity. ORTEP plot drawn at 50 % probability level.

(2.4025(7) Å and 2.4569(8) Å) have similar lengths compared to the other two structures (2.4298(9) Å[197] and 2.450(3) Å/ 2.392(3) Å[193]), but in contrast to the sum of the covalent radii of cobalt and chloride (2.243 Å), this bond length is elongated.[71] The Co-N bond lengths are within the expectations with lengths of 2.1272(19) Å–2.152(2) Å. The Co-N bond lengths of **Co1** are slightly shorter (2.116(4) Å–2.141(4) Å), but also within the normal range for cobalt-nitrogen bonds. The bite angles between N-Co-N are narrowed for the tris-bipyridine complex by two degree, which is a consequence of the sterical demand of three large bidentate ligands.

Cyclic Voltammetry

Figure 4.31 shows the cyclic voltammogram and the square wave of **Co3** measured in degassed MeCN at room temperature. The sample was prepared with a concentration of 1 mM, and the acetonitrile was degassed prior to use. The redox potentials were referenced to the ferrocenium couple. Under these conditions, one reversible oxidation wave is detected at 0.73 V, which is assigned to an oxidation on the dimethylglyoxime ligand.[198] Surprisingly, this signal is reported in nearly any literature.[199,200] In contrast to that, everyone reported both cobalt-based reduction signals. The first reduction potential is located at -1.00 V and displayed an irreversible behavior. The signal is assigned to the reduction of the cobalt(III) center to obtain a cobalt(II+) species. The reduction is followed by a loss of chloride ligand and therefore irreversible.[201–203] The second reduction is detected at -1.50 V and assigned to a further reduction of the cobalt center to generate a Co(I+) species.

Table 4.8: Selected bond length [Å] and angles [°] of **Co1** and **Co2**. The corresponding structures are shown in Figure 4.30.

	Co1	**Co2**
Crystal system	trigonal	monoclinic
Space group	P 31	P2(1)/c
Co1-Cl1	-	2.4569(8)
Co1-Cl2	-	2.4025(7)
Co(1)-N(1)	2.126(4)	2.142(2)
Co(1)-N(2)	2.141(4)	2.1272(19)
Co(1)-N(3)	2.119(4)	2.152(2)
Co(1)-N(4)	2.125(4)	2.1285(19)
Co(1)-N(5)	2.116(4)	-
Co(1)-N(6)	2.138(4)	-
Cl2-Co1-Cl1	-	98.54(2)
N1-Co1-N2	77.21(16)	75.75(7)
N3-Co-N4	77.89(16)	75.78(8)
N5-Co1-N6	77.30(15)	-

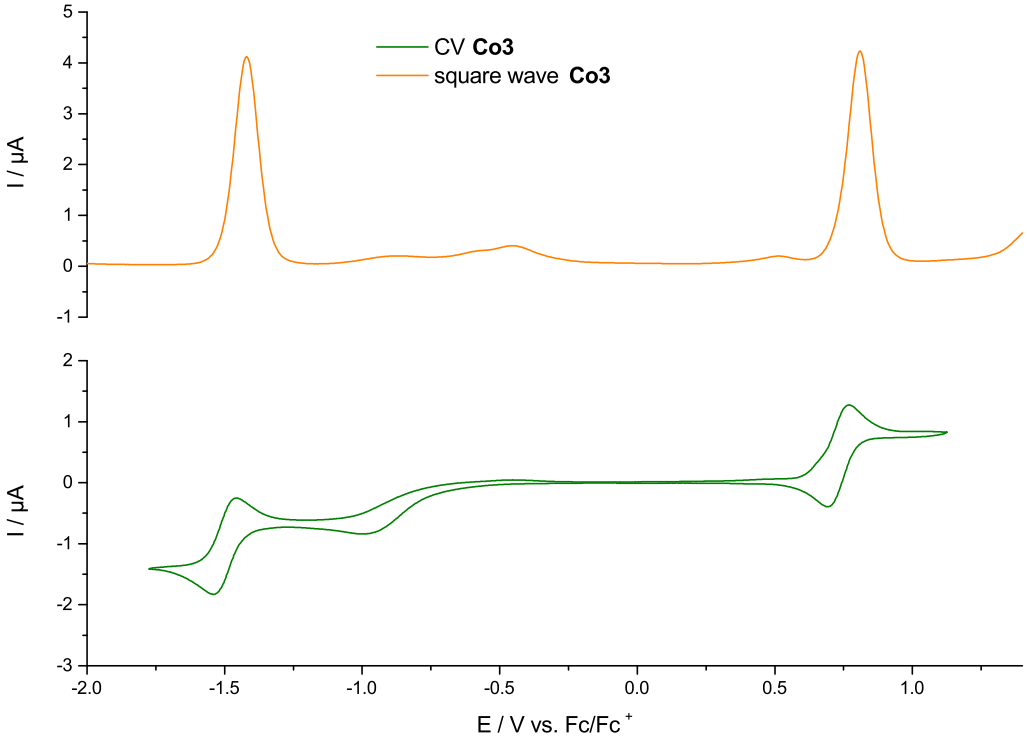

Figure 4.31: Cyclic voltammogram and square wave of **Co3** measured in degassed MeCN at room temperature.

Opposed to the first reduction signal, this one shows a quasi-reversible behavior. For the upcoming photocatalytic water reduction experiments, only the reduction signals of **Co3** are of interest.

4.5 Summary

As described in Chapter 3, it was possible to synthesize nine completely new ligands for the synthesis of iridium complexes with the general structure $[Ir(C\hat{}N)_2(N\hat{}N)]PF_6$. The general scaffold of the N^N ligands was newly designed, and therefore the synthesis proved to be a challenging task. For the synthesis of the largest ligand **L9**, it was necessary to conduct a total number of 413 experiments. It was necessary to rearrange the synthetic route multiple times to obtain the desired molecules. Until now, no molecule was reported in the literature with a 1,10-phenanthroline and a fused thiophene with varying substituents. The yields of the synthesized ligands range between 49 % and 96 %. The ligand **L7** is an exception. It was isolated, with a yield of only 18 %, and it was not possible to enhance the yield after several trials. Due to the challenging and time-consuming syntheses, the optimization of the yields was only a secondary target. It might be possible to achieve higher yields for the ligands **L2**–**L9** if further efforts are put in the fine-tuning of these reactions.

Due to the diimine structure of the phenanthroline, these compounds are attractive candidates for the synthesis of metal complexes. After the challenging ligand syntheses, the iridium complex procedure was more straightforward because of a large number of iridium complexes reported in the literature and synthesized under nearly identical conditions. It was possible to isolate the iridium complexes with high purity and high yields (52 %– 89 %). The spectroscopic and electrochemical properties of **PS1**–**PS9** support the idea of introducing the iridium complexes as photosensitizers in photocatalytic water reduction experiments. Since only the diimine ligand of the iridium complexes was varied, it was possible to derive a correlation between the structural changes of the neutral ligand and the measured spectroscopic properties. It can be summarized that the extension of the delocalized π system from **PS1** to **PS9** results in a redshift of the absorption as well as the emission spectra. The fluorescence data also shows a reduced quantum yield by extending the diimine structure, while the fluorescence lifetime is prolonged through the extension.

While the photosensitizer systems are based on iridium complexes as a noble metal, the focus of the catalyst syntheses was on the introduction of non-noble metals as catalytic centers for the water reduction experiments. It was possible to obtain four different complexes: two of them are based on iron and two on cobalt. The iron and cobalt complexes showed paramagnetic behavior by itself or minor paramagnetic impurities that made the characterization challenging. Mass spectrometry was also challenging due to the loss of ligands during the ionization process. However, finally, it was possible to guarantee the existence of the compounds.

It was possible to isolate eight crystal structures from the 22 key compounds (ligands, Ir-, Fe- or Co complexes). After the synthesis and characterization part of this thesis that produced the individual building blocks for the two-component systems, it can be summarized that all compounds showed promising properties to function well as a component in the photocatalytic water reduction experiments. Therefore, these complexes were introduced to the application part of this thesis to evaluate the abilities of the individual components for acting as photosensitizers or catalysts in photocatalytic water reduction.

5 Two-Component Systems in Photocatalytic Water Splitting

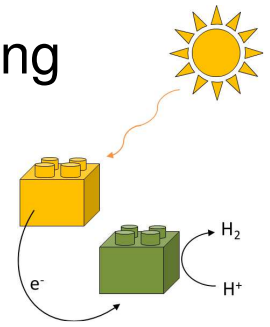

5.1 Photocatalytic Water Reduction Catalysis

5.1.1 Water Splitting Apparatus

The water splitting experiments were conducted on an apparatus specially designed for this purpose. A schematic representation and a photograph are shown in Figure 5.1. The center of the apparatus is a double-walled glass reactor, which is connected to an automatic gas burette *via* a condenser. Since it is essential to work under oxygen-free conditions, the system is connected to a Schlenk line, which is again connected to a vacuum pump and an argon cylinder. The apparatus is equipped with a 300 W xenon lamp that is connected to a fiber optic to create photocatalytic conditions. The samples are irradiated with the fiber optic which is introduced into a quartz glass tube. The double-walled reaction vessel and the condenser are connected to a thermostat to prevent heating and guarantee a constant temperature during the irradiation (25 °C). The whole apparatus operates under isobar conditions. The gas burette automatically increases their volume when gas is evolved in the closed system to maintain the initial pressure. The automatic gas burette is also connected to a computer, which detects the syringe movement and calculates the evolved gas volume at any time during the experiment. The reactor is also connected to a GC *via* the condenser. After the irradiation when the measurement is stopped, a valve is opened to the GC and the gas that was evolved during the water splitting experiment is analyzed. The GC uses argon as carrier gas, a 5 Å molsieve column and a TCD detector.

To guarantee reproducible results, a standard procedure for the water splitting experiments was developed, and every measurement was repeated at least for two times. First of all, it was essential to work under anaerobic conditions. For this purpose, the solutions for the water reduction experiments were freshly prepared every day and subjected to three freeze-pump-thaw cycles. The water splitting apparatus was tested for tightness and evacuated and flushed with argon three

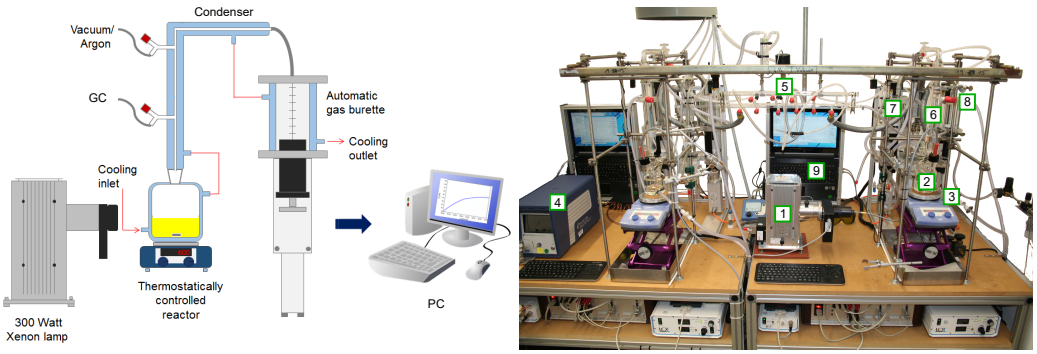

Figure 5.1: Left: Schematic representation of the apparatus for the photocatalytic water splitting experiments. Right: Picture of the water splitting apparatus: 1. Xe-lamp, 2. Reaction vessel, 3. Cooling inlet, 4. GC, 5. Vacuum/argon, 6. Condenser, 7. Automatic gas burette, 8. Cooling outlet, 9. PC.

times. The photosensitizer and catalyst were weighted into two separate vials, which were also evacuated three times and flushed with argon before the water splitting solution was added to the vials. The solutions were then transferred to the water splitting apparatus: first, the photosensitizer solution and second, the catalyst solution. Afterward, the valve to the gas burette was opened, and the reaction was equilibrated for five minutes in the dark. Immediately after this five minutes, the measurement was started on PC, and the Xe-lamp was turned on. The reaction in the water reduction vessel maintained constant at 25 °C during the irradiation, which was guaranteed by a cooling jacket around the vessel and the condenser, which was connected to a cryostat.

5.1.2 Data Evaluation

For the measurement and the analysis of the reduction experiments, it is essential to consider the properties of the used solvents. For example, the vapor pressure of the solvents was taken into account for accurate results. Therefore, for every measurement series, two reproducible 'blind values' were determined, averaged and subtracted from the volume of the real water splitting experiment. The 'real' evolved hydrogen volume was calculated by using Equation 5.1. Every measurement was at least repeated two times to guarantee reproducible results.

$$V(H_2) = V - a \cdot \frac{(T_{smooth} - T_0) \cdot (V + V_{reactor})}{T_{smooth} + 273.15\ K} \tag{5.1}$$

In this formula, which is derived from the van der Waals equation, V(H_2) refers to the final hydrogen volume, V is the measured uncorrected volume from the reduction experiment. $V_{reactor}$ is the volume inside the water splitting apparatus. This volume is determined before every water splitting measurement, and it also considers the

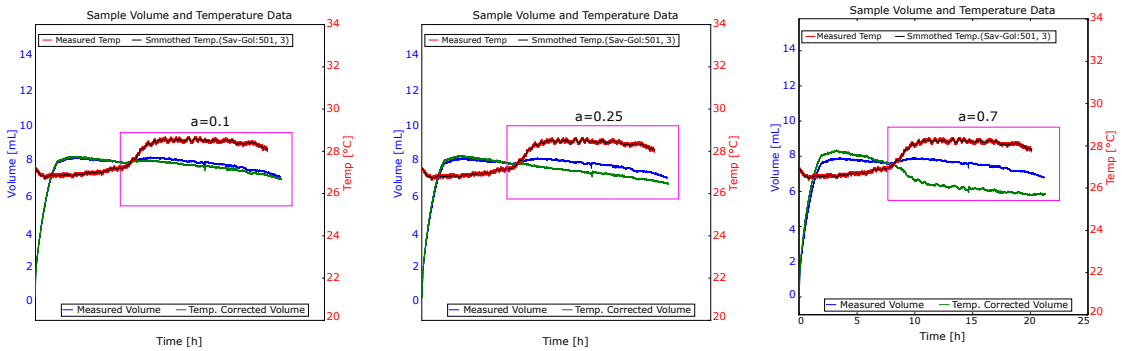

Figure 5.2: Temperature correction with different pre-exponential factors. Left: a= 0.1, a was chosen too small, temperature influences still available. Center: a= 0.25, this value was suitable for the temperature-correction. Right: a = 0.7, the volume was overcorrected.

used volume for the experiments. T_{smooth} is the smoothed temperature, which is obtained by the application of the Savitzky-Golay filter to the raw temperature data. This filter uses a polynomial regression to create a smoothed value for every measured temperature data. T_0 is the average temperature data recorded at the beginning of the measurement. The temperature is detected outside the reactor to take the conditions in the room where the experiment takes place into account to avoid errors caused by ambient temperature changes. The a is a pre-exponential factor which must be chosen in such a way that the correction of the temperature influences is suitable.

Three different examples that illustrate the influence of the pre-exponential factor on the corrected volume are given in Figure 5.2. If a is chosen too small, there still be temperature influences on the gas curve (a = 0.1) as depicted on the left side of the figure. If a is chosen too high (right side of the figure), the volume is overcorrected, and temperature influences, which are not existent are taken into account (a= 0.7). Consequently, it is important to ascertain a suitable value for the pre-exponential factor a, here shown in the middle of Figure 5.2. For the evaluation of the obtained data, a python program was written during this thesis, which calculates the corrected volume automatically. It is also possible to calculate the turnover number (TON) for the tested systems. With this program, it was possible to save much time for the data analysis.

The TON of the water reduction systems is calculated with respect to either the photosensitizer or the catalyst. For the photosensitizer, the TON was calculated using the molar volume of hydrogen of 24.480 L·mol^{-1} and the corrected volume, which is obtained by using Equation 5.1. The amount of substance n(PS) for the photosensitizer results from the weighted portion of the photosensitizer. For the generation of one molecule H_2, the PS must undergo two cycles to transfer two

electrons, which are required for the formation of H_2. Thus, the fraction to calculate the TON must be multiplied by 2.

$$TON_{PS} = 2 \cdot \frac{\frac{V_{corr}}{V_m H_2}}{n(PS)} = 2 \cdot \frac{n(H_2)}{n(PS)} \tag{5.2}$$

The calculation for the catalyst-based TON is done analogously except that the CAT undergo only one cycle to generate one molecule hydrogen.

$$TON_{CAT} = \frac{\frac{V_{corr}}{V_m H_2}}{n(CAT)} = \frac{n(H_2)}{n(CAT)} \tag{5.3}$$

5.1.3 Catalyst Screening: Noble or Non-Noble Catalysts

In the first water reduction experiments, the iridium photosensitizers **PS1**–**PS9** that are shown in Figure 4.8 were tested in combination with K_2PtCl_4, a standard literature-known noble catalyst. The platinum complex was already tested in combination with a huge variety of iridium photosensitizers and achieved for all reported systems good activities.[108,115,177,178,204] This catalyst is therefore well-investigated and established as a heterogeneous catalyst, which forms Pt nanoparticles during the photocatalytic water reduction. Unfortunately, when the iridium complexes **PS2**–**PS9** were tested in combination with this Pt catalyst, no hydrogen evolution was detected. Only the reference photosensitizer **PS1** showed hydrogen evolution in combination with the Pt CAT. One hypothesis for this results is the *in situ* formation of an inactive Pt compound. The structure might be similar to a bimetallic one-component system, but with no hydrogen evolution ability. In this theory, the platinum is coordinated and no Pt nanoparticles could be formed, which results finally in an inactive system. This hypothesis seems realistic on closer examination of the N^N ligand of **PS2**–**PS9**. The thiophene rings represent possible ligands for platinum coordination. To prove or disprove this theory, a sample of **PS6** and K_2PtCl_4, which was prepared under water reduction conditions, was subjected to NMR and mass spectrometry. Two possible Ir-Pt structures that might be formed during the water reduction experiment are shown in Figure 5.3. Unfortunately, no sign for an Ir-Pt dyad was found either in the NMR nor the mass spectrum. Nevertheless, the theory should not be discarded at this time for two reasons: First, only minor peak shifts could be expected for the NMR spectrum through coordination of the platinum and second, in mass spectrometry it is not unusual that fragmentations occur during ionization and no molecular ion could be observed. Both spectra, NMR and mass, show only the molecular signals of **PS6** and the mass spectrum shows

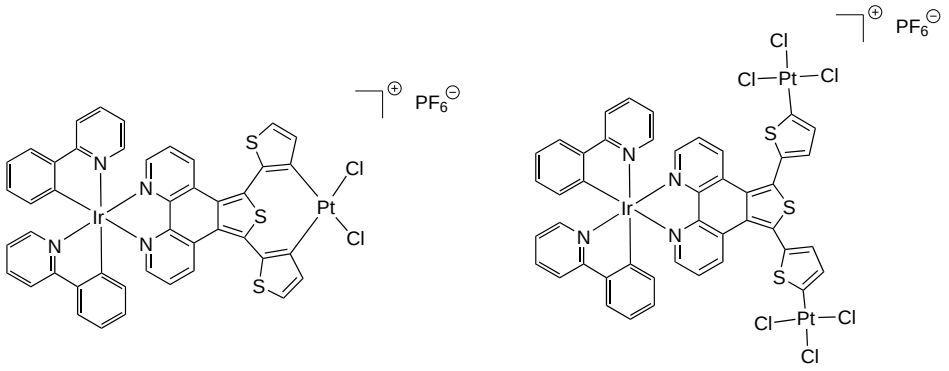

Figure 5.3: Possible structures of inactive iridium-platinum-based supramolecular systems.

additionally signals with a higher m/z ratio that could not be assigned to a structure. A second point, which supports the inactive dyad theory must be explained in a broader context. Bernhard and DiSalle investigated two-component water reduction systems consisting of iridium photosensitizers with pendant pyridyl groups and K_2PtCl_4 as catalyst. They argued that through the incorporation of a pyridine group, coordination of the colloidal platinum is possible and therefore the electron transfer is no more diffusion dependent but rather intramolecular. They also tested a similar iridium photosensitizer with a terminal phenyl instead of a pyridyl group, and this complex showed in the water reduction experiments a strongly decreased hydrogen production. They also changed the catalyst to a fully coordinated rhenium complex $[Rh(bpy)_2Cl_2]Cl$, which yielded again in a less active system.[108] The results of Bernhard's group support the theory of an inactive iridium-platinum system, because **PS8** and **PS9** are complexes with pendant pyridyl groups and they were inactive as every other photosensitizer tested here. If the hydrogen evolution with the here presented photosensitizers proceeds *via* the same mechanism as described for the iridium-platinum arrangements of Bernhard, at least hydrogen evolution should be detected for **PS8** and **PS9**. Consequently, it can be assumed that no nanoparticles are formed, which might be the result of an Ir-Pt complex where the thiophene rings are coordinated by the platinum.

After the unsuccessful attempts with the standard platinum catalyst, the non-precious catalysts, which were introduced in Chapter 4.4, were tested in the photocatalytic experiments. **Fe1**, **Fe2**, **Co1** and **Co3** were tested in combination with **PS1** as photosensitizer. The conditions like solvent, solvent ratio, pH or sacrificial reductant varied for every catalyst since they were only active under certain conditions. The individual parameters are summarized in Table 5.1 and the hydrogen evolution curves are shown in Figure 5.4. Every catalyst except **Co3**, was tested without the adjustment of the pH. It was tried to measure the hydrogen evolution for a two-component system with **Co3** without the adjustment of the pH, but unfortunately

Table 5.1: Catalyst Screening for photocatalytic water reduction experiments under irradiation with a 300 W Xe-lamp. **PS1** was used as photosensitizer, all other reagents and parameters are given in the table.

Catalyst	n(PS1) [μmol]	n(CAT) [μmol]	SR	c(SR) [mol/L]	solvents (ratio)	pH	TON_{PS}
Fe1	20	2.5	TEA	0.5	THF:H_2O (4:1)	-	28
Fe2	20	2.5	TEA	0.5	THF:H_2O (4:1)	-	49
Co1	20	2.5	TEOA	0.5	MeCN:H_2O (1:1)	-	30
Co3	12	5	TEOA	0.38	MeCN:H_2O (1:1)	8.4	41

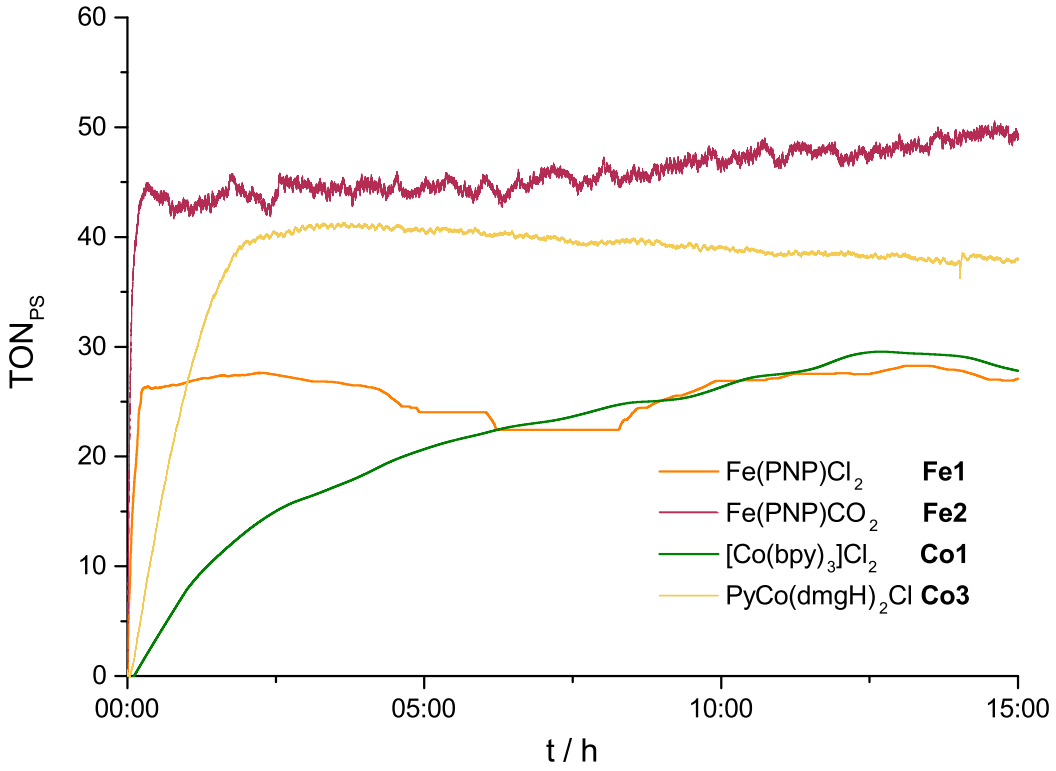

Figure 5.4: Photocatalytic hydrogen evolution with $[Ir(ppy)_2phen]PF_6$ **PS1** with different catalysts. The systems were measured under different conditions (solvents, sacrificial reductant, pH) that are listed in Table 5.1. The sample of **Fe1** was only measured once.

no hydrogen evolution was observed. The cobalt catalyst **Co1** was also tested with THF and H_2O as solvent mixture and TEA as sacrificial reductant like **Fe1** and **Fe2**, but this led to a significantly decreased hydrogen evolution with a TON_{PS} of 9 instead of a TON of 30 that was obtained with the conditions listed in Table 5.1. The catalysts **Fe1** and **Co1** achieved a similar activity, but the hydrogen evolution curves showed an important, additional information; while **Fe1** is already inactive after a few minutes is the cobalt catalyst active for additional 15 hours. For the generation of hydrogen, it is favorable to develop a system that exhibits a long lifetime but only with high activity. Hence, for these two reasons **Fe1** and **Co1** were no longer used as catalysts for further photocatalytic hydrogen experiments. The second pair, which features comparable activities with TONs of 49 and 41, was **Fe2** and **Co3**. Although **Fe2** possessed the highest hydrogen evolution ability, **Co3** was chosen after this screening as catalyst for the two-component measurements with different iridium photosensitizers. Two reasons influenced this decision: First, the slightly longer lifetime for **Co3** of two hours compared to the system-lifetime of less than 30 minutes for **Fe2**. Second, since the synthesis of **Fe2** is more complicated and time-consuming as the synthesis of **Co3** this was also important for the decision. For further screenings and the measurements of the nine different photosensitizers **PS1**–**PS9** larger quantities of catalyst are necessary. Thus, it was also a practical decision to perform the experiments with **Co3** as the catalyst.

Due to the choice of the fully-coordinated cobalt catalyst, it should be possible to prevent the formation of an inactive dyad as occurred through the application of the platinum catalyst K_2PtCl_4. During the catalyst screening, only **PS1** was used as PS, but the inactive supramolecular Ir-Pt systems were formed with the thiophene-containing photosensitizers. Therefore, it was a pleasant result that every photosensitizer, except one, showed hydrogen evolution under the application of **Co3**.

5.1.4 Photocatalytic Condition Optimization

Before all synthesized iridium photosensitizers were tested, it was necessary to elucidate the ideal conditions for this combination of CAT and PS in the photocatalytic water reduction experiments. As standard system, $[Ir(ppy)_2phen]PF_6$ **PS1** and $PyCo(dmgH)_2Cl$ **Co3** was chosen due to the highest similarity of this combination to literature-known complexes and also to the newly designed photosensitizers presented here. All preliminary experiments (see Table 5.2) were carried out with these two components and after the discovery of the ideal conditions, **PS2**–**PS9** were tested. In the first attempts (Entry 1–4), a PS:CAT ratio of 1:2 was chosen for possible subsequent comparison of the two-component systems with the synthesized dyads that will be presented in Chapter 6. They are composed of one photosensitizer

Table 5.2: Evaluation of the ideal conditions for water reduction experiments with **PS1**, **Co3** as CAT and TEOA as SR in 20 mL solvent.

Entry	n(PS) [μmol]	n(CAT) [μmol]	ratio PS:CAT	solvent-ratio MeCN:H_2O	c(TEOA) [M]	pH	TON_{PS}
1	1	2	1:2	3:2	0.016	7	-
2	1	2	1:2	3:2	0.016	7.5	-
3	1	2	1:2	3:2	0.016	8	-
4	1	2	1:2	3:2	0.50	8	-
5	15	5	3:1	1:1	0.38	7	15
6	12	5	2.4:1	1:1	0.38	7	17
7	12	5	2.4:1	1:1	0.38	8.4	32
8	12	5	2.4:1	1:1	0.38	9.5	20
9	12	5	2.4:1	1:1	0.38[a]	8.4	-

a) TEA was used as SR

unit and two catalytic centers. The acetonitrile-water-ratio of 3:2 was chosen due to practical reasons (Entry 1–4). The systems must be completely dissolved during the water reduction experiments and with this ratio, this was guaranteed. TEOA was chosen as SR. TEOA is known as the best sacrificial donor for a combination of iridium photosensitizer and cobalt catalyst.[56,86,131,132,205,206] It was also tested, if TEA is a more suitable sacrificial reductant, but no hydrogen evolution was detected (Entry 9). The TEOA concentration was taken from literature.[126,133] The activity of cobaloxime-based photocatalytic systems depends strongly on the pH of the used solvents. In general, the ideal range is within 6-9, but even if the pH is not ideal, a decreased hydrogen evolution can be detected. For the iridium-cobalt ratio of 1:2 different pH values were tested (Entry 1–3), which were already successful for other literature reported systems.[126,207] Unfortunately, under these conditions no hydrogen evolution was observed.

Next, the concentration of TEOA was enhanced to 0.5 M, which also led to no hydrogen production (Entry 4). Since the first attempts were unsuccessful, the concentrations of the two components and their ratio were changed. Now the system was tested with two different PS to CAT ratios of 3:1 and 2.4:1 (Entry 5–9). Additionally, the solvent ratio was changed to 1:1. Even with this higher amount of water, the complexes were entirely dissolved for the water reduction experiments. The 2.4:1 ratio system showed a slightly higher activity (Entry 6) compared to the 3:1 ratio (Entry 5), and consequently this was kept for the next measurements. With these new conditions, different pH values were tested between 7 and 9.5. The pH was adjusted with HCl or NaOH in the aqueous TEOA solution before it was mixed with MeCN. It was apparent that the system with an initial pH of 8.4 exhibited the highest activity (Entry 7). This is not a surprise since Du, Knowles, and Eisenberg outlined this issue in their paper a few years ago. They assumed that with a pH below

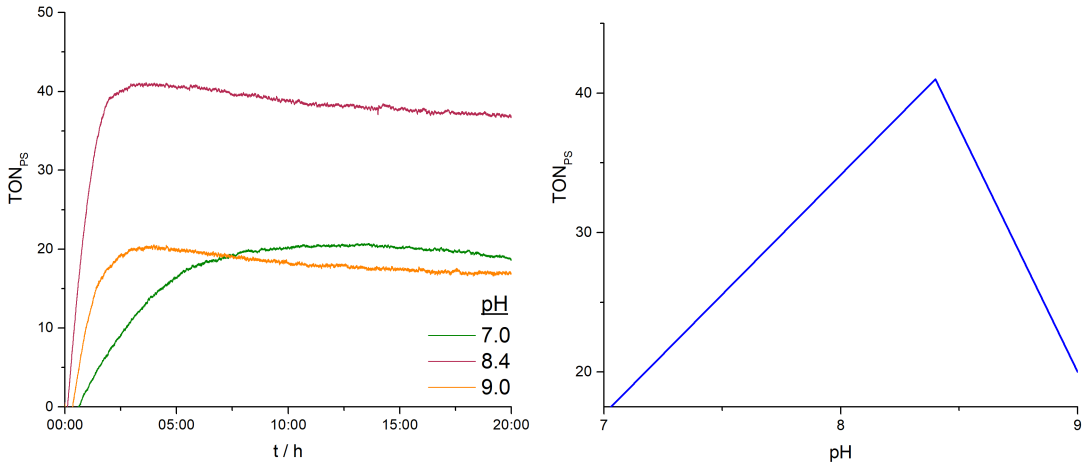

Figure 5.5: Water reduction experiments conducted at three different pH values. Conditions: 12 μmol **PS1**, 5 μmol **Co3**, 5 %vol TEOA in 20 mL solvent (MeCN:H_2O 1:1).

7.0, it is possible that TEOA is protonated or $TEOA^+$ is not capable of transferring an electron to the photosensitizer as it is required to restart the catalytic cycle. Similarly, the activity drops at a pH of 9.5. One hypothesis of the Eisenberg group was that the protonation of the cobaloxime became unfavorable and the driving force for the H_2 production is significantly reduced.[207] The hydrogen evolution curves for the pH tests are depicted in Figure 5.5. As an overall result of the screening for the ideal reaction conditions, the parameters of Entry 7 were transferred to all other hydrogen evolution measurements with the photosensitizers **PS2**–**PS9** and **Co3** as catalyst.

5.1.5 Evaluation of New Photosensitizers

Altogether, nine different photosensitizers were tested under the conditions that were figured out in the last section (Table 5.2, Entry 7). The lifetimes of the investigated systems range between 1.5 h and more than 20 h. The water reduction curves are shown in Figure 5.7. The curve shapes are entirely different; the systems with high activities (**PS1**–**PS5**) degrade fast, during the first five hours. The systems with the delayed hydrogen evolution, **PS6**, **PS8** and **PS9**, are almost inactive for the first five hours and only then, they started the hydrogen generation. Bernhard and DiSalle reported a similar result.[108] They tested a rhenium catalyst in combination with the iridium photosensitizer **Irbpy2** shown in Figure 5.6. The iridium complex was composed

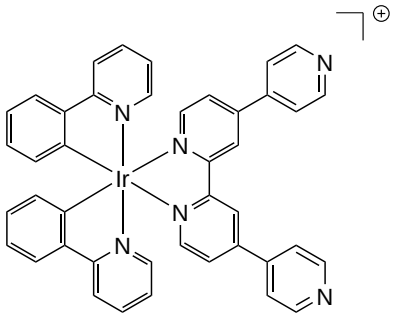

Irbpy2

Figure 5.6: Ir complex with pendant pyridyl groups used by Bernhard and DiSalle.[108]

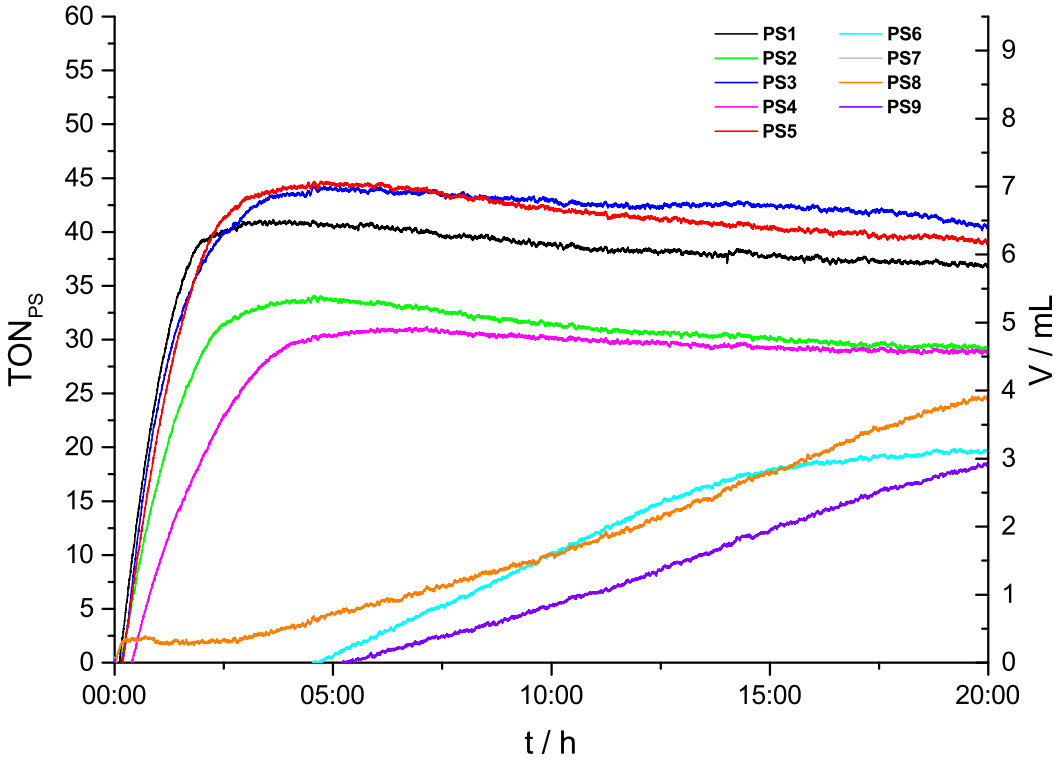

Figure 5.7: Water reduction experiments of all photosensitizers. Conditions: 12 μmol **PS1**–**PS9**, 5 μmol **Co3**, 5 vol% TEOA in 20 mL solvent (MeCN:H_2O 1:1). The pH of the reaction media was adjusted to 8.4.

of two phenylpyridine ligands and one bipyridine with a pyridine extension in *para* position on each pyridine. The shape of the hydrogen evolution curve was completely changed and equals the shape of the **PS1–PS5** when K_2PtCl_4 was used as catalyst. Unfortunately, this catalyst was already tested with **PS2–PS9** and resulted in inactive two- or one-component systems. Bernhard and DiSalle did not explain the different-shaped curves in their paper. They applied a second system with two pyridine groups in the backbone of the N^N ligand with alkyl chains as linker between the pyridines and the bipyridine. Interestingly, this photosensitizer resulted in a hydrogen evolution curve with the familiar, expected shape that was also obtained with **PS1**–**PS5**. One assumption focuses on the aromaticity of the N^N ligand linked to terminal pyridines in combination with certain catalysts. This setup lead to the delayed hydrogen evolution as observed for **PS8** and **PS9**, but the exact reason stays unclear up to this moment. One hypothesis is that a temporary PS-CAT connection is generated *via* the pyridine that hampers a successful electron transfer between the two components and results in an inactive compound.

After every measurement with the iridium complexes **PS1**–**PS9**, the evolved gas was analyzed by gas chromatography to ensure the evolution of hydrogen. An exemplary GC spectrum of the measurement with **PS3** and **Co3** in TEOA and MeCN:H_2O is shown in Figure 5.8. The strongly broadened, intensive peak at the beginning of

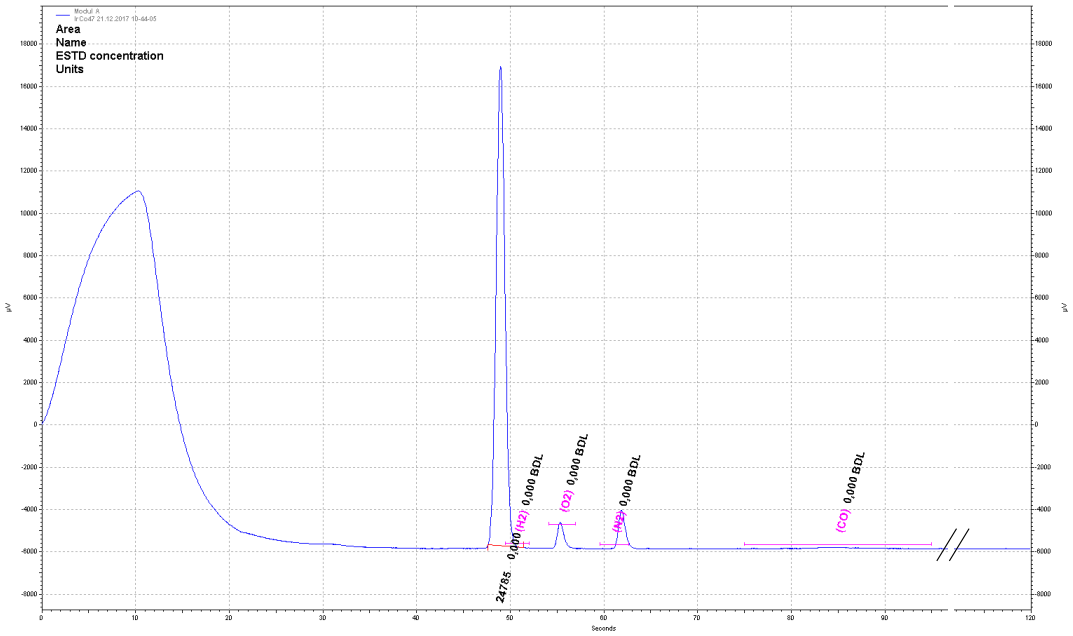

Figure 5.8: GC analysis that was conducted after the water reduction experiment of **PS3**, **Co3** and TEOA in a mixture of MeCN:H_2O at a pH of 8.4.

the spectrum is a pressure burst caused by the GC apparatus. The highest signal is automatically assigned to the H_2 peak. The common gases that could be evolved during the measurements were calibrated for this GC. The small oxygen and nitrogen peaks were also assigned automatically, are caused by the experimental setup. Due to the presence of two water splitting apparatus, it was necessary to switch the connections to the GC after every measurement and the O_2 and N_2 peaks were residuals from the air and not evolved during the water reduction experiment. With this analytic method, it was possible to ascertain the evolution of hydrogen for every measurement with the photosensitizers **PS1**–**PS9**.

The highest TON of 44 is achieved for the photosensitizers **PS3** and **PS5**, followed by **PS1** with a TON of 41. This PS is only used as a reference, and the scaffold of the N^N linker differs the most from the other eight systems. The TONs of **PS2** and **PS4** are the next in the ranking of the most active PS, but in a greater distance with 34 and 31. The next drop in activity leads to the photosensitizers **PS6**, **PS8** and **PS9**, which also show the delayed start of hydrogen production. The lowest TON of 18.5 is detected for **PS9**. **PS6** exhibits a TON of 20 and **PS8** of 24.5. An exception within the series of the tested photosensitizers is **PS7**, which is still inactive under the applied conditions. All volumes and TONs of the investigated photosensitizers are summarized in Table 5.3. Compared to other iridium photosensitizers that were tested in photocatalytic hydrogen evolution experiments in combination with a cobaloxime catalyst, these systems are only medium active. Zhang and Artero investigated a system of $[Ir(ppy)_2bpy]^+$ with a modified cobaloxime. The catalyst

Table 5.3: Summarized water reduction results. All samples contained: 12 μmol **PSX**, 5 μmol **Co3**, 5 % vol TEOA, MeCN:H_2O (1:1). The pH was adjusted to 8.4 and the samples were constantly irradiated with visible light (Xe-lamp).

Entry	PS	V(H_2) [mL]	n(H_2) [μmol]	TON$_{PS}$	TON$_{CAT}$
1	**PS1**	6.5	266	41	49
2	**PS2**	5.3	217	34	41
3	**PS3**	7.0	286	44	53
4	**PS4**	4.8	196	31	37
5	**PS5**	7.1	290	44	49
6	**PS6**	3.1	127	20	25
7	**PS7**	-	-	-	-
8	**PS8**	3.9	159	24.5	30
9	**PS9**	2.9	118	18.5	22

had instead of the hydroxyl groups of the dimethylglyoxime alkyl chains at this position to make the catalyst more resilient. Even if the parameters and conditions of their measurements and that one reported here are not comparable, a TON of 614 is much higher than the highest TON of 44 that is obtained with **PS3** and **PS5**.[205] A second group also investigated a cobaloxime similar catalyst, which is based on a tetradentate macrocycle and two chloride ligands in axial position with $[Ir(ppy)_2bpy]^+$ as photosensitizer. Unfortunately, they did not declare, if the TON is catalyst- or photosensitizer-based. If it was the TON$_{PS}$, they achieved a TON of 180. If the TON was based on the catalyst, the TON for the photosensitizer was 1620, which is also superior to the here reported TONs.[206]

Interestingly, it was possible to correlate the length of the N^N ligands with the hydrogen evolution ability. The photosensitizers with small N^N ligands show a higher activity, whereas the large ligands seem to diminish the hydrogen evolution ability of the PS, which might be caused by the electron transfer within the large photosensitizers. After the excitation with Xe light, the electron is localized on the diimine ligand (LUMO) and with an increased conjugated system, the delocalization of the electrons that should be transferred to the catalyst is enhanced, which hampers a fast electron transfer.

The solvents were removed after the photocatalytic experiments, and the residues were subjected to mass spectrometry to evaluate if the photosensitizer or the catalyst limits the hydrogen evolution. None of the mass spectra show a sign of an intact catalyst, which is a result that is supported by many other publications. They already ascertained that the loss of the dimethylglyoxime and pyridine ligands are possible, and irradiation with light accelerates the processes. This is an counterintuitive result due to the normally high stability of a bidentate ligand like dimethylglyoxime. Additionally to the ligand-loss, it is possible that the glyoxime, both as free and

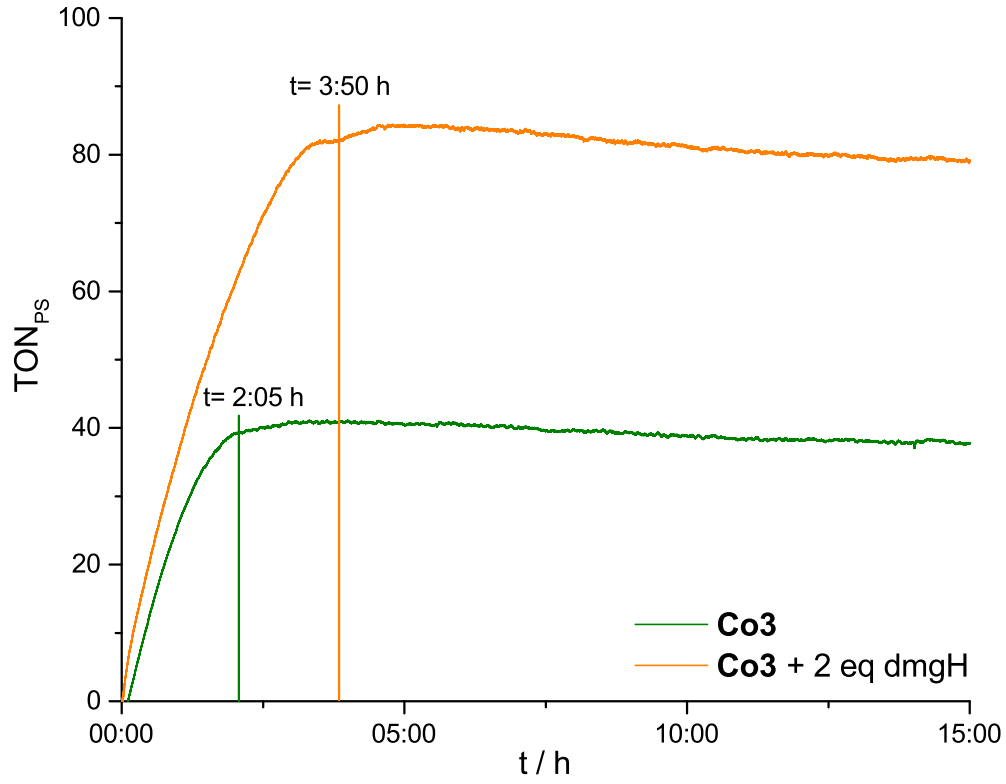

Figure 5.9: Photocatalytic hydrogen evolution experiments with additional free ligand dmgH (orange) and without the addition of free ligand (green). Conditions: 12 μmol **PS1**, 5 μmol **Co3** 5 % vol TEOA in 20 mL MeCN:H_2O (1:1). The pH was adjusted to 8.4.

coordinated ligand, can be hydrogenated and lead to an inactive form of the cobalt catalyst.[133,208] Figure 5.9 depicts an additional water splitting experiment that was conducted based on these results. The orange curve shows the hydrogen evolution when two additional equivalents of free dimethylglyoxime ligand were added to the sample. The system exhibits two benefits toward the standard measurements: The sample is twice as active as the standard sample, which contained only **Co3** and no free dimethylglyoxime. Additionally, the orange sample is earlier active and produces more hydrogen in a shorter time. The time of degradation is prolonged in this sample by one hour and 45 minutes to 3:50 h. This indicates that the cobaloxime catalyst **Co3** is the limiting reagent in this photocatalytic reactions and more stable ligands can prevent the fast degradation of the catalyst and generate more active system. This theory was already tested in literature. They exchanged the dimethylglyoxime ligand (dmgH) by the BF_2-bridged form (dmgBF_2), which resulted in an enhanced stability of the catalysts through an enhanced stability against hydrogenation.[123,127,209] However, the discussion should return to the results of the mass spectra that were recorded after the water reduction experiments. The signals of the investigated photosensitizers show no consistent result what happened to the photosensitizers during the photocatalysis. Some of the photosensitizers are still intact after 20 h of irradiation. For **PS1**, **PS2**, **PS6**, and **PS8** the mass peak are found and this indicated

that these PS are not limiting the hydrogen evolution, even after 20 h. Whereas the other photosensitizers (**PS3–PS5**, **PS7**, and **PS9**) are decomposed during the 20 h photocatalytic experiments. For **PS3**, the ester-containing photosensitizer, the decomposition lead to **PS1**, whereas **PS4** (-COOH) and **PS5** (-Br) decomposes to **PS2**. **PS9** decomposes to the unsubstituted analogue photosensitizer **PS8**. Special consideration should be given to **PS7**, which is the only photosensitizer that leads to a complete inactive photocatalytic system. The photosensitizer reacts during the irradiation to the non-halogenated iridium complex **PS6**. The timeframe of the decomposition to **PS6** presumes to be longer than the degradation of the cobalt catalyst. Otherwise, hydrogen evolution must occur since the *in situ* formed **PS6** is known as an active photosensitizer (see Table 5.3, Entry 6).

It can be summarized, that besides of the ranking of the most-active PS in this section, it is possible to show that the lifetime of these photocatalytic water reduction systems is limited by the cobalt catalyst and not by the photosensitizer.

5.1.6 Concentration Effects

After the determination of the activities of **PS1**–**PS9**, some measurements were conducted in which the concentrations of sacrificial reductant, photosensitizer and water reduction catalyst were varied. All measurements were carried out with **PS2**, **Co3** and TEOA in a mixture of acetonitrile and water (1:1).

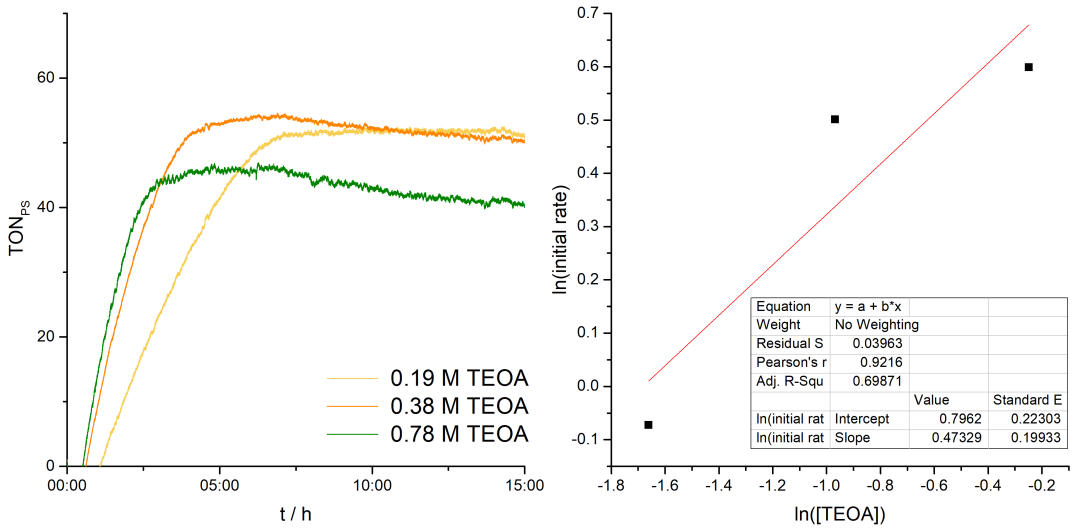

Figure 5.10: Left: 6 μmol **PS2**, 5 μmol **Co3**, and varying volumes of TEOA in 20 mL solvent (MeCN:H_2O, 1:1). The pH of the reaction media was adjusted to 8.4. Right: Kinetic plot of the measured data.

First, the amount of TEOA was altered within a concentration of 0.19 M–0.78 M, while the concentrations of PS and CAT were kept constant. The hydrogen evolution curves and the kinetic analysis are shown in Figure 5.10. The activities of the inves-

tigated samples are identical for a concentration of 0.19 M and 0.38 M during the experiments, but the latter degrades faster. A further increase of the concentration to 0.78 M TEOA leads to reduced hydrogen evolution. Even in the lowest concentrated sample, the sacrificial donor is present in a significant excess (PS to TEOA, 1:630) and therefore, it is not limiting for these Ir-Co hydrogen evolution systems. This result is further supported by the kinetic data, which reveals a reaction order of approximately 0.5. Additionally, the generated H_2 volume was correlated to the amount of TEOA, and for the lowest concentration, only 8.9 % of the provided TEOA was consumed. In contrast to the lower concentrations, a higher amount of TEOA decreases the hydrogen evolution. It could have been caused by a more drastic change of the reaction media, which is unfavorable for the hydrogen evolution. The results indicate that TEOA does not reductively quench the excited photosensitizer **PS2***. This would lead to an increased TON with a higher amount of TEOA due to a higher quenching propability.[68] This will be explained later in Chapter 5.2.2 based on the conducted quenching experiments.

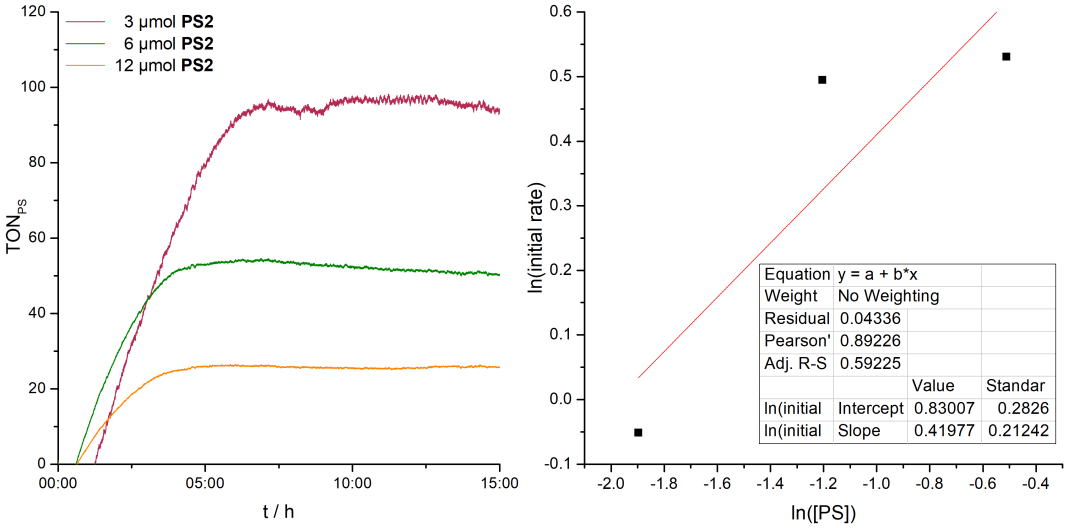

Figure 5.11: Varying amounts of **PS2**, 5 μmol **Co3**, 5 %vol TEOA in 20 mL solvent (MeCN:H_2O, 1:1). The pH of the reaction media was adjusted to 8.4. Right: Kinetic plot of the measured data.

Figure 5.11 shows the results of the concentration experiments with a varying amount of **PS2**. The CAT and TEOA concentrations were fixed in this samples. The kinetic analysis is also depicted in Figure 5.11. The hydrogen evolution is enhanced with a smaller quantity of photosensitizer. Even at lower concentrations, hydrogen evolution occurs. The TON is doubled by a reduction of the amount of PS from 12 μmol to 6 μmol, while the evolved volume is nearly constant. A radical enhancement is achieved by reducing the amount of **PS2** to 3 μmol in the reaction mixture. It is also observed that lowering the concentration leads to a more delayed hydrogen evolution, while this effect is not detected for the samples with 6 μmol and 12 μmol. The delayed hydrogen evolution for the lowest PS concentration might be

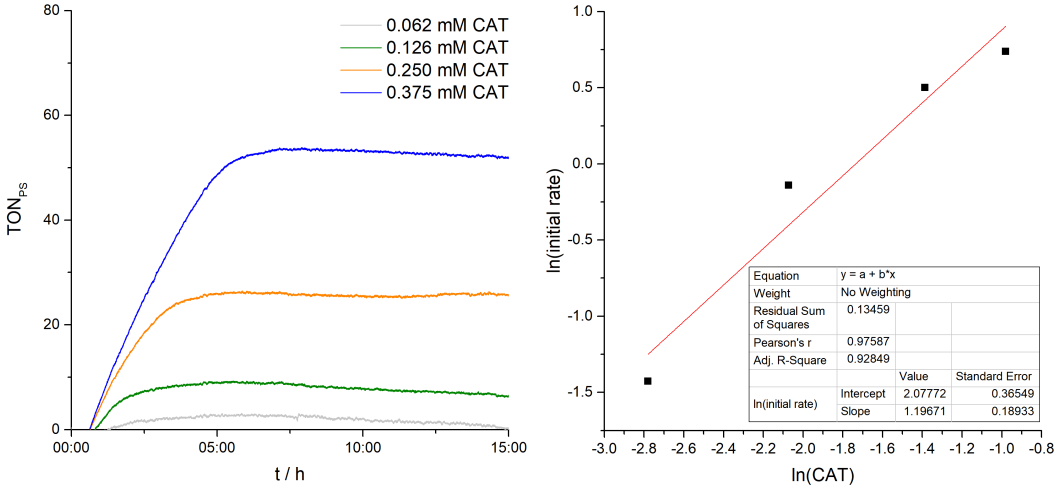

Figure 5.12: Left: 12 μmol **PS2**, varying amounts of **Co3**, 5 %vol TEOA in 20 mL solvent (MeCN:H_2O, 1:1). The pH of the reaction media was adjusted to 8.4. Right: Kinetic analysis of the Co-concentration series.

caused by the diffusion-dependent electron transfer from the PS to the CAT. Through a kinetic analysis of the concentration series, a reaction order of approximately 0.5 was determined. As already reported for the TEOA concentration, this setup with TEOA as SR, an iridium PS, and a Co CAT is independent of the PS concentrations within the investigated concentration range.

The last measurements should display a dependence of the catalyst-based TON_{CAT} on the catalyst concentration. The amount of **Co3** was varied, while the other parameters kept constant. The hydrogen evolution curves and the kinetic data are shown in Figure 5.12. Four different samples were investigated. Opposed to the photosensitizer-concentration measurements, the activity of the investigated systems is increased by increasing the catalyst concentration. This indicates that the catalyst is the H_2-limiting reagent in these Ir-Co two-component systems.

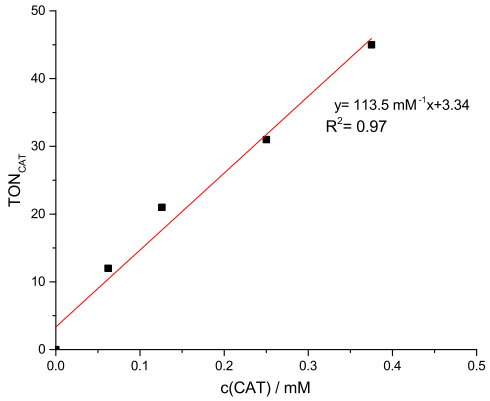

Figure 5.13: $TONs_{CAT}$ against the applied catalyst concentrations.

It was a conclusion that was already made before; after the measurements with the additional amount of dimethylglyoxime (see Figure 5.9). The kinetic analysis reveals that the reaction is first order with respect to the catalyst concentration, and that in the investigated catalyst concentration range this compound is the rate-limiting reagent. The linear fit of $TONs_{CAT}$ *versus* the cobalt concentrations is depicted in Figure 5.12 to get an inside into the hydrogen evo-

lution mechanisms, which occur at the catalytic cobalt center during the hydrogen evolution. The plot is shown in Figure 5.13 and demonstrates a good linearity ($R^2 = 0.97$). This supports the theory of a heterolytic (or monometallic or single-Co reaction) pathway.[68,210–212] This mechanism involves only one active catalytic center, which generates the hydrogen molecule. In a first step a cobalt hydride (Co-H) is formed, and after the attack of a second proton, the hydride decomposes heterolytically, and hydrogen is evolved. Therefore, this mechanism must show a linear relationship between TON_{CAT} and the applied amount of cobalt catalyst. The second mechanism, which is possible for these cobalt catalysts, is a two single-Co or a homolytic mechanism. As the name already implies, it involves two cobalt hydrides, which evolve hydrogen by a homolytic, reductive elimination of H_2. If this mechanism is present in the investigated system, the TON will show a dependence on $[Co]^2$.[68,210]

5.2 Spectroscopic Characteristics of Water Splitting Systems

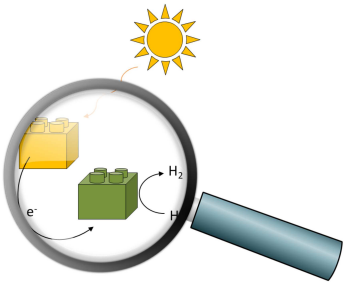

5.2.1 UV-Vis Spectroscopy during Water Reduction

UV-Vis spectroscopy was conducted during the water reduction experiments to elucidate the mechanism for the hydrogen evolution under the application of the cobaloxime **Co3** as catalyst and varying iridium photosensitizers. Therefore, a sample of the standard **PS1** and **Co3** was prepared in a cuvette with the same concentrations and under the same conditions as in the water reduction experiments. The sample was illuminated with a 300 W Xe-lamp, which was also used in the water splitting experiments, and a series of absorption spectra were recorded in different time intervals. The UV-Vis spectra are shown in Figure 5.3.

The spectra show two prominent absorption bands. The first strongly broadened absorption band appears at 600 nm after 25 minutes of irradiation. This absorption band disappears again after 55 minutes. Further illumination with the Xe-lamp gives rise of an additional absorption band that is located at 465 nm. The water reduction experiments in the apparatus were also carried out with only one of the essential components, and this led to no observable hydrogen evolution. Therefore, it is concluded that both components are necessary for the generation of an active water reduction system and hence, for the rise of the two above mentioned absorption bands.

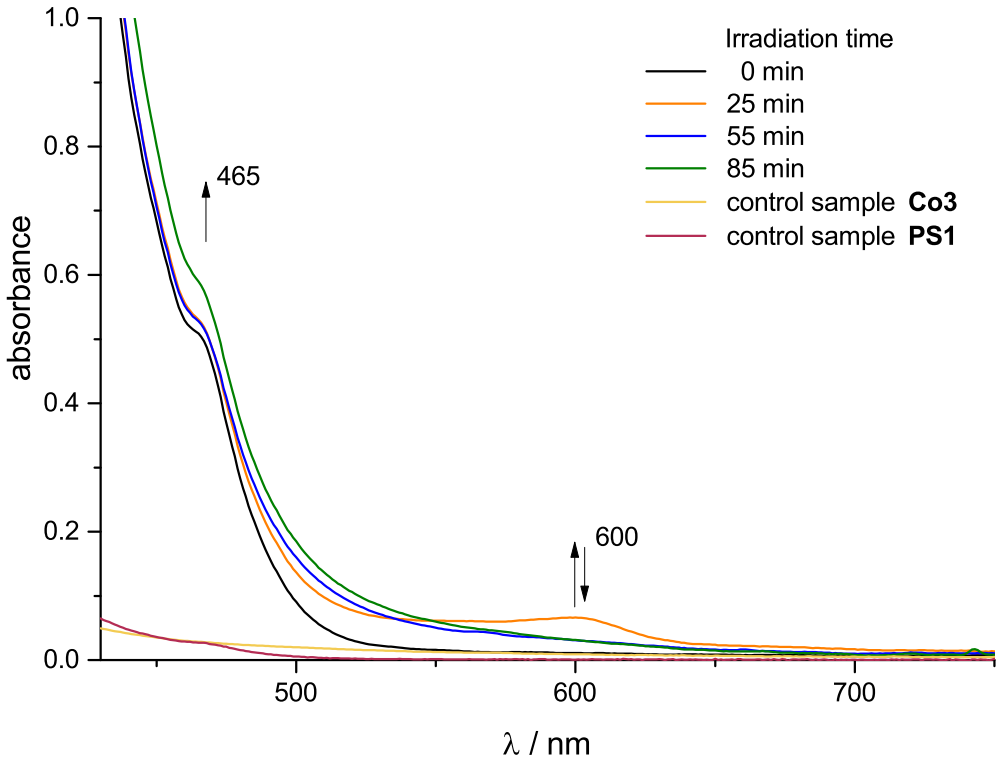

Figure 5.14: Time-dependent UV-Vis spectra of **PS1** and **Co3** with 5 vol% TEOA in MeCN:H_2O (1:1) at a pH of 8.4 under irradiation with a 300 W Xe-lamp.

The absorption band at 465 nm is assigned to a Co(II) species, which is in accordance with similar results that were already reported in literature.[68,205,213,214] The absorption band appears in photocatalytic and also in electrocatalytic experiments if an active cobalt catalyst is formed. This is even coherent with the possible mechanisms for the water reduction, which were outlined in the background Chapter 2.3.3. The broad absorption band at 600 nm is assigned to either a Co(I) species or a Co(III) hydride.[215,216] During the hydrogen evolution experiment, it is proposed that the Co(I) species is oxidized to a Co(III) hydride, which absorption band is located at 615 nm and therefore, both absorption bands might be superimposed by each other. The *in situ* formation of the active catalyst also explains the induction period of 25 minutes until hydrogen evolution is observed. The mechanism, which is reported in the literature for cobaloximes in water reduction involves the formation of a Co(III) hydride, which is capable of evolving hydrogen either by the homolytic or heterolytic reaction pathway. In Chapter 5.1.6, it was already figured out that the water reduction with these photosensitizers and catalyst **Co3** proceeds *via* a heterolytic pathway. After the UV-Vis investigation, it is also possible to specify the individual cobalt species, which are involved in the hydrogen evolution.

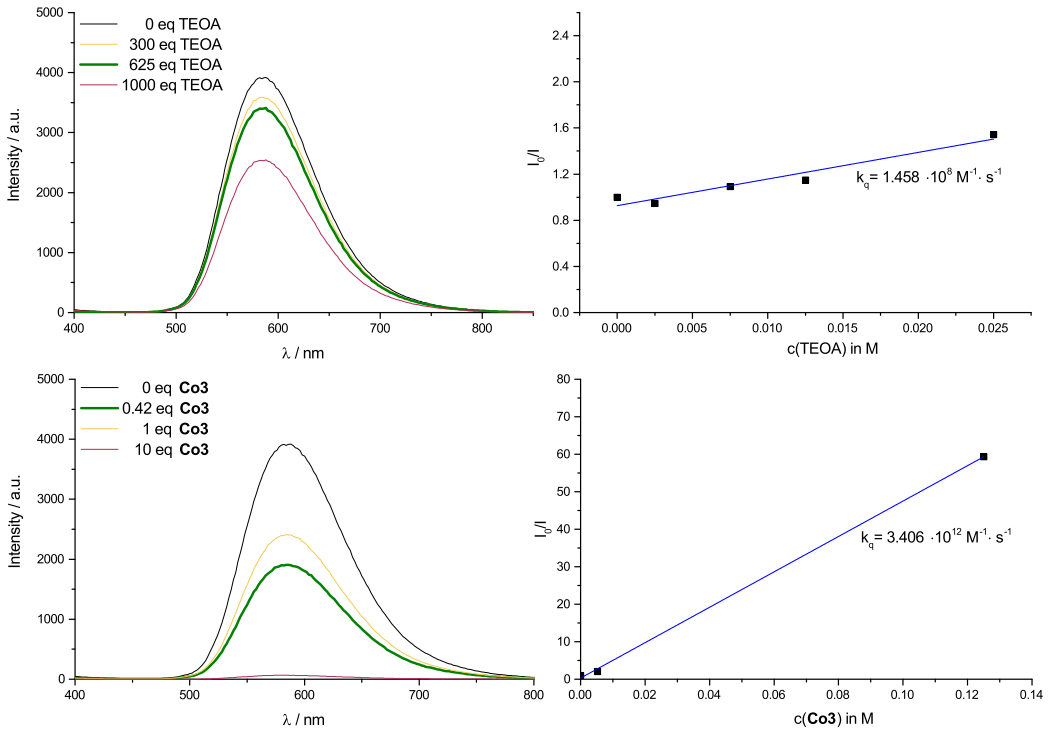

Figure 5.15: Left: Quenching studies of **PS2** measured at an excitation wavelength of 260 nm in deaerated MeCN while adding defined amounts of TEOA (top) or **Co3** (bottom) with a fixed concentration of **PS2**. Right: Stern-Volmer plot of quenching studies with TEOA (top) and **Co3** (bottom).

5.2.2 Fluorescence Spectroscopy

Until now, the mechanistic considerations were mostly focused on the cobalt catalyst. The processes of the photosensitizers during the water reduction should also be analyzed in more detail under the application of fluorescence spectroscopy. In Chapter 2.3.2 two different mechanisms were described for the quenching of an excited photosensitizer. After the excitation of a photosensitizer with light, the PS* can accept an electron from the sacrificial donor and is therefore negatively charged (PS^{*-}). This process is called reductive quenching. In contrast, if the excited photosensitizer donates an electron to the catalyst, it is called oxidative quenching.[217] To elucidate which of these two processes is valid for the photosensitizers **PS1**–**PS9**, fluorescence spectroscopy was conducted.

The quenching experiments were carried out with **PS2** as an exemplary photosensitizer for this new class of PS presented in this thesis. The excited **PS2*** is quenched with known amounts of either the sacrificial reductant TEOA or the catalyst **Co3**. The results are shown in Figure 5.15. The green, bold emission spectra show the equivalents of TEOA or **Co3** that were used in the water splitting experiments. Both substances quench the excited state of **PS2**, but the cobalt catalyst quenches **PS2*** more effectively under the same conditions as during the photocatalytic hydrogen

evolution experiment. With these equivalents of quencher, the intensity of the **Co3** quenching experiment is 1907 which corresponds to a quenching rate of 51.3 %. The intensity of the TEOA experiment is 3398, which is equivalent to a quenching rate of 13.2 %. This is also supported by the Stern-Volmer plots of both experiments, which are also depicted in Figure 5.15. The quenching constants k_q were calculated with the Stern-Volmer equation that was introduced in Chapter 2.3.1. For **Co3**, a quenching constant of $3.046 \cdot 10^{12}$ $M^{-1}s^{-1}$ is obtained, while k_q for TEOA is four magnitudes smaller with $1.458 \cdot 10^{8}$ $M^{-1}s^{-1}$. The diffusion constant of MeCN k_{diff} is $2.2 \cdot 10^{10} M^{-1}s^{-1}$.[218] This not only implies that **Co3** is the more effective quencher for this photosensitizer, but rather that there is a static process involved in oxidative quenching. While the reductive quenching, which is also present in these Ir-Co water splitting systems, is a diffusion-limited process.[201]

Another aspect, which influences the degradation of the excited state, is the oxidation potential of the sacrificial donor and the reduction potential of the catalyst compared to the potentials of the photosensitizer.[134] This aspect will be discussed in Chapter 5.3.1 and, it will be evaluated if the electrochemistry supports the oxidative or the reductive quenching mechanism. Until now, an oxidative quenching pathway for the excited PS is more favored due to the quenching results presented above.

After the evaluation of the present quenching mechanism, the fluorescence lifetimes, which were calculated in Chapter 4.3.3 are correlated with the results of the water reduction experiments. The photosensitizer-based TONs are plotted against the emission lifetimes of **PS1**–**PS9** and they reveal a structure-activity correlation. The corresponding plot is shown in Figure 5.16. It is clearly evident that the more compact systems **PS1**, **PS2**, **PS3**, and **PS5** exhibit the highest activity in water reduction. All four iridium complexes show a short emission lifetime, whereas the larger iridium photosensitizers (**PS6**, **PS8**, **PS9**) have longer emission lifetimes and lower TONs. The lifetime of **PS7** is excluded due to the inactivity during the water reduction experiments. **PS4** is not shown in the correlation plot due to a prolonged emission lifetime, which was not measurable with our device. It is not unusual that the extension of a ligand results in an increased emission lifetime as observed for **PS6**, **PS8**, and **PS9**.[60,180] Through excitation, an electron is transferred from the HOMO to the LUMO of the complex. The HOMO of this iridium complexes is localized on the phenylpyridine ligands. In contrast, the LUMO is localized on the N^N ligands and partly on the iridium center. For the ligands presented here, the excited electron is delocalized over a huge molecule, and this finally leads to an increased emission lifetime. Nevertheless, it is somehow a surprise that the introduction of the methyl substituents in **PS9** lead to such a high emission lifetime. This is caused by the hyperconjugation of the methyl groups that results in a greater delocalization of the excited electron. The group of Burn and Lo investigated six different-sized iridium photosensitizers. They figured out that the small photosensitizers investigated

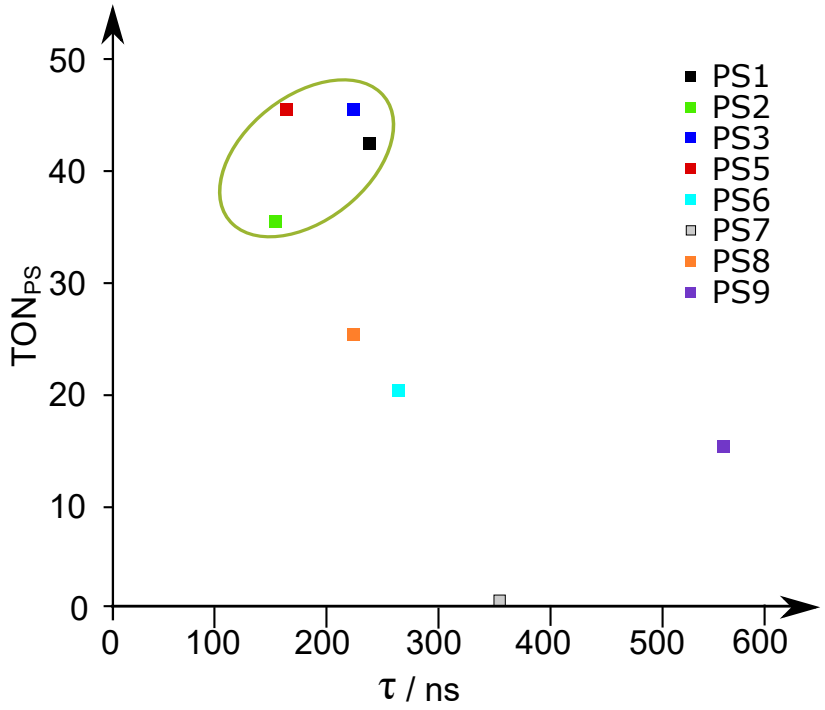

Figure 5.16: Correlation of emission lifetime data with the TONs, obtained from water reduction catalysis.

by them showed hydrogen evolution, whereas the larger systems displayed no detectable activity. Although they measured the emission lifetimes with short τ for small systems and high τ for large molecules, they got not to the point that there was a correlation between the emission properties and the water reduction data.[87] Unfortunately, there are also publications that disagree with this theory. The systems with prolonged molecular structures did have longer lifetimes, but also a higher hydrogen evolution ability.[92,115] But these iridium complexes are composed of phenylpyridines or bipyridine with a phenyl extension. From this controversial results it is obvious that the hydrogen evolution capacity is not only determined by the excited-state lifetime. Therefore, it is reasonable to assume that there must be other factors or properties, which influence the water reduction experiments like the choice of catalyst. As already shown before, the cobaloxime **Co3** is the hydrogen evolution-limiting compound due to fast degradation of the catalyst. With another more persistent catalyst, the results of the emission lifetime-TON-plot might look different. It is possible, that then rather the degradation of the photosensitizers determine the activities of the investigated systems than the degradation of the catalyst. This would suggest a higher activity of the prolonged photosensitizers, which was not observed in our experiments due to the short lifetime of the cobalt complex.[92,115] However, under the applied conditions (solvent, concentrations, pH) and the use of catalyst **Co3**, the correlation of the excited-state lifetimes with the photosensitizer activities is valid and reveals an obvious structure-activity correlation.

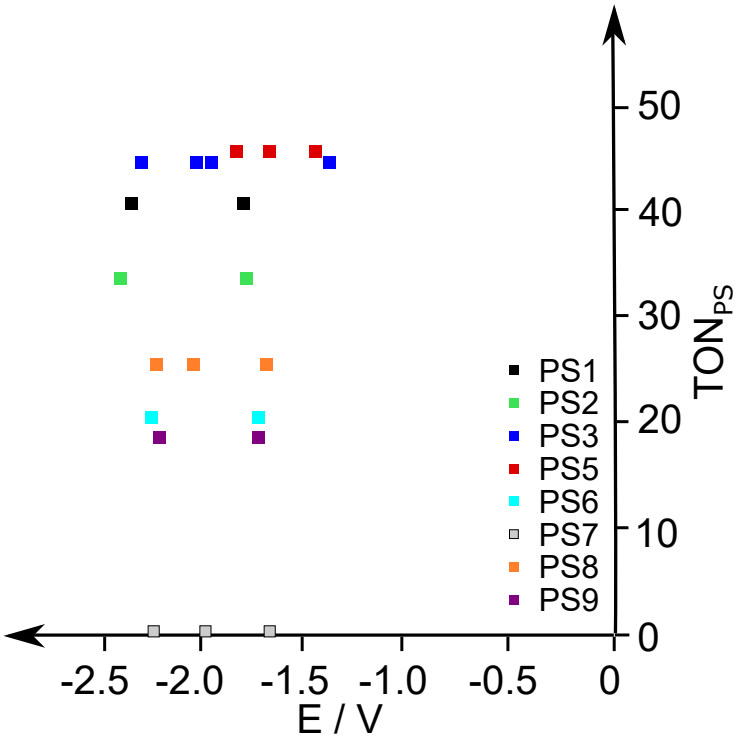

Figure 5.17: Ligand-based redox potentials of the tested iridium photosensitizers plotted against their TONs obtained through the water reduction experiments.

5.3 Electrochemical Characteristics of Iridium-Cobalt Water Reduction Systems

5.3.1 Cyclic Voltammetry

In the previous sections, only spectroscopic properties were discussed concerning the hydrogen evolution ability of the investigated photosensitizers. In this section, the electrochemical properties will be the focus of the discussion. Like it was conducted with the excited state lifetimes and the PS-based TONs, the ground state potentials were plotted against the iridium-based TONs to evaluate a possible correlation of the electrochemical properties with the ability to act as a photosensitizer during the photocatalytic hydrogen production. The redox potentials were already reported in Chapter 4.3.4. Since the Ir^{+III}/Ir^{+IV} potentials of all photosensitizers were quite similar, they are neglected in this graph. The ground state potential-TON plot is shown in Figure 5.17. For the most active photosensitizers **PS3** and **PS5**, the lowest reduction potentials are detected with -1.41 V and -1.47 V. It is not possible to reveal a correlation between the potentials and TONs for the other photosensitizers. Therefore, it might be a coincidence that the most active photosensitizers also exhibit the lowest reduction potentials.

Until now, only the ground state potentials of the iridium complexes were evaluated. Since the water reduction is a light-driven process that requires an excited photosensitizer, the redox potentials of the excited state will be calculated and discussed concerning the photocatalytic activity of the particular photosensitizer.

The oxidation or reduction strength might vary widely from the ground state potentials, and an initially thermodynamical unfavored electron transfer process is triggered by light to transfer the electron. Therefore, the reduction and oxidation potentials of the excited state were estimated under the application of Hess´s law of heat summation with the emission maxima obtained from the fluorescence measurements (see Chapter 4.3.3) and the ground state potentials obtained from the CV analysis (see Chapter 4.3.4).[110] The required equations are 2.13 and 2.14, which were already introduced in Chapter 2.3.2. Since the driving force for an electron transfer is a change of the Gibbs energy, ΔG^0 was also calculated. This change was calculated with Equation 5.4, where n is the number of transferred electrons, F the Faraday constant (96485 C/mol) and E^0 the relevant ground state potential.

$$\Delta G^0 = -n \cdot F \cdot E^0 \tag{5.4}$$

The calculations of the excited state redox potentials ($E^0(PS^*/PS^-)$, $E^0(PS^*/PS^+)$) for every photosensitizer reveal the superior properties of the excited state photosensitizer PS*. Both, oxidative and reductive potentials, are more favorable for the desired electron transfer compared to the ground state process.

The calculations are summarized in Table 5.4 and will be discussed by means of one example. **PS2** is chosen to explain the results. After this discussion, the results of Chapter 5.2.2 will be connected to the electrochemical consideration, and hopefully, it is possible to make a statement, if the oxidative or reductive quenching pathway is more favored for these iridium-cobalt systems. The measured and calculated redox potentials of **PS2** are shown in a schematic representation in Figure 5.18. **PS2** exhibits a ground state oxidation potential of 0.87 V. In contrast, the excited state potential was calculated with - 1.29 V, which is an excellent potential for an oxidation process. The reduction potential for the ground state (-1.77 V) is more negative compared to the excited state potential (0.39 V). Hence, the excited state process is more favored, too. Since both redox potentials of the light-driven processes are more advantageous, the Gibbs energy is taken into account, too. Again for **PS2**, the Gibbs energy ΔG^0 of the oxidation process (PS/PS^+) was calculated with -84 kJ/mol in contrast to the Gibbs energy of the excited state oxidation (PS^*/PS^+) with 124 kJ/mol. Opposed to the before discussed superior properties regarding the redox potentials of the excited state, a balanced image is given for the Gibbs energies. In this case, the oxidation of the ground state is more preferred, but the

Table 5.4: Measured and calculated redox potentials for the ground and the excited state of the photosensitizers **PS1**–**PS9**.

			Ground state[b,c]				Excited state[b,c,d]			
PS	λ_{em}[a] **eV**	ΔG^0 **PS/PS***	E^0 **PS/PS$^+$**	ΔG^0 **PS/PS$^+$**	E^0 **PS/PS$^-$**	ΔG^0 **PS/PS$^-$**	E^0 **PS*/PS$^+$**	ΔG^0 **PS*/PS$^+$**	E^0 **PS*/PS$^-$**	ΔG^0 **PS*/PS$^-$**
1	2.18	-210	0.86	-83	-1.76	170	-1.31	127	0.42	-40
2	2.16	-208	0.87	-84	-1.77	171	-1.29	124	0.39	-37
3	2.09	-202	0.88	-84	-1.41	136	-1.22	117	0.68	-66
5	2.12	-204	0.88	-85	-1.47	142	-1.24	120	0.65	-63
6	2.10	-203	0.87	-84	-1.72	166	-1.23	119	0.38	-37
7	2.13	-206	0.88	-85	-1.66	160	-1.25	121	0.47	-45
8	2.10	-203	0.89	-86	-1.70	164	-1.22	118	0.41	-39
9	2.08	-201	0.86	-83	-1.72	166	-1.22	118	0.37	-35

a) λ_{em} were taken from emission spectra b) redox potentials are given in V c) Gibbs energy are given in kJ/mol
d) Excited state potentials were estimated using Hess law.

reduction of the excited state is more likely to occur due to a negative Gibbs energy (-37 kJ/mol) and a favored excited state reduction potential.

Up to now, only the potentials of the photosensitizers were discussed, but for an oxidation or reduction process, it is necessary to have a suitable counterpart. Therefore, the potentials of the catalyst and sacrificial reductant must be considered to understand the relevant electrochemistry. The redox potentials of the catalyst were determined by CV analysis and already described in Chapter 4.4.2. The relevant potential for the oxidative quenching process is -1.50 V, which belongs to the reduction of the Co^{II+}/Co^{I+} couple. For the reductive quenching process, the redox potential of TEOA to $TEOA^+$ must be known, which was taken from literature with a value of 0.82 V.[219]

Table 5.5: Calculated energy differences between the catalyst **Co3** or the sacrificial reductant TEOA and **PS2** for the reduction and oxidation processes of the ground and excited state.

	ΔE	ΔE	
	$Co^{II+/I+}$	$TEOA^{0\pm/I+}$	ΔG^0 [kJ/mol]
$PS^{*/+}$	-0.21	-	124
$PS^{/+}$	-2.37	-	-84
$PS^{*/-}$	-	-0.43	-37
$PS^{/-}$	-	-2.59	171

$\Delta E = E_{Red} - E_{Ox}$

For each process, ΔE was determined. The four processes are: Oxidation of the ground and excited state PS by cobalt (oxidative quenching) or, reduction of the ground and excited state by TEOA (reductive quenching). The calculations for both excited state quenching reactions yield only minor energy differences. The ground

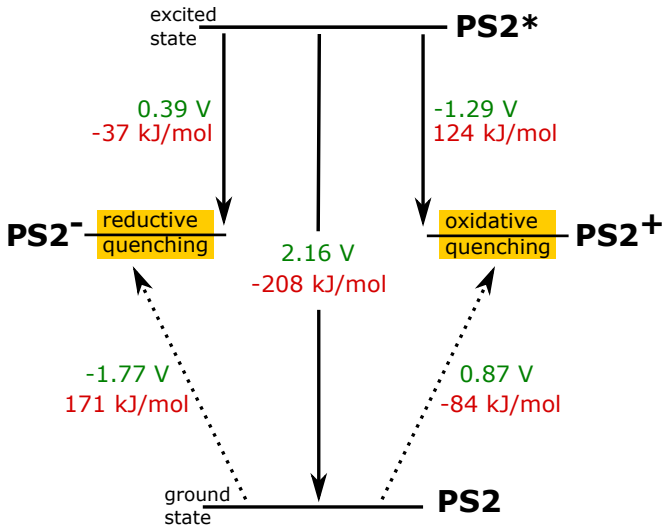

Figure 5.18: Schematic representation of the ground and excited state potentials for **PS2**.

state potential-differences are higher, and therefore, only the excited state reactions are realistic. Since both energy differences are similar with -0.21 V and -0.43 V, it is assumed that a mixture of reductive and oxidative quenching is the most suitable option for the degradation of the excited state. But the above presented data indicate a slight benefit of the reductive quenching over the oxidative quenching pathway due to a negative Gibbs energy (-37 kJ/mol *vs.* 124 kJ/mol) and the energy difference (-0.21 V *vs.* -0.43 V).

It can be summarized that the discussion of the electrochemical properties with regard to the quenching mechanism does not reveal unambiguously if reductive or oxidative quenching is present for this iridium-cobalt two-component systems. While the fluorescence study slightly prefers the oxidative quenching, for the electrochemical discussion the result is reversed. Therefore, it can be concluded that a mixture of oxidative and reductive quenching might be present in these systems.

5.4 Summary

This chapter covered the application of the synthesized iridium, iron and cobalt complexes in the photocatalytic water reduction. A high variety of water reduction experiments were conducted. Altogether, nine different iridium photosensitizers, four non-noble catalysts (two iron and two cobalt systems), and one noble platinum catalyst were tested as components for the photocatalytic hydrogen evolution. Except for the platinum catalyst, all systems showed hydrogen evolution. To elucidate the optimum conditions for the hydrogen evolution experiments, the pH, the solvent, the mixing proportion of the solvents (organic *vs.* H_2O), the amount of sacrificial reductant, the concentrations of the key compounds photosensitizer and catalyst and

the ratio of PS and CAT were altered. The following conditions were chosen after the screening experiments for an optimized hydrogen evolution: 12 μmol PS, 5 μmol **Co3**, 5 vol% TEOA in 20 mL MeCN:H_2O (1:1) at a pH that was adjusted to 8.4.

The highest activity for the hydrogen evolution was achieved under the application of **PS3** and **PS5** (both TONs$_{PS}$ = 44) with **Co3** as catalyst, while **PS7** showed an underwhelming result with no hydrogen evolution. An attempt was made to connect the activity to structural, spectroscopic, and electrochemical properties of the photosensitizers. It was possible to show a correlation between excited state lifetimes and their ability to act as photosensitizers. The systems with short, excited state lifetimes (~150 ns) exhibited the highest activity. These photosensitizers (**PS1**–**PS5**) were also the most structurally-compact complexes. The iridium compounds were designed with increasing aromaticity, which was achieved through a growing N^N ligand size. This leads to a higher delocalization of excited electrons and might be one reason for the reduced hydrogen evolution ability of the large iridium complexes. The unusual, delayed hydrogen evolution of **PS6**, **PS8**, and **PS9** cannot be explained with the spectroscopic results. The inactivity of **PS7** also remains unexplained. Besides the correlation of the spectroscopic properties with the activity, an attempt was made to investigate whether there is a correlation between the water splitting activities and the redox potentials, but there was no obvious connection between these two parameters.

The water reduction experiments also showed that the SR concentration had only minor influences on the hydrogen evolution. However, it looked quite different when the PS concentration was altered. A lower PS concentration resulted in higher activity. The reduction of the catalyst concentration showed the opposite behavior

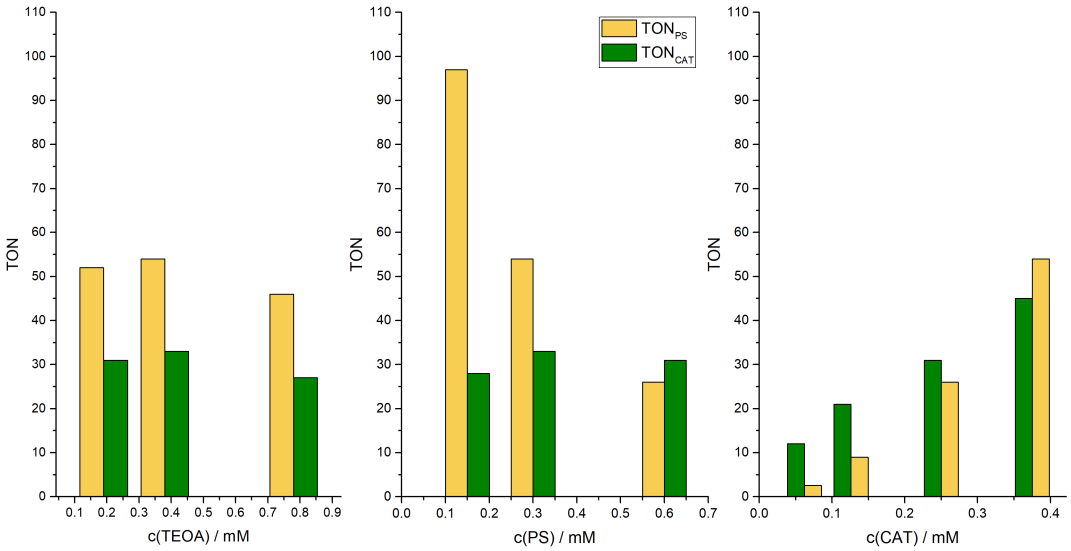

Figure 5.19: Development of TON$_{PS}$ and TON$_{CAT}$ depending on the sacrificial reductant, photosensitizer, or catalyst concentration.

with less activity. This relation is summarized in Figure 5.19. The experiments also revealed the presence of a monometallic Co mechanism for the reduction of H^+. The measurements also showed the limiting role of the cobalt catalyst for water reduction. It was supported by mass spectrometry analyses after the irradiation that showed the presence of the original photosensitizers, but no sign of the cobalt catalyst. This was further supported by the approaches with additional dmgH ligand. The cobalt catalyst degraded fast during the photocatalytic experiments, and with additional ligand, the two-component system showed higher activity and a prolonged lifetime. UV-Vis measurements during the irradiation experiments indicated the presence of a Co(I) species or a Co(III) hydride, which is responsible for the reduction of the protons. While the mechanism at the cobalt catalyst during the hydrogen evolution was mostly clarified (Co(III) hydride, monometallic), the mechanism at the iridium photosensitizer was not unambiguously resolved. Fluorescence-quenching experiments and thermodynamic calculations suggested a mixture of reductive and oxidative quenching. While the quenching studies slightly supported the oxidative quenching pathway, the thermodynamic calculations favored the reductive quenching mechanism. Therefore, a mixture of both was preferred for the iridium-cobalt systems.

After all, the experiments showed that the non-noble complexes could be superior catalysts compared to noble metals. For a long-term application, it is necessary to improve the stability of these systems, for example, through less labile ligands of the cobalt catalyst. In literature, there are already suggestions for how to deal with this challenge and improve the properties of the catalyst.[53,54,68,201,207,212]

PS8 and **PS9** will be revisited for the synthesis of bimetallic iridium-cobalt systems. With their terminal pyridine groups, they are perfectly suited for the coordination of a second metal. In this context, they will be discussed in more detail.

6 Synthesis and Characterization of Iridium-Cobalt One-Component Systems

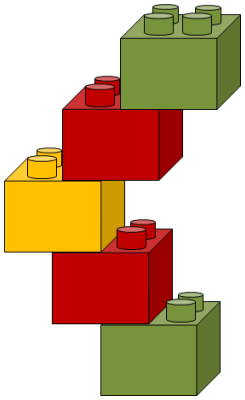

6.1 Synthetic Strategy

The last part of this thesis focuses on the synthesis of two one-component systems, which are based on an iridium photosensitizer and a cobalt catalyst side. It can be assumed that the connection between the individual components, which were already used and proven to be active in Chapter 5, results in an enhanced hydrogen evolution through a directional electron transfer from the PS to the CAT. Besides the development of this new iridium-cobalt one-component systems, the role of the bridging-ligand should also be investigated. Therefore, two different bridging ligands were chosen to evaluate the role of the connecting unit between the PS and the CAT; first, a fully conjugated system and second, an oxygen-bridged ligand that interrupts the delocalization of the electrons in this huge systems.

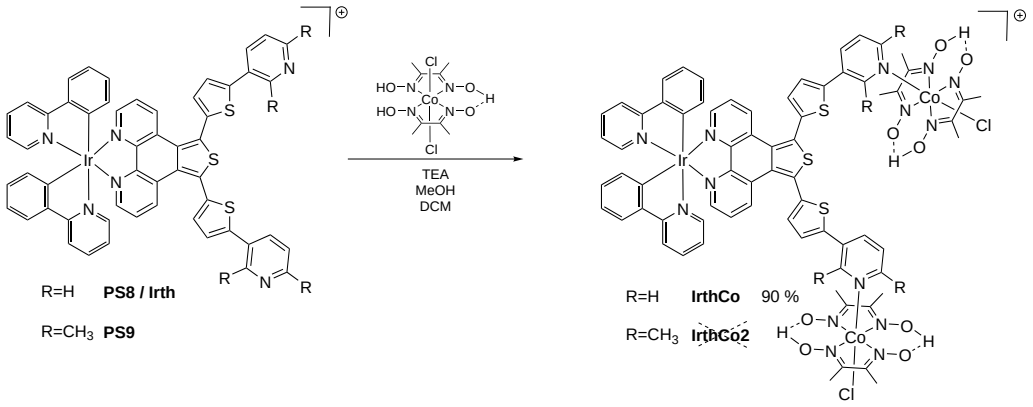

Scheme 6.1: Synthetic strategy for the preparation of the iridium-cobalt one-component systems **IrthCo** and **IrthCo2**.

For the first one-component system [**IrthCo**]PF_6, **PS8** (which will be called [**Irth**]PF_6 in the following chapter for a better identification with the corresponding one-component system)is chosen as partner for the coordination to a cobaloxime complex. The additionally required cobaloxime precursor **Co3-1** will be synthesized from

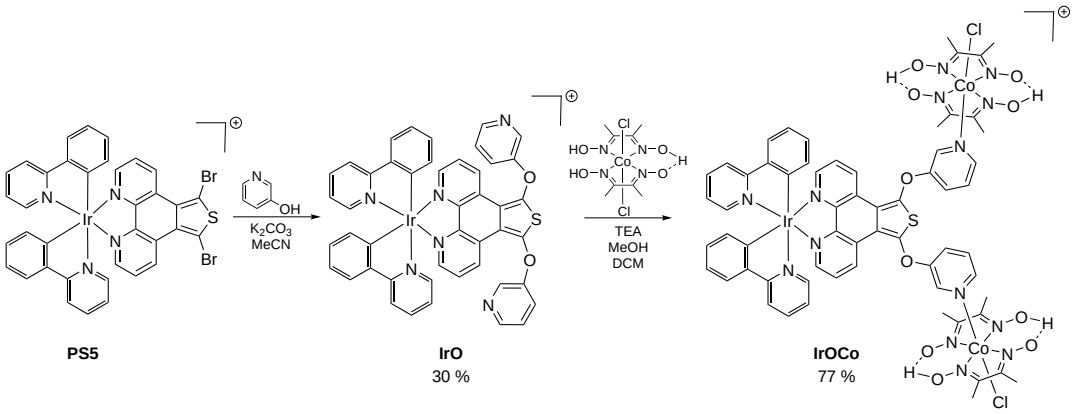

Scheme 6.2: Synthetic strategy for the preparation of **IrOCo**, an oxygen-bridged iridium-cobalt one-component system.

cobalt chloride and dimethylglyoxime. The conversion of the cobalt precursor with **PS8** will accomplish the synthesis of the first iridium-cobalt system with a large conjugated ligand system that connects one iridium center with two cobalt units. The reaction pathway is depicted in Scheme 6.1.

For the second one-component system [**IrOCo**]PF_6, whose synthesis is shown in Scheme 6.2, the preparation procedure will be altered. **PS5** will get introduced in a Williamson ether synthesis with 4-hydroxypyridine to obtain the final iridium complex [**IrO**]PF_6 for the bimetallic complex synthesis. The iridium complex with

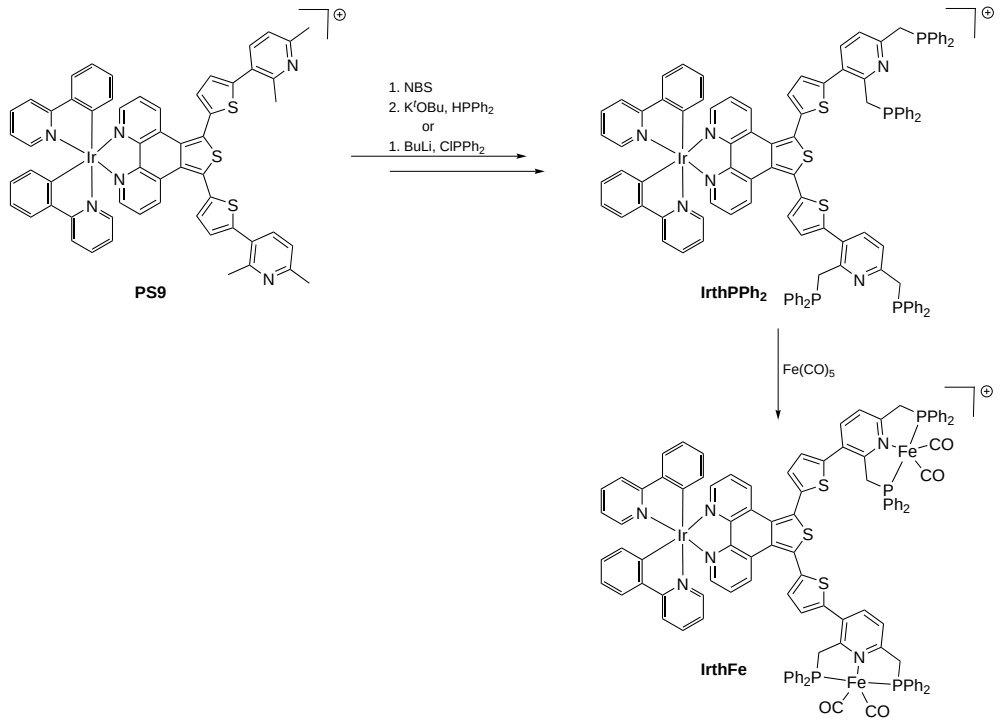

Scheme 6.3: Synthetic strategy for the preparation of an iridium-iron one-component system **IrthFe**.

the oxygen-bridged ligand [**IrO**]PF_6 will be used afterward in a complex-reaction with **Co3-1** as already reported for [**IrthCo**]PF_6.

For the preparation of the last supramolecular system, the iridium PS remains unchanged and the catalyst center will be represented by an iron complex. The preparation strategy for this dyad is shown in Scheme 6.3. In a first step, the methyl groups of **PS9** will be converted to methyldiphenylphospine groups. Afterward the isolated pincer ligand **IrthPPh**$_2$ will be coordinated to an iron(0) carbonyl to realize the preparation of the third dyad [**IrthFe**]PF_6.

6.2 Synthesis and Characterization

For the synthesis of the iridium-cobalt dyads, a multi-step strategy was chosen. The preparation of the iridium complexes (**PS8/Irth** and **PS5**) was already described in Chapter 4.3. The first supramolecular system that will be presented is an ongoing development of the iridium complex **Irth**, which already provides two extra nitrogen donor functionalities for a possible coordination to an additional metal. Therefore, the cobaloxime motive was introduced into the molecule. It was a straightforward procedure including two single reactions. In the first step, the precursor of the cobaloxime was prepared from cobalt chloride and dimethylglyoxime. The reaction to obtain the precursor **Co3-1** was already described in Chapter 4.4.2. In the second step, **Co3-1** was introduced into the conversion with the iridium complex [**Irth**]PF_6, which finally resulted in the synthesis of the first supramolecular molecule [**IrthCo**]PF_6 with a yield of 90.1 %. The product was isolated by precipitation as pale yellow solid. The structure is shown in Figure 6.1. The ^{15}N NMR spectrum of this compound unambiguously evidences the successful synthesis. The peak of the free pyridine-nitrogen of the iridium precursor complex is located at 316 ppm. After the conversion, the signal of the same nitrogen is located at 213 ppm caused by the coordination to the cobalt. The ^{15}N NMR spectrum of an Ir-Co dyad will be shown for the second system [**IrOCo**]PF_6. A second proof for the successful preparation was also given by mass spectrometry, whose spectrum is shown in Figure 6.1. The mass peak (a) shows the formation of the desired molecule **IrthCo** in accordance with the theoretical mass peak and the isotopic distribution. The base peak is identified as [**IrthCo**-Co(dmgH)$_2$Cl] (b). Also shown in the ESI spectrum is the peak of the precursor iridium complex **Irth** as singly (c1) and doubly charged ion (c2). The last signal at 289.0337 m/z is identified as $[Co(dmgH)_2]^+$ (d). Since the NMR spectra showed only signals for the pure target molecule, it was assumed that all signals, except the mass peak, are a consequence of the used ionization method.

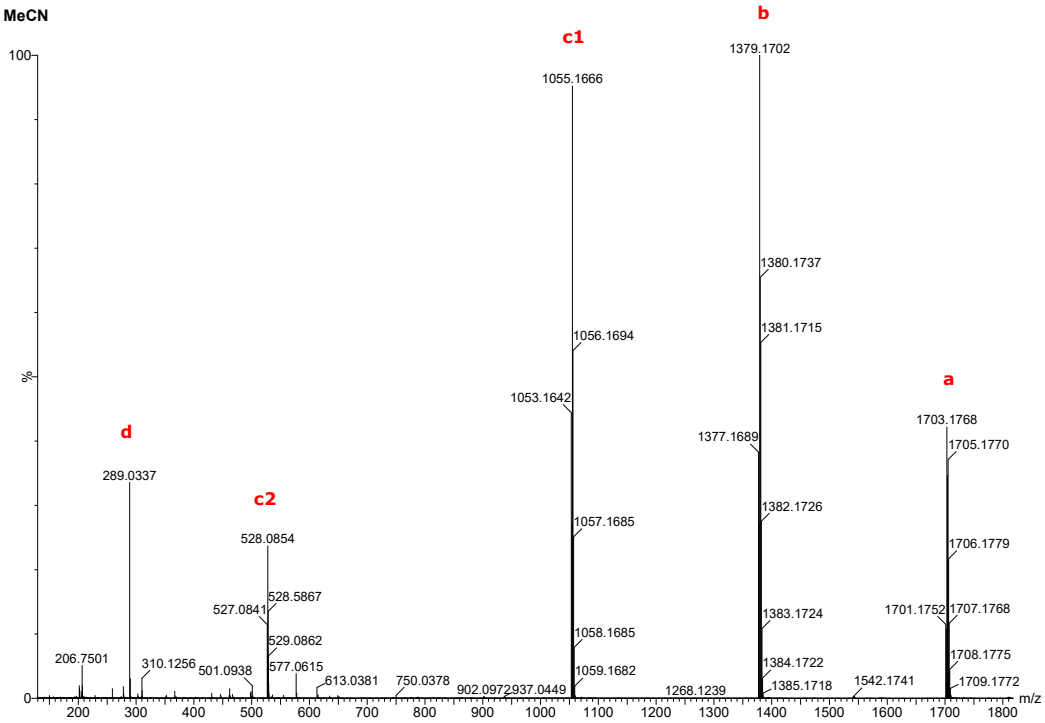

Figure 6.1: ESI(pos) mass spectrum of **IrthCo** measured in MeCN. Mass peaks are quoted with letters: a) [**IrthCo**]$^+$, b) [**IrthCo**-Co(dmgH)$_2$Cl]$^+$, c) **Irth** as singly (c1) and doubly (c2) charged ion, d) [Co(dmgH)$_2$]$^+$.

Additional to [**IrthCo**]PF_6, it was tried to synthesize a similar dyad using **PS9** as iridium precursor. Due to the high similarity of **Irth** and **PS9**, it was assumed that the synthesis would be straightforward and without any difficulties. This assumption was proven to be wrong. It was not possible to isolate the desired product [**IrthCo2**]PF_6. The ^{15}N NMR and the mass spectra feature only the signals of **PS9** and, no sign of **IrthCo2** was found. Under the application of a second procedure, **PS9** was introduced in a synthesis with $CoCl_2$ and dimethylglyoxime in ethanol. This yielded again not the desired product. To figure out, if the target molecule was not built as a consequence of electronic effects generated by the ligand structure of **PS9**, the experiment was repeated with 2,6-lutidine as a strongly simplified version of the ligand structure of **PS9**. This attempt did also not yield the desired complex, but a crystal structure of the molecule that was formed instead was isolated. The structure is shown in Figure 6.2. The structure shows that the pyridine is protonated during the synthesis, and the cobalt-center is four-fold coordinated by chloride. Based on this results, it was concluded that electronic effects were not the reason for the unsuccessful synthesis of **IrthCo2** rather than the sterical demand of the methyl groups that prevented the coordination to the cobalt center.[133,199,220,221]

The second dyad [**IrOCo**]PF_6 was prepared with a slightly modified synthetic strategy as the systems before, which is shown in Figure 6.2. The synthesis of **PS5** was already reported in Chapter 4.3.

The iridium complex was introduced into an etherification with 3-hydroxypyridine under basic conditions. This resulted in the desired dipyridinyl ether iridium complex [**IrO**]PF_6 with two new nitrogen donor functionalities. The yield of the reaction was unfortunately low with 30 % due to side reactions like the formation of the monopyridinyl ether iridium complex. The desired product was isolated after column chromatography with acetonitrile and saturated potassium nitrate solution. The final step to obtain the one-component system [**IrOCo**]PF_6 was conducted as already described for [**IrthCo**]PF_6. It was also successful for [**IrOCo**]PF_6, which was isolated by precipitation with a yield of 76.8 %. The molecule was experimentally verified by NMR and IR spectroscopy, mass spectrometry and elemental analysis. The ^{15}N NMR spectrum of the precursor complex [**IrO**]PF_6 and the final product [**IrOCo**]PF_6 are shown in Figure 6.3. All nitrogen signals were assigned by the analysis of the ^{15}N-HMBC spectrum. The ^{15}N spectrum, depicted in the figure, shows a shift of the free pyridine-nitrogen (**IrO**) marked with a green star from 320 ppm to 213 ppm in the Ir-Co dyad (**IrOCo**). This high-field shift of the supramolecular

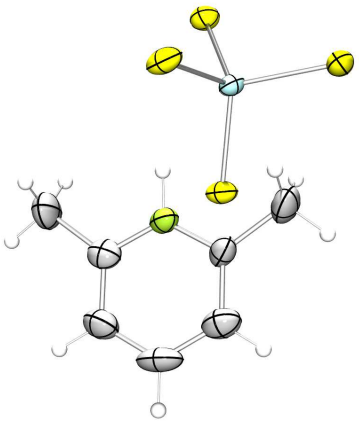

Figure 6.2: ORTEP representation of the crystal structure obtained by the conversion of 2,6-lutidine with $CoCl_2 \cdot 6\ H_2O$ and $dmgH_2$.

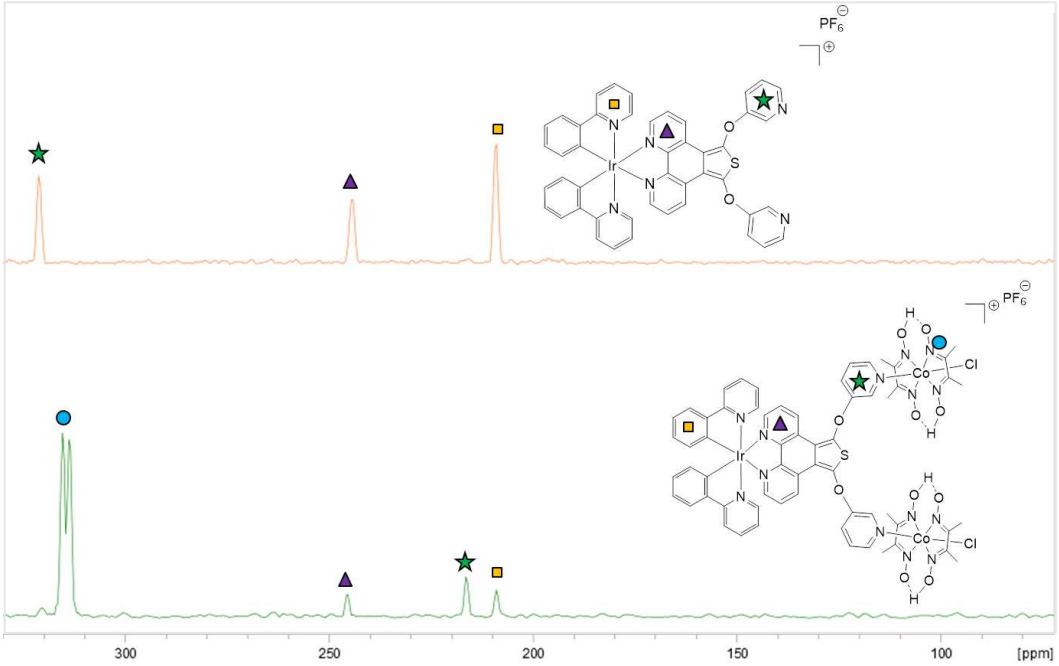

Figure 6.3: ^{15}N spectra of the iridium precursor and the analogue **IrOCo** system measured in CD_2Cl_2.

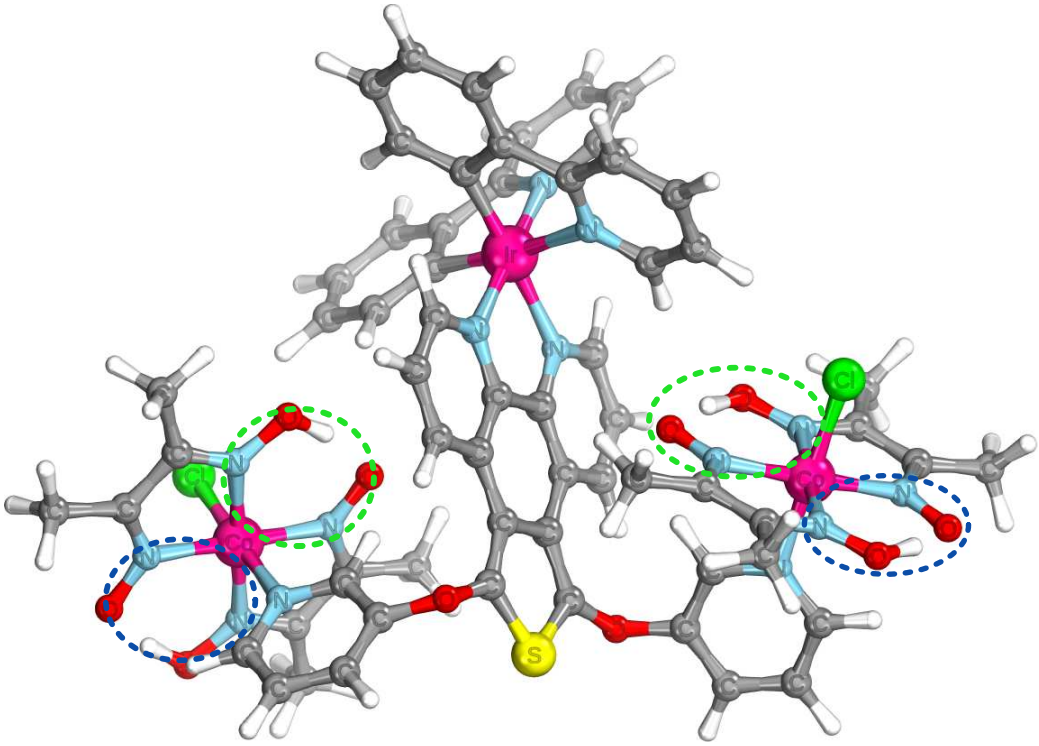

Figure 6.4: Geometry optimized structure of [**IrOCo**]PF_6. The distinguishable nitrogen atoms are marked with different colored circles (green and blue).

system [**IrOCo**]PF_6 seems unusual at the first moment, since a low-field shift is expected for this system. The length of the Co-N bond between the cobalt and the pyridine causes this shift. The pyridine is incorporated into the electron shell of the cobalt atom through the coordination of the nitrogen. The increased electron density caused by the electron shell of cobalt shields the nitrogen nucleus from the strength of the magnetic field and results in a high-field shift. The spectrum of [**IrOCo**]PF_6 shows an additional feature. There are two nitrogen signals for the dimethylglyoxime ligands marked with a blue circle. These two signals are not observed in the ^{15}N spectrum of [**IrthCo**]PF_6, which shows only one nitrogen peak for the dimethylglyoxime of both catalytic units. This implies a slightly different chemical environment of the catalytic cobalt centers in [**IrOCo**]PF_6.

Two reasons are worked out for this behavior: First, the nitrogens within one catalytic center are different from each other, for example one dmgH ligand and the second one or within one dmgH ligand as depicted in Figure 6.4 and marked with the different colored circles. Second, both cobalt centers distinguish from each other through different orientations of the catalytic units. Which of these two explanations is right for [**IrOCo**]PF_6 can only be verified through a crystal structure analysis. The mass spectrum of [**IrOCo**]PF_6 shows the molecular ion at 1571 m/z for the positive charged iridium-cobalt complex but due to fragmentation, the base peak (1247 m/z) belongs to the dyad with only one catalytic cobalt center [**IrOCo**-Co$(dmgH)_2Cl$].

Furthermore, the pure iridium complex ion [**IrO**] (923 m/z) is also detected due to fragmentation during the ionization. This results are in accordance with the mass spectrum analysis of [**IrthCo**]PF_6.

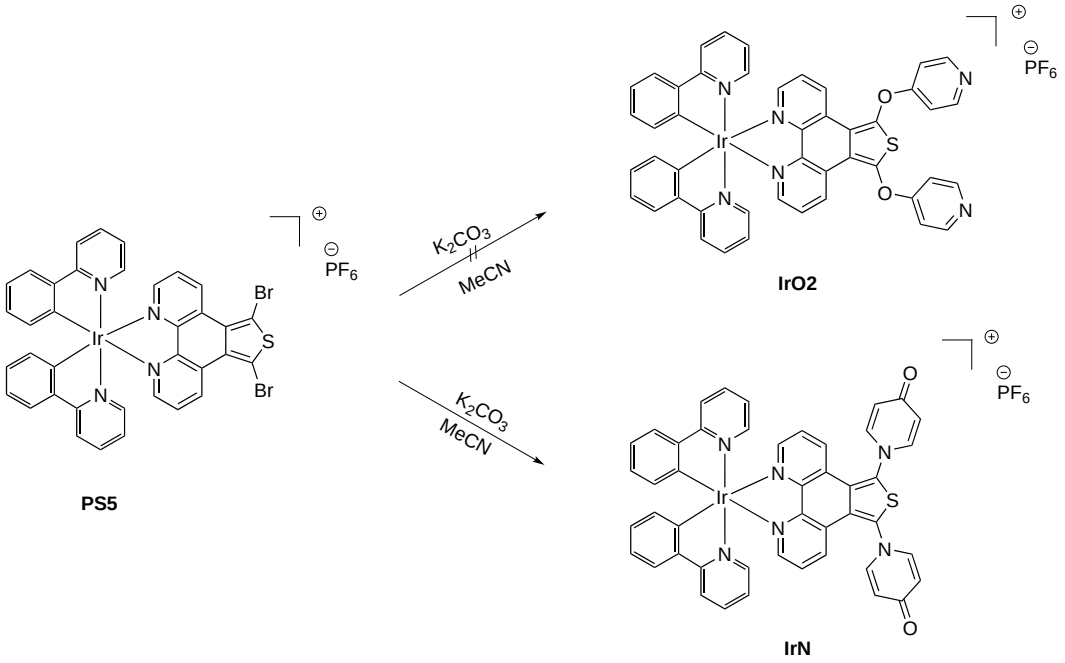

Scheme 6.4: Unsuccessful synthesis of the *para*-connected dipyridinyl ether iridium complex **IrO2**. Instead of the desired product, the synthesis yield a nitrogen-bridged iridium complex **IrN**.

It was also tried to prepare the *para* dipyridine iridium ether complex under the application of the same procedure, but unfortunately, this led to an iridium complex that was bridged over the nitrogen ([**IrN**]PF_6) instead of the oxygen ([**IrO2**]PF_6). The reaction is shown in Scheme 6.4. Due to the missing nitrogen donor this complex was not used for the further synthesis of another iridium-cobalt dyad. The initially desired structure could have give further insides into the electron transfer from the PS to the CAT with a changed connection of the iridium complex to the cobalt unit. The identification of this undesired product was made by crystal structure analysis. It is not possible to identify [**IrN**]PF_6 by the standard procedures due to the same molecular mass, very similar NMR spectra and an identical elemental analysis compared to the desired product [**IrO2**]PF_6.

The last presented synthesis is the preparation of an Ir-Fe dyad, starting with the conversion of **PS9**. The first attempts focused on the direct synthesis of an iridium complex with diphenylphosphine groups at the 2,6-positions on the pyridines. Therefore, **PS9** was introduced to a reaction with *n*BuLi and chlorodiphenylphosphine. Unfortunately, this resulted in the synthesis of $BuPPh_2$ and **PS9**, which was still unmodified after the reaction. For this reason, *n*BuLi was exchanged by *t*BuLi, but this led to the same result. In a third attempt, it was tried to carry out the reaction

at higher temperatures again with *n*BuLi. This time, **PS9** was transformed, but it was not possible to identify the occurred substances. It was neither **PS9** nor $BuPPh_2$. It was also tried to use different solvents like Et_2O, THF, dioxane or benzene, but unfortunately all experiments failed. Finally, the conditions were changed to more drastic ones. The base was again altered to the superbase *n*BuLi/KO*t*Bu and Et_2O was used as solvent. With these conditions, it was again only possible to isolate the iridium complex and $BuPPh_2$.

Table 6.1: Condition screening for the conversion of **PS9** to obtain the pincer ligand **IrthPPh$_2$** for the bimetallic Ir-Fe dyad.

Entry	solvent	base	T [°C]	ratio [PS9:base]	result[a]
1	Et_2O	*n*BuLi	0	1:2.2	$BuPPh_2$ and **PS9**
2	Et_2O	*n*BuLi	reflux	1:2.2	n. i., no **PS9**, no **IrthPPh$_2$**
3	Et_2O	tBuLi	0	1:2.2	$BuPPh_2$ and **PS9**
4	THF	*n*BuLi	reflux	1:2.2	n. i., no **PS9**, no **IrthPPh$_2$**
5	benzene	*n*BuLi	10	1:2.2	$BuPPh_2$ and **PS9**
6	dioxane	*n*BuLi	20	1:2.2	n. i., no **PS9**, no **IrthPPh$_2$**
7	THF	*n*BuLi+TMEDA	0	1:2.1	$BuPPh_2$ and **PS9**
8	THF	*n*BuLi/KOtBu	0	1:2.1	**PS9**
9	THF	*n*BuLi/KOtBu	0	1:6.3	n. i., no **PS9**, no **IrthPPh$_2$**
10	Et_2O	*n*BuLi/KOtBu	0	1:6.3	$BuPPh_2$ and **PS9**

a) n.i.: not identified product

The solvent was again changed to THF, but this also results in a collection of unidentified products and non of them was the desired iridium complex **IrthPPh$_2$** or the precursor complex **PS9**. All experiments were also realized with the ligand **L9** instead of the iridium complex, which led also not to the desired product. The results of the whole screening with **PS9** are summarized in Table 6.1.

After this unsuccessful conversion of **PS9**, the synthesis route was altered. Since the direct preparation of the pincer ligand **IrthPPh$_2$** for the iron coordination failed, it was tried to synthesize the bromine derivative of ligand **L9** and transform them afterward to the corresponding PPh_2 groups. This was tried with a radical bromination with NBS and the radical starter AIBN under the irradiation with light. The reaction is shown in Scheme 6.5. Unfortunately, this resulted only in the mono- or disubstituted ligand and not the desired fourfold substituted 1,10-phenanthroline derivative. Additionally, the bromination occurred at the thiophene rings and not as required at the methyl groups of **L9**. The experiment was repeated with the corresponding iridium complex **PS9**, but yielded also an unfavored product. For this reason the preparation of the supramolecular iridium-iron assembly **IrthFe** was canceled since it was not possible to obtain the desired precursor **IrthPPh$_2$**.

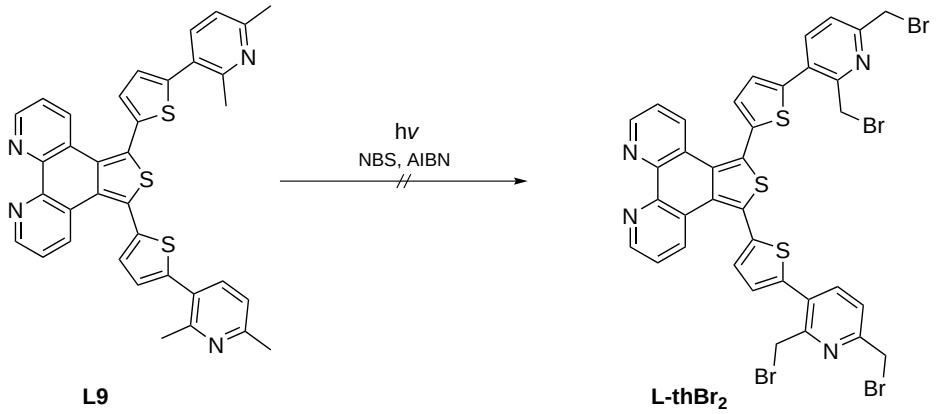

Scheme 6.5: Radical bromination of **L9** with NBS and AIBN to obtain **L-thBr**$_2$.

6.3 Spectroscopy

6.3.1 UV-Vis Spectroscopy

Since it is known, that the spectroscopic properties are of great importance for a complete characterization of these compounds and for the performance of photochemical reactions, the UV-Vis spectra of both dyads, [**IrthCo**]PF_6 and [**IrOCo**]PF_6, and the corresponding iridium precursors, [**Irth**]PF_6 and [**IrO**]PF_6, were recorded. The spectra of the four compounds are shown in Figure 6.5 and the UV-Vis data are summarized in Table 6.2. All assignments were made with the assistance of the ligand and iridium complex spectra and DFT calculations. The samples had a concentration of $\sim 2.5 \cdot 10^{-5}$ M, prepared in deaerated CH_2Cl_2 and measured at room temperature.

The four complexes exhibit strong absorptions in the UV region. In general, [**Irth**]PF_6 and [**IrthCo**]PF_6 show a more intense absorption compared to [**IrO**]PF_6 and [**IrOCo**]PF_6. The absorptions of [**IrO**]PF_6 around 250 nm–270 nm are mainly based on LLCT transitions localized on the phenylpyridine, while the LL'CT transitions occur from the phenylpyridine to the diimine ligand. There is also a small amount of MLCT transitions from the iridium center to the cyclometalating ppy ligand (L = ppy, L'= diimine, M= metal (here: iridium or cobalt)). For the corresponding supramolecular assembly [**IrOCo**]PF_6 with the cobalt units as additional electron-withdrawing groups, the composition of the absorption processes are slightly altered. The LLCT transitions on the ppy ligand are strongly reduced. Instead, the L'L'CT transitions localized on the diimine ligand are more prominent and an additional L'L$^{\#}$CT is detected from the dmgH unit to the N^N ligand (L$^{\#}$= dmgH). There are also ML'CT transitions from the cobalt center to the phenanthroline ligand. Two other MLCT transitions are assigned to electron density shifts of the iridium and

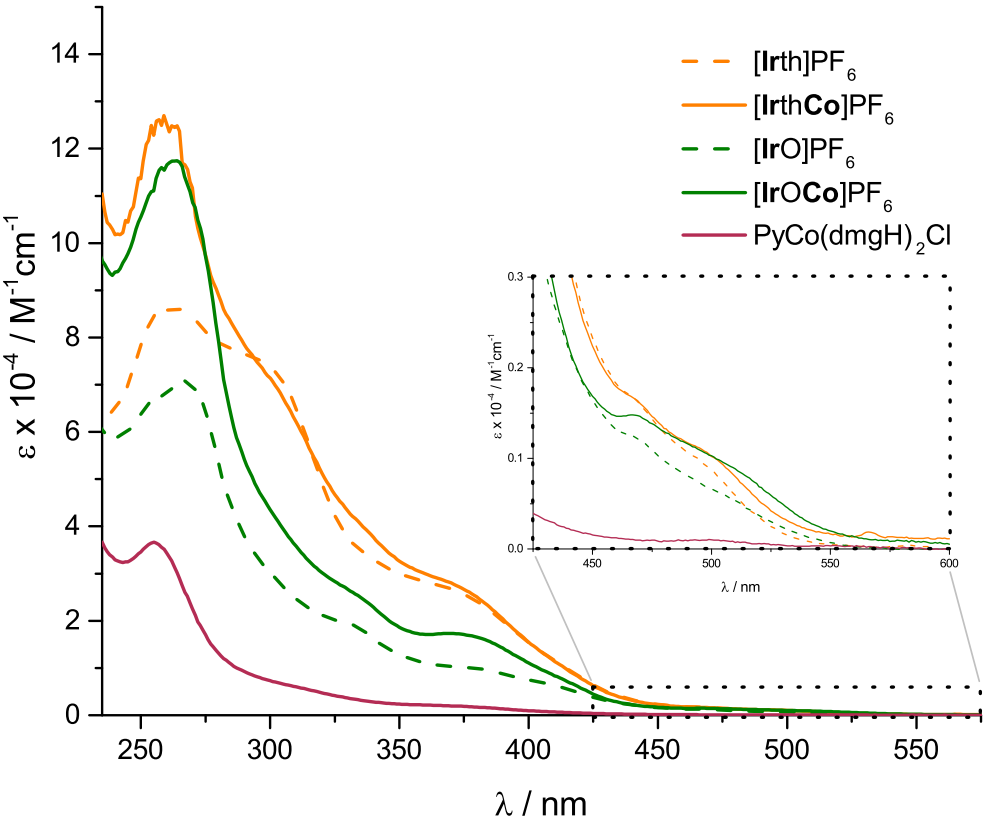

Figure 6.5: UV-Vis spectra of [**IrthCo**]PF_6 in comparison to the precursor iridium complex [**Irth**]PF_6 and [**IrOCo**]PF_6 in comparison to the precursor iridium complex [**IrO**]PF_6. All spectra were measured in deaerated CH_2Cl_2 at room temperature.

cobalt d electrons to a π^* orbital of the phenylpyridine. The comparison of [**Irth**]PF_6 and [**IrthCo**]PF_6 show a similar result for the absorption bands around 260 nm. For [**Irth**]PF_6 only ligand-centered transitions are present; LLCT on the phenylpyridine ligand, L'L'CT transitions on the diimine unit and interligand transitions from the CˆN to the NˆN ligands (LL'CT) and conversely from the NˆN group to the CˆN ligands (L'LCT). Through the introduction of the cobaloxime groups, the inter- and intraligand transitions are completed by the L'MCT and ML'CT transitions from the diimine ligand to the cobaloxime or from the cobaloxime to the diimine groups. Additionally, there are also the L'L$^{\#}$ transitions from the dmgH to the NˆN ligand. After this brief introduction of the present absorption processes around 250 nm, it can be summarized that the most-contributing transitions are ligand-centered and only minor contribution are based on MLCT processes.

The next absorptions range between 300 nm–350 nm and show a reduced absorption intensity (ϵ= 18000–63000 $M^{-1}{\cdot}cm^{-1}$) compared to the first UV region (ϵ> 65000 $M^{-1}{\cdot}cm^{-1}$). The absorption shoulder of [**Irth**]PF_6 and [**IrthCo**]PF_6 at approximately 310 nm is assigned to intraligand π to π^* transitions located on the ppy ligand. For the dyad, additional intraligand transitions from the ppy to the dmgH

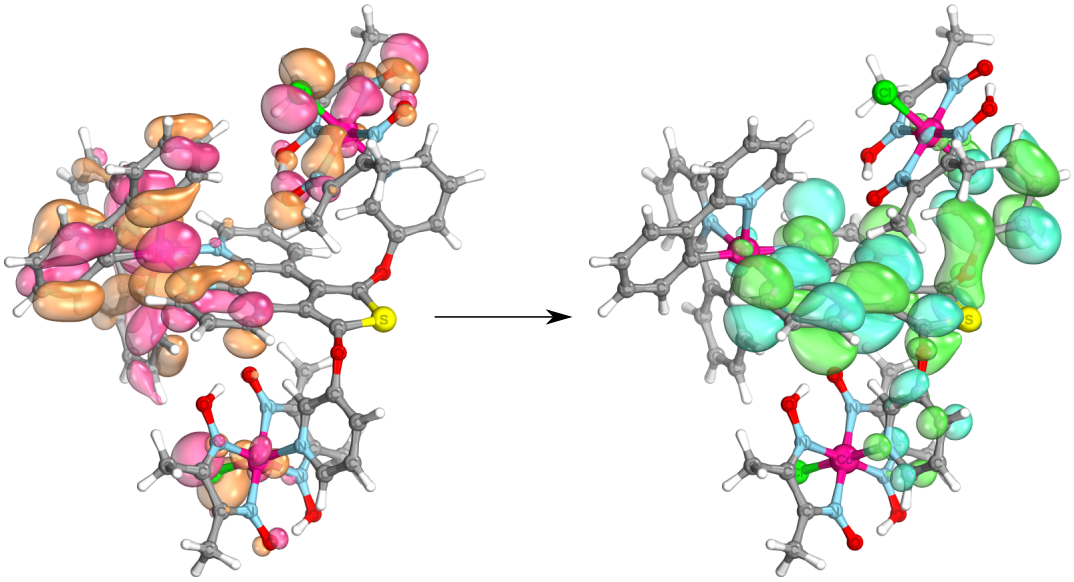

Figure 6.6: Frontier orbitals of [**IrOCo**]PF_6 involved in the evolution of the absorption band located at 335 nm. The donor orbitals are shown in pink/orange and the acceptor orbitals are shown in green/turquoise.

group are calculated. The oxygen-bridged systems show a red-shifted absorption band at ~335 nm. These absorption bands are assigned to phenylpyridine-based intraligand (LLCT) and ppy to diimine interligand (LL'CT) transitions. The [**IrOCo**]PF_6 system show additional ML'CT and L$^{\#}$L'CT transitions. The involved orbitals are shown in Figure 6.6. The absorption in the range of approximately 375 nm is present for all four systems. The signal arise from π to π^* transitions that are first localized on the phenylpyridine and through excitation the LUMOs are located on the diimine ligands. Up to now, the ligand-centered transitions, both intra- and intermolecular, are the dominating processes for the four complexes.

The absorption bands, which are observed in the visible region beyond 420 nm corresponded mainly to metal to ligand charge transfer processes from the iridium centers to N^N ligands. As expected, the signals exhibit a weak absorption ($\epsilon <$ 8000 $M^{-1}{\cdot}cm^{-1}$) as characteristic for MLCT transitions. An example for each dyad is shown in Figure 6.7.

To sum up, the UV-Vis spectra of the supramolecular assemblies [**IrthCo**]PF_6 and [**IrOCo**]PF_6 show identical signals as the corresponding iridium ([**Irth**]PF_6, [**IrO**]PF_6) and cobalt (**Co3**) complexes. They exhibit no new features and show simply the sum of the individual spectra. This is also confirmed by a summation of the individual spectra of [**Irth**]PF_6 and **Co3** and, [**IrO**]PF_6 and **Co3** with a subsequent comparison with the corresponding dyad spectra.

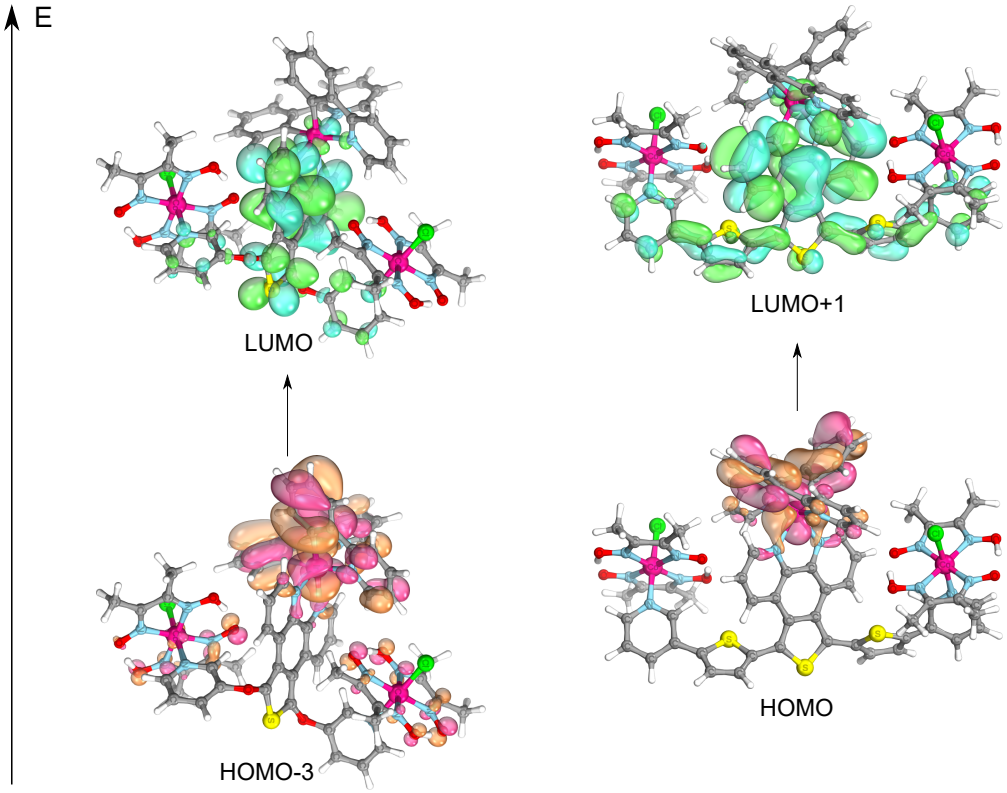

Figure 6.7: Purely MLCT-based transitions for **IrOCo** (left) and **IrthCo** (right), which occur beyond 420 nm.

6.3.2 Fluorescence Spectroscopy

For a complete characterization of the synthesized iridium-cobalt one-component systems, they were submitted to different fluorescence spectroscopy methods. All samples were prepared with a concentration of ~2.5 $\cdot 10^{-5}$ M in CH_2Cl_2. Prior to use, all dissolved samples were applied to at least four freeze-pump-thaw cycles to guarantee an oxygen-free environment. The results of the different fluorescence methods are summarized in Table 6.2.

Figure 6.8 shows the unnormalized emission spectra of both dyads ([**IrthCo**]PF_6, [**IrOCo**]PF_6) and the corresponding iridium complexes [**Irth**]PF_6 and [**IrO**]PF_6. The emission maximum is shifted for the thiophene-bridged system to shorter wavelength through coordination to the cobaloxime, whereas the shift for [**IrOCo**]PF_6 is directed to higher wavelengths. However, more important is the high emission of [**IrO**]PF_6 compared to the other three complexes as the most prominent feature. The emission of [**Irth**]PF_6 as second most emissive complex is 20 magnitudes lower as the emission of [**IrO**]PF_6. It is known that conjugated systems show lower emission intensities compared to less- or non-conjugated systems due to an increased amount of non-radiative decay pathways while the radiative ones decrease.[108,222] The drastically lowered emission of [**IrthCo**]PF_6 and [**IrOCo**]PF_6 compared to their pure

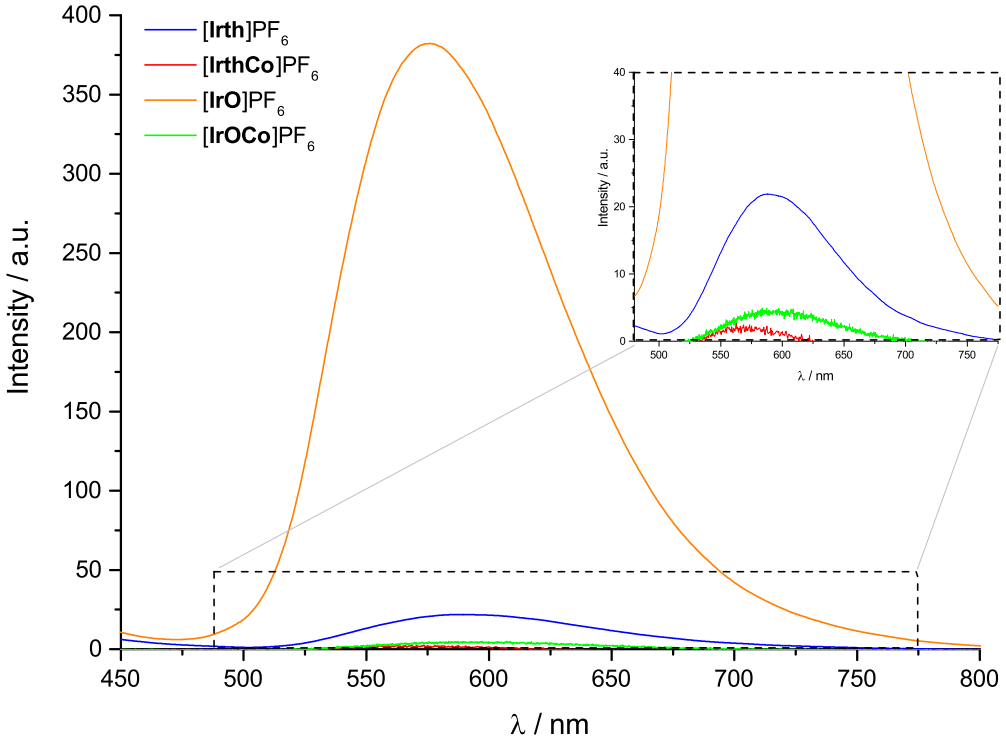

Figure 6.8: Unnormalized fluorescence spectra of [**IrthCo**]PF_6, [**IrOCo**]PF_6 in comparison to the precursor iridium complexes [**Irth**]PF_6 and [**IrO**]PF_6. All spectra were measured in deaerated CH_2Cl_2 at room temperature, λ_{ex} = 260 nm.

iridium complexes is also an expected result for such bimetallic systems.[128,223] For [**IrthCo**]PF_6 the emission intensity is lowered by 91 % and for [**IrOCo**]PF_6 by 99 %. This is already an indication for an intramolecular electron or energy transfer from the singlet excited state of the iridium unit to the cobaloxime moiety.[52,224,225] For an unambiguous identification of an intramolecular process, it is necessary to conduct time-resolved fluorescence spectroscopy.

The quantum yield ϕ is also calculated for all four compounds. The results further support the observations of the fluorescence quenching through coordination of cobaloxime units to the iridium complexes. [$Ir(ppy)_2$phen]PF_6 was again chosen as the reference with ϕ = 14 % at an excitation wavelength of 450 nm. The equation that is used for the calculation of the quantum yields was already introduced in Chapter 4.3.3. The highest ϕ is obtained for [**IrO**]PF_6 with 0.713 %, followed by [**Irth**]PF_6 with 0.059 % relative to $[Ir(ppy)_2(phen)]^+$. The supramolecular systems exhibit only quantum yields of 0.034 % for [**IrOCo**]PF_6 and 0.018 % for [**IrthCo**]PF_6. The comparison with other literature-known Ir-Co systems is not possible at this point for various reasons: Artero and Fontecave determined the quantum yield during the hydrogen evolution experiment and the group of Elias reported two dyads, but one dyad showed no emission and the other one had a quantum yield calculated with a different reference compound.[127,131,132] However, the second

Table 6.2: Summarized photophysical properties of the iridium precursors and the Ir-Co dyads measured in CH_2Cl_2 at room temperature.

System	λ_{abs} (ϵ) [nm] ($M^{-1}\cdot cm^{-1}$)	λ^a_{em} [nm]	τ^b [ns]	ϕ^c [%]
[**Irth**]PF_6	256 (85154), 265 (85949), 296 (75211), 370 (26786), 413 (10609), 468 (1652), 499 (898)	588	211	0.059
[**IrthCo**]PF_6	258 (127009), 268 (115596), 300 (70665), 333 (41108), 374 (26696), 468 (1652), 502 (992)	572	172	0.018
[**IrO**]PF_6	254 (66595), 268 (70753), 334 (18764), 382 (9778), 412 (6063), 470 (1201)	576	314	0.713
[**IrOCo**]PF_6	251(106944), 264 (117468), 273 (103097), 333 (25689), 376 (16997), 470 (1464), 512 (845)	592	247	0.034

a) λ_{em} were measured at an excitation wavelength of 260 nm
b) Excited state lifetimes were determined with TCSPC
c) λ_{ex}=450 nm; [$Ir(ppy)_2(phen)$]PF_6 was used as reference substance (ϕ= 14.0 %), measured in degassed CH_2Cl_2.[172]

dyad of the Elias group showed the same tendency and the emission is quenched through the coordination to the cobaloxime.[131]

As last fluorescence method, the excited state lifetimes are determined under the application of the TCSPC technique. The equations, necessary for the data evaluation, were already introduced in Chapter 4.3.3. Through the assembly of the iridium and cobalt units, τ is decreased for both one-component systems. The excited state degrades faster due to an improved electron transfer from the PS to the CAT, which finally results in a shorter emission lifetime. Hence, the hypothesis of a faster, improved intramolecular electron transfer is further supported. It would also imply a reduced hydrogen evolution ability for the oxygen-bridged dyad [**IrOCo**]PF_6 compared to [**IrthCo**]PF_6 due to the higher τ (247 ns *vs.* 172 ns). This will be discussed later in Chapter 7.2.2 with regard to the photocatalytic hydrogen evolution experiments. While the excited state lifetime for [**Irth**]PF_6 is determined with 211 ns, the corresponding oxygen-bridged iridium complex exhibits a slightly longer lifetime with 314 ns. Compared to **PS1** (τ= 234 ns), the reference complex for the photosensitizers introduced in Chapter 4.3, the lifetime of the ether-containing system is slightly prolonged.[226]

6.4 Electrochemistry

For a discussion of the electrochemical properties the two dyads and their corresponding iridium complexes are characterized by cyclic voltammetry. All samples were prepared with a concentration of 1 mM and measured at room temperature in deaerated MeCN with tetrabutylammonium nitrate (TBAN) as supporting analyte un-

der an argon atmosphere. All peaks are quoted relative to the ferrocene/ferrocenium couple (Fc/Fc^{+}). A three electrode arrangement was used consisting of a Pt working electrode, Ag/ $Ag(NO)_3$ reference electrode and a Pt wire as counter electrode. The potentials, which were obtained from the CVs, are summarized in Table 6.3 and the spectra are shown in Figure 6.9.

The pure cobaloxime catalyst **Co3** is also plotted in Figure 6.9 for an easier identification of the catalyst-based signals in the dyad CVs. However, starting with the iridium-based oxidation signals. The potentials of the Ir^{III+}/Ir^{IV+} oxidations are quite similar with 0.87 V–0.90 V for all four iridium-containing complexes. For the thiophene-bridged systems an additional oxidation process at 1.20 V ([**Irth**]PF_6) and 1.21 V ([**IrthCo**]PF_6) is present. This peaks are assigned to thiophene-based oxidations.[187] The cobaloxime-centered oxidation potentials at 0.73 V–0.77 V are assigned to an oxidation of the dmgH ligands.[198]

Table 6.3: Summarized electrochemical data for both Ir-Co dyads, the corresponding iridium complexes and **Co3** reference complex measured in MeCN and referenced to the ferrocenium couple.

System	E_{Ox} [V] (Δ E[mV])	E_{Red} [V] (ΔE [mV])
Co3	0.73 (79)	-1.00[a], -1.50 (83)
[**IrO**]PF_6	0.89 (130)	-1.70 (58), -2.29 (136)
[**IrOCo**]PF_6	0.90 (78), 0.77 (77)	-0.92[a], -1.46 (81), -1.68 (65), -2.29 (53)
[**Irth**]PF_6	1.20[b], 0.89 (133)	-1.70 (75), -2.04 (107), -2.25[a]
[**IrthCo**]PF_6	1.21 (78), 0.87 (52), 0.75 (96)	-0.95[a], -1.47 (102), -1.74 (102), -2.03 (57), -2.20 (73)

a) $E_{p,a}$ b) $E_{p,c}$

The first reduction occurs at -1.00 V for **Co3**, -0.92 V for [**IrOCo**]PF_6 and -0.95 V for [**IrthCo**]PF_6. They are assigned to an irreversible reduction of Co^{III+} to Co^{II+}. This change of the oxidation state is followed by a release of the axial chloride ligand.[201–203] For the second reduction from Co^{II+} to Co^{I+} the potentials of the dyads and the reference cobaloxime are again slightly different. The reduction process occurs at -1.50 V for **Co3**, -1.46 V for [**IrOCo**]PF_6 and -1.47 V for the thiophene-bridged system. These results show that the pyridine-containing iridium complexes influence the cobalt-centered redox potentials. The connection of the Ir-Co units lead to an anodic shift of both, oxidation and reduction potentials. It is also observed that this effect is more pronounced for the oxygen-bridged dyad compared to [**IrthCo**]PF_6.

The ligand-centered reductions, which occur at more negative potentials are also affected by the molecular environment. Therefore, an influence of the cobalt catalyst is visible. The first ligand-based reduction for the oxygen-bridged [**IrOCo**]PF_6 system is shifted from -1.70 V to a more positive potential with -1.68 V, while the second

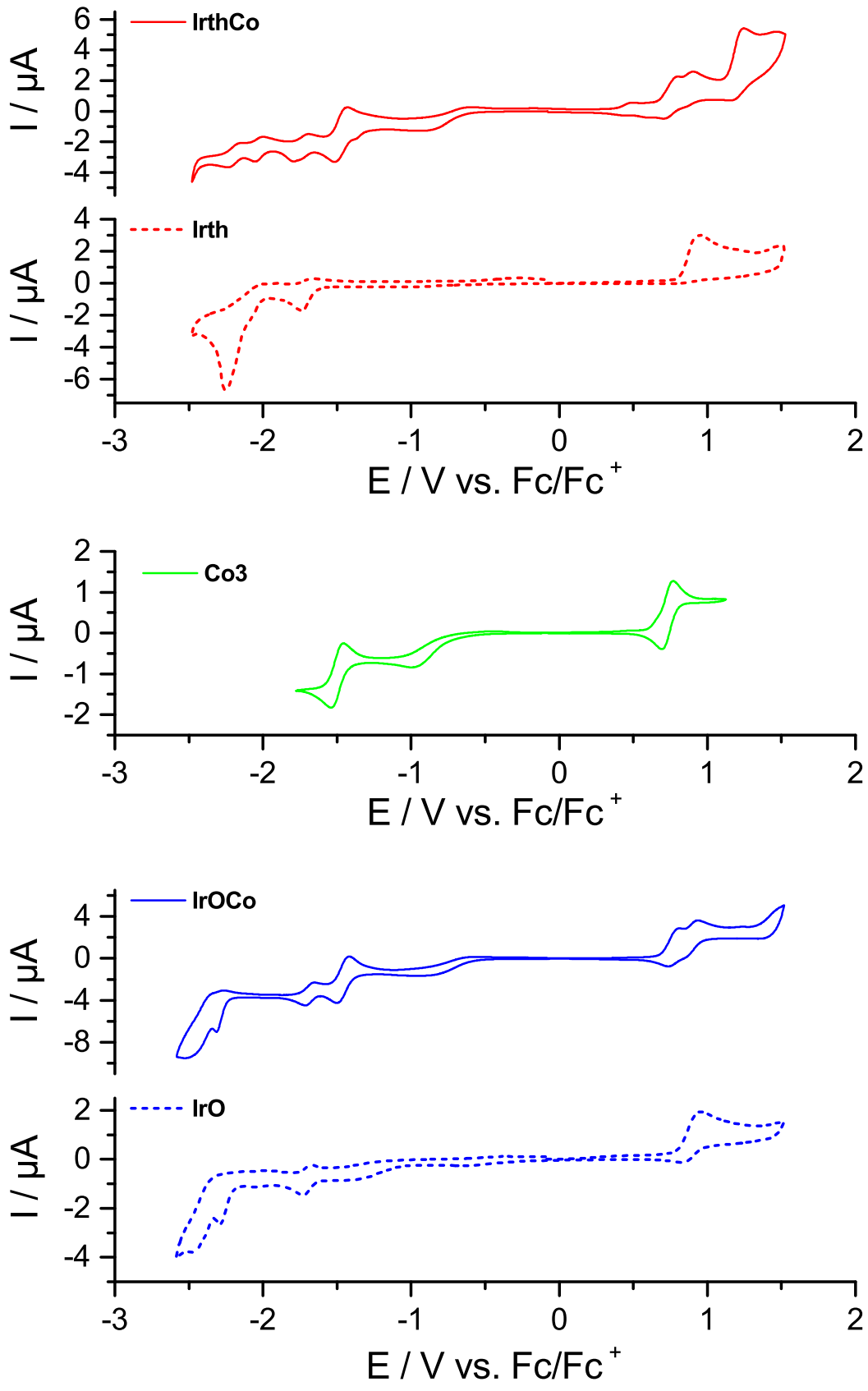

Figure 6.9: CV spectra of both dyads, [**IrthCo**]PF_6 and [**IrOCo**]PF_6, the corresponding iridium precursors, [**Irth**]PF_6 and [**IrO**]PF_6, and **Co3** measured in MeCN.

potential remains unchanged at -2.29 V after the coordination to the cobalt. The second one-component system, containing the thiophene bridge [**IrthCo**]PF_6 shows the same reduction behavior. The potential for the first ligand-reduction (-1.70 V) stays the same compared to [**Irth**]PF_6. In contrast, the second reduction potential is slightly less negative (-2.03 V) compared to [**Irth**]PF_6 with a potential of -2.04 V. The CV of this ligand exhibits a third reduction process, which shows the highest effect on the coordination to the cobalt center with a change in the potential from -2.25 V to -2.20 V.

It can be summarized that both metal centers, iridium and cobalt, influence the redox potentials of the other metal. While the iridium-centered oxidations stay nearly unchanged after the coordination of the cobalt, the effect is more pronounced for the reduction processes that are assigned to ligand-based reductions. Opposed to the effect that cobalt has on the iridium center, the iridium complex show a strong influence on the cobalt redox processes. Both one-component CVs share less negative potentials compared to the precursor compounds [**Irth**]PF_6, [**IrO**]PF_6 and **Co3** which is caused by the electron-withdrawing character of both metal centers. These results were also observed for other iridium-cobalt and ruthenium-cobalt one-component systems that are reported in the literature.[129,131,132]

7 Iridium-Cobalt One-Component Systems in Photocatalytic Proton Reduction

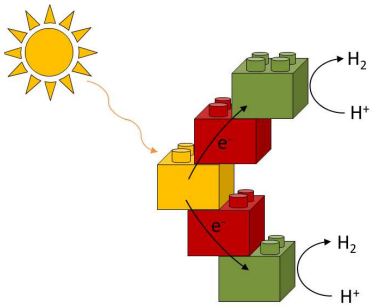

7.1 Photocatalytic Proton Reduction Catalysis

After the synthesis, and the spectroscopic and electrochemical characterization of [**IrthCo**]PF_6, [**IrOCo**]PF_6 and the iridium precursors, they were introduced to the photocatalytic hydrogen evolution experiments. They were tested on the same apparatus as described in Chapter 5.1.1 and the data evaluation was done as described in Chapter 5.1.2. The results were confirmed by twofold determinations, and the evolution of hydrogen was confirmed by GC analysis. Only the catalyst based TON is calculated differently for the dyads. One iridium-cobalt system contained two catalytic units and therefore, the TON is divided by two to obtain the real turnover number for one catalytic center.

$$TON_{CAT} = \frac{\frac{V_{corr}}{V_m H_2}}{2 \cdot n(dyad)} = \frac{n(H_2)}{2 \cdot n(dyad)} \tag{7.1}$$

The calculation for TON_{PS} was already explained in Chapter 5.1.2 in Equation 5.2. For the dyads, n(PS) is substituted by n(dyad). In a first step, the parameters, which resulted in hydrogen evolution with the iridium-cobalt two-component systems, were transferred to the iridium-cobalt one-component-systems. Unfortunately, for the dyads no gas evolution was detected under the application of the two-component parameters. Hence, new conditions must be found, which lead finally to the desired hydrogen evolution. This behavior of supramolecular Ir-Cobaloxime systems towards the application of water as proton source was already observed for the other literature-known dyads.[127,131,132] The application of water facilitates the dissociation of the pyridine-cobalt coordination and leads to a reduced activity.[56,133,134] In a second attempt, the conditions of the Elias group were tested for [**IrthCo**]PF_6 and [**IrOCo**]PF_6. Elias *et al.* published in 2017 an iridium-cobalt dyad that was tested with a concentration of 0.1 mM in MeCN, 0.05 mM HBF_4 and 0.5 M TEOA.[132] Under the application of these conditions, it was possible to achieve hydrogen evolution

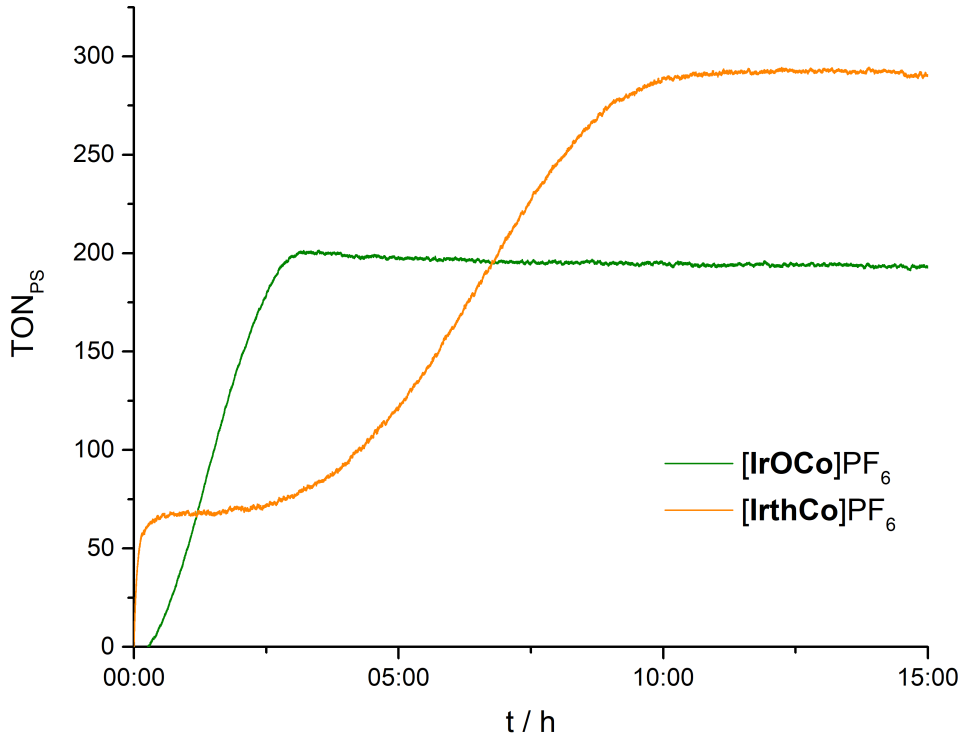

Figure 7.1: Proton reduction experiments of [**IrthCo**]PF_6 and [**IrOCo**]PF_6. The one-component samples contained 0.1 mM dyad in 20 mL MeCN with 0.5 M TEOA and 0.05 M HBF_4.

for both dyads. It is worth mentioning that the proton source was changed due to the adjusted conditions. While water is used as proton source in the experiments with the two-component systems, the dyads need a more acidic proton source which is provided here by HBF_4. Hence, the term water splitting or water reduction is wrong for these systems and will be replaced by the more general term proton reduction.

The first hydrogen evolution curves that were obtained with the Elias conditions are shown in Figure 7.1. With a photosensitizer-based TON of 293, the trimetallic system with the thiophene bridge ([**IrthCo**]PF_6) shows a surprisingly high activity. Considerably less active is the oxygen-bridged system [**IrOCo**]PF_6 with a TON_{PS} of 200. The thiophene and oxygen bridge must cause these different results since all other components and conditions were equal in both experiments. It is not the first time that the nature of the bridging ligand is discussed as a key compound to influence the electron transfer from the PS to the CAT.[51,128,129,227,228] One theory is that the thiophene-linked dyad ([**IrthCo**]PF_6) with the fully conjugated scaffold provides a more efficient intramolecular electron transfer from the excited photosensitizer to the catalyst. Another hypothesis focuses on the oxygen-bridged system and assumes a slowed down electron transfer within [**IrOCo**]PF_6 caused by the electronegative oxygen. It is alternatively possible that a reversed reaction occurs after the donation of the electron by the photosensitizer, and the electron gets

re-accepted by the photosensitizer. Without other analytical methods like transient absorption spectroscopy, it is not possible to clarify the mechanisms that influence the electron transfer within both systems.

The shape of the hydrogen evolution curves is interesting and partly unusual. While the curve shape of [**IrOCo**]PF_6 is as expected with a high slope at the beginning and afterward a fast decreasing hydrogen evolution characterized by a plateau, the other dyad [**IrthCo**]PF_6 shows a different behavior. The system evolves hydrogen for a short time and is then nearly inactive for 3.5 h and subsequently, the hydrogen evolution restarts. This delayed hydrogen evolution is unusual for molecular photocatalytic systems. There are two different theories what caused this behavior: First, the system degrades during the induction period or formed *in situ* the active species, which then evolves the hydrogen. This seems unlikely because [**Irth**]PF_6 (**PS8** in the previous Chapters), the precursor of the [**IrthCo**]PF_6 dyad, shows a similar behavior in the two-component experiments (see Chapter 5). **PS8** was submitted to mass spectrometry after the water splitting experiments and was still unchanged after 20 h under irradiation with Xe light. The second theory is based on the molecular scaffold of the dyad, especially the structure of the connection between PS and CAT. DiSalle and Bernhard observed a similar behavior for an iridium complex as photosensitizer with the structure $[Ir(ppy)_2(N\hat{}N)]^+$ with a bipyridine with terminal pyridine groups as diimine ligand and $[Rh(bpy)_2Cl_2]Cl$ as molecular catalyst. The same photosensitizer combined with K_2PtCl_4, which forms colloidal nanoparticles during the catalysis, showed the typical hydrogen evolution curve without the induction period. Unfortunately, they did not explain this behavior.[108] The assumption made here is that the conjugated ligand scaffold in combination with these molecular rhenium and cobalt catalysts hampers the electron transfer to the catalyst. It is possible that it is a phenomenon that arises due to the delocalization of the excited electron. But the scientific explanation stays unclear up to now and must be investigated again in future projects. The group of Mei Wang reported a one-component system consisting of a porphyrin PS and a cobaloxime CAT, which were connected *via* an entirely conjugated linker. They also reported a hydrogen evolution curve that showed an induction period, but they also did not explain the behavior.[52]

After the photocatalytic experiments, the solvents were removed and the samples were analyzed by mass spectrometry. The spectra show, that both dyads are destroyed during the measurement. The stability-limiting factor is the cobaloxime unit of the supramolecular assemblies. For [**IrthCo**]PF_6 the mass of the precursor complex **Irth** is found with 1055.17 m/z. The cobaloxime complex seems to be destroyed. Neither the mass signal for $Co(dmgH)_2Cl$ nor any other sign of the cobalt species is identified in the spectrum. For the oxygen-bridged dyad [**IrOCo**]PF_6, neither the iridium complex **IrO** nor the cobalt complex are intact. The mass analysis shows

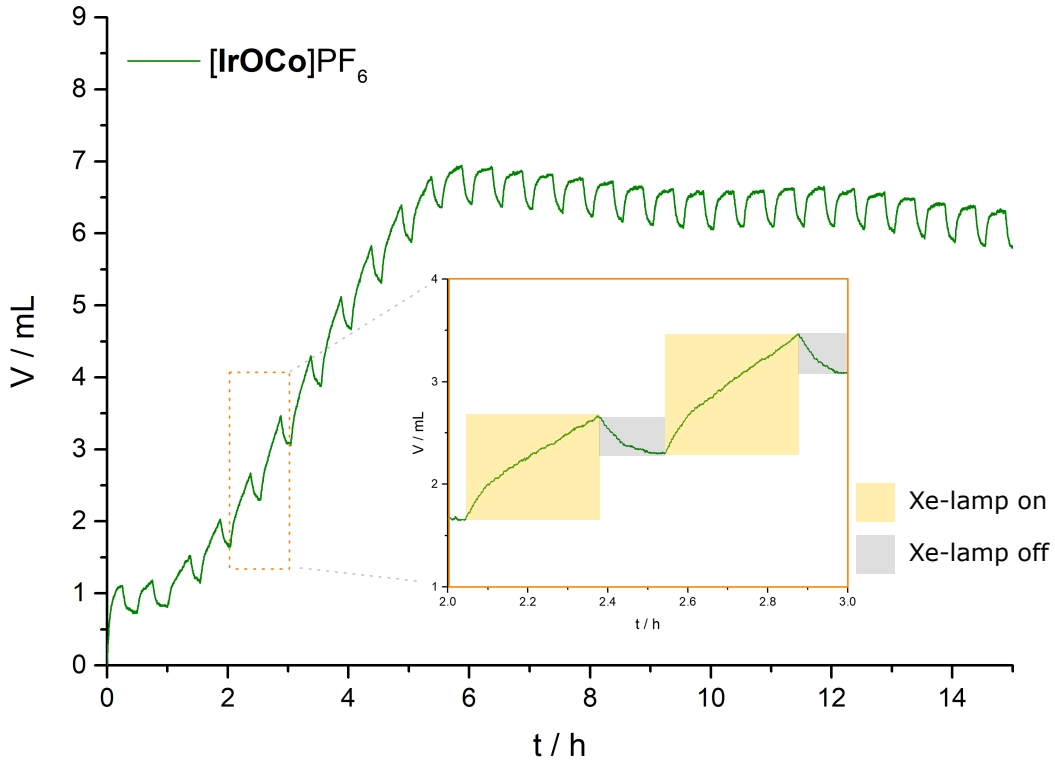

Figure 7.2: Photocatalytic experiment during which the light was turned on and off periodically. Conditions: 0.1 mM [**IrOCo**]PF_6 in 20 mL MeCN with 0.5 M TEOA and 0.05 M HBF_4.

only the signal for $[Ir(ppy)_2]^+$, while the irradiation with Xe light destroyed the cobalt complex entirely.

7.1.1 Influences of Device Parameters

This short section will deal with two changes that were made on the photocatalytic proton reduction apparatus and tested in two separate experiments. Before the tests were carried out, it was already expected that they would influence the hydrogen evolution ability.

In the first experiment, it should be ensured that the hydrogen evolution with the synthesized one-component systems is indeed a photocatalytic process and requires the illumination with light to be active. For this reason, the shutter control of the xenon lamp was programmed to open and close periodically. The obtained "zigzag" hydrogen evolution curve is shown in Figure 7.2. The irradiation cycle was programmed on 20 minutes, while the dark cycle lasted 10 minutes. The increase of evolved gas, which is observed after the lamp was turned on, is attributed to a hydrogen evolution caused by [**IrOCo**]PF_6. But there is also an expansion of the gas volume due to a rise of temperature within the reactor caused by the high-energy

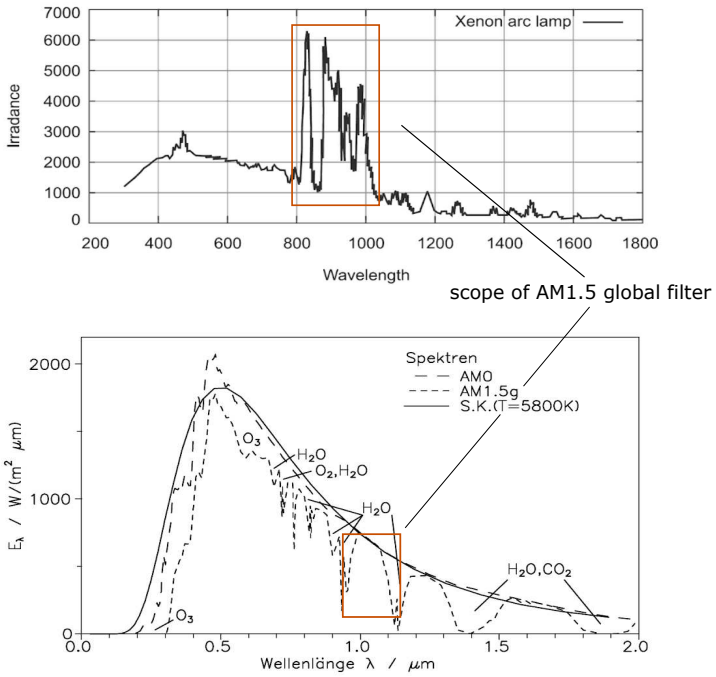

Figure 7.3: Top: Exemplary spectrum of a xenon arc lamp. Bottom: Solar spectrum at different regions on earth. Marked in orange is the scope of an AM1.5 global filter.[229,230]

xenon lamp. When the shutter is closed, the gas evolution curve shows a negative slope. As a temperature rise results in an expansion of gas, a temperature drop lead to a contraction of the volume within the apparatus. Additional to this contraction, the hydrogen evolution stops in the dark. For this system, no TON is calculated due to a challenging correction under the application of the blank volume, but the overall evolved volume is compared to the sample of [**IrOCo**]PF_6, which was irradiated for the whole duration of the experiment, and the evolved volumes correspond to each other. The experiment was also conducted with [**IrthCo**]PF_6. The dyad with the thiophene linker shows the same behavior under irradiation and during the dark cycle. Therefore, it is concluded that the hydrogen evolution with these iridium-cobalt dyads is a photocatalytic process, which would not proceed without the irradiation of light. For the second experiment, the irradiation wavelength was manipulated for a better understanding of the optimum parameters regarding the required wavelengths for the photocatalytic hydrogen evolution. However, before the results are presented here, a few general remarks about the xenon light source. Xenon light is widely used in scientific applications for photocatalytic reactions that should simulate the solar spectrum.[10,231–235] The xenon and solar spectrum are shown in Figure 7.3. Examination of both spectra shows the high similarity of the xenon and the solar spectrum. An AM1.5 global filter is used for our light source to eliminate the peaks between 800 nm–1000 nm, which are missing in the natural solar spectrum. AM referred to air mass and 1.5 corresponds to an zenith angle. That is the angle under which the solar irradiation hits the earth, of ~49 °. The

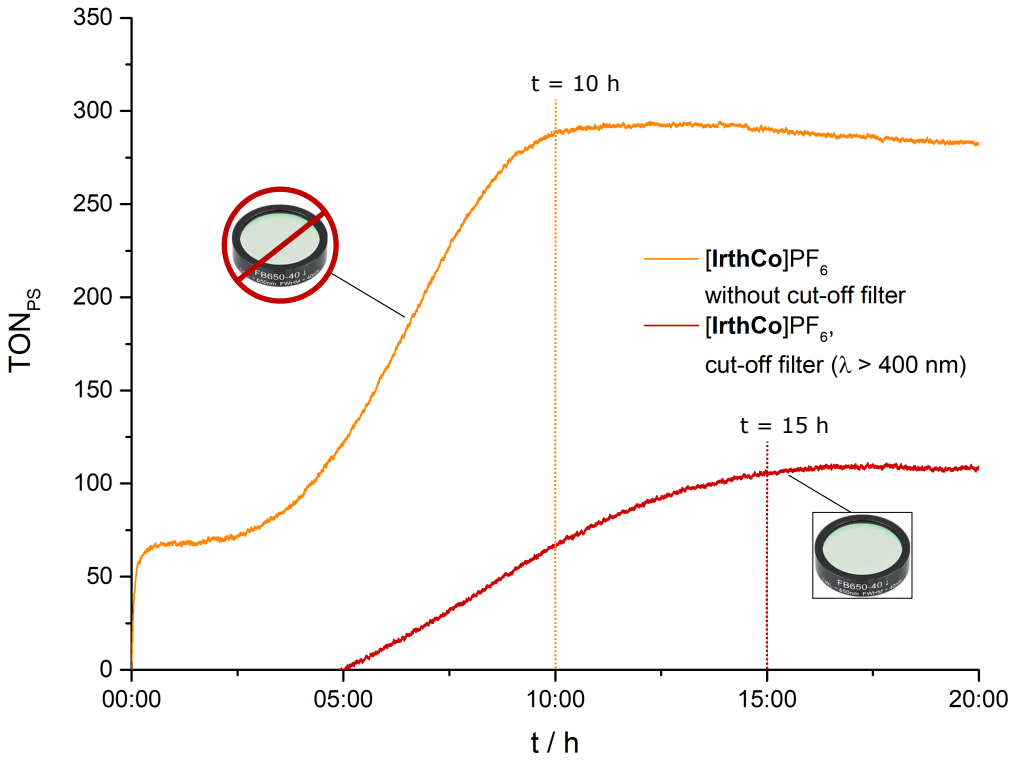

Figure 7.4: Photocatalytic experiment with and without cut-off filter (λ= 400 nm). Conditions: 0.1 mM [**IrthCo**]PF_6 in 20 mL MeCN with 0.5 M TEOA and 0.05 M HBF_4.

value of AM1.5 is valid at many places on earth with an average temperature of 25 °C. Under the application of the "AM1.5 global filter", the xenon lamp generates a spectrum, which is close to the solar spectrum on earth.[229,230]

Additionally to the AM1.5 global filter that was used in every experiment a 400 nm longpass filter was installed. For this trial, the longpass filter was introduced between the xenon lamp and the reaction vessel. This filter cuts off all wavelengths that are shorter than 400 nm and the sample will be irradiated with light that has wavelengths longer than 400 nm. It is known that iridium complexes suffer from photodegradation during the irradiation with light. The iridium complexes with the general formula $[Ir(C^N)_2(N^N)]^+$ loose the N^N ligand and coordinate solvent molecules, which was already explained in Chapter 2.3.2. The degradation of the iridium photosensitizers is enhanced by the irradiation with UV light and therefore, it can be assumed that the introduction of the 400 nm longpass filter results in a system with a longer lifetime.[43,88,204] The obtained gas evolution curve for this experiment is depicted in Figure 7.4. The evolution curves of [**IrthCo**]PF_6 with the application of the cut-off filter and without it are shown for a better comparison. As expected, the sample, which was irradiated with Xe light under application of the cut-off filter (λ > 400 nm) shows a prolonged lifetime of 15 h compared to the 10 h lifetime of the standard sample. Unfortunately, the filter sample exhibits also a

reduced activity. This is caused by the high absorption of the dyads in the UV region, while at wavelengths longer than 400 nm only minor absorptions are detected. The UV spectra of the one-component systems are already shown in Chapter 6.3.1. By cutting off the required wavelengths, it is possible to demonstrate that the dyad exhibits a prolonged lifetime, but also a reduced hydrogen production. Interestingly, the induction period disappeared in this sample. This suggests that exposure of the sample to UV light is a trigger for the unnatural shape of the control curve.

7.1.2 Influences of Concentrations

As already done for the iridium-cobalt two-component systems, the consequences of concentration changes of the key compounds are evaluated. Therefore, the dyads were exposed to a higher proton source concentration during the photocatalytic experiments. The concentration of HBF_4 was doubled for this reason. The result of this attempt under the application of [**IrOCo**]PF_6 is shown in Figure 7.5. The activity is lowered to a photosensitizer-based TON of 145 with a concentration of 0.1 M HBF_4 (0.05 M HBF_4, TON= 213). The experiment shows that HBF_4 is not the hydrogen evolution-limiting factor in the photocatalytic proton reduction under these conditions. Since it is known that the activity of cobaloximes strongly depends on the pH value of the used solvents, this could be one reason for a decreased gas evolution, because the solution is more acidic with an increased amount of HBF_4.[68,126,210,236,237]

Unfortunately, it was not possible to determine the pH of the proton reduction sample due to the absence of an aqueous medium and, pH electrodes and pH paper were developed for the measurement in aqueous media. This is a problem, which is already known in literature, but no solution was found yet to determine the pH of non-aqueous solutions accurately.[210] Another explanation for the less active system is the protonation of the two cobalt glyoximato ligands. Through the incorporation of two additional hydrogen atoms, the oxidation state of cobalt will change, which might lead to a decomposition of the catalyst.[203] The experiment with the enhanced acid concentration also shows

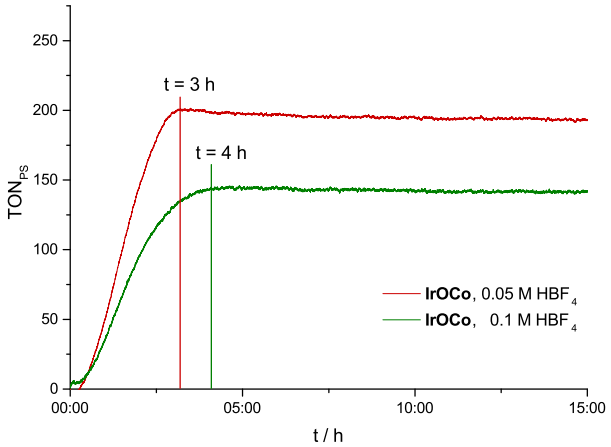

Figure 7.5: Photocatalytic hydrogen evolution experiment with an increased HBF_4 concentration.

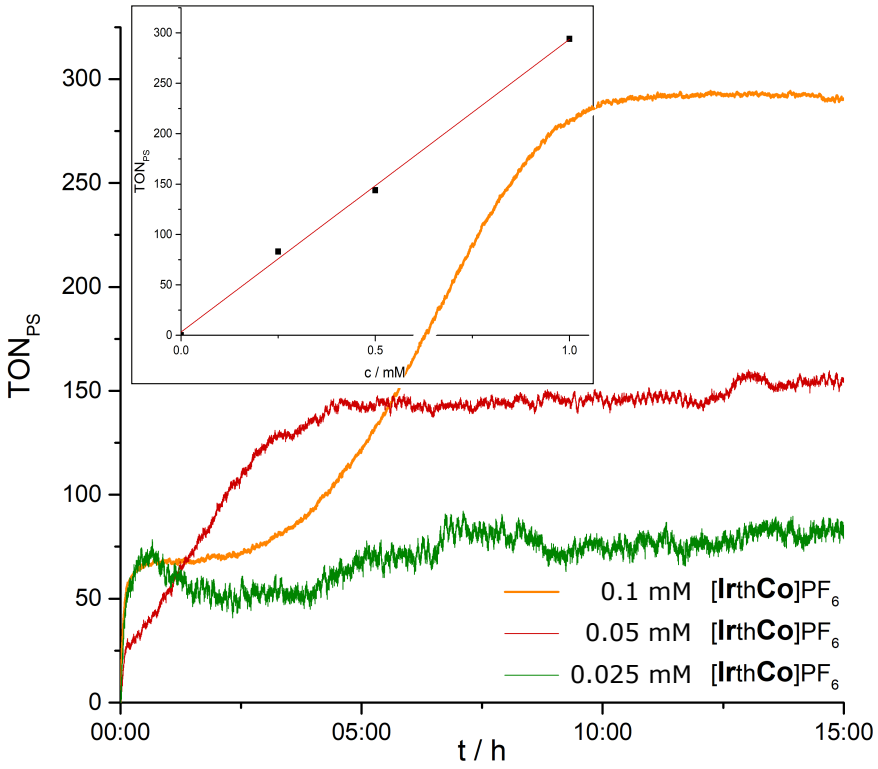

Figure 7.6: Proton reduction experiment with [**IrthCo**]PF_6 measured with different concentrations 0.1 mM (orange), 0.05 mM (red) 0.025 mM (green) in 20 mL MeCN with 0.5 M TEOA and 0.05 M HBF_4. Inset: Linear concentration dependency of hydrogen evolution.

a slightly prolonged lifetime from 3 h to 4 h until the dyad [**IrOCo**]PF_6 degrades. The higher HBF_4 concentration also inhibits the degradation of the catalyst, which is the reaction-limiting component. Therefore, explanation one with the non-optimum pH range appears to be the more suitable explanation. The experiment was also conducted with [**IrthCo**]PF_6, which shows the same result with a decreased hydrogen production that is also prolonged.

During the next experiments, the concentration of the one-component systems was altered to get a more precise understanding of the mechanisms during the hydrogen evolution under irradiation. The standard samples were prepared and measured with a concentration of 0.1 mM dyad. Therefore, the concentration was reduced for the next samples to 0.05 mM and 0.025 mM and these measurements show already a high signal-to-noise ratio, especially the 0.025 mM sample. Due to this fact, the concentrations were not further reduced to guarantee reliable results. The hydrogen evolution curves for [**IrthCo**]PF_6 are shown in Figure 7.6. It is not possible to obtain a smoother curve for the lowest concentration experiment because the environmental changes has a stronger influence on this measurement compared to the other ones. It is interesting that the induction time and therefore the unusual curve shape, which is evident at a concentration of 0.1 mM, vanishes at lower concentrations. The

reason for this behavior stay unclear, but might be a concentration effect that is only present at certain concentrations. Another result that is obtained from the concentration measurements is that the hydrogen evolution does not collapse at the lowest concentration. If there was a doubt that the electron transfer in this iridium-cobalt systems is not intramolecular, this should convince the most skeptics. In case of an intermolecular transfer, the hydrogen evolution would have decreased more drastically at the minimal concentration. However, since there is a sufficient amount of hydrogen which is evolved at a concentration of 0.025 mM, it is a significant indicator for an intramolecular acting system. The measurements with the second dyad [**IrOCo**]PF_6 provides the same results.

There is a second result, which is obtained from the concentration-dependent measurements. The inset in Figure 7.6 shows a linear correlation between the applied concentration of [**IrthCo**]PF_6 and the evolved hydrogen volume. This correlation was observed before, for the two-component systems introduced in Chapter 5. Another two-component system reported by the Eisenberg group consisting of a Pt(II) photosensitizer and a cobaloxime catalyst showed the same behavior.[68] The analysis of the measurements reveal that the hydrogen evolution proceeds *via* a heterolytic mechanism for the cobalt center. As already mentioned in the background Chapter in Equation 2.16, for the generation of one molecule hydrogen one active cobalt center is necessary. Whereas in a second-order reaction, two cobalt centers are required for the evolution of one molecule hydrogen. If the reactions of [**IrthCo**]PF_6 or [**IrOCo**]PF_6 would be of second-order, a square dependence of the gas evolution on the dyad concentration should be obtained.[238] The results of the concentration-dependent measurements are an essential step forward in figuring out the overall reaction mechanism for hydrogen evolution with these iridium-cobalt dyads.

7.1.3 One-Component- vs. Two-Component System

Since there is an ongoing discussion whether two-component- or one-component systems are the more efficient approach for the photocatalytic hydrogen production, this should be tested with the synthesized iridium-cobalt systems in this last section.[3,51,52,205,239] While it is known, that the multi-component systems act *via* the intermolecular electron transfer, it is discussed for the supramolecular assemblies whether they act also *via* the inter- or *via* the intramolecular electron transfer pathway.

In this section only [**IrthCo**]PF_6 and the corresponding multi-component system were tested. For the oxygen-bridged dyad [**IrOCo**]PF_6, a suitable two-component-system is lacking. Therefore, **PS6** and **Co3** were chosen as analogue two-component-system for the [**IrthCo**]PF_6 dyad. Both systems were tested under identical conditions

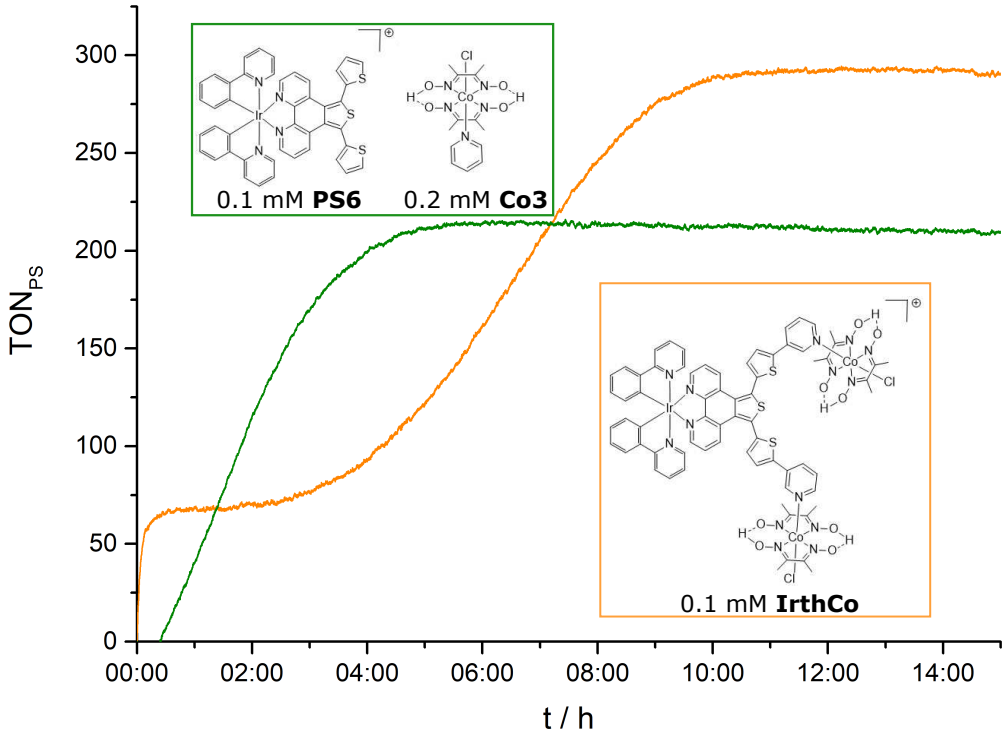

Figure 7.7: Comparison of photocatalytic proton reduction experiments of one- and two-component system [**IrthCo**]PF_6 and **PS6**/**Co3**. Dyad: 0.1 mM two-component system: 0.1 mM PS, 0.2 mM CAT; both in 20 mL MeCN, 0.05 M HBF_4 and 0.5 M TEOA.

with the equivalent concentrations. The concentration of the cobalt catalyst was twice as high as the photosensitizer concentration due to a ratio of iridium:cobalt within the dyad of 1:2. The results of the experiment are shown in Figure 7.1. The two-component system shows the usual curve shape, which is attributed to the missing of the pyridyl groups on the diimine ligand. The comparison of both approaches shows that the one-component system achieved a higher TON as the two-component system. The combination of **PS6** and **Co3** reaches only a TON of 213 compared to the 293 of [**IrthCo**]PF_6. While [**IrthCo**]PF_6 presumably transfers the electron from the PS to the CAT *via* the intramolecular pathway, the two-component system (**PS6**, **Co3**) performs the electron transfer through an intermolecular process. The concentrations of the individual components were low during this test, which makes a successful collision of PS and CAT more unlikely and therefore, the two-component approach less active. The intermolecular electron transfer is strongly diffusion-dependent. In contrast to that, the electron transport in the supramolecular arrangements is directional and not influenced by the compound concentrations or used solvents. These results indicate two different electron transfer mechanisms for the contrary approaches. Here, it can be concluded that the one-component system is more suitable for a more efficient electron transfer, but examples from the literature also show comparisons in which the results are swapped and the two-component system is more efficient.[51]

This is one interpretation of the obtained data. Another one raises serious doubts about the integrity of [**IrthCo**]PF_6 during the catalysis. The dyad shows a strong initial hydrogen evolution during the first 30 minutes, but then for approximately two hours, nearly no hydrogen is evolved. After this plateau time, the hydrogen generation restarts and produced more gas as the two-component system. These data can also suggest that the system decomposes after the first 30 minutes and formed during the "plateau"-time a new photosensitizer and catalyst which is then responsible for the proton reduction. This hypothesis is based on the curve shape and, when the initial TON_{PS} is subtracted from the overall reached TON_{PS} (293-67) the new turnover number is 226, that is nearly the same as the TON of the two-component system with TON_{PS} = 213. Therefore, it is not possible to exclude the hypothesis that the original dyad gets destroyed through excitation and a new dyad is formed *in situ* to evolve hydrogen.

7.2 Spectroscopic Characteristics of Proton Reduction Systems

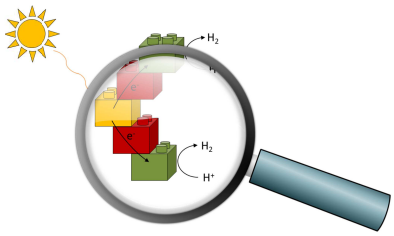

7.2.1 UV-Vis Spectroscopy during Proton Reduction

During the photocatalytic hydrogen evolution, it was also tried to identify the metal species that are responsible for the proton reduction during the process. Figure 7.8 shows the irradiation experiment of [**IrOCo**]PF_6, which was conducted with the same concentrations of the individual components as the photocatalytic proton reduction experiments. The sample was irradiated with a 300 W Xe-lamp and the spectra were recorded at different time intervals. The experiment was also carried out with [**IrthCo**]PF_6 and provided the same results.

Both dyads feature an absorption band at approximately 370 nm. This absorption band became less intense after the beginning of irradiation with Xe light and is assigned to the initially introduced Ir^{III+}–Co^{+III} dyad. After 46 minutes of irradiation, a new absorption band appears at 425 nm. This new signal, which rise during the irradiation time, is correlated to a cobalt(II) species.[57,211,240] After further irradiation with xenon light, a second absorption band rise at 590 nm. This signal features a strongly broadened and less intense shape. Due to comparisons with other cobaloxime complexes, which were also investigated with UV-Vis spectroscopy, the absorption band is assigned to a Co(I) species or a Co(III) hydride. Both are possible key compounds for the hydrogen evolution under the application

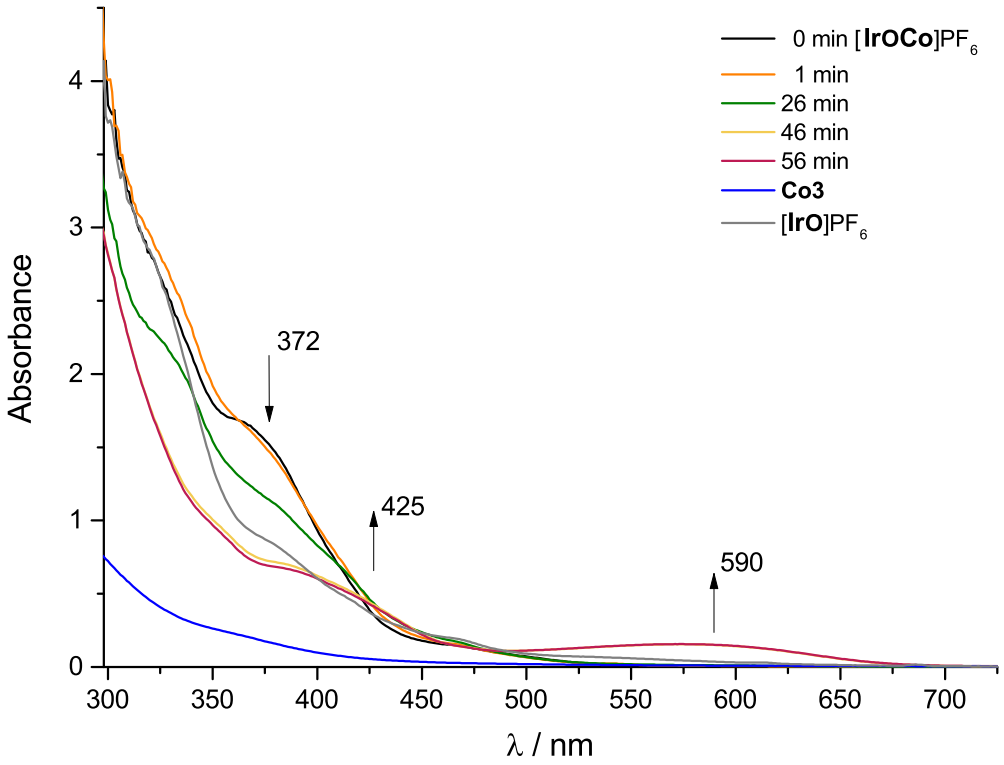

Figure 7.8: UV-Vis irradiation spectra of [**IrOCo**]PF_6 recorded in different time intervals. [**IrO**]PF_6 and **Co3** were plotted as reference spectra. Conditions: 0.1 mM [**IrOCo**]PF_6, 0.1 M in deaerated MeCN with 0.05 M HBF_4 and 0.5 M TEOA at room temperature.

of cobaloximes.[210,215,216] To ensure that the species are only formed under photocatalytic conditions with precisely this Ir-Co system, the experiment was repeated with the corresponding iridium precursor complex [**IrO**]PF_6 and the cobaloxime **Co3** in separate samples. As expected, this control measurements show no sign of the absorption bands, which were grown during the irradiation of the [**IrOCo**]PF_6 sample. Hence, it is concluded that both metal centers are essential for the formation of an active hydrogen-evolving species. As mentioned above, the experiment was also conducted with [**IrthCo**]PF_6. The signals are identical for the measurements, but the time scale is prolonged. For example, the absorption band at 590 nm appeared after 3.5 h of irradiation, compared to less than one hour for [**IrOCo**]PF_6. Considering the hydrogen evolution curves that are shown in the previous Chapter, the results of the UV-Vis irradiation experiment and the proton reduction measurements are consistent; during the hydrogen evolution, the thiophene-bridged system shows a much longer reaction time compared to the oxygen-bridged system.

To ensure that the species at 425 nm arose from a Co(II) complex and the absorption band at 590 nm from neither a Co(I) species or a Co(III) hydride, the dyad was also submitted to spectroelectrochemistry. The spectroelectrochemical measurements were carried out in MeCN at a potential of -1 V and -1.6 V to detect the changes

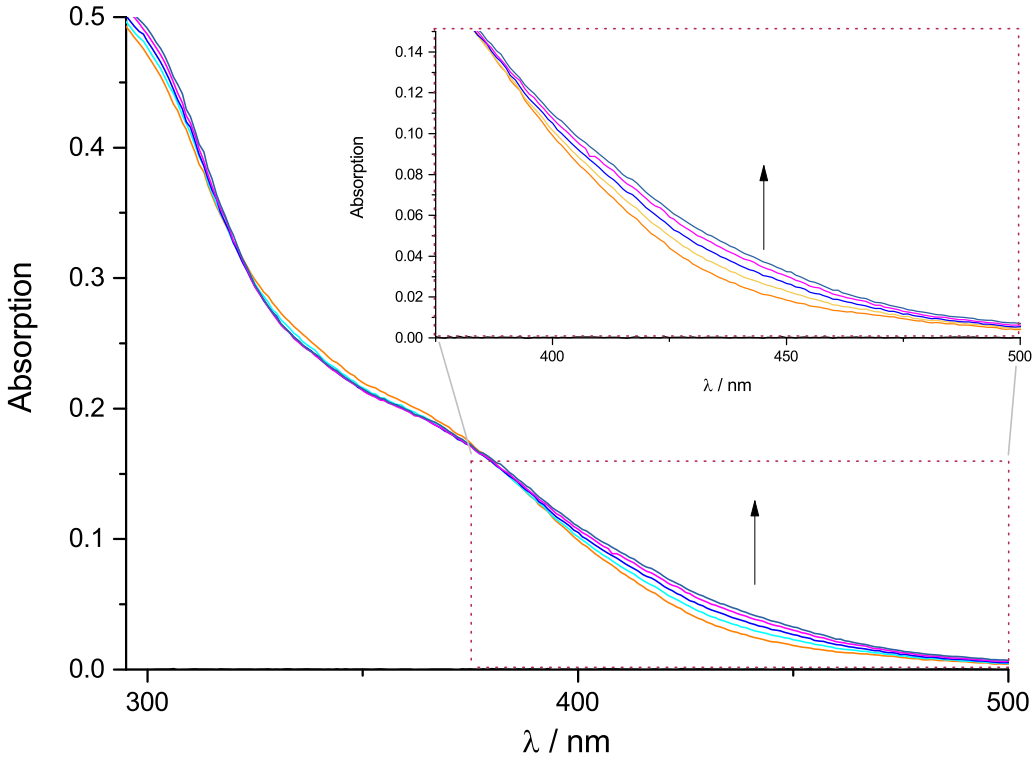

Figure 7.9: Spectroelectrochemistry of [**IrthCo**]PF_6 (c= 1 mM) at a potential of -1 V in deaerated MeCN under argon atmosphere and room temperature.

caused by the reduction of the cobalt complex. Figure 7.9 depicts the reduction of Co(III). At approximately 435 nm, an absorption band appears during the measurement and the species at 425 nm of the before carried out UV-Vis irradiation experiment is confirmed as a Co(II) species. Unfortunately, the second electrochemical measurement shows no sign of a Co(I) or a Co(III)H. After a thorough analysis, the reason was identified: A measurement in pure MeCN provide no proton source for the formation of an active hydrogen-evolving catalyst.

7.2.2 Fluorescence Spectroscopy

For the iridium-cobalt dyads, it were also essential to identify the quenching mechanisms of the excited iridium complexes. Therefore, quenching experiments with TEOA were conducted. Figure 7.10 shows the spectra obtained through the fluorescence quenching of [**IrthCo**]PF_6 in dependence of the TEOA concentration. The samples were prepared with a fixed concentration of $2.5{\cdot}10^{-5}$ M and the TEOA concentrations were altered between 0 M–$2.5{\cdot}10^{-2}$ M. All samples were submitted to at least three freeze-pump-thaw cycles. A concentration of $1.3{\cdot}10^{-3}$ M TEOA was equivalent to 500 eq TEOA, which corresponds to the ratio of [**IrthCo**]PF_6:TEOA (1:500) that is used in the photocatalytic proton reduction experiments.

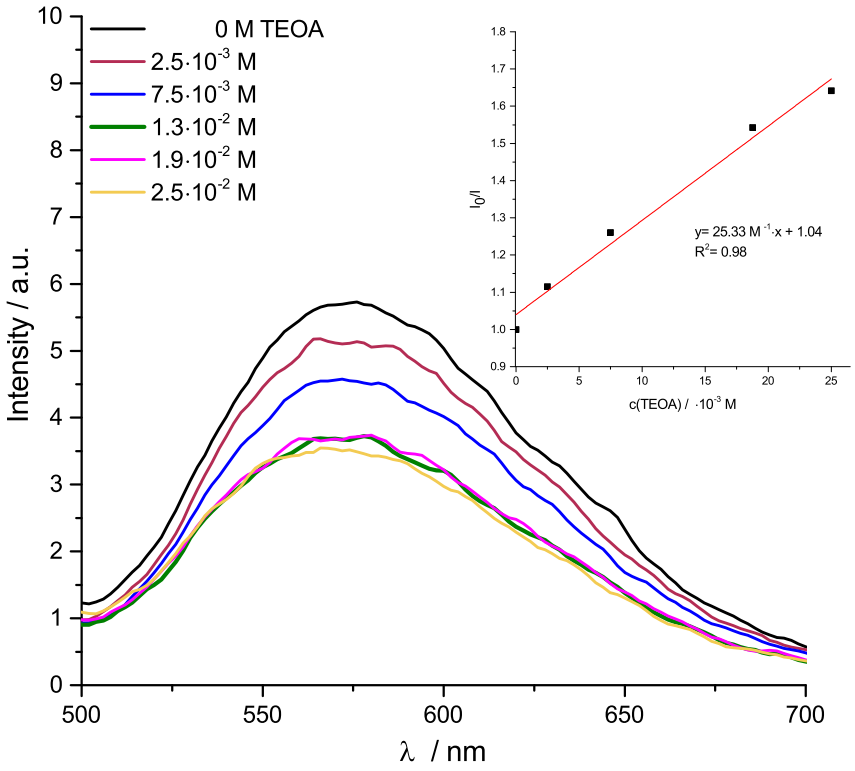

Figure 7.10: Fluorescence quenching of [**IrthCo**]PF_6 ($2.5{\cdot}10^{-5}$ M) with a varying TEOA concentration from 0–$2.5{\cdot}10^{-2}$ M in MeCN. Inset: Stern-Volmer plot for the quenching experiments.

Usually, quenching experiments are performed with either the sacrificial reductant (reductive quenching) or the catalyst (oxidative quenching). Through the permanent connection of photosensitizer and catalyst, it is not possible to vary the catalyst concentration without adding additional catalyst to the samples and this would not be equivalent to the reduction measurements. Therefore, only quenching experiments with TEOA were conducted. Assuming a dynamic quenching behavior, the system consisting of [**IrthCo**]PF_6, MeCN and TEOA shows a good linearity ($R^2 = 0.98$) in the calculated Stern-Volmer plot. Under the application of the Stern-Volmer-equation (2.8 in Chapter 2.3.1) and the excited state lifetime of 172 ns, the bimolecular quenching rate constant was calculated. With a k_q of $1.5{\cdot}10^8$ $M^{-1}s^{-1}$ TEOA shows only moderate quenching. The diffusion constant k_{diff} for MeCN is taken from literature with $2.2{\cdot}10^{10}$ $M^{-1}s^{-1}$.[218] The quenching constant of TEOA is two magnitudes smaller as the acetonitrile diffusion constant. It can therefore be concluded that the quenching with TEOA is a diffusion-limited process, which is disadvantageous opposed to the intramolecular quenching process triggered by the cobalt catalyst.[201] This is also observed by considering the quenching graphs. If the sacrificial donor completely quenches the excited state of the iridium complex, no emission should be detected. The maximum quenching that is achieved was just 35.3 %. It was also discovered that the quenching rate reaches a plateau at a concentration of $1.3{\cdot}10^{-3}$ M and higher concentrations lead not to higher quenching

rates. It can therefore be summarized that the quenching of the excited iridium state is generated by an electron or energy transfer from the PS to the cobaloxime unit of the supramolecular system. This further supports the hypothesis of a directional electron transfer of this iridium-cobalt systems.

7.3 Summary

This section summarizes the results of the previous Chapter, dealing with the iridium-cobalt one-component systems. Finally, it was possible to synthesize two different iridium-cobalt dyads. One of these systems was synthesized starting with an already in Chapter 4.3 introduced iridium complex, **PS8** or [**Irth**]PF_6. For the second compound ([**IrO**]PF_6), a new iridium complex with terminal pyridyl groups that were connected to the N^N ligand *via* an oxygen-bridge was synthesized. Both iridium complexes were incorporated *via* a covalent linkage to the catalytic cobaloxime units. The dyads and the precursor iridium complexes were characterized by standard methods like NMR spectroscopy, mass spectrometry, and elemental analysis. To ascertain that the spectroscopic and electrochemical properties were suitable for the photocatalytic proton reduction experiments, they were also analyzed by cyclovoltammetry, UV-Vis- and fluorescence (standard emission, excited state lifetime) spectroscopy.

The two dyads were first tested as hydrogen-evolving devices under the same conditions as the iridium-cobalt two-component systems, but unfortunately they showed no activity in the photocatalytic water splitting. Therefore, the proton source water was substituted by HBF_4 as a stronger proton source. The photocatalytic proton reduction was carried out under the same conditions as the Elias group reported for their iridium-cobalt dyads.[131,132] With these adjustments, it was possible to generate highly active iridium-cobalt systems. [**IrthCo**]PF_6 achieved a photosensitizer-based TON of 293 (10 h), and the oxygen-bridged system [**IrOCo**]PF_6 reached a TON of 203 (3 h) before the dyads degraded. Only four other iridium-cobalt dyads are known in the literature. Two were reported by the Elias group in 2016 and 2017, one by the Fontecave group in 2008, and one was recently published in the PhD thesis of Regina Meinhard from our group.[127,131,132,241] Only the Fontecave system achieved a higher TON (with regard to the PS) of 420 (15 h). The systems of Elias exhibited TONs of 224 (35 h) and 251 (3 h), and the system of R. Meinhardt achieved a TON of 12.5. Hence, [**IrthCo**]PF_6 is the second most active system that appears in the literature, while [**IrOCo**]PF_6 shows the second worst activity. If the TONs were calculated at the same time as [**IrthCo**]PF_6 degraded (10 h), then the system of Fontecave reached a TON of approximately 320, and the Elias systems reached a strongly reduced TON for one system of 80 and for the other one of 251.

The measurement of the Ir-Co dyad of R. Meinhardt was terminated after three hours; therefore, this TON has been excluded from the discussion. Even after this ranking, a comparison of the individual systems is complicated and must be treated with caution. Neither measurement was performed under identical conditions as the other ones. The solvent, sample concentrations, sacrificial donor, or light source were changed.

However, it is possible to compare both systems that were presented here. The thiophene-bridged system showed a higher activity under identical conditions compared to [**IrOCo**]PF_6. The intention behind the introduction of thiophene groups as a bridging unit was to use the excellent ability of thiophene groups to act as electron transfer agents already used in semiconductors.[140–144] This assumption that an optimized electron transfer is possible with molecular systems bearing thiophene groups for the photocatalytic hydrogen evolution was right. The oxygen-bridged system was chosen for two reasons: First, they are more easily synthesized compared to the first system and, second, the system was not entirely conjugated and therefore, well-suited for a linker comparison. These two dyads showed that the conjugated [**IrthCo**]PF_6 dyad is beneficial for photocatalytic proton reduction. This might also be reasoned by a shorter, excited state lifetime of 172 ns for the iridium unit after the irradiation with light compared to 247 ns for [**IrOCo**]PF_6.

The more active iridium-cobalt compound was also compared to the corresponding two-component system. It was shown that the system with the connection of the individual units exhibited superior properties (prolonged system lifetime and higher overall activity) in the photocatalytic proton reduction experiments. All analyses that were conducted indicate an intermolecular electron transfer from the PS to the CAT for the two-component system, while the results for the one-component system strongly support the hypothesis of an intramolecular, directional electron transfer. This process is, therefore, no longer diffusion-dependent like the electron transfer of two-component systems.

The mechanistic considerations of the photocatalytic hydrogen evolution of these two dyads revealed that the excited state iridium photosensitizer is mostly quenched through the intramolecular electron transfer with minor contributions of the sacrificial reductant to the quenching process. While the processes on the iridium unit are mostly identified, it is more challenging for the cobaloxime unit. The UV-Vis measurements during the photocatalytic experiment showed the evolution of a cobalt(II) species. After this step, it was not clarified if the second signal belonged to a Co(III) hydride or a Co(I) species. At last, it was shown that the proton reduction proceeded *via* a monometallic reaction pathway. For the evolution of one molecule of hydrogen, one cobalt center was necessary.

8

Summary

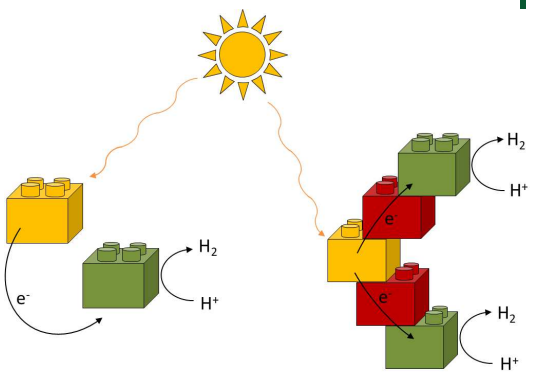

The aim of this thesis was the synthesis, characterization, and evaluation of new, partly non-noble, molecular photocatalytic systems for the hydrogen evolution. The focus of the first part led to the design and synthesis of a novel kind of neutral chelating diimine ligand. The basic structure of this ligand included a 1,10-phenanthroline with a fused thiophene on the center ring of the phenanthroline. Only one patent is reported with a similar system consisting of a fused 2,9-phenanthroline-thiophene structure.[242] There are also only a few examples with fused pyrrole rings on a phenanthroline ring, which is the highest similarity that can be found in literature.[170,243] However, all these systems were synthesized *via* other synthesis routes. This fused ring structure was attractive for our application due to a coplanar arrangement caused by the aromatic character of the molecule. The planar structure should later result in an enhanced electron transfer in the light-driven hydrogen evolution.

Due to the completely novel structure of the ligand, many efforts were made to obtain the desired product. In the end, a modification of the Hinsberg-thiophene synthesis yielded the desired fused-ring structure. Based on this structure, it was possible to synthesize six other new ligands by a direct conversion of the starting material **L4**. In a broader sense, the reaction products again yielded six additional novel diimine ligands. The molecules that were successfully used as ligands for the iridium complex synthesis are shown in Figure 8.1. All diimine structures were characterized by NMR and IR spectroscopy, mass spectrometry, and elemental analysis. UV-Vis spectra were additionally recorded for the diimine systems that were introduced to the iridium complex synthesis, and finally, it was possible to obtain single crystal x-ray structures for **L5**, **L6**, **L7**, and **L9**. Unfortunately, these crystal structures did not support the theory of a complete coplanar arrangement for the ligands. Although the fused diimine structure showed a nearly coplanar arrangement with a maximal deviation of 4.66 ° for **L6**, the extended heterocyclic rings exhibited a large twist out of the plane. Certainly, through the coordination of the iridium center, it might still be possible to achieve the coplanar arrangement of all ligand structures.

The conversion of the synthesized ligands yielded a small library of nine photosensitizers. Only the first iridium complex (**PS1**) was already reported in literature, but it

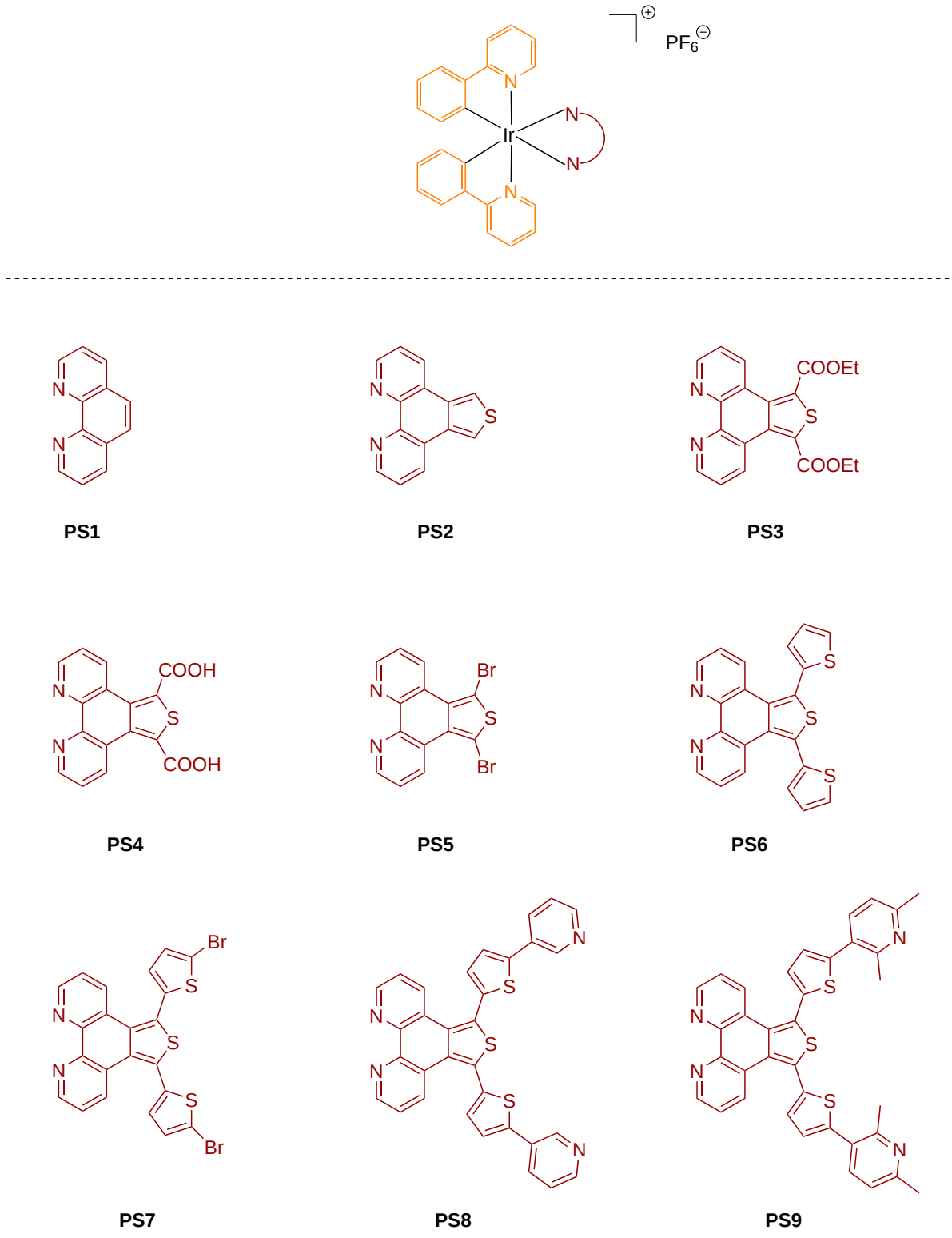

Figure 8.1: A selection of nine different ligands and iridium photosensitizer synthesized during this thesis. Except **PS1**, all ligands and complexes were literature unknown.

was only used as a reference complex for a better classification of the new iridium systems.[60,175,180,185]

The final iridium complexes are shown again in Figure 8.1. They were characterized by the standard procedures, NMR and IR spectroscopy, elemental analysis, and mass spectrometry. The spectroscopic and electrochemical properties were determined by means of UV-Vis, many fluorescence spectroscopy methods, and cyclic voltammetry. It was additionally possible to obtain a single crystal x-ray structure analysis for **PS2**, **PS5** and **PS6**. Unlike the hypothesis that was made for the design of these novel fused diimine ligands, they still showed no coplanar arrangement in the second sphere of the diimine structure. It was assumed at the beginning that this would support a more efficient electron transfer from the PS to the CAT. However, the new iridium complexes exhibited good activity in combination with the cobaloxime **Co3** in the photocatalytic water splitting experiments. The cobaloxime complex was chosen after a catalyst screening of non-noble iron and cobalt compounds. After the analysis of the water splitting data, it was possible to work out the desired structure–activity correlation between the photosensitizer structure and the evolved amount of hydrogen, as shown in Figure 8.2.

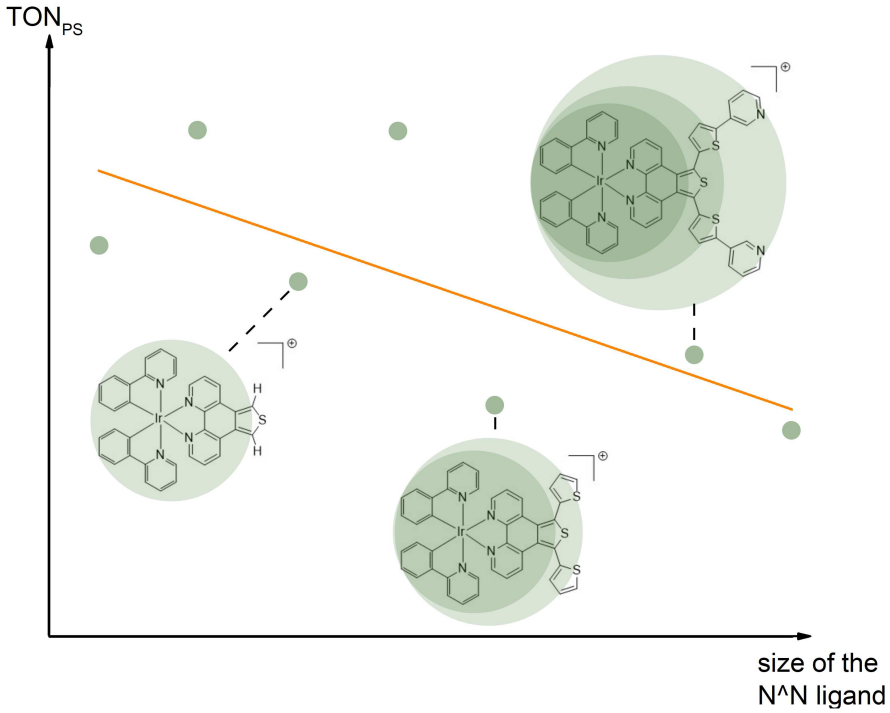

Figure 8.2: Correlation of the photosensitizer-based TON *versus* the size of the diimine ligand coordinated to the iridium center.

With the increasing size of the diimine ligand, the ability to generate hydrogen *via* photocatalytic water splitting was reduced. The size of the N^N ligand was equal to the number of coordination spheres. **PS2**–**PS5** boasted one coordination sphere,

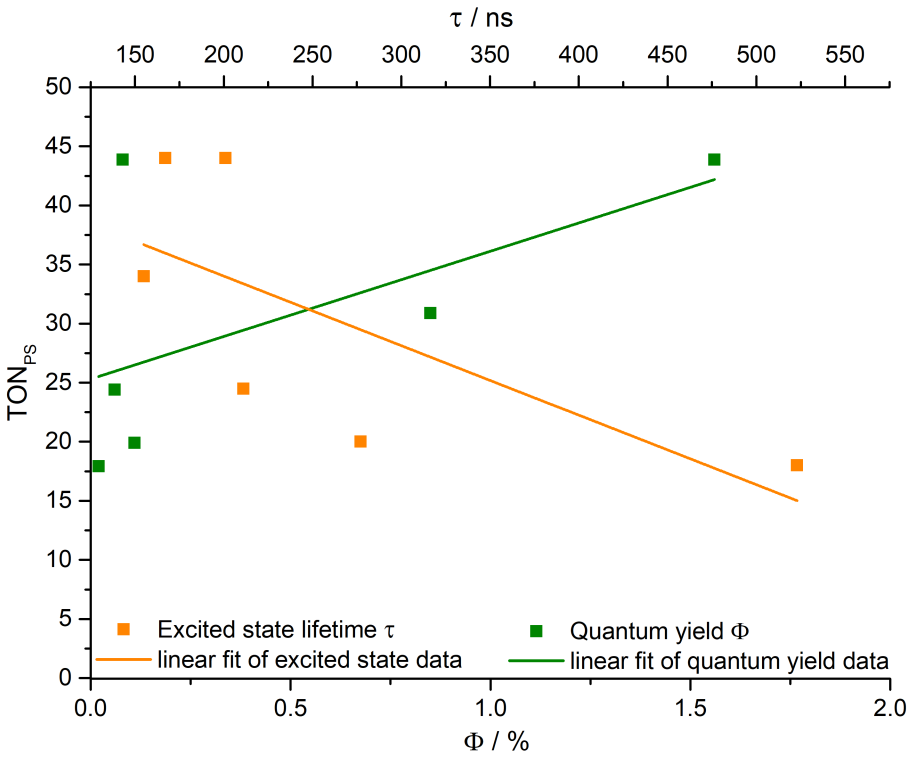

Figure 8.3: Data plot of the photosensitizer-based TON *versus* the excited state lifetime τ and the quantum yield Φ.

PS6 and **PS7** two, and **PS8** and **PS9** three coordination spheres. The degree of planarity was also associated with the number of coordination spheres. While the smallest photosensitizers had a nearly planar diimine backbone, the other complexes showed a twist in the second sphere on the diimine ligand. It can also be assumed, based on the ligand crystal structure of **L9**, that there is an additional twist in the third coordination sphere for the largest photosensitizers. Therefore, it is acceptable to postulate an enhanced electron transfer ability for **PS2**–**PS5** with their coplanar orientation. The results showed that the more extended the diimine structure got, the more reduced the hydrogen evolution capacity.

The spectroscopic and electrochemical properties of the photosensitizers were analyzed with regard to their water splitting results to work out possible relationships. The excited state lifetime τ and the quantum yield ϕ of the iridium complexes showed a correlation with the calculated photosensitizer-based TONs for the hydrogen evolution. The activity of the investigated iridium-cobalt two-component systems decreased with a prolonged excited state lifetime of the photosensitizer. The electron transfer to the catalyst seemed to have become more unfavorable, which might be reasoned by recombination processes or side reactions that became more attractive with larger τ. In contrast to that the quantum yield ϕ showed a linear behavior toward the TON_{PS}. A lower quantum yield is associated with an increased amount of non-radiative decays of the excited iridium complexes. The

correlation plots of the spectroscopic properties with the evolved hydrogen volume are illustrated in Figure 8.3.

The last part of this thesis was dedicated to the synthesis of iridium-cobalt one-component systems. **PS8** was an ideal candidate for this through the terminal free nitrogen donor functionalities on the diimine ligand. The iridium complex was successfully brought to synthesis with a cobaloxime precursor $Co(dmgH)(dmgH_2)Cl_2$. The isolated bimetallic system [**IrthCo**]PF_6 possessed one light-absorbing iridium center and two proton-reducing cobalt centers. As a counterpart to this fully conjugated dyad, a second one ([**IrOCo**]PF_6) was synthesized, bearing two oxygen bridges at the previous positions of the second sphere thiophene rings. The systems were again analyzed by common standard procedures (NMR, Mass spectrometry, EA, IR, UV-Vis, fluorescence and CV).

Both systems were introduced into the photocatalytic water splitting experiments, but unfortunately, no hydrogen was generated. One hypothesis was that water facilitated the ligand (dmgH) exchange on the catalyst part as well as the dissociation of the cobalt-pyridine bond.[133] The proton source was changed afterward to a more acidic one with HBF_4. Under these conditions, hydrogen evolution was achieved for both systems. The not entirely conjugated [**IrOCo**]PF_6 showed an activity that was reduced by 31 % compared to [**IrthCo**]PF_6. A filter experiment with an UV cut-off filter that cuts off all UV irradiation showed that UV radiation led to a faster degradation of the dyads, but these wavelengths are also necessary to push the systems to a higher overall activity. Lastly, [**IrthCo**]PF_6 was compared to the corresponding two-component system (**PS6**+**Co3**). The dyad showed an activity that was 38 % higher than the activity of the two-component system. The more active Ir-Co assembly might use an intramolecular pathway for the electron transfer from the PS to the CAT, while the e^- transfer of the separated system is based on intermolecular processes. It shall not be concealed that there are doubts about the integrity of [**IrthCo**]PF_6 while the photocatalytic reaction is in progress. The proton reduction curve of [**IrthCo**]PF_6 showed a fast hydrogen evolution within the first 30 minutes. After an additional induction period of two hours, the H_2 evolution restarted. If the first evolution part was subtracted from the overall TON of 293, a TON of approximately 226 was obtained. This was nearly identical to the two-component result with a TON of 203. Hence, some questions remain unanswered regarding the molecular structure of [**IrthCo**]PF_6 present during the photocatalytic experiments and, consequently, the electron transfer mechanism.

However, the results showed that the Ir-Co dyads were able to compete with the literature-known systems, which might deal with similar problems. Only an Ir-Co system of Fontecave *et al.* showed a higher activity as the [**IrthCo**]PF_6 dyad. Two other linked structures were reported by the Elias group, but they were less active

Table 8.1: Summarized results of proton reduction experiments reported here and elsewhere.

Entry	System	TON_{PS}	Conditions	Source
1	**IroxaCo**	420	0.55 mM dyad, 600 eq TEA [TEAH]BF4 in acetone	Fontecave *et al.*[127]
2	**IrthCo**	293	0.1 mM dyad, 0.05 M HBF_4, 0.5 M TEOA in MeCN	this work
3	**IrpicCo**	251	0.1 mM dyad, 0.05 M HBF_4, 0.5 M TEOA in MeCN	Elias *et al.*[132]
4	**IrterpyCo**	224	0.1 mM dyad, 0.1 M HBF_4, 1 M TEOA in MeCN	Elias *et al.*[131]
5	**PS6/Co3**	213	0.1 mM **PS6**, 0.2 mM **Co3**, 0.05 M HBF_4, 0.5 M TEOA in MeCN	this work
6	**IrOCo**	203	0.1 mM dyad, 0.05 M HBF_4, 0.5 M TEOA in MeCN	this work
7	**IrthCo**	110	0.1 mM dyad, 0.05 M HBF_4, 0.5 M TEOA in MeCN, cut-off filter (<400 nm)	this work

than [**IrthCo**]PF_6 yet slightly more active than [**IrOCo**]PF_6. A ranking of all known Ir-Co systems is given in Table 8.1.

The mechanistic investigations for the supramolecular assemblies suggested similar processes as for the iridium-cobalt two-component systems: The iridium complex was quenched by the catalyst unit with minor contributions to reductive quenching through TEOA as sacrificial reductant. Therefore, the systems seemed to be quenched by a mixture of oxidative and reductive pathways with a focus on the oxidative mechanism. On the catalyst part, a monometallic involvement of cobalt in the hydrogen evolution was confirmed. It was also shown by UV-Vis spectroscopy that during the catalysis, a Co(II) species was built while the existence of whether it was a Co(III)H or a Co(I) species or both species simultaneously was not absolutely clarified. As done before with the two-component systems, the excited state lifetime τ showed a correlation with the photosensitizer-based TON while the quantum yield Φ did not support the linear relationship that was ascertained for the two-component systems. The quenching rates of the iridium precursors and the Ir-Co dyads suggested another pathway to return to the ground state after excitation, which might be of non-radiative nature like an energy or electron transfer.

Based on the results obtained from this thesis, many improvements in iridium-cobalt systems are possible and necessary to make them more attractive for their wider applications as hydrogen evolution systems. The suggestions derived from the results obtained in this thesis should be divided and considered for the three building blocks PS, bridge, and CAT, starting with the PS. Long-term applications must spare the expensive and limited metals like iridium. Organic molecules or systems that are based on cheap and non-noble metals are of interest to the application, but there is a lot of research to conduct to make it economic and usable on an industrial scale. An objective that is reachable on a smaller timescale is the improvement of iridium photosensitizer stability. This can be achieved by a more stable ligand structure like tridentate molecules, which protect the complex against a fast degradation triggered by the irradiation with light.

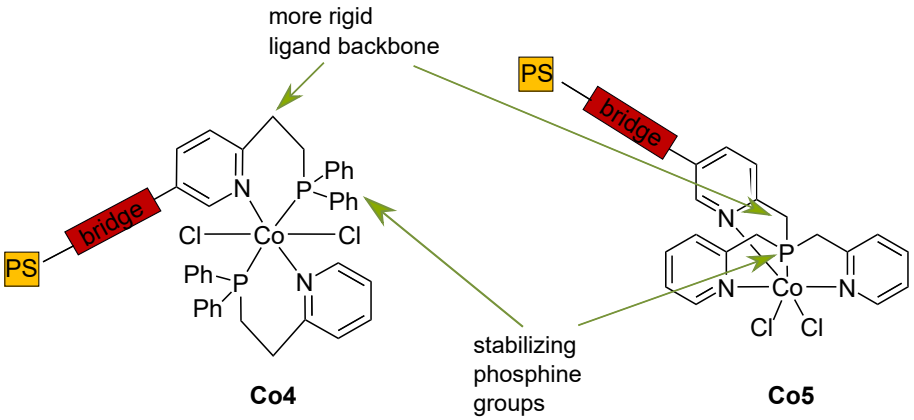

Figure 8.4: Two possible improvements toward a more stable cobalt catalyst.

The bridge should remain as shown here. Through the thiophene structure, it is possible to adsorb the system on a surface. This makes the dyads more attractive for the technical application due to a better separation from the reaction media and the products.

The catalyst part requires the most improvement because it was the limiting building block for the photocatalytic hydrogen evolution. The literature already showed approaches to obtain more stable cobaloxime catalysts like the substitution of the dmgH ligand by BF_2-derivatives or the addition of phosphines that stabilize the intermediate formed during the hydrogen evolution. Since the reasons for the catalyst degradation are known as 1) ligand degradation and 2) Co-pyridine dissociation, these are the parts that have to be adjusted first before other improvements could be made. Figure 8.4 shows two possible structures that might improve the stability of these cobalt complexes.

9 Experimental

9.1 General Laboratory Working Techniques

Some of the syntheses were conducted excluding contact with air and moisture. Therefore it was worked under inert atmosphere applying standard Schlenk-technique. Solvents (CH_2Cl_2, $CHCl_3$, dioxane, toluene, THF, ethanol, methanol, acetone) were dried under the application of literature procedures and stored over molecular sieves or used from a *MBraun* solvent purification system MB SPS 800 (Et_2O, MeCN, DMF). The utilization of Schlenk procedures is marked in the appropriate synthesis procedures. The chemicals for the conducted syntheses were purchased from abcr, Alfa Aesar, Fisher Scientific, Sigma-Aldrich or TCI.

9.2 Equipment

Cyclic Voltammetry

Cyclic and square-wave voltammograms were performed on a *Metrohm PAR101* potentiostat in MeCN with 0.1 M NBu_4PF_6 and an analyte concentration of 0.001 mol/L at room temperature with the following three electrode arrangement: Pt working electrode (1 mm diameter), Ag/ 0.01 M $AgNO_3$, 0.1 M NBu_4PF_6 in MeCN as reference electrode and a Pt wire as counter electrode. Ferrocene was added as internal standard after the measurements and all potentials are referenced relative to the Fc/Fc^+ couple. All measurements were carried out under argon atmosphere, with absolute and degassed solvents.

DFT Calculations

The DFT calculations were conducted by Patrick Müller, who is also a member of the Bauer group. All calculations were done with ORCA 3.0.3.[244] The geometries were optimized using the PBEh-3c functional.[245] The Grimme dispersion correction with Becke-Johnson damping was utilized for the calculations. The time-dependent

DFT (TD-DFT) approach was used for the UV-Vis calculations. The calculations utilized all electron scalar relativistic basis sets of triple ζ quality[246] and the ZORA approach[247] to account for relativistic effects. The functional of choice for all TD-DFT calculations was the LC-BLYP functional.[248–250] The RIJCOSX approximation implemented in ORCA was used to speed up the hybrid calculations. The tight convergence criterion was imposed on all calculations.

Elementary Analysis

The elementary analyses were performed on an *Elementar Vario MICRO Cube*.

Fluorescence Spectroscopy

The fluorescence spectra were recorded on a *JASCO FP-8300*. All samples were prepared with five freeze-pump-thaw cycles. Only solvents of spectroscopy grade were used (CH_2Cl_2 (ROTISOLV >99.8 %, UV/IR-Grade/ Carl Roth) or MeCN (SPECTRONORM/VWR)). All samples were measured at room temperature. When not otherwise mentioned, the measurements were conducted applying the following parameters: Extinction and emission bandwidth: 5 nm, response time 10 msec, data interval 0.5 nm and scan speed 500 nm/min.

Gas Chromatography

The gas chromatography were conducted on an *Inficon FUSION* micro gas chromatograph equipped with a TCD detector. An Et-Molsieve 5A column (10 m; 0.25 mm ID) was used. Argon was used as carrier gas. A backflush injector was used with an injector temperature of 90 °C. Samples were taken for 60 seconds from the water splitting apparatus.

IR Spectroscopy

The IR spectra were recorded on a *Bruker Vertex 70* equipped with FT-IR .

NMR Spectroscopy

The spectra were recorded on a *Bruker Avance 500* and a *Bruker Ascend 700* spectrometer with 500 MHz (^{1}H), 125 MHz (^{13}C), 50.7 MHz (^{15}N) and 202.4 MHz (^{31}P). TMS was used as reference (δ=0 ppm) for all chemical shifts on the δ-scale of the ^{1}H and ^{13}C spectra. The ^{1}H spectra were calibrated by using the protons of the solvent as reference peak. The ^{13}C spectra were calibrated with respect to the deuterated solvent peak. Ammonia was used as reference substance (δ = 0 ppm) for ^{15}N spectra and an 85 % aqueous solution of phosphoric acid was used as reference substance (δ = 0 ppm) ^{31}P spectra.

Mass Spectrometry

All samples were measured on a high resolution magnetic sector field mass spectrometer DFS (*Thermo Scientific*). As ionization method, EI was used with 70 eV and an ion source temperature of 200 °C. The second used ionization method was CI with a source temperature of 80 °C and a resolution of R=1000. The third ionization method that was used is ESI. The measurements were performed on a *Waters* quadrupole time-of-flight mass spectrometer "SYNAPT G2". For ESI^{+} measurements MeOH or MeCN were used as solvents.

Time-Correlated Single Photon Counting (TCSPC)

The excited state lifetimes were measured on a *Horiba Ultima-01-DD*. All samples were prepared with a concentration of $2.5{\cdot}10^{-5}$ M and five freeze-pump-thaw cycles. Only CH_2Cl_2 of spectroscopy grade were used for the measurements(ROTISOLV >99.8 %, UV/IR-Grade/ Carl Roth). The measurements were conducted with a 374 nm LASER diode and a minimum of 10000 counts were collected for every measurement. The data analysis was done with the software DAS6 provided by Horiba.

UV-Vis Spectroscopy

UV-Vis absorption spectra were recorded on a *Varian Cary 50* UV/Vis Spectrophotometer at room temperature. Unless otherwise stated, the spectra were recorded with solvents of spectroscopy grade CH_2Cl_2 (ROTIDRY >99.8 %, UV/IR-Grade/ Carl Roth) or MeCN (SPECTRONORM/VWR).

X-ray Single Crystal Structure Analysis

Intensity data for the X-ray single crystal structure analysis were collected on a *Bruker AXS SMART APEX* diffractometer with kryoflex low temperature device. The data was recorded at 130 K with a MoKα radiation of 0.71073 Å. The obtained data were treated with SAINT and SADABS for data reduction and absorption correction.[251] Hydrogen positions were obtained from differential Fourier syntheses and then refined at idealized positions $U_{iso}(H) = 1.2\ U_{eg}(C)$. In some cases, strongly disordered solvent molecules were processed with SQUEEZE.[252,253]

Photocatalytic Water Splitting/Proton Reduction

The water splitting apparatus was cleaned after each measurement with aqua regia and purged afterward with VE water, acetone and ethyl acetate. The apparatus was tested for tightness by pressurizing the whole apparatus and monitor the changes within the reactor with the computer. Afterward the reactor was evacuated three-times and purged with argon. Before the reactions were started the overall volume of the reactor was determined and submitted to the computer program.

For the two-component systems, a solvent mixture of MeCN:H_2O:TEOA (1:1 (20 mL): 5 %vol) was used. Prior to use, the mixture was adjusted to the pH with concentrated HCl or 1 M NaOH and degassed by three freeze-pump-thaw cycles. The PS and CAT amounts were weighted in two separate vials and evacuated for three-times and purged with argon. After adding 10 mL of the solvent mixture to the PS and 10 mL to the CAT vial, the PS solution was added first to the water splitting reactor. Afterward 10 mL of the CAT solution was added and the apparatus was closed and the sample was led alone for five minutes to equilibrate in the dark. Immediately after this five minutes, the measurement was started, by first starting the measurement program and then turn on the Xe lamp. For the one-component systems the process was nearly equivalent. This time only one vial was required to weight in the dyad. The whole solvent mixture (20 mL) was added to the purged vial after the freeze-pump-thaw cycles and the complete solution was added to reactor all at once. The calculation of TON_{PS} and TON_{CAT} is described in the corresponding Chapter 5, and 7. Every measurement was repeated at least twice to guarantee a reproducible result.

9.3 Syntheses

9.3.1 Ligands

Synthesis of 1,10-Phenanthroline-5,6-dione (1)[254]

An ice cold solution of 42 mL concentrated HNO_3 and 80 mL concentrated H_2SO_4 was added dropwise to a mixture of 8.00 g (44.3 mmol, 1 eq) 1,10-phenanthroline and 7.92 g (66.6 mmol, 1.5 eq) KBr. The reaction mixture was stirred for 3 h at 130 °C. The reaction was stopped by pouring the mixture on 700 g ice and neutralize it with 240 mL 16 M NaOH. The aqueous solution was extracted with CH_2Cl_2 (6 x 250 mL). The combined organic layers were evaporated. The yellow crude product was recrystallized from 290 mL EtOH. The pure product was isolated as fine yellow powder.

Yield: 7.54 g (80.8 %)

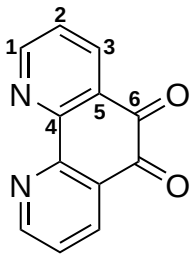

1

^{1}H NMR (500 MHz, $CDCl_3$): δ (ppm) 7.57 (dd, $^3J_{HH}$ = 7.9 Hz, 4.7 Hz, 2H, H^2); 8.47 (dd, $^3J_{HH}$ = 7.9 Hz, $^4J_{HH}$ = 1.9 Hz, 2H, H^3); 9.09 (dd, $^3J_{HH}$ = 4.7 Hz, $^4J_{HH}$ = 1.9 Hz, 2H, H^1).

^{13}C NMR (125 MHz, $CDCl_3$): δ (ppm) 125.6 (CH, C^2); 128.1 (C_q, C^5); 137.3 (CH, C^3); 152.9 (C_q, C^4); 156.4 (CH, C^1); 178.7 (C_q, C^6).

MS-EI: m/z (%) 210.02 (28) $[M]^+$; 182.02 (100) $[M\text{-}2O]^+$.

Elemental analysis: calcd. for $C_{12}H_6N_2O_2$: C, 68.57; H, 2.88; N, 13.33. found: C, 68.29; H, 3.10; N, 13.26.

Synthesis of diethyl 2,2'-thiodiacetate (2)[255]

20.00 g (133.2 mmol; 1 eq) 2,2'-Thiodiacetic acid was added to 196 mL dry EtOH and 8 mL concentrated H_2SO_4. The light yellow solution was refluxed overnight. Afterwards, the solution was cooled down to 0∘C and 30 mL water was added. The aqueous solution was extracted with Et_2O (1 x 100 mL, 4 x 50 mL) and washed with Na_2CO_3 solution (2 x 50 mL). The organic layers were concentrated in vacuum and a light yellow liquid was obtained as product.

Yield: 23.21 g (84.5 %)

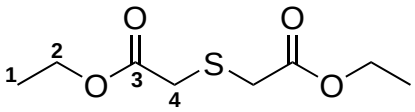

2

^{1}H NMR (500 MHz, $CDCl_3$): δ (ppm) 1.00 (t, $^3J_{HH}$ = 7.1 Hz, 6H, H^1); 3.10 (s, 4H, H^4); 3.89 (q, $^3J_{HH}$ = 7.1 Hz, 4H, H^2).

^{13}C NMR (125 MHz, $CDCl_3$): δ (ppm) 13.8 (CH_3, C^1); 33.3 (CH_2, C^2); 61.0 (CH_2, C^4); 169.31 (C_q, C^3).

MS-EI: m/z (%) 206.00 (28) $[M]^+$.

Elemental analysis: calcd. for $C_8H_{14}S_1O_4$: C, 46.59; H, 6.84; S, 15.54. found: C, 46.55; H, 6.73; S, 15.57.

Synthesis of thieno[3,4-f][1,10]phenanthroline-5,7-dicarboxylic acid (L4)

The reaction was conducted under inert atmosphere. 3.51 g potassium were dissolved in dry MeOH. 5.01 g (23.8 mmol, 1 eq) 1,10-phenanthroline-5,6-dione and 4.99 g (24.2 mmol, 1 eq) diethyl-2'2-thiodiacetate were mixed in 40 mL dry MeOH at 0 °C in a second flask and the potassium methanolate solution was added slowly. During this process the color chanced from yellow to black. The solution was stirred for 3 h at ambient temperature. After this time, a solid was formed. 500 mL water was added to the mixture and the reaction solution was concentrated to 250 mL. The suspension was filtered and 65 mL concentrated HCl was added. The obtained solid was filtered, washed with diethyl ether and dried under vacuum.

Yield: 7.42 g (96.1 %)

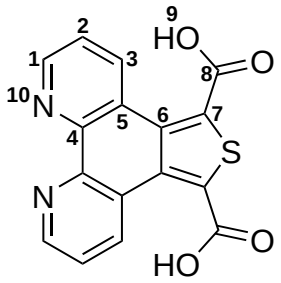

L4

^{1}H NMR (500 MHz, DMSO d_6): δ (ppm) 8.18 (dd, $^{3}J_{HH}$ = 8.5 Hz, 4.9 Hz, 2H, H^2); 9.15 (dd, $^{3}J_{HH}$ = 4.9 Hz, $^{4}J_{HH}$ = 1.4 Hz, 2H, H^1); 10.00 (dd, $^{3}J_{HH}$ = 8.5 Hz, $^{4}J_{HH}$ = 1.4 Hz, 2H, H^3).

^{13}C NMR (125 MHz, DMSO d_6): δ (ppm) 125.7 (CH or C_q, C^2 or C^5); 126.5 (C_q, C^2 or C^5); 132.9 (C_q, C^6 or C^7); 134.0 (C_q, C^6 or C^7); 139.2 (C_q, C^4); 141.5 (CH, C^3); 147.3 (CH, C^1); 163.3 (C_q, C^8).

^{15}N NMR (70.9 MHz, DMSO d_6): δ (ppm) 245.83 (s, N^{10}).

MS-ESI (pos): m/z 325.03 $[M+H]^+$.

ATR-IR ($\tilde{\nu}$ [cm-1]): 3275, 2922, 2353, 1890, 1715, 1691, 1614, 1562, 1537, 1510, 1423, 1351, 1306, 1230, 1198, 1057, 966, 939, 824, 802, 768, 760, 723, 638, 621, 584, 505, 484, 461, 446, 419, 405, 349, 262, 230.

Synthesis of thieno[3,4-f][1,10]phenanthroline (L2)

0.2991 (0.9 mmol) of **L4** was heated in a Schlenk flask containing a cold finger. During this process the color changed from yellow to black and a yellow solid sublimed on the cold finger. The solid was removed and washed with $CHCl_3$. The organic layer was concentrated under vacuum and a light yellow powder obtained.

Yield: 0.19 g (86.1 %)

^{1}H NMR (500 MHz, $CDCl_3$): δ (ppm) 7.56 (dd, $^{3}J_{HH}$ = 8.0 Hz, 4.5 Hz, 2H, H^2); 8.15 (s, 2H, H^7); 8.50 (dd, $^{3}J_{HH}$ = 8.0 Hz, $^{4}J_{HH}$ = 1.7 Hz, 2H, H^3); 9.04 (dd, $^{3}J_{HH}$ = 4.5 Hz, $^{4}J_{HH}$ = 1.7 Hz, 2H, H^1).

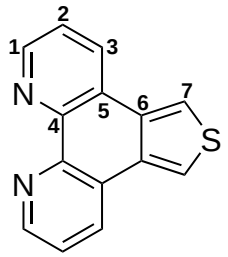

L2

^{13}C NMR (125 MHz, $CDCl_3$): δ (ppm) 118.8 (CH, C^7); 123.8 (CH, C^2); 125.4 (C_q, C^5); 131.9 (CH, C^3); 133.4 (C_q, C^6); 146.2 (C_q, C^4); 149.7 (CH, C^1).

^{15}N NMR (50.7 MHz, $CDCl_3$): δ (ppm) 304.01 (s, N^8).

MS-ESI (pos): m/z 237.05 $[M+H]^+$.

UV-Vis (CH_2Cl_2): λ_{abs} [nm] (ϵ \ $M^{-1}{\cdot}cm^{-1}$) 240 (17792), 255 (24875), 265 (33922), 294 (6697), 325 (4377), 340 (4410).

ATR-IR ($\tilde{\nu}$ [cm-1]): 3365, 3047, 2928, 2854, 1608, 1568, 1553, 1508, 1481, 1443, 1402, 1315, 1257, 1175, 1115, 1028, 935, 872, 802, 771, 741, 723, 700, 619, 575, 555, 519, 430, 409, 382, 301, 220.

Synthesis of diethyl thieno[3,4-f][1,10]phenanthroline-5,7-dicarboxylate (L3)

1.00 g (3.09 mmol, 1 eq) **L4** was added to a solution of 12 mL EtOH and 1.5 mL concentrated H_2SO_4 and refluxed for four days. The orange suspension was evaporated and the crude product was dissolved in $CHCl_3$ and washed with 1 M Na_2CO_3. The organic layer was concentrated under vacuum and a pale rose solid was isolated as product.

Yield: 0.58 g (49.1 %)

^{1}H NMR (500 MHz, $CDCl_3$): δ (ppm) 1.48 (t, $^3J_{HH}$= 7.1 Hz, 6H, H^{10}); 4.51 (q, $^3J_{HH}$= 7.1 Hz, 4H, H^9); 7.56 (dd, $^3J_{HH}$= 4.3 Hz, 8.4 Hz, 2H, H^2); 9.09 (dd, $^3J_{HH}$= 4.3 Hz, $^4J_{HH}$= 1.6 Hz, 2H, H^1); 9.44 (dd, $^3J_{HH}$= 8.3 Hz, $^4J_{HH}$= 1.6 Hz, 2H, H^3).

^{13}C NMR (125 MHz, $CDCl_3$): δ (ppm) 14.2 (CH_3, C^{10}); 62.6 (CH_2, C^9); 123.0 (CH, C^2); 124.0 (C_q, C^5); 130.2 (C_q, C^7); 135.9 (CH, C^3); 136.5 (C_q, C^6); 146.7 (C_q, C^4); 150.9 (CH, C^1); 162.6 (C_q, C^8).

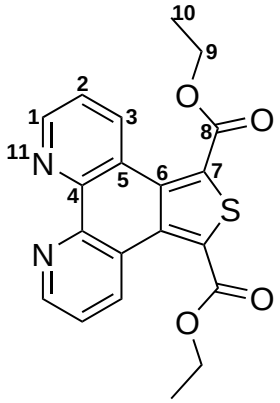

L3

^{15}N NMR (50.7 MHz, CD_2Cl_2): δ (ppm) 303.91 (s, N^8).

MS-ESI (pos): m/z 381.09 $[M+H]^+$.

Elemental analysis: calcd. for $C_{20}H_{16}S_1N_2O_4$: C, 63.15; H, 4.24; N, 7.36; S, 8.43. found: C, 62.44; H, 4.33; N, 7.11; S, 8.40.

UV-Vis (CH_2Cl_2): λ_{abs} [nm] ($\epsilon \setminus M^{-1}\cdot cm^{-1}$) 232 (28834), 266 (16368), 279 (8453), 286 (5884), 311 (611), 325 (342).

ATR-IR ($\tilde{\nu}$ [cm-1]): 3124, 2974, 2924, 2899, 1705, 1553, 1508, 1472, 1404, 1389, 1364, 1315, 1252, 1217, 1175, 1153, 1136, 1099, 1065, 1055, 1016, 903, 849, 814, 762, 741, 729, 640, 582, 518, 451, 405, 388, 366, 325.

Synthesis of diethyl thieno[3,4-f][1,10]phenanthroline-5,7-dicarboxylate (3)

0.35 g (1.08 mmol, 1 eq) **L4** was added to a solution of 4 mL MeOH and 0.5 mL concentrated H_2SO_4 and refluxed for two days. The brown solution was evaporated and the crude product was dissolved in $CHCl_3$ and washed with saturated Na_2CO_3 and water. The organic layer was concentrated under vacuum and a pale rose solid was isolated as product.

Yield: 0.11 g (28.9 %)

^{1}H NMR (500 MHz, $CDCl_3$): δ (ppm) 4.04 (s, 6H, H^9); 7.57 (dd, $^3J_{HH}$= 4.4 Hz, 8.5 Hz, 2H, H^2); 9.09 (dd, $^3J_{HH}$= 4.4 Hz, $^4J_{HH}$= 1.6 Hz, 2H, H^1); 9.45 (dd, $^3J_{HH}$= 8.4 Hz, $^4J_{HH}$= 1.6 Hz, 2H, H^3).

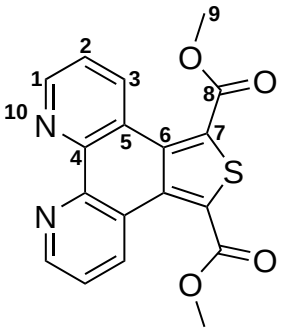

3

^{13}C NMR (125 MHz, $CDCl_3$): δ (ppm) 53.7 (CH_3, C^9); 123.4 (CH, C^2); 124.3 (C_q, C^5); 130.1 (C_q, C^7); 136.2 (CH, C^3); 137.1 (C_q, C^6); 146.1 (C_q, C^4); 151.3 (CH, C^1); 163.3 (C_q, C^8).

^{15}N NMR (50.7 MHz, CD_2Cl_2): δ (ppm) 304.06 (s, N^{10}).

MS-ESI (pos): m/z 353.06 $[M+H]^+$.

Elemental analysis: calcd. for $C_{18}H_{12}S_1N_2O_4$: C, 61.36; H, 3.43; N, 7.95; S, 9.10. found: C, 57.06; H, 4.15; N, 7.47; S, 7.83.

Synthesis of 5,7-dibromothieno[3,4-f][1,10]phenanthroline (L5)

3.00 g (9.3 mmol; 1 eq) of **L4** was suspended in 186 mL water and 7.40 g (41.6 mmol, 4.5 eq) were added and stirred overnight. During this time the color changed from yellow to orange. The reaction suspension was extracted with $CHCl_3$ (5 x 100 mL) and the organic layers were neutralized with 150 mL 16 M NaOH. The combined organic layers were evaporated subsequently. The crude product was recrystallized from 60 mL MeCN and isolated as pale brown solid.

Yield: 2.64 g (72.4 %)

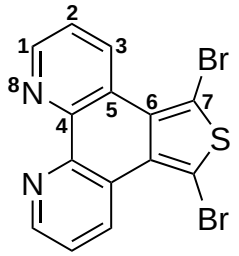

L5

^{1}H NMR (500 MHz, $CDCl_3$): δ (ppm) 7.53 (dd, $^{3}J_{HH}$ = 8.3 Hz, 4.4 Hz, 2H, H^2); 9.02 (dd, $^{3}J_{HH}$ = 4.4 Hz, $^{4}J_{HH}$ = 1.6 Hz, 2H, H^1); 9.52 (dd, $^{3}J_{HH}$ = 8.3 Hz, $^{4}J_{HH}$ = 1.6 Hz, 2H, H^3).

^{13}C NMR (125 MHz, $CDCl_3$): δ (ppm) 106.3 (C_q, C^7); 123.0 (CH, C^2); 124.8 (C_q, C^5); 129.8 (C_q, C^6); 131.3 (CH, C^3); 146.6 (C_q, C^4); 150.0 (CH, C^1).

^{15}N NMR (50.7 MHz, CD_2Cl_2): δ (ppm) 305.86 (s, N^8).

MS-EI: m/z (%) 393.77 (100) $[M]^+$; 233.97 (56) $[M\text{-}2Br]^+$.

Elemental analysis: calcd. for $C_{14}H_6S_1N_2Br_2$: C, 42.67; H, 1.53; N, 7.11; S, 8.14. found: C, 41.63; H, 1.88; N, 7.19; S, 7.99.

UV-Vis (CH_2Cl_2): λ_{abs} [nm] ($\epsilon \setminus M^{-1}\cdot cm^{-1}$) 247 (834), 261 (12873), 268 (16266), 333 (3232), 349 (2448).

ATR-IR ($\tilde{\nu}$ [cm-1]): 2924, 2854, 1705, 1556, 1506, 1435, 1404, 1323, 1209, 1182, 1142, 1101, 1022, 1003, 903, 845, 804, 762, 735, 640, 625, 517, 467, 407, 384.

Synthesis of 5,7-di(thiophen-2-yl)thieno[3,4-f][1,10]phenanthroline (L6)

The reaction was carried out under Ar atmosphere. 0.16 g (0.4 mmol, 1 eq) **L5**, 0.12 g (1.0 mmol, 2.5 eq) 2-thienylboronic acid and 0.28 g (1.3 mmol, 3.5 eq) K_3PO_4 were added to a Schlenk flask. Afterward, 0.06 g (0.05 mmol, 0.07 eq) $Pd(PPh_3)_4$ was added to the flask with 5 mL of dry, oxygen-free DMF and heated to 100 °C. After the reaction time of 142.5 h the mixture was extracted with $CHCl_3$ and washed with EDTA solution to remove palladium residuals. The crude product was purified by column chromatography over SiO_2 with THF.

Yield: 0.08 g (54.3 %)

^{1}H NMR (500 MHz, $CDCl_3$): δ (ppm) 7.23 (dd, $^{3}J_{HH}$ = 5.2 Hz, 3.5 Hz, 2H, H^{10}); 7.27 (dd, $^{3}J_{HH}$ = 8.4 Hz, 4.4 Hz, 2H, H^2); 7.31 (dd, $^{3}J_{HH}$ = 3.5 Hz, $^{4}J_{HH}$ = 1.2 Hz, 2H, H^{11}); 7.59 (dd, $^{3}J_{HH}$ = 5.2 Hz, $^{4}J_{HH}$ = 1.2 Hz, 2H, H^9); 8.15 (dd, $^{3}J_{HH}$ = 8.4 Hz, $^{4}J_{HH}$ = 1.7 Hz, 2H, H^3); 8.95 (dd, $^{3}J_{HH}$ = 4.4 Hz, $^{4}J_{HH}$ = 1.7 Hz, 2H, H^1).

^{13}C NMR (125 MHz, $CDCl_3$): δ (ppm) 123.0 (CH, C^2); 128.3 (CH, C^{10}); 128.9 (CH, C^9); 129.7 (CH, C^{11}); 130.3 (C_q, C^6); 130.9 (C_q, C^5); 132.6 (CH, C^3); 134.7 (C_q, C^8); 136.0 (C_q, C^7); 147.0 (C_q, C^4); 149.6 (CH, C^1).

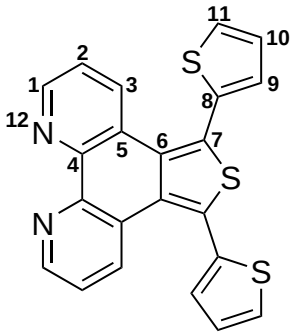

L6

^{15}N NMR (50.7 MHz, $CDCl_3$): δ (ppm) 305.59 (s, N^{12}).

MS-ESI (pos): m/z 823.02 $[2M+Na]^+$; 401.02 $[M+H]^+$.

Elemental analysis: calcd. for $C_{22}H_{12}S_3N_2$: C, 65.97; H, 3.02; N, 6.99; S, 24.01. found: C, 65.15; H, 3.59; N, 6.78; S, 22.19.

UV-Vis (CH_2Cl_2): λ_{abs} [nm] (ϵ \ $M^{-1}\cdot cm^{-1}$) 247 (24932), 267 (23900), 272 (24061), 290 (16460), 330 (7254), 344 (7082).

ATR-IR ($\tilde{\nu}$ [cm-1]): 3063, 1547, 1462, 1427, 1396, 1350, 1310, 1240, 1219, 1176, 1082, 1045, 937, 916, 898, 845, 804, 738, 694, 615, 579, 517, 503, 424, 325.

Synthesis of 5,7-bis(5-bromothiophen-2-yl)thieno[3,4-f][1,10]phenanthroline (L7)

0.17 g (0.4 mmol, 1 eq) **L6** and 0.34 g (1.9 mmol, 4.5 eq) NBS were suspended in 9 mL water and stirred overnight at ambient temperature. The orange suspension was extracted with 3 x 25 mL $CHCl_3$ and the organic layers were neutralized with 3 x 50 mL 1 M NaOH. The organic phase was concentrated and the obtained solid was recrystallized with 30 mL MeCN to isolate a pale yellow solid.

Yield: 0.04 g (17.7 %)

^{1}H NMR (500 MHz, $CDCl_3$): δ (ppm) 7.08 (d, $^3J_{HH}$= 3.8 Hz, 2H, H^{10}); 7.20 (d, $^3J_{HH}$= 3.8 Hz, 2H, H^9); 7.35 (dd, $^3J_{HH}$= 8.3 Hz, 4.4 Hz, 2H, H^2); 8.27 (dd, $^3J_{HH}$= 8.3 Hz, $^4J_{HH}$= 1.6 Hz, 2H, H^3); 8.99 (dd, $^3J_{HH}$= 4.4 Hz, $^4J_{HH}$= 1.6 Hz, 2H, H^1).

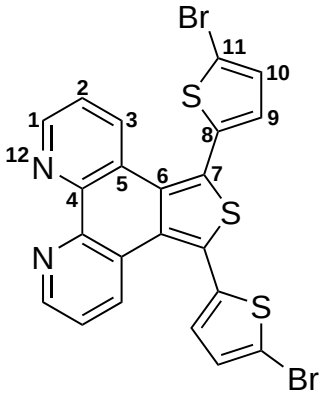

L7

^{13}C NMR (125 MHz, $CDCl_3$): δ (ppm) 115.3 (C_q, C^{11}); 123.1 (CH, C^2); 125.2 (C_q, C^5); 129.3 (C_q, C^8); 130.1 (CH, C^9); 131.0 (CH, C^{10}); 131.1 (C_q, C^6); 132.4 (CH, C^3); 135.9 (C_q, C^7); 146.9 (C_q, C^4); 149.8 (CH, C^1).

^{15}N NMR (50.7 MHz, $CDCl_3$): δ (ppm) 305.74 (s, N^{12}).

MS-ESI (pos): m/z 558.84 $[M+H]^+$; 580.83 $[M+Na]^+$.

Elemental analysis: calcd. for $C_{22}H_{10}S_3N_2Br_2$: C, 47.33; H, 1.81; N, 5.02; S, 17.23. found: C, 51.59; H, 3.21; N, 4.72; S, 15.52.

UV-Vis (CH_2Cl_2): λ_{abs} [nm] ($\epsilon \setminus M^{-1}\cdot cm^{-1}$) 250 (27088), 259 (28423), 267 (28839), 272 (27989), 294 (17289), 326 (9087), 343 (8549).

ATR-IR ($\tilde{\nu}$ [cm-1]): 3047, 2917, 1697, 1616, 1572, 1551, 1518, 1427, 1400, 1369, 1342, 1209, 1161, 1126, 1089, 1024, 1007, 972, 928, 882, 814, 800, 767, 739, 723, 702, 663, 635, 571, 554, 517, 498, 447, 368, 314.

Synthesis of 2-thienylboronic acid (7)[151]

The reaction was conducted under inert atmosphere. 12 mL thiophene (149.90 mmol, 1 eq) were mixed together with 150 mL of dry THF and cooled down to -78 °C under an argon atmosphere. Afterward, 93 mL (148.80 mmol, 1 eq) of 1.6 M *n*BuLi were added slowly over a syringe and stirred for further 30 min at -78 °C. The mixture was warmed up to -20 °C during which a second flask was prepared with 24 mL (215.30 mmol, 1.4 eq) of trimethyl borate and 100 mL dry THF. Both reaction mixtures were cooled down to -78 °C, combined and stirred for one hour. The reaction was stopped by the addition of 250 mL of 1 M HCl and extracted with

CH_2Cl_2. The organic phase was evaporated and the crude product was recrystallized from 150 mL water. The product was isolated as white solid.

Yield: 12.42 g (64.2 %)

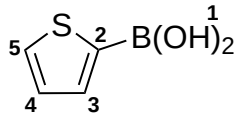

7

^{1}H NMR (500 MHz, DMSO d_6): δ (ppm) 7.17 (dd, $^3J_{HH}$ = 4.69 Hz, 3.40 Hz, 1H, H^4); 7.68 (dd, $^3J_{HH}$ = 3.40 Hz, $^4J_{HH}$ = 0.94 Hz, 1H, H^3); 7.73 (dd, $^3J_{HH}$ = 4.69 Hz, $^4J_{HH}$ = 0.93 Hz, 1H, H^5); 8.16 (s, 2H, H^1).

^{13}C NMR (125 MHz, DMSO d_6): δ (ppm) 127.5 (C_q, C^2); 128.5 (CH, C^4); 132.0 (CH, C^5); 136.4 (CH, C^3).

MS-EI: m/z (%) 128.03 (100) $[M]^+$; 110.01 (23) $[M\text{-}OH]^+$; 84.00 (92) $[C_4H_4S]^+$; 57.94 (41) $[C_2H_2S]^+$; 44.96 (39) $[CHS]^+$.

Elemental analysis: calcd. for $C_4H_5SBO_2$: C, 37.55; H, 3.94; S, 25.06. found: C, 37.68; H, 4.23; S, 24.91.

Synthesis of 3-(thiophen-2-yl)pyridine (22)[256]

The reaction was conducted under inert atmosphere. 1.23 mL (12.66 mmol, 1 eq) 3-bromopyridine, 4.8 mL (15.19 mmol, 1.2 eq) 2-tributylstannyl thiophene and 1.46 g (1.27 mmol, 0.1 eq) $Pd(PPh_3)_4$ 100 mL were dissolved in dry, oxygen-free toluene and 18.5 mL dry, oxygen-free DMF. The reaction mixture was stirred for 66 h at 100 °C. Afterward the black mixture was cooled down and filtrated, which results in a dark green solution. The solvent was removed and the crude product was purified by column chromatography with EtOAc:Hex (1:1).

Yield: 1.69 g (78.8 %)

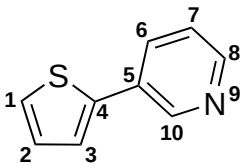

22

^{1}H NMR (500 MHz, $CDCl_3$): δ (ppm) 7.08 (dd, $^{3}J_{HH}$ = 5.2 Hz, $^{4}J_{HH}$ = 3.8 Hz, 1H, H^{10}); 7.26 (dd, $^{3}J_{HH}$ = 8 Hz, 4.8 Hz, $^{5}J_{HH}$ = 0.8 Hz, 1H, H^{3}); 7.31-7.32 (m, 2H, H^{8}, H^{9}); 7.81 (ddd, 8 Hz, $^{4}J_{HH}$ = 2.4 Hz, 1.6 Hz, 1H, H^{4}); 8.47 (dd, $^{3}J_{HH}$ = 4.8 Hz, $^{4}J_{HH}$ = 1.6 Hz, 1H, H^{2}); 8.85 (dd, $^{4}J_{HH}$ = 2.4 Hz, $^{5}J_{HH}$ = 0.6 Hz, 1H, H^{6}).

^{13}C NMR (125 MHz, $CDCl_3$): δ (ppm) 123.7 (CH, C^{3}); 124.3 (CH, C^{8}); 126.1 (CH, C^{9}); 128.3 (CH, C^{10}); 130.5 (C_q, C^{5}); 133.0 (CH, C^{4}); 140.5 (C_q, C^{7}); 147.1 (CH, C^{2}); 148.6 (CH, C^{6}).

^{15}N NMR (50.7 MHz, $CDCl_3$): δ (ppm) 312.98 (s,N^{1}).

MS-ESI(pos): m/z 162.04 $[M+H]^+$.

Synthesis of 3-(5-bromothiophen-2-yl)pyridine (23)

1.69 g (0.01 mol, 1 eq) of **22** and 2.80 g (0.016 mol, 1.5 eq) NBS were added to a solution of 1600 mL $CHCl_3$/CH_3COOH and stirred overnight at room temperature. The yellow solution was neutralized with 1200 mL of 1 M NaOH. The organic phase was concentrated at the rotary evaporator and the crude product was purified by gradient column chromatography with EtOAC:Hex.

Yield: 1.79 g (63.6 %)

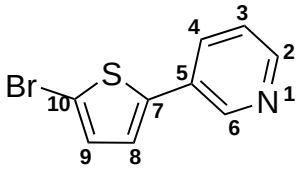

23

^{1}H NMR (500 MHz, $CDCl_3$): δ (ppm) 6.99 (d, $^{3}J_{HH}$ = 3.9 Hz, 1H, H^{9}); 7.03 (d, $^{3}J_{HH}$ = 3.9 Hz, 1H, H^{8}); 7.23 (dd, $^{3}J_{HH}$ = 4.9 Hz, 8.0 Hz, 1H, H^{3}); 7.68 (dd, $^{3}J_{HH}$ = 8.0 Hz, $^{4}J_{HH}$ = 1.7 Hz, 1H, H^{4}); 8.47 (dd, $^{3}J_{HH}$ = 4.9 Hz, $^{4}J_{HH}$ = 1.3 Hz, 1H, H^{2}); 8.73 (d, $^{4}J_{HH}$ = 1.7 Hz, 1H, H^{6}).

^{13}C NMR (125 MHz, $CDCl_3$): δ (ppm) 112.8 (C_q, C^{10}); 123.6 (CH, C^{3}); 124.4 (CH, C^{8}); 129.6 (C_q, C^{5}); 131.1 (CH, C^{9}); 132.6 (CH, C^{4}); 141.8 (C_q, C^{7}); 146.5 (CH, C^{6}); 148.8 (CH, C^{2}).

^{15}N NMR (50.7 MHz, $CDCl_3$): δ (ppm) 312.42 (s, N^{1}).

MS-ESI(pos): m/z 241.95 $[M+H]^+$.

Elemental analysis: calcd. for C_9H_6SNBr: N, 5.83; C, 45.02; H, 2.52; S, 13.35. found: N, 2.77; C, 45.62; H, 2.77; S, 13.07.

Synthesis of 3-(5-(tributylstannyl)thiophen-2-yl)pyridine (18)

The reaction was conducted under inert atmosphere. 1.01 g (4.2 mmol, 1 eq) of **23** was dissolved in 28 mL dry THF and cooled down to -78 °C. While 2.9 mL of 1.6 M *n*BuLi (4.6 mmol, 1.1 eq) were added *via* a syringe the reaction mixture became dark red. The solution was stirred for 1 h at this temperature. Afterwards 1.13 mL (4.2 mmol, 1 eq) of $SnBu_3Cl$ were added and stirred for an additional hour. The solution was washed with saturated $NaHCO_3$ and the organic phase was evaporated. The product was isolated as brown oil.

Yield: 1.71 g (91.2 %)

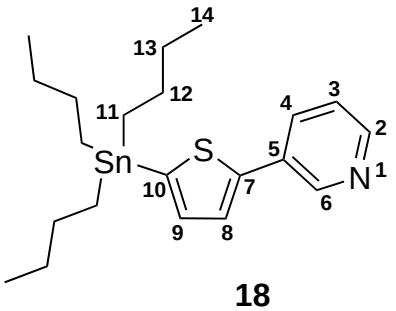

18

^{1}H NMR (500 MHz, $CDCl_3$): δ (ppm) 0.91 (t, $^3J_{HH}$= 7.4 Hz, 9H, H^{14}); 1.15 (m, 6H, H^{11}); 1.37 (m, 6H, H^{13}); 1.60 (m, 6H, H^{12}); 7.17 (d, $^3J_{HH}$= 3.4 Hz, 1H, H^9); 7.26 (d, $^3J_{HH}$= 3.4 Hz, 1H, H^8); 7.46 (dd, $^3J_{HH}$= 4.9 Hz, 8.0 Hz, 1H, H^3); 7.85 (dd, $^3J_{HH}$= 8.0 Hz, $^4J_{HH}$= 1.5 Hz, 1H, H^4); 8.46 (dd, $^3J_{HH}$= 4.9 Hz, $^4J_{HH}$= 1.5 Hz, 1H, H^2); 8.89 (d, $^4J_{HH}$= 1.7 Hz, 1H, H^6).

^{13}C NMR (125 MHz, $CDCl_3$): δ (ppm) 11.0 (CH_2, C^{11}); 13.7 (CH_3, C^{14}); 27.3 (CH_2, C^{13}); 29.0 (CH_2, C^{12}); 123.6 (CH, C^3); 125.3 (CH, C^8); 130.7 (C_q, C^5); 132.9 (CH, C^4); 136.6 (CH, C^9); 138.7 (C_q, C^{10}); 146.0 (C_q, C^7); 147.1 (CH, C^6); 148.1 (CH, C^2).

^{15}N NMR (50.7 MHz, $CDCl_3$): δ (ppm) 312.86 (s, N^1).

MS-ESI(pos): m/z 452.14 $[M+H]^+$.

Elemental analysis: calcd. for $C_{21}H_{33}SNSnr$: N, 3.11; C, 56.02; H, 7.39; S, 7.12. found: N, 3.50; C, 57.68; H, 7.55; S, 7.33.

Synthesis of 5,7-bis(5-(pyridin-3-yl)thiophen-2-yl)thieno[3,4-f][1,10]phenanthroline (L8)

The reaction was carried out under argon atmosphere. 0.38 g (0.96 mmol, 1 eq) of **L5** and 0.95 g (2.11 mmol, 2.2 eq) of **18** were mixed together with 0.16 g (0.14 mmol, 0.15 eq) $Pd(PPh_3)_4$ in 20.5 mL dry, oxygen-free toluene and 5.5 mL dry oxygen-free DMF. The cross-coupling reaction was refluxed for 72 h. While the mixture was allowed to cool down to room temperature, a solid precipitated. The solid was isolated and washed with Et_2O. The light orange powder was dried under vacuum.

Yield: 0.37 g (69.5 %)

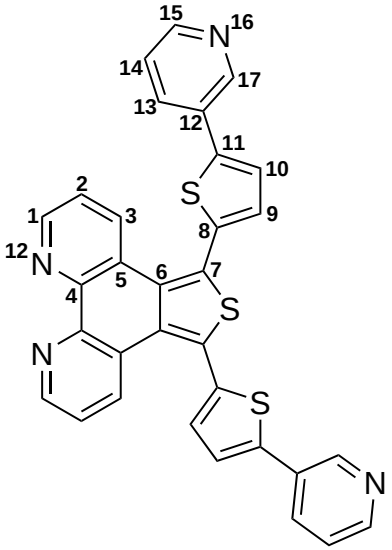

L8

^{1}H NMR (500 MHz, $CDCl_3$): δ (ppm) 7.31–7.34 (m, 2H, H^2, H^9); 7.34 (d, $^3J_{HH}$ = 4.43 Hz, 2H, H^2); 7.37 (dd, 2H, H^{14}); 7.49 (d, $^3J_{HH}$ = 3.66 Hz, 2H, H^{10}); 7.93 (ddd, 2H, H^{13}); 8.38 (dd, $^3J_{HH}$ = 8.34 Hz, $^4J_{HH}$ = 1.54 Hz, 2H, H^3); 8.59 (dd, $^3J_{HH}$ = 4.81 Hz, $^4J_{HH}$ = 1.43 Hz, 2H, H^{15}); 8.96 (d, $^4J_{HH}$ = 1.83 Hz, 2H, H^{17}); 8.98 (dd, $^3J_{HH}$ = 4.46 Hz, $^4J_{HH}$ = 1.54 Hz, 2H, H^1).

^{13}C NMR (125 MHz, $CDCl_3$): δ (ppm) 123.1 (CH, C^2); 123.9 (CH, C^{14}); 125.1 (CH, C^{10}); 125.6 (C_q, C^5); 129.8 (C_q, C^7); 130.0 (C_q, C^{12}); 130.9 (CH, C^9); 131.1 (C_q, C^6); 132.7 (CH, C^3); 133.2 (CH, C^{13}); 135.1 (C_q, C^8); 143.8 (C_q, C^{11}); 147.0 (C_q, C^4); 147.1 (CH, C^{17}); 149.3 (CH, C^{15}); 149.9 (C_q, C^1).

^{15}N NMR (50.7 MHz, $CDCl_3$): δ (ppm) 306.63 (s, N^{12}); 313.81 (s, N^{16}).

MS-ESI(pos): m/z 555.08 $[M+H]^+$; 278.04 $[M+2H]^{2+}$.

UV-Vis (CH_2Cl_2): λ_{abs} [nm] (ϵ \ $M^{-1}\cdot cm^{-1}$) 260 (24068), 267 (26210), 272 (26022), 304 (25600), 327 (17890), 347 (13309), 443 (801).

ATR-IR ($\tilde{\nu}$ [cm-1]): 3059, 2980, 1674, 1574, 1562, 1551, 1519, 1433, 1409, 1400, 1309, 1257, 1180, 1165, 1122, 1092, 1080, 1039, 1022, 957, 942, 926, 889, 827, 795, 741, 717, 700, 633, 617, 588, 557, 519, 424, 393, 304.

Synthesis of 2,6-dimethyl-3-(thiophen-2-yl)pyridine (15)[256]

The reaction was carried out under Ar atmosphere. 2 mL (15.4 mmol, 1 eq) of 3-bromo-2,6-dimethylpyridine and 5.9 mL (18.5 mmol, 1.2 eq) of 2-tributylstannyl thiophene were added to a Schlenk flask with 125 mL dry, degassed toluene and 22.5 mL dry, degassed DMF. Secondly, 1.78 g (1.5 mmol, 0.1 eq) of $Pd(PPh_3)_4$ was added under an argon atmosphere and the solution was stirred for six days at 105 °C. After completion of the reaction, the solvent was removed. The green oil was mixed with $CHCl_3$:TEA (4:1) and filtered over silica. The solvent was removed and the white precipitate was discarded and the oil was purified by column chromatography with Hex: EtOAC.

Yield: 2.65 g (90.9 %)

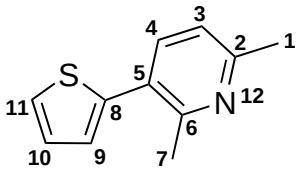

15

^{1}H NMR (500 MHz, $CDCl_3$): δ (ppm) 2.55 (s, 3H, H^7); 2.62 (s, 3H, H^1); 7.00 (d, $^3J_{HH}$= 7.90 Hz, 1H, H^3); 7.06 (dd, $^3J_{HH}$= 3.56 Hz, $^4J_{HH}$= 1.23 Hz, 1H, H^9); 7.09 (dd, $^3J_{HH}$= 5.10 Hz, 3.56 Hz, 1H, H^{10}); 7.35 (dd, $^3J_{HH}$= 5.10 Hz, 1.23 Hz, 1H, H^{11}); 7.54 (d, $^3J_{HH}$= 7.90 Hz, 1H, H^4).

^{13}C NMR (125 MHz, $CDCl_3$): δ (ppm) 24.0 (CH_3, C^7); 24.3 (CH_3, C^1); 120.6 (CH, C^3); 125.8 (CH, C^{11}); 126.8 (CH, C^9); 127.4 (CH, C^{10}); 138.1 (CH, C^4); 141.3 (C_q, C^8); 155.5 (C_q, C^2); 157.1 (C_q, C^6).

^{15}N NMR (50.7 MHz, $CDCl_3$): δ (ppm) 312.42 (s, N^{12}).

MS-ESI(pos): m/z 190.07 $[M+H]^+$.

Elemental analysis: calcd. for $C_{11}H_{11}SN$: N, 7.40; C, 69.80; H, 5.86; S, 16.94. found: N, 6.86; C, 66.86; H, 6.02; S, 15.00.

Synthesis of 3-(5-bromothiophen-2-yl)-2,6-dimethylpyridine (16)

2.65 g (14 mmol, 1 eq) of **15** and 3.74 g (21 mmol, 1.5 eq) NBS were added to a mixture of 340 mL $CHCl_3$:CH_3COOH (1:1). The mixture was stirred for 8 h at room temperature and afterward neutralized with 3 x 150 mL 1 M NaOH. The organic phase was washed with 200 mL H_2O and removed at the rotary evaporator. As product a yellow oil was obtained.

Yield: 3.75 g (99.8 %)

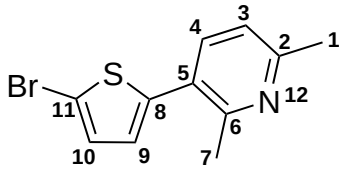

16

^{1}H NMR (500 MHz, $CDCl_3$): δ (ppm) 2.53 (s, 3H, H^7); 2.59 (s, 3H, H^1); 6.79 (d, $^3J_{HH}$ = 3.78 Hz, 1H, H^9); 7.00 (d, $^3J_{HH}$ = 7.89 Hz, 1H, H^3); 7.02 (d, $^3J_{HH}$ = 3.78 Hz, 1H, H^{10}); 7.46 (d, $^3J_{HH}$ = 7.89 Hz, 1H, H^4).

^{13}C NMR (125 MHz, $CDCl_3$): δ (ppm) 23.9 (CH_3, C^7); 24.4 (CH_3, C^1); 112.3 (C_q, C^{11}); 120.7 (CH, C^3); 127.2 (CH, C^9); 130.3 (CH, C^{10}); 137.9 (CH, C^4); 142.9 (C_q, C^8); 155.5 (C_q, C^2); 157.6 (C_q, C^6).

^{15}N NMR (50.7 MHz, $CDCl_3$): δ (ppm) 313.2 (s, N^{12}).

MS-EI: m/z (%) 268.93 (100) $[M]^+$; 188.03 (155) $[M\text{-}Br]^+$.

Elemental analysis: calcd. for $C_{11}H_{10}SNBr$: N, 5.22; C, 49.27; H, 3.76; S, 11.96. found: N, 5.10; C, 50.25; H, 4.00; S, 11.38.

Synthesis of 2,6-dimethyl-3-(5-(tributylstannyl)thiophen-2-yl)pyridine (17)

The reaction was carried out under Ar atmosphere. A Schlenk flask was charged with 1 mL of dry THF and 1.33 g (5.0 mmol, 1 eq) of **16** and cooled down to -78 °C. Afterward, 3.45 mL of 1.6 M *n*BuLi (5.5 mmol, 1.1 eq) were added, which led to a color change from yellow to red. After 30 min stirred at this temperature 1.5 mL $SnBu_3Cl$ (5.5 mmol, 1.1 eq) were added to the solution *via* a syringe. The solution was brought slowly to room temperature and stirred for two additional hours. The crude product was worked up by adding it to ethyl acetate and saturated $NaHCO_3$ solution. The combined organic phases were evaporated and the isolated brown oil was subjected to column chromatography with EtOAc: Hex (1:1). A yellow oil was obtained as product.

Yield: 1.95 g (82.1 %)

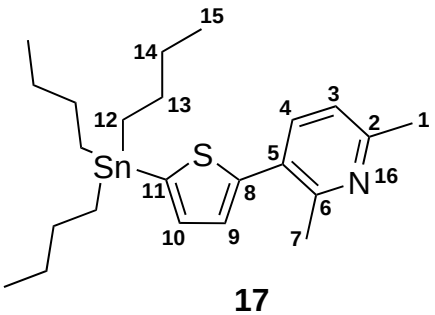

17

^{1}H NMR (500 MHz, $CDCl_3$): δ (ppm) 0.91 (t, $^{3}J_{HH}$ = 7.32 Hz, 9H, H^{15}); 1.14 (m, 6H, H^{12}); 1.36 (m, 6H, H^{14}); 1.59 (m, 6H, H^{13}); 2.55 (s, 3H, H^{7}); 2.64 (s, 3H, H^{1}); 7.00 (d, $^{3}J_{HH}$ = 7.80 Hz, 1H, H^{3}); 7.15 (d, $^{3}J_{HH}$ = 3.31 Hz, 1H, H^{10}); 7.20 (d, $^{3}J_{HH}$ = 3.31 Hz, 1H, H^{9}); 7.58 (d, $^{3}J_{HH}$ = 7.80 Hz, 1H, H^{4}).

^{13}C NMR (125 MHz, $CDCl_3$): δ (ppm) 11.3 (CH_2, C^{12}); 14.0 (CH_3, C^{15}); 24.5 (CH_3, C^{7}); 24.6 (CH_3, C^{1}); 27.6 (CH_2, C^{14}); 29.4 (CH_2, C^{13}); 120.9 (CH, C^{3}); 127.6 (C_q, C^{5}); 128.3 (CH, C^{9}); 136.1 (CH, C^{10}); 138.0 (C_q, C^{11}); 138.2 (CH, C^{4}); 147.3 (C_q, C^{8}); 155.4 (C_q, C^{2}); 156.9 (C_q, C^{6}).

^{15}N NMR (50.7 MHz, $CDCl_3$): δ (ppm) 312.2 (s, N^{16}).

MS-ESI(pos): m/z 474.22 $[M+H]^+$.

Elemental Analysis: calcd. for $C_{23}H_{37}SNSnr$: N, 2.93; C, 57.57; H, 7.80; S, 6.70. found: N, 2.94; C, 57.74; H, 7.78; S, 5.95.

Synthesis of 5,7-bis(5-(2,6-dimethylpyridin-3-yl)thiophen-2-yl)thieno[3,4-f][1,10]phenanthroline (L9)

The reaction was conducted under inert atmosphere. 0.037 g (0.10 mmol, 1 eq) of **L5** and 0.1 g (0.21 mmol, 2.1 eq) of **17** were added to a Schlenk flask with dry and oxygen-free toluene and DMF. 0.01 g (0.01 mmol, 0.1 eq) of $Pd(PPh_3)_4$ was added in counterflow to the mixture and the reaction was stirred at 105 °C for 72 h. The mixture was allowed to cool down to ambient temperature while a white solid precipitated. The solvent was filtered off and the solid was washed with toluene. The powder was dried under vacuum and identified as the desired product.

Yield: 0.04 g (68.9 %)

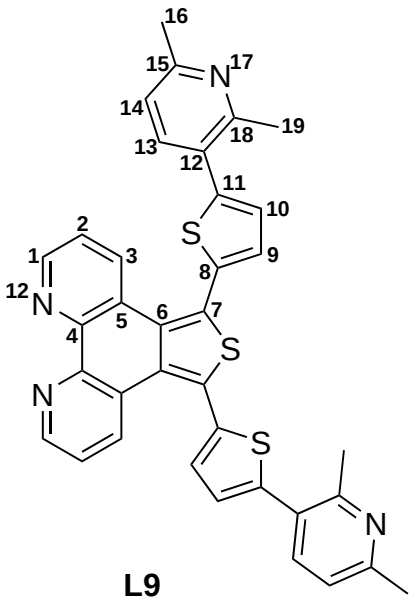

L9

^{1}H NMR (500 MHz, $CDCl_3$): δ (ppm) 2.62 (s, 6H, H^{16}); 2.78 (s, 6H, H^{18}); 7.10 (d, $^{3}J_{HH}$= 7.72 Hz, 2H, H^{14}); 7.22 (d, $^{3}J_{HH}$= 3.65 Hz, 2H, H^{9}); 7.33 (d, $^{3}J_{HH}$= 3.65 Hz, 2H, H^{10}); 7.34 (d, $^{3}J_{HH}$= 4.43 Hz, 2H, H^{2}); 7.70 (d, $^{3}J_{HH}$= 7.85 Hz, 2H, H^{13}); 8.37 (dd, $^{3}J_{HH}$= 8.35 Hz, $^{4}J_{HH}$= 1.60 Hz, 2H, H^{3}); 9.00 (dd, $^{3}J_{HH}$= 4.43 Hz, $^{4}J_{HH}$= 1.60 Hz, 2H, H^{1}).

^{13}C NMR (125 MHz, $CDCl_3$): δ (ppm) 24.1 (CH_3, C^{16}); 24.3 (CH_3, C^{19}); 121.1 (CH, C^{14}); 123.1 (CH, C^{2}); 125.7 (C_q, C^{12}); 127.9 (CH, C^{9}); 130.0 (CH, C^{10}); 130.0 (C_q, C^{7}); 131.0 (C_q, C^{6}); 132.6 (CH, C^{3}); 135.0 (C_q, C^{8}); 138.3 (CH, C^{13}); 144.7 (C_q, C^{11}); 147.1 (C_q, C^{4}); 149.8 (CH, C^{1}); 155.3 (C_q, C^{15}); 157.7 (C_q, C^{18}).

^{15}N NMR (50.7 MHz, $CDCl_3$): δ (ppm) 305.9 (s, N^{12}); 313.1 (s, N^{17}).

MS-ESI(pos): m/z 633.12 $[M+Na]^+$; 611.14 $[M+H]^+$; 306.07 $[M+2H]^{2+}$.

Elemental Analysis: calcd. for CHN_4S_3: N, 9.17; C, 70.79; H, 4.29; S, 15.75. found: N, 8.76; C, 69.69; H, 4.67; S, 14.55.

UV-Vis (CH_2Cl_2): λ_{abs} [nm] (ϵ \ $M^{-1}{\cdot}cm^{-1}$) 252 (38642), 268 (44509), 273 (44810), 295 (34733), 347 (15561), 443 (359).

ATR-IR ($\tilde{\nu}$ [cm-1]): 3055, 2982, 2957, 2916, 2845, 1651, 1589, 1560, 1549, 1462, 1429, 1402, 1371, 1259, 1188, 1161, 1128, 1094, 1026, 959, 943, 933, 899 887, 833, 818, 802, 739, 694, 671, 648, 617, 608, 590, 573, 544, 514, 473, 422, 397, 352, 303.

Synthesis of 2,6-bis(chloromethyl)pyridine (20)

5.00 g (35.95 mmol, 1 eq) 2,6-pyridinedimethanol was added under Ar atmosphere to a Schlenk flask and 20 mL (0.28 mol, 7.7 eq) thionyl chloride were added under ice cooling. Afterward the reaction was warmed up to room temperature and stirred for 1 h. Once the time was over, the mixture was heated to 55 °C and stirred at that temperature for 4 h. After cooling down the reaction, 41 mL pentane were added. The obtained precipitate was filtered off and washed with pentane. Afterward, the solid was suspended in water and neutralized with 1 M NaOH. The precipitate was again filtered off, washed with water and dried under vacuum.

Yield: 4.71 g (74.5 %).

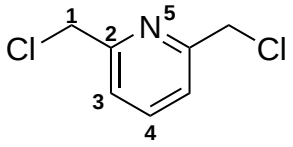

20

^{1}H NMR (500 MHz, DMSO d_6): δ (ppm) 4.78 (s, 4H, H^1); 7.52 (d, $^3J_{HH}$ = 7.8 Hz, 2H, H^3); 7.90 (t, $^3J_{HH}$ = 7.9 Hz, 1H, H^4).

^{13}C NMR (125 MHz, DMSO d_6): δ (ppm) 46.6 (s, CH_2, C^1); 122.9 (s, CH, C^3); 138.7 (s, CH, C^4); 156.3 (s, C_q, C^2).

^{15}N NMR (50.7 MHz, DMSO d_6): δ (ppm) 313.2 (s, N^5).

MS-EI: m/z (%) 77.00 (28) $[C_5H_3N]^+$; 104.03 (49) $[C7H6N]^+$; 140.00 (74) $[C_7H_7ClN]^+$; 174.96 (100) $[M]^+$.

Elemental analysis: calcd. for $C_7H_7Cl_2N$: C, 47.76; H, 4.01; N, 7.96 found: C, 47.75; H, 4.22; N, 7.82.

ATR-IR ($\tilde{\nu}$ [cm-1]): 246, 279, 295, 403, 433, 528, 557, 615, 671, 750, 823, 891, 1091, 1147, 1164, 1255, 1297, 1431, 1458, 1575, 1591, 1828, 1911, 1992, 2167, 2318, 2850, 2962, 3008, 3070.

Synthesis of 2,6-Bis[(diphenylphosphino)methyl]pyridine (21)

The reaction was carried out under Ar atmosphere. 57 mL dry THF and 2 mL (11.4 mmol, 2 eq) $HPPh_2$ were added to a Schlenk flask. Afterward 2.56 g (22.7 mmol, 4 eq) KO*t*Bu was added and the solution was cooled down. At 0 °C, 1.03 g (5.68 mmol, 1 eq) of **20** was added and slowly warmed up to room temperature, at which the solution was stirred for 24 h. The solvent was removed under vacuum and the obtained solid was extracted with a mixture of degassed CH_2Cl_2 and water. The organic phase was transferred to a second flask and the aqueous phase was again washed with 38 mL CH_2Cl_2. Afterward, the organic layers were combined and the solvent was removed under inert gas. The isolated solid was recrystallized from a mixture of 32 mL of dry and degassed $CHCl_3$ and acetone (1:1). The precipitated colorless solid **21** was dried under vacuum.

Yield: 1.63 g (58.6 %).

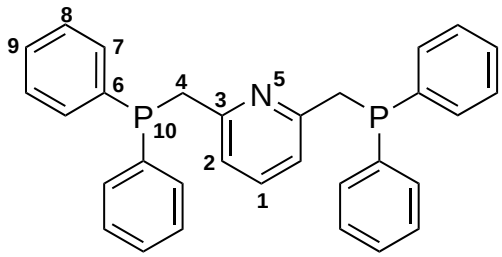

21

^{1}H NMR (500 MHz, $CDCl_3$): δ (ppm) 3.59 (s, 2H, H^4); 6.72 (d, $^3J_{HH}$ = 7.7 Hz, 1H, H^2); 7.21 (t, $^3J_{HH}$ = 7.7 Hz, 1H, H^1); 7.29–7.30 (m, 3H, H^8, H^9); 7.42–7.45 (m, 2H, H^7).

^{13}C NMR (125 MHz, $CDCl_3$): δ (ppm) 38.9 (d, CH_2, C^4); 121.0 (s, CH, C^2); 128.5 (d, CH, C^8); 128.7 (s, CH, C^9); 133.1 (d, CH, C^7); 136.2 (s, CH, C^1); 138.7 (d, C_q, C^6); 157.8 (d, C_q, C^3).

^{15}N NMR (50.7 MHz, $CDCl_3$): δ (ppm) 314.2 (s, N^5).

^{31}P-NMR (202.5 MHz, $CDCl_3$): δ (ppm) -10.6 (s, P^{10}).

MS-ESI (pos): m/z 476.17 $[M+H]^+$.

ATR-IR ($\tilde{\nu}$ [cm-1]): 608, 694, 740, 750, 812, 832, 910, 932, 994, 994, 1025, 1066, 1084, 1097, 1155, 1185, 1220, 1266, 1302, 1408, 1431, 1448, 1480, 1566, 1577, 1588, 2901, 2944, 3043, 3066.

9.3.2 Iridium Complexes

Synthesis of Iridium Dimer[257]

1.00 g (3.35 mmol, 1 eq) $IrCl_3 \cdot x\ H_2O$ was added to a solution of 1.1 mL (7.37 mmol, 2.2 eq) 2-phenylpyridine, 15 mL H_2O and 45 mL 2-ethoxyethanol during a violet color occurred. The color changes again after 24 h under reflux. After this time, the product was filtered off and washed with 90 mL acetone and ethanol, each. The yellow solid was dissolved in 115 mL CH_2Cl_2, 37 mL toluene and 15 mL hexane and afterward reduced to 75 mL. The solution was seasoned overnight in the refrigerator and the precipitate was filtered off and dried under vacuum.

Yield: 1.30 g (85.5%–98.6 %)

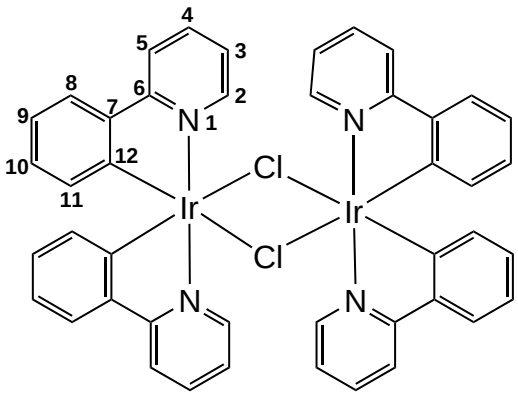

IrDimer

^{1}H NMR (500 MHz, CD_2Cl_2): δ (ppm) 5.92 (dd, $^3J_{HH}$= 7.85 Hz, $^4J_{HH}$= 0.85 Hz, 4H, H^{11}); 6.65 (dddd, $^3J_{HH}$= 7.85 Hz, 8.20 Hz, $^4J_{HH}$= 1.36 Hz, 4H, H^{10}); 6.84–6.89 (m, 4H, H^3, H^9); 7.60 (dd, $^3J_{HH}$= 7.73 Hz, $^4J_{HH}$= 1.36 Hz, 4H, H^8); 7.83 (dddd, $^3J_{HH}$= 7.89 Hz, $^3J_{HH}$= 7.10 Hz, $^4J_{HH}$= 1.51 Hz, 4H, H^4); 7.98 (dddd, $^3J_{HH}$= 7.89 Hz, 4H, H^5); 9.30 (ddd, $^3J_{HH}$= 5.74 Hz, $^4J_{HH}$= 1.51 Hz, $^5J_{HH}$= 0.71 Hz, 4H, H^2).

^{13}C NMR (125 MHz, CD_2Cl_2): δ 118.7 (CH, C^5); 121.4 (CH, C^9; 122.6 (CH, C^3); 123.7 (CH, C^8); 129.1 (CH, C^{10}); 130.4 (CH, C^{11}); 136.6 (CH, C^4); 144.0 (C_q, C^7); 144.9 (C_q, C^{12}); 151.5 (CH, C^2); 168.1 (C_q,C^6).

^{15}N NMR (50.7 MHz, CD_2Cl_2): δ (ppm) 216.24 (s, N^1).

MS-ESI(pos): m/z 501.09 $[1/2\ M\text{-}2Cl]^+$.

Elemental Analysis: calcd. for $C_{44}H_{32}Cl_2Ir_2N_4$: C, 49.29; H, 3.01; N, 5.23. found: C, 50.83; H, 3.82; N, 4.98.

Synthesis of PS1[103]

The substance was synthesized by a procedure described previously.[103] 0.15 g (0.15 mmol, 1 eq) $[Ir(ppy)_2Cl]_2$ and 0.05 g (0.3 mmol, 2.2 eq) anhydrous 1,10-phenanthroline were added to 6.5 mL ethylene glycol. To improve the solubility of the substances, 1 mL CH_2Cl_2 were added and the solution was stirred at 150 °C while it refluxed vigorously. At the next day, 90 mL H_2O were added and the solution was extracted with Et_2O. To the aqueous phase 10 mL of a 0.6 M NH_4PF_6 was added whereby a yellow solid precipitated. The solid was separated and dried in vacuum.

Yield: 0.22 g (85.9 %)

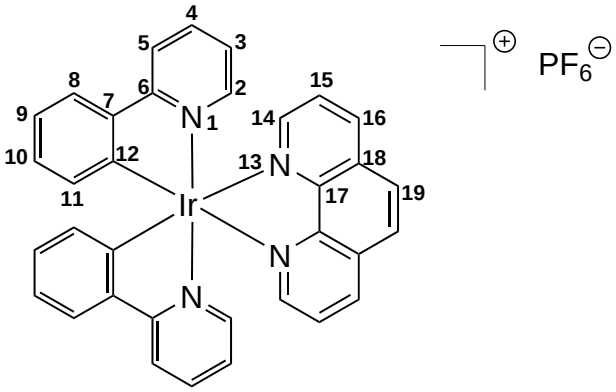

PS1

^{1}H NMR (500 MHz, MeCN): δ (ppm) 6.42 (dd, $^3J_{HH}$= 7.6 Hz, $^4J_{HH}$= 1.3 Hz, 2H, H^{11}); 6.88 (ddd, $^3J_{HH}$= 5.9 Hz; 7.8 Hz, $^4J_{HH}$= 1.5 Hz, 2H, H^3); 6.99 (ddd, $^3J_{HH}$= 7.6 Hz; 7.5 Hz, $^4J_{HH}$= 1.4 Hz, 2H, H^{10}); 7.11 (ddd, $^3J_{HH}$= 7.5 Hz; 7.7 Hz, $^4J_{HH}$= 1.3 Hz, 2H, H^9); 7.45 (ddd, $^3J_{HH}$= 5.9 Hz, $^4J_{HH}$= 1.5 Hz, $^5J_{HH}$= 0.8 Hz, 2H, H^2); 7.80 (ddd, $^3J_{HH}$= 8.0 Hz; 7.8 Hz, $^4J_{HH}$= 1.5 Hz, 2H, H^4); 7.87 (m, 4H, H^{15} oder H^8); 8.08 (ddd, $^3J_{HH}$= 8.0 Hz, $^4J_{HH}$= 1.5 Hz, $^5J_{HH}$= 0.8 Hz, 2H, H^5);

8.26 (s, 2H, H^{19}); 8.33 (dd, $^{3}J_{HH}$= 5.1 Hz, $^{4}J_{HH}$= 1.5 Hz, 2H, H^{14}); 8.71 (dd, $^{3}J_{HH}$= 8.3 Hz, $^{4}J_{HH}$= 1.5 Hz, 2H, H^{16}).

^{13}C NMR (125 MHz, MeCN): δ (ppm) 119.8 (CH, C^{5}); 122.6 (CH, C^{9}); 123.3 (CH, C^{3}); 124.9 (CH, C^{8}); 126.8 (CH, C^{15}); 128.3 (CH, C^{19}); 130.3 (CH, C^{10}); 131.6 (C_q, C^{18}); 131.7 (CH, C^{11}); 138.4 (CH, C^{16}); 138.5 (CH, C^{4}); 144.3 (C_q, C^{7}); 146.9 (C_q, C^{17}); 149.4 (CH, C^{2}); 149.8 (C_q, C^{12}); 151.2 (CH, C^{14}); 167.5 (C_q, C^{6}).

^{15}N NMR (50.7 MHz, MeCN): δ (ppm) 209.32 (s, N^{1}); 243.11 (s, N^{13}).

^{31}P NMR (202 MHz, MeCN): δ -144.48.

MS-ESI(pos): m/z 681.17 $[M\text{-}PF_6]^+$.

Elemental Analysis: calcd. for $C_{34}H_{24}IrN_4PF_6$: C, 49.45; H, 2.93; N, 6.78. found: C, 49.48; H, 3.48; N, 6.71.

UV-Vis (CH_2Cl_2): λ_{abs} [nm] (ϵ \ $M^{-1}{\cdot}cm^{-1}$) 253 (52016), 278 (70901), 342 (17129), 378 (8484), 413 (3578), 465 (1008).

ATR-IR ($\tilde{\nu}$ [cm^{-1}]): 3036, 2323, 1731, 1608, 1581, 1560, 1512, 1479, 1438, 1425, 1417, 1317, 1269, 1242, 1230, 1162, 1124, 1065, 1031, 1008, 937, 894, 831, 757, 738, 721, 669, 628.

Synthesis of PS2

0.15 g (0.146 mmol,1 eq) $[Ir(ppy)_2Cl]_2$ and 0.073 g (0.309 mmol, 2.1 eq) **L2** were dissolved in 22 mL CH_2Cl_2 and refluxed for 20 h. The solvent was removed and the crude product was purified by column chromatography with MeCN:KNO_3 (20:1). The product fraction was washed with an aqueous phase of NH_4PF_6. The product was isolated as a yellow powder.

Yield: 0.147 g (88.6 %)

^{1}H NMR (500 MHz, CD_2Cl_2): δ (ppm) 6.39 (dd, $^{3}J_{HH}$= 7.6 Hz, 2H, H^{11}); 6.90 (ddd, $^{3}J_{HH}$= 7.4 Hz, 5.9 Hz, $^{4}J_{HH}$= 1.5 Hz, 2H, H^{3}); 6.99 (ddd, $^{3}J_{HH}$= 7.6 Hz, $^{4}J_{HH}$= 1.4 Hz, 2H, H^{10}); 7.11 (ddd, $^{3}J_{HH}$= 7.6 Hz, $^{4}J_{HH}$= 1.2 Hz, 2H, H^{9}); 7.47 (ddd, $^{3}J_{HH}$= 5.9 Hz, $^{4}J_{HH}$= 1.7 Hz, $^{5}J_{HH}$= 0.7 Hz, 2H, H^{2}); 7.73 (dd, $^{3}J_{HH}$= 8.1 Hz, 5.1 Hz, 2H, H^{15}); 7.78 (m, 4H, H^{4}, H^{8}); 7,98 (m, 2H, H^{5}); 8.15 (dd,

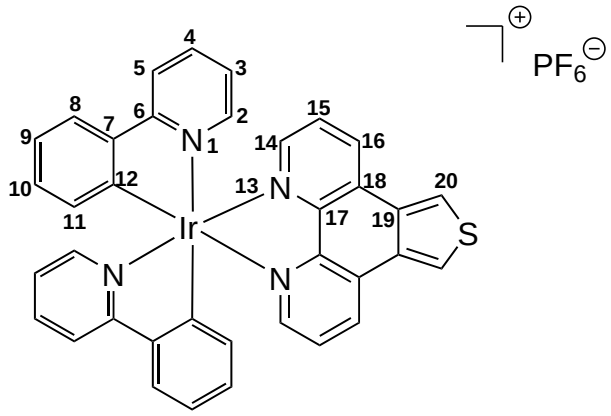

PS2

$^{3}J_{HH}$ = 5.1 Hz, $^{4}J_{HH}$ = 1.4 Hz, 2H, H^{14}); 8.53 (s, 2H, H^{20}); 8.80 (dd, $^{3}J_{HH}$ = 8.1 Hz, $^{4}J_{HH}$ = 1.4 Hz, 2H, H^{16}).

^{13}C NMR (125 MHz, CD_2Cl_2): δ (ppm) 120.3 (CH, C^{5}); 122.7 (CH, C^{20}); 122.7 (C_q, C^{19}); 123.2 (CH, C^{9}); 123.6 (CH, C^{3}); 125.3 (CH, C^{8}); 128.0 (CH, C^{15}); 129.3 (C_q, C^{18}); 131.2 (CH, C^{10}); 132.1 (CH, C^{11}); 134.3 (CH, C^{16}); 138.6 (CH, C^{4}); 144.2 (C_q, C^{7}); 147.9 (C_q, C^{17}); 148.9 (CH, C^{3}); 150.0 (CH, C^{14}); 150.1 (C_q, C^{12}); 168.3 (C_q, C^{6}).

^{15}N NMR (50.7 MHz, CD_2Cl_2): δ (ppm) 209.04 (s, N^{1}); 244.74 (s, N^{13}).

^{31}P NMR (202 MHz, CD_2Cl_2): δ (ppm) -144.44.

MS-ESI(pos): m/z 737.14 $[M\text{-}PF_6]^+$.

Elemental Analysis: calcd. for $C_{36}H_{24}IrN_4PF_6$: C, 49.03; H, 2.74; N, 6.35; S, 3.64. found: C, 48.34; H, 3.01; N, 6.40; S, 3.34.

UV-Vis (CH_2Cl_2): λ_{abs} [nm] (ϵ \ $M^{-1}{\cdot}cm^{-1}$) 264 (68361), 271 (72042), 303 (29060), 365 (10060), 414 (3298), 498 (408).

ATR-IR ($\tilde{\nu}$ [cm^{-1}]): 3047, 2341, 1606, 1583, 1562, 1477, 1460, 1439, 1412, 1313, 1306, 1269, 1228, 1164, 1122, 1064, 1032, 945, 877, 835, 785, 754, 727, 686, 671, 654, 628.

Synthesis of PS3

0.1 g (0.09 mmol, 1 eq) of $[Ir(ppy)_2Cl]_2$ and 0.07 g (0.21 mmol, 2.2 eq) **L3** were refluxed for 48 h in 19 mL CH_2Cl_2. After allowing the mixture to cool down to room temperature, 10 mL of a 0.6 M NH_4PF_6 were added to the reaction mixture. The organic phase was separated, evaporated and the orange solid was dried in under vacuum.

Yield: 0.17 g (79.6 %)

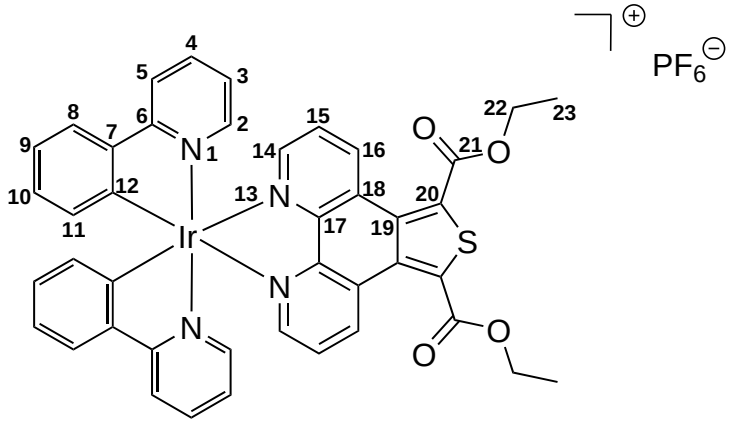

PS3

^{1}H NMR (500 MHz, CD_2Cl_2): δ (ppm) 1.50 (t, $^{3}J_{HH}$ = 7.2 Hz, 6H, H^{23}); 4.55 (q, $^{3}J_{HH}$ = 7.2 Hz, 4H, H^{22}); 6.39 (dd, $^{3}J_{HH}$ = 7.6 Hz, $^{4}J_{HH}$ = 1.0 Hz, 2H, H^{11}); 6.90 (ddd, $^{3}J_{HH}$ = 7.4 Hz, 6.0 Hz, $^{4}J_{HH}$ = 1.5 Hz, 2H, H^{3}); 6.99 (ddd, $^{3}J_{HH}$ = 7.5 Hz, $^{4}J_{HH}$ = 1.3 Hz, 2H, H^{10}); 7.12 (ddd, $^{3}J_{HH}$ = 7.5 Hz, $^{4}J_{HH}$ = 1.0 Hz, 2H, H^{9}); 7.45 (ddd, $^{3}J_{HH}$ = 6.0 Hz, $^{5}J_{HH}$ = 0.5 Hz, 2H, H^{2}); 7.78 (m, 6H, H^{4}, H^{8}, H^{15}); 7.99 (m, 2H, H^{5}); 8.28 (dd, $^{3}J_{HH}$ = 5.1 Hz, $^{4}J_{HH}$ = 1.4 Hz, 2H, H^{14}); 9.89 (dd, $^{3}J_{HH}$ = 8.6 Hz, $^{4}J_{HH}$ = 1.4 Hz, 2H, H^{16}).

^{13}C NMR (125 MHz, CD_2Cl_2): δ (ppm) 14.3 (CH_3, C^{23}); 63.9 (CH_2, C^{22}); 120.3 (CH, C^{5}); 123.3 (CH, C^{9}); 123.7 (C_q, C^{3}); 125.4 (CH, C^{8}); 127.5 (CH, C^{15}); 128.1 (C_q, C^{18}); 131.2 (CH, C^{10}); 132.1 (CH, C^{11}); 133.2 (C_q, C^{20}); 134.9 (C_q, C^{19}); 138.5 (CH, C^{16}); 138.7 (CH, C^{4}); 144.1 (C_q, C^{7}); 148.4 (C_q, C^{17}); 148.9 (CH, C^{2}); 150.2 (C_q, C^{12}); 151.4 (CH, C^{14}); 162.3 (C_q, C^{21}); 168.3 (C_q, C^{6}).

^{15}N NMR (50.7 MHz, CD_2Cl_2): δ (ppm) 208.75 (s, N^{1}); 242.86 (s, N^{13}).

^{31}P NMR (202 MHz, CD_2Cl_2): δ (ppm) -144.48.

MS-ESI(pos): m/z 881.18 $[M\text{-}PF_6]^+$.

Elemental Analysis: calcd. for $C_{42}H_{32}N_4SO_4IrPF_6$: C, 49.17; H, 3.14; N, 5.46; S, 3.12. found: C, 49.72; H, 3.80; N, 5.22; S, 2.87.

UV-Vis (CH_2Cl_2): λ_{abs} [nm] (ϵ \ $M^{-1}{\cdot}cm^{-1}$) 257 (63490), 280 (79685), 384 (10141), 412 (4798), 468 (1178), 496 (825).

ATR-IR ($\tilde{\nu}$ [cm^{-1}]): 3041, 2924, 1709, 1637, 1607, 1584, 1562, 1522, 1477, 1439, 1418, 1391, 1367, 1317, 1306, 1281, 1229, 1184, 1165, 1142, 1109, 1080, 1065, 1029, 1009, 912, 876, 835, 810, 756, 727, 669, 644, 628.

Synthesis of PS4

0.07 g (0.21 mmol, 2.2 eq) **L4**, 0.10 g (0.09 mmol, 1 eq) of $[Ir(ppy)_2Cl]_2$ and 0.05 g (0.51 mmol, 5.7 eq) Na_2CO_3 were given to 7 mL CH_2Cl_2 and 7 mL MeOH. The suspension was stirred for one day. Afterward, additional 5 mL CH_2Cl_2 were added to the green solution and the mixture was acidified with 1 M HCl, which changed the color to yellow. The solvents were removed and the crude product was purified by column chromatography with MeCN and saturated KNO_3 (20:1).

Yield: 0.04 g (53.4 %)

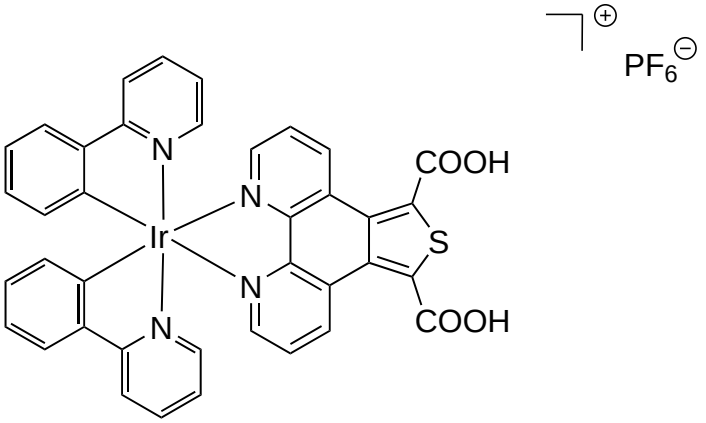

PS4

MS-ESI(pos): m/z 825.12 $[M\text{-}PF_6]^+$.

UV-Vis (CH_2Cl_2): λ_{abs} [nm] (ϵ \ $M^{-1}{\cdot}cm^{-1}$) 256 (37123), 286 (29959), 328 (14375), 382 (5735), 479 (2097).

ATR-IR ($\tilde{\nu}$ [cm^{-1}]): 3205, 3065, 2922, 2848, 1716, 1699, 1607, 1581, 1562, 1477, 1410, 1340, 1269, 1229, 1163, 1126, 1065, 1047, 1032, 829, 758, 731, 694, 669, 662.

Synthesis of PS5

0.02 g (0.19 mmol, 1 eq) $[Ir(ppy)_2Cl]_2$ and 0.16 g (0.40 mmol, 2 eq) **L5** were dissolved in 20 mL ethylene glycol. The yellow suspension was stirred for 48 h at 150 °C. For the workup, 40 mL H_2O and 3 x 40 mL Et_2O were added for extraction. The organic phases were discarded and the aqueous phase was heated to cast out ether residuals. 20 mL of a 0.6 M NH_4PF_6 solution were added to the aqueous phase, while a yellow solid precipitated. The solid was isolated and dried under vacuum.

Yield: 0.30 g (73.8 %)

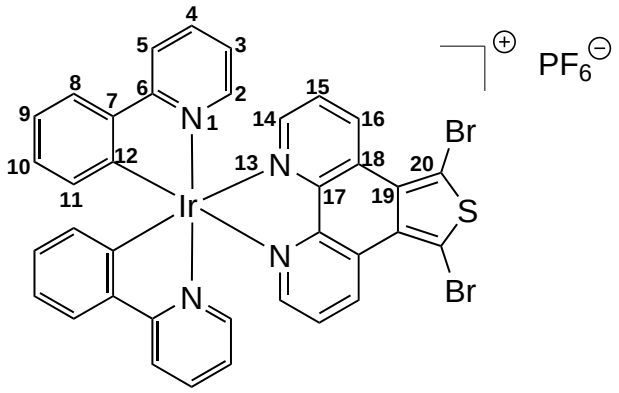

PS5

^{1}H NMR (500 MHz, CD_2Cl_2): δ (ppm) 6.40 (dd, $^3J_{HH}$= 7.6 Hz, $^4J_{HH}$= 0.8 Hz, 2H, H^{11}); 7.00 (ddd, $^3J_{HH}$= 8.1 Hz, 5.9 Hz, $^4J_{HH}$= 1.4 Hz, 2H, H^3); 7.03 (ddd, $^3J_{HH}$= 8.7 Hz, 7.6 Hz, $^4J_{HH}$= 1.3 Hz, 2H, H^{10}); 7.16 (ddd, $^3J_{HH}$= 8.0 Hz, 7.6 Hz, $^4J_{HH}$= 1.2 Hz, 2H, H^9); 7.49 (ddd, $^3J_{HH}$= 5.9 Hz, $^4J_{HH}$= 1.6 Hz, $^5J_{HH}$= 0.7 Hz, 2H, H^2); 7.84 (m, 4H, H^4, H^8); 7.87 (dd, $^3J_{HH}$= 8.6 Hz, 5.2 Hz, 2H, H^{15}); 8.04 (ddd, $^3J_{HH}$= 8.1 Hz, $^4J_{HH}$= 1.4 Hz, $^5J_{HH}$= 0.7 Hz, 2H, H^5); 8.27 (dd, $^3J_{HH}$= 5.2 Hz, $^4J_{HH}$= 1.3 Hz, 2H, H^{14}); 9.98 (dd, $^3J_{HH}$= 8.6 Hz, $^4J_{HH}$= 1.3 Hz, 2H, H^{16}).

^{13}C NMR (125 MHz, CD_2Cl_2): δ (ppm) 110.2 (C_q, C^{20}); 120.0 (CH, C^5); 122.9 (CH, C^9); 123.4 (CH, C^3); 125.0 (CH, C^8); 127.6 (CH, C^{15}); 128.6 (C_q, C^{19}); 128.7 (C_q, C^{18}); 130.8 (CH, C^{10}); 131.7 (CH, C^{11}); 133.3 (CH, C^{16}); 138.4 (CH, C^4); 143.7 (C_q, C^7); 148.0 (C_q, C^{17}); 148.4 (CH, C^2); 149.7 (C_q, C^{12}); 150.2 (CH, C^{14}); 167.8 (C_q, C^6).

^{15}N NMR (50.7 MHz, CD_2Cl_2): δ (ppm) 209.56 (s, N^1); 244.57 (s, N^{13}).

MS-ESI(pos): m/z 894.95 $[M\text{-}PF_6]^+$.

Elemental Analysis: calcd. for $C_{36}H_{22}Br_2IrN_4PF_6$: C, 41.59; H, 2.13; N, 5.39; S, 3.08. found: C, 41.33; H, 2.69; N, 5.53; S, 3.39.

UV-Vis (CH_2Cl_2): λ_{abs} [nm] (ϵ \ $M^{-1}\cdot cm^{-1}$) 253 (61244), 269 (80450), 276 (81528), 332 (20145), 374 (13943), 469 (1130), 505 (748).

ATR-IR ($\tilde{\nu}$ [cm^{-1}]): 3038, 1607, 1580, 1564, 1475, 1448, 1438, 1418, 1408, 1315, 1306, 1267, 1227, 1209, 1165, 1084, 1065, 1032, 1011, 937, 889, 865, 833, 812, 764, 738, 727, 669, 629.

Synthesis of PS6

0.10 g (0.09 mmol, 1 eq) of $[Ir(ppy)_2Cl]_2$ and 0.07 g (0.18 mmol, 2 eq) of **L6** were added to 13 mL of ethylene glycol and 2 mL CH_2Cl_2. The mixture was stirred overnight at 150 °C. The organic phase was concentrated afterwards and the obtained orange solid was dissolved in 10 mL CH_2Cl_2. To this solution 12 mL of a 0.6 M NH_4PF_6 solution were added and stirred overnight. The organic phase was separated and evaporated. The obtained orange solid was dried in vacuum.

Yield: 0.15 g (81.3 %)

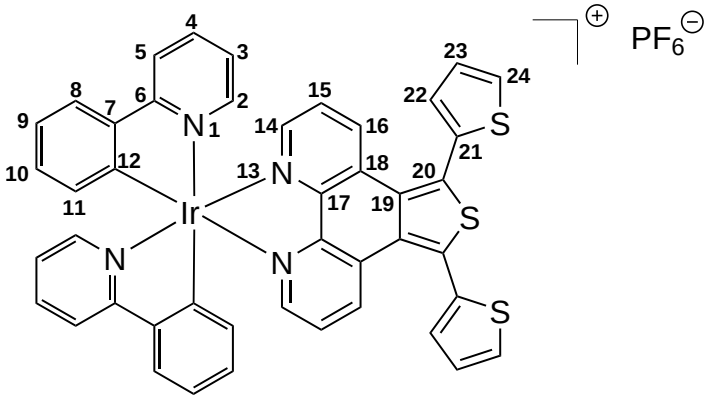

PS6

^{1}H NMR (500 MHz, MeCN): δ (ppm) 6.35 (dd, $^3J_{HH}$= 7.6 Hz, $^4J_{HH}$= 0.8 Hz, 2H, H^9); 6.96 (ddd, $^3J_{HH}$= 7.6 Hz, 7.5 Hz, $^4J_{HH}$= 1.3 Hz, 2H, H^{10}); 6.99 (ddd, $^3J_{HH}$= 7.6 Hz, 5.8 Hz, $^4J_{HH}$= 1.4 Hz, 2H, H^3); 7.08 (dd, $^3J_{HH}$= 7.5 Hz, $^4J_{HH}$= 1.2 Hz, 2H, H^{11}); 7.34 (dd, $^3J_{HH}$= 3.6 Hz, 5.2 Hz, 2H, H^{23}); 7.45 (dd, $^3J_{HH}$= 3.6 Hz, $^4J_{HH}$= 1.2 Hz, 2H, H^{24}); 7.48 (dd, $^3J_{HH}$= 5.2 Hz, 8.5 Hz, 2H, H^{15}); 7.61 (ddd, $^3J_{HH}$= 5.8 Hz, $^4J_{HH}$= 1.6 Hz, $^5J_{HH}$= 0.7 Hz, 2H, H^2); 7.80 (dd, $^3J_{HH}$= 5.2 Hz, $^4J_{HH}$= 1.2 Hz, 2H, H^{22}); 7.85 (m, 4H, H^4, H^8); 8.07—8.10 (m, 4H, H^5, H^{14}); 8.37 (dd, $^3J_{HH}$= 8.5 Hz, $^4J_{HH}$= 1.4 Hz, 2H, H^{16}).

^{13}C NMR (125 MHz, MeCN): δ (ppm) 119.8 (CH, C^5); 122.6 (CH, C^{11}); 123.4 (CH, C^3); 124.9 (CH, C^8); 127.1 (CH, C^{15}); 128.8 (CH, C^{23}); 129.1 (C_q, C^{19}); 129.4 (C_q, C^{20} or C^{18}); 130.2 (CH, C^{22}); 130.4 (CH, C^{10}); 130.5 (CH, C^{24}); 131.6 (CH, C^9); 132.3 (C_q, C^{21}); 132.8 (C_q, C^{20} or C^{18}); 133.9 (CH, C^{16}); 138.5 (CH, C^4); 144.1 (C_q, C^7); 148.3 (C_q, C^{17}); 149.4 (CH, C^2); 149.8 (CH, C^{14}); 150.4 (C_q, C^{12}); 167.5 (C_q, C^6).

^{15}N NMR (50.7 MHz, MeCN): δ (ppm) 209.33 (s, N^1); 243.47 (s, N^{13}).

^{31}P NMR (202 MHz, MeCN): δ (ppm) -144.48.

MS-ESI (pos): m/z 901.10 $[M\text{-}PF_6]^+$.

Elemental Analysis: calcd. for $C_{44}H_{28}N_4S_3IrPF_6$: C, 50.52; H, 2.70; N, 5.36; S, 9.19. found: C, 49.95; H, 3.50; N, 5.25; S, 9.22.

UV-Vis (CH_2Cl_2): λ_{abs} [nm] (ϵ \ $M^{-1}\cdot cm^{-1}$) 254 (69071), 269 (71270), 336 (20258), 366 (15401), 474 (1079), 495 (724).

ATR-IR ($\tilde{\nu}$ [cm^{-1}]): 2922, 2852, 1668, 1607, 1581, 1477, 1460, 1439, 1421, 1406, 1311, 1267, 1242, 1227, 1200, 1182, 1163, 1063, 1032, 1006, 951, 875, 831, 810, 756, 727, 706. 669, 629.

Synthesis of PS7

0.04 g (0.04 mmol, 1 eq) of $[Ir(ppy)_2Cl]_2$ and 0.04 g (0.07 mmol, 2 eq) of **L7** were dissolved in 5 mL ethylene gylcol and 2 mL CH_2Cl_2, and refluxed overnight at 150°C. Afterwards the reaction mixture was concentrated and the remaining solid was dissolved in CH_2Cl_2 and stirred together with 10 mL of 0.6 M NH_4PF_6. The solids were evaporated and the orange solid was dried under vacuum.

Yield: 0.07 g (84.9 %)

^{1}H NMR (500 MHz, CD_2Cl_2): δ (ppm) 6.40 (d, $^3J_{HH}$= 7.5 Hz, 2H, H^{11}); 6.99 (dd, $^3J_{HH}$= 5.9 Hz, $^4J_{HH}$= 1,22 Hz, 2H, H^3); 7.01 (ddd, $^3J_{HH}$= 8.2 Hz, 7.5 Hz, $^4J_{HH}$= 1.1 Hz, 2H, H^{10}); 7.14 (ddd, $^3J_{HH}$= 8.2 Hz, 7.6 Hz,$^4J_{HH}$= 1.0 Hz, 2H, H^9); 7.23 (d, $^3J_{HH}$= 3.8 Hz, 2H, H^{23}); 7.32 (d, $^3J_{HH}$= 3.8 Hz, 2H, H^{22}); 7.51 (m, 2H, H^2); 7.53 (dd, $^3J_{HH}$= 8.5 Hz, 5.1 Hz, 2H, H^{15}); 7.83 (m, 4H, H^4, H^8); 8.01 (d, $^3J_{HH}$= 8.2 Hz, 2H, H^5); 8.17 (dd, $^3J_{HH}$= 5.1 Hz, $^4J_{HH}$= 1.0 Hz, 2H, H^{14}); 8.53 (dd, $^3J_{HH}$= 8.5 Hz, $^4J_{HH}$= 1.0 Hz, 2H, H^{16}).

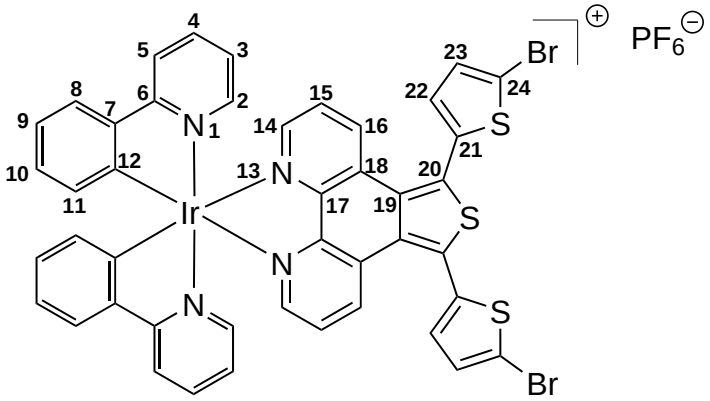

PS7

^{13}C NMR (125 MHz, CD_2Cl_2): δ (ppm) 116.3 (C_q, C^{24}); 119.9 (CH, C^5); 122.8 (CH, C^9); 123.3 (CH, C^3); 124.9 (CH, C^8); 127.2 (CH, C^{15}); 129.0 (C_q, C^{18}); 129.5 (C_q, C^{19}); 130.8 (CH, C^{10}); 131.2 (CH, C^{23}); 131.7 (CH, C^{22}); 131.7 (CH, C^{11}); 132.5 (C_q, C^{20}); 133.7 (C_q, C^{21}); 134.1 (CH, C^{16}); 138.3 (CH, C^4); 143.7 (C_q, C^7); 148.0 (C_q, C^{17}); 148.6 (CH, C^2); 149.9 (C_q, C^{12}, C^{14}); 167.8 (C_q, C^6).

^{15}N NMR (50.7 MHz, CD_2Cl_2): δ (ppm) 208.73 (s, N^1); 244.35 (s, N^{13}).

^{31}P NMR (202 MHz, CD_2Cl_2): δ (ppm) -144.48.

MS-ESI(pos): m/z 1058.93 $[M\text{-}PF_6]^+$.

Elemental Analysis: calcd. for $C_{44}H_{26}N_4S_3Br_2IrPF_6$: C, 43.90; H, 2.18; N, 4.65; S, 7.99. found: C, 43.82; H, 2.87; N, 4.58; S, 7.82.

UV-Vis (CH_2Cl_2): λ_{abs} [nm] (ϵ \ $M^{-1}{\cdot}cm^{-1}$) 256 (74117), 269 (75774), 335 (21601), 375 (16205), 410 (6567), 468 (1083), 500 (637).

ATR-IR ($\tilde{\nu}$ [cm^{-1}]): 3041, 2922, 2852, 1607, 1581, 1562, 1477, 1459, 1439, 1425, 1406, 1335, 1315, 1267, 1227, 1202, 1182, 1163, 1126, 1105, 1062, 1029, 1011, 972, 945, 876, 835, 804, 756, 727, 669, 629.

Synthesis of PS8

0.01 g (0.20 mmol, 2.1 eq) **L8** and 0.10 (0.09 mmol, 1 eq) $[Ir(ppy)_2]_2$ were dissolved in 10 mL ethylene glycol. 2 mL CH_2Cl_2 were added for a better solubility. The solution was refluxed for 16 h. CH_2Cl_2 was added again and also 10 mL 0.06 M NH_4PF_6. The solution was stirred for a few hours and the organic phase was

evaporated afterward. The crude product was purified by column chromatography with MeCN:saturated KNO_3 (10:1), which results in six different fractions. The product was isolated as orange solid.

Yield: 0.125 g (52.4 %)

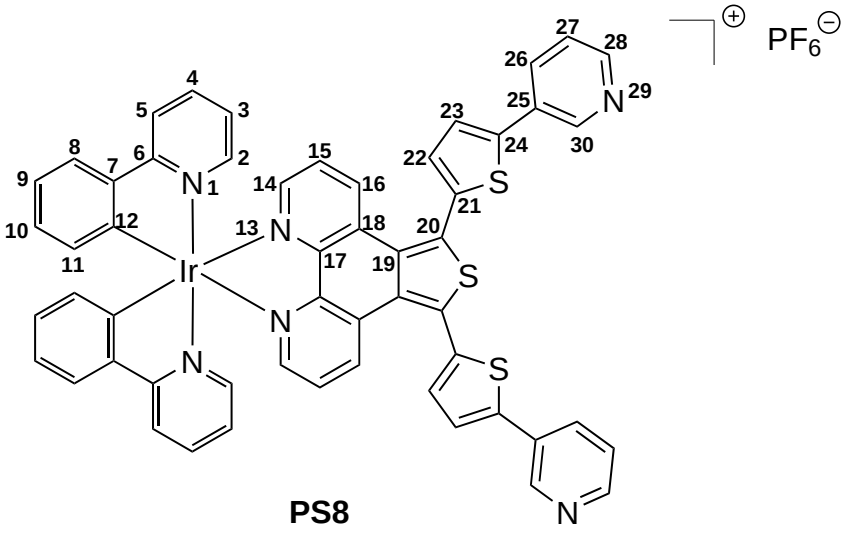

PS8

^{1}H NMR (500 MHz, CD_2Cl_2): δ (ppm) 6.37 (dd, $^{3}J_{HH}$= 7.7 Hz, $^{4}J_{HH}$= 0.7 Hz, 2H, H^{11}); 6.95–6.99 (m, 4H, H^{3}, H^{10}); 7.09 (ddd, $^{3}J_{HH}$= 8.1 Hz, 7.5 Hz, $^{4}J_{HH}$= 1.2 Hz, 2H, H^{9}); 7.39 (ddd, $^{3}J_{HH}$= 8.0 Hz, 5.0 Hz, $^{5}J_{HH}$= 0.5 Hz, 2H, H^{27}); 7.43 (d, $^{3}J_{HH}$= 3.6 Hz, 2H, H^{23}); 7.47 (d, $^{3}J_{HH}$= 8.5 Hz, 5.3 Hz, 2H, H^{15}); 7.50 (ddd, $^{3}J_{HH}$= 5.8 Hz, $^{4}J_{HH}$= 1.6 Hz, $^{5}J_{HH}$= 0.8 Hz, 2H, H^{2}); 7.57 (dd, $^{3}J_{HH}$= 3.6 Hz, 2H, H^{22}); 7.76–7.81 (m, 4H, H^{4}, H^{8}); 7.97–7.99 (m, 4H, H^{5}, H^{26}); 8.14 (dd, $^{3}J_{HH}$= 5.2 Hz, $^{4}J_{HH}$= 1.4 Hz, 2H, H^{14}); 8.58 (dd, $^{3}J_{HH}$= 4.8 Hz, $^{4}J_{HH}$= 1.6 Hz, 2H, H^{28}); 8.60 (dd, $^{3}J_{HH}$= 8.5 Hz, $^{4}J_{HH}$= 1.4 Hz, 2H, H^{16}); 8.94 (dd, $^{4}J_{HH}$= 2.0 Hz, 2H, H^{30}).

^{13}C NMR (125 MHz, CD_2Cl_2): δ (ppm) 22.1 (CH, C^{32}); 120.3 (CH, C^{5}); 123.2 (CH, C^{9}); 123.7 (CH, C^{3}); 124.2 (CH, C^{27}); 125.3 (CH, C^{8}); 126.0 (CH, C^{22}); 127.5 (CH, C^{15}); 129.6 (C_q, C^{19} or C^{20} or C^{21}); 129.7 (C_q, C^{19} or C^{20} or C^{21}); 129.7 (C_q, C^{19} or C^{20} or C^{21}); 131.2 (CH, C^{10}); 132.1 (CH, C^{23}); 132.8 (CH, C^{11}); 133.4 (CH, C^{26}); 133.5 (C_q, C^{25}); 134.5 (CH, C^{16}); 138.7 (CH, C^{4}); 144.1 (C_q, C^{7}); 145.2 (C_q, C^{24}); 147.4 (CH, C^{30}); 148.4 (C_q, C^{17}); 149.0 (CH, C^{2}); 149.9 (CH, C^{28}); 150.2 (CH, C^{14}); 150.3 (C_q, C^{12}); 168.2 (C_q, C^{6}).

^{15}N NMR (50.7 MHz, CD_2Cl_2): δ (ppm) 208.74 (s, N^{1}); 244.16 (s, N^{13}); 316.30 (s, N^{29}).

^{31}P NMR (202 MHz, CD_2Cl_2): δ (ppm) -144.46.

MS-ESI(pos): m/z 1055.17 $[M\text{-}PF_6]^+$; 528.08 $[((M+H)\text{-}PF_6)/2]$.

Elemental Analysis: calcd. for $C_{54}H_{34}N_6S_3IrPF_6$: C, 54.04; H, 2.86; N, 7.00; S, 8.01. found: C, 53.40; H, 3.24; N, 6.72; S, 7.44.

UV-Vis (CH_2Cl_2): λ_{abs} [nm] (ϵ \ $M^{-1}\cdot cm^{-1}$) 256 (85154), 265 (85949), 296 (75211), 370 (26786), 413 (10609), 468 (1652), 499 (898).

ATR-IR ($\tilde{\nu}$ [cm^{-1}]): 3039, 2922, 1607, 1581, 1562, 1522, 1477, 1446, 1410, 1313, 1267, 1257, 1226, 1199, 1184, 1163, 1124, 1063, 1029, 966, 875, 835, 798, 756, 729, 702, 669, 629.

Synthesis of PS9

0.03 g (0.049 mmol, 2.1 eq) **L9** and 0.026 g (0.023 mmol, 1 eq) $[Ir(ppy)_2Cl]_2$ were dissolved in 2 mL ethylene glycol and 1 mL CH_2Cl_2. The solution was refluxed for 24 h and subsequently added to 10 mL 0.6 M NH_4PF_6 solution and 10 mL CH_2Cl_2. The two phase mixture was stirred for 2 hours. The organic phase was filtered and concentrated under vacuum. The crude complex was purified by column chromatography with MeCN:saturated KNO_3 20:1. **PS9** was isolated as solid crystalline solid.

Yield: 0.054 g (87.7 %)

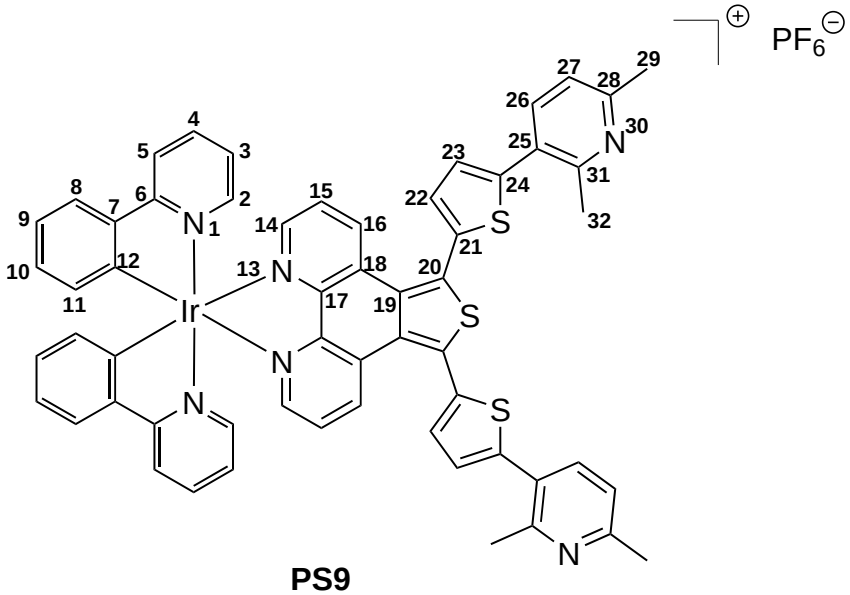

PS9

^{1}H NMR (500 MHz, CD_2Cl_2): δ (ppm) 2.71 (s, 6H, H^{29}); 2.84 (s, 6H, H^{32}); 6.37 (dd, $^3J_{HH}$= 7.7 Hz, $^4J_{HH}$= 0.7 Hz, 2H, H^{11}); 6.96 (m, 4H, H^3, H^{10}); 7.10 (ddd,

$^{3}J_{HH}$= 8.1 Hz, 7.5 Hz, $^{4}J_{HH}$= 1.2 Hz, 2H, H^{9}); 7.38 (d, $^{3}J_{HH}$= 3.6 Hz, 2H, H^{22}); 7.40 (d, $^{3}J_{HH}$= 8.1 Hz, 2H, H^{27}); 7.47 (d, $^{3}J_{HH}$= 3.6 Hz, 2H, H^{23}); 7.49 (ddd, $^{3}J_{HH}$= 5.9 Hz, $^{4}J_{HH}$= 1.6 Hz, $^{5}J_{HH}$= 0.7 Hz, 2H, H^{2}); 7.52 (dd, $^{3}J_{HH}$= 8.5 Hz, 5.2 Hz, 2H, H^{15}); 7.77 (m, 4H, H^{4}, H^{8}); 7.97 (ddd, $^{3}J_{HH}$= 7.8 Hz, 2H, H^{5}); 8.09 (d, $^{3}J_{HH}$= 8.1 Hz, 2H, H^{26}); 8.14 (dd, $^{3}J_{HH}$= 5.2 Hz, $^{4}J_{HH}$= 1.4 Hz, 2H, H^{14}); 8.57 (dd, $^{3}J_{HH}$= 8.5 Hz, $^{4}J_{HH}$= 1.4 Hz, 2H, H^{16}).

^{13}C NMR (125 MHz, CD_2Cl_2): δ (ppm) 22.1 (CH, C^{32}); 22.2 (CH, C^{29}); 120.3 (CH, C^{5}); 123.2 (CH, C^{27}); 123.5 (CH, C^{9}); 123.7 (CH, C^{3}); 125.4 (CH, C^{8}); 127.6 (CH, C^{15}); 128.6 (C_q, C^{25}); 129.5 (C_q, C^{18}); 129.8 (C_q, C^{19}); 129.9 (CH, C^{22}); 131.2 (CH, C^{23}); 131.5 (CH, C^{10}); 132.1 (CH, C^{11}); 133.1 (C_q, C^{20}); 134.4 (C_q, C^{21}); 134.5 (CH, C^{16}); 138.8 (CH, C^{4}); 142.8 (CH, C^{26}); 144.1 (C_q, C^{7}); 148.5 (C_q, C^{17}); 148.9 (CH, C^{2}); 150.3 (CH, C^{12},C^{14}); 153.8 (C_q, C^{28}); 156.2 (C_q, C^{31}); 168.3 (C_q, C^{6}).

^{15}N NMR (50.7 MHz, CD_2Cl_2): δ (ppm) 208.7 (s, N^{1}); 243.9 (s, N^{13}); 258.6 (s, N^{30}).

^{31}P NMR (202 MHz, CD_2Cl_2): δ (ppm) -144.48.

MS ESI (pos): m/z 1111.23 $[M\text{-}PF_6]^+$.

Elemental Analysis: calcd. for $C_{58}H_{42}N_6S_3IrPF_6$: C, 55.45; H, 3.37; N, 6.69; S, 7.66. found: C, 54.16; H, 3.86; N, 6.48; S, 7.03.

UV-Vis (CH_2Cl_2): λ_{abs} [nm] (ϵ \ $M^{-1}\cdot cm^{-1}$) 255 (75440), 263 (78171), 270 (77950), 280 (71832), 337 (25798), 370 (21054), 470 (1811), 498 (898).

ATR-IR ($\tilde{\nu}$ [cm^{-1}]): 3035, 2922, 1607, 1583, 1560, 1477, 1446, 1439, 1423, 1408, 1389, 1373, 1308, 1267, 1226, 1199, 1165, 1124, 1101, 1063, 1031, 964, 876, 835, 808, 758, 729, 669.

Synthesis of IrN

0.10 g (0.096 mmol, 1 eq) of **PS5**, 0.02 g (0.21 mmol, 2.5 eq) 4-hydroxypyridine and 0.21 g (1.52 mmol, 16 eq) K_2CO_3 were added to 20 mL MeCN and refluxed for 4 days. Afterward, the mixture was allowed to cool down, filtrated and washed with MeCN. The organic phase was evaporated and, the residue was purified by column chromatography with MeCN:KNO_3 (25:1). The solvent of the product fraction was evaporated and the solid was dissolved in CH_2Cl_2. The remaining solid was filtered

off and the organic layer was treated with an aqueous NH_4PF_6 solution. The product was isolated from the organic phase as an orange crystalline solid.

Yield: 0.03 g (29.7 %)

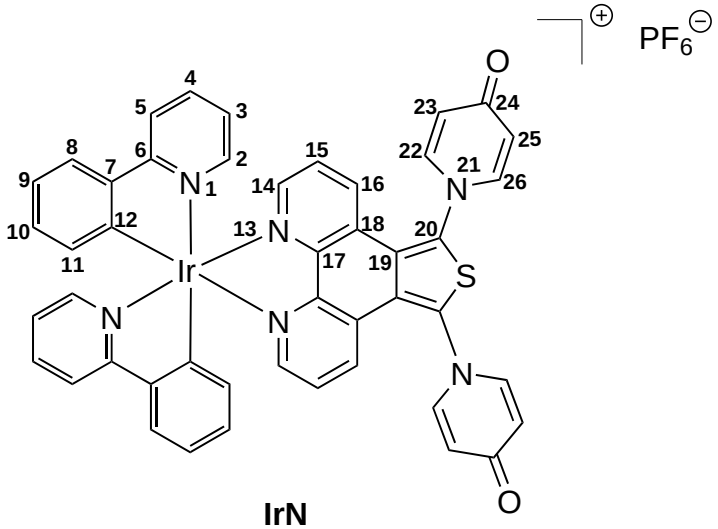

IrN

^{1}H NMR (700 MHz, CD_2Cl_2): δ (ppm) 6.34 (dd, $^{3}J_{HH}$ = 7.6 Hz, $^{4}J_{HH}$ = 0.7 Hz, 2H, H^{11}); 6.49 (dd, $^{3}J_{HH}$ = 7.7 Hz, $^{4}J_{HH}$ = 2.8 Hz, 2H, H^{22} or H^{26}); 6.56 (dd, $^{3}J_{HH}$ = 7.7 Hz, $^{4}J_{HH}$ = 2.8 Hz, 2H, H^{22} or H^{26}); 6.95–6.97 (m, 4H, H^{3}, H^{10}); 7.09 (ddd, 2H, $^{3}J_{HH}$ = 8.0 Hz, 7.5 Hz, $^{4}J_{HH}$ = 1.1 Hz, 2H, H^{9}); 7.48 (dd, $^{3}J_{HH}$ = 5.8 Hz, $^{4}J_{HH}$ = 0.7 Hz, 2H, H^{2}); 7.54 (dd, $^{3}J_{HH}$ = 7.7 Hz, $^{4}J_{HH}$ = 2.6 Hz, 2H, H^{23} or H^{25}); 7.61 (dd, $^{3}J_{HH}$ = 8.2 Hz, 5.3 Hz, 2H, H^{15}); 7.71 (dd, $^{3}J_{HH}$ = 7.7 Hz, $^{4}J_{HH}$ = 2.6 Hz, 2H, H^{23} or H^{25}); 7.74–7.77 (m, 4H, H^{4}, H^{8}); 7.90 (dd, $^{3}J_{HH}$ = 8.2 Hz, $^{4}J_{HH}$ = 1.3 Hz, 2H, H^{14}); 7.95 (d, $^{3}J_{HH}$ = 8.1 Hz, 2H, H^{5}); 8.20 (dd, $^{3}J_{HH}$ = 5.3 Hz, $^{3}J_{HH}$ = 1.3 Hz, 2H, H^{16}).

^{13}C NMR (176 MHz, CD_2Cl_2): δ (ppm) 120.2 (CH, C^{5}); 121.0 (CH, C^{22} or C^{26}); 121.1 (CH, C^{22} or C^{26}); 123.3 (CH, C^{9}); 124.0 (CH, C^{3}); 125.3 (CH, C^{8}); 126.9 (C_q, C^{18}); 127.3 (C_q, C^{19}); 128.6 (CH, C^{15}); 131.1 (CH, C^{10}); 132.1 (CH, C^{11}); 134.0 (CH, C^{14}); 137.6 (C_q, C^{20}); 138.6 (CH, C^{4}); 140.9 (CH, C^{23} or C^{25}); 141.0 (CH, C^{23} or C^{25}); 144.2 (C_q, C^{7}); 149.0 (C_q, C^{17}); 149.4 (CH, C^{2}); 149.9 (C_q, C^{12}); 151.0 (CH, C^{16}); 167.8 (C_q, C^{6}); 178.5 (C_q, C^{24}).

^{15}N NMR (70.9 MHz, CD_2Cl_2): δ (ppm) 131.02 (s, N^{21}); 208.38 (s, N^{13}); 245.86 (s, N^{1}).

^{31}P NMR (202 MHz, CD_2Cl_2): δ (ppm) -145.17.

MS-ESI(pos): m/z 923.18 $[M]^+$.

Elemental Analysis: calcd. for $C_{46}H_{30}N_6SO_2IrPF_6$: C, 51.73; H, 2.83; N, 7.87; S, 3.00. found: C, 51.54; H, 3.49; N, 7.39; S, 2.42.

ATR-IR ($\tilde{\nu}$ [cm^{-1}]): 3054, 2922, 2852, 1736, 1643, 1629, 1607, 1581, 1556, 1477, 1439, 1416, 1335, 1267, 1248, 1229, 1178, 1144, 1105, 1063, 1032, 1011, 964, 875, 835, 808, 758, 729, 667, 646, 628.

Synthesis of IrO

0.20 g (0.192 mmol, 1 eq) of **PS5**, 0.0474 g (0.481 mmol, 2.5 eq) 3-hydroxypyridine and 0.43 g (3.08 mmol, 16 eq) K_2CO_3 were added to 41 mL MeCN and refluxed for 4 days. Afterward, the mixture was allowed to cool down, filtrated and washed with MeCN. The organic phase was evaporated and the residue was purified by column chromatography with MeCN:KNO_3 (20:1). The solvent of the product fraction was evaporated and the solid was dissolved in CH_2Cl_2. The remaining solid was filtered off and the organic layer was treated with an aqueous NH_4PF_6 solution. The product was isolated from the organic phase as an orange crystalline solid.

Yield: 0.062 g (30.2 %)

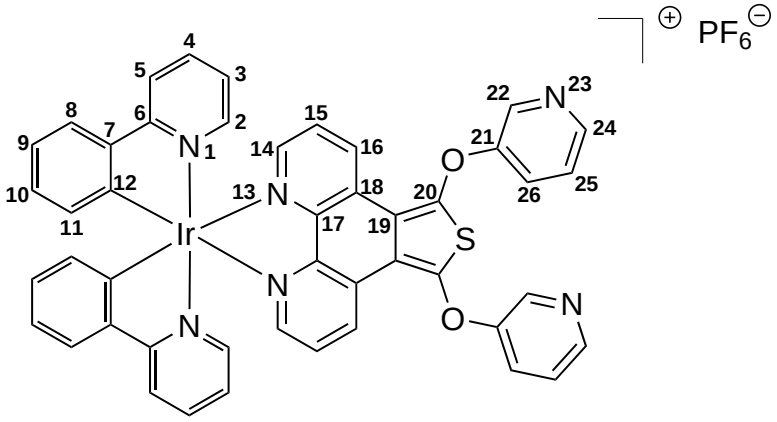

IrO

^{1}H NMR (500 MHz, CD_2Cl_2): δ (ppm) 6.35 (dd, $^3J_{HH}$= 7.5 Hz, $^4J_{HH}$= 1.0 Hz, 2H, H^{11}); 6.97 (ddd, $^3J_{HH}$= 7.5 Hz, 7.6 Hz, $^4J_{HH}$= 1.3 Hz, 2H, H^{10}); 6.99 (ddd, $^3J_{HH}$= 8.0 Hz, 5.8 Hz, $^4J_{HH}$= 1.4 Hz, 2H, H^3); 7.09 (ddd, $^3J_{HH}$= 8.0 Hz, 7.6 Hz, $^4J_{HH}$= 1.1 Hz, 2H, H^9). 7.40 (ddd, $^3J_{HH}$= 8.4 Hz, 4.7 Hz, $^5J_{HH}$= 0.5 Hz, 2H, H^{25}); 7.53 (ddd, $^3J_{HH}$=5.8 Hz, $^4J_{HH}$= 1.6 Hz, $^5J_{HH}$= 0.7 Hz 2H, H^2); 7.59 (dd, $^3J_{HH}$= 8.4 Hz, 5.3 Hz, 2H, H^{15}); 7.63 (ddd, $^3J_{HH}$= 8.5 Hz, $^4J_{HH}$= 3.0 Hz, 1.3 Hz, 2H, H^{26}); 7.76 (dd, $^3J_{HH}$= 8.0 Hz, $^4J_{HH}$= 1.2 Hz, 2H, H^8); 7.79 (ddd, $^3J_{HH}$= 8.3 Hz, 8.0 Hz, $^4J_{HH}$= 1.6 Hz, 2H, H^4); 7.98 (d, $^3J_{HH}$= 8.3 Hz, 2H, H^5); 8.07 (dd, $^3J_{HH}$= 5.3 Hz, $^4J_{HH}$= 1.5 Hz, 2H, H^{14}); 8.48 (dd, $^3J_{HH}$= 4.7 Hz,

$^{4}J_{HH}$ = 1.3 Hz, 2H, H^{24}); 8.61 (d, $^{4}J_{HH}$ = 2.9 Hz, 2H, H^{22}); 8.98 (dd, $^{3}J_{HH}$ = 8.4 Hz, $^{4}J_{HH}$ = 1.5 Hz, 2H, H^{16}).

^{13}C NMR (125 MHz, CD_2Cl_2): δ (ppm) 115.9 (C_q, C^{19}); 120.3 (CH, C^{5}); 123.2 (CH, C^{9}); 123.8 (CH, C^{3}); 125.2 (CH, C^{25}); 125.3 (CH, C^{8}); 125.5 (CH, C^{26}); 128.5 (CH, C^{15}); 129.0 (C_q, C^{18}); 131.1 (CH, C^{10}); 132.1 (CH, C^{11}); 135.6 (CH, C^{16}); 138.7 (CH, C^{4}); 140.4 (CH, C^{22}); 144.2 (C_q, C^{7}); 147.3 (CH, C^{24}); 148.5 (C_q, C^{17}); 148.6 (C_q, C^{20}); 149.2 (CH, C^{2}); 149.6 (CH, C^{14}); 150.2 (C_q, C^{12}); 154.5 (C_q, C^{21}); 168.2 (C_q, C^{6}).

^{15}N NMR (70.9 MHz, CD_2Cl_2): δ (ppm) 209.12 (s, N^{1}); 244.19 (s, N^{13}); 321.15 (s, N^{23}).

^{31}P NMR (202 MHz, CD_2Cl_2): δ (ppm) -144.57.

MS-ESI: m/z 877.22 $[M-H+Na, M+Na]^+$; 855.23 $[2M+Na]^+$; 439.11 $[M+Na]^+$.

Elementary Analysis: calcd. for $C_{46}H_{30}N_6O_2SIrPF_6$: C, 51.73; H, 2.83; N, 7.87; S, 3.00. found: C, 51.55; H, 3.41; N, 7.32; S, 2.82.

UV-Vis (CH_2Cl_2): λ_{abs} [nm] ($\epsilon \setminus M^{-1}\cdot cm^{-1}$) 254 (66595), 268 (70753), 334 (18764),382 (9778), 412 (6063), 470 (1201).

9.3.3 Catalysts

Synthesis of Fe1

The reaction was conducted under inert atmosphere. 0.15 g (0.31 mmol, 1 eq) **22** was dissolved in 4 mL dry oxygen-free CH_2Cl_2 and, 0.04 g (0.31 mmol, 1 eq) $FeCl_2$ was dissolved in 3 mL dry oxygen-free ethanol. The ethanol solution was added to the CH_2Cl_2 solution, which resulted in a precipitation of a dark yellow solid. The solution was filtered off and the solid was washed two times with 2 mL dry oxygen-free ethanol. Afterward the solid was dried under vacuum.

Yield: 0.11 (57.1 %)

MS-ESI (pos): m/z 634.05 $[M+2O+H]^+$ 582.06 $[M-Cl+O]^+$; 566.06 $[M-Cl]^+$ 476.17 $[M-FeCl_2]^+$.

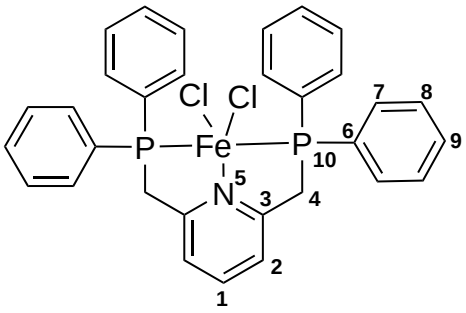

Fe1

Elemental analysis: calcd. for $C_{34}H_{27}NCl_2FeP_2$: C, 61.82; H, 4.52; N, 2.33. found: C, 60.50; H, 4.58; N, 2.38.

ATR-IR ($\tilde{\nu}$ [cm^{-1}]): 3052, 1598, 1566, 1481, 1456, 1432, 1407, 1382, 1330, 1284, 1182, 1099, 1029, 999, 842, 823, 798, 752, 736, 686, 597, 540, 503, 462, 432, 418, 358, 341, 295, 270.

Synthesis of Fe2

The reaction was conducted under inert atmosphere. 0.05 g sodium were added carefully to 1.04 g mercury in a Schlenk flask to obtain 5 % Na/Hg. Afterward 0.20 g(0.32 mmol, 1 eq) of **22** and 10 mL dry, oxygen-free THF were added to the Schlenk flask. CO gas was passed through the solution for 30 minutes. During this time, the color of the solution changed from yellow to violet. Afterward, the solution was passed through celite, evaporated under inert atmosphere and dried under vacuum.

Yield: 0.03 g (16.8 %)

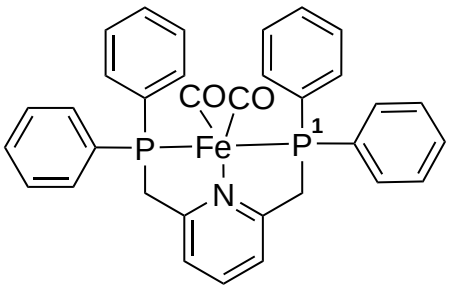

Fe2

^{31}P NMR (202 MHz, C_6D_6): δ (ppm) 71.98 (s, P^1).

MS-ESI (pos): m/z 530.14 $[M\text{-}2CO+H]^+$; 508.16 $[M\text{-}Fe(CO)_2+H+2O]^+$; 492.16 $[M\text{-}Fe(CO)_2+H+O]^+$; 476.17 $[M\text{-}Fe(CO)_2+H]^+$.

ATR-IR ($\tilde{\nu}$ [cm^{-1}]): 3056, 2960, 2922, 2854, 1944, 1904, 1462, 1433, 1103, 831, 812, 787, 760, 750, 739, 716, 704, 689, 619, 608, 582, 571, 536, 509, 480, 465, 449, 428, 411, 382, 359, 338, 257.

Synthesis of Co1

0.45 g (1.9 mmol, 1 eq) $CoCl_2 \cdot 6\ H_2O$ and 1.0 g (6.4 mmol, 3.4 eq) 2,2'-bipyridine were mixed together and dissolved in 45 mL methanol. The solution was stirred overnight at 40 °C. Afterward the solvent was removed and the obtained solid was dried in vacuum.

Yield: 0.71 (70.8 %)

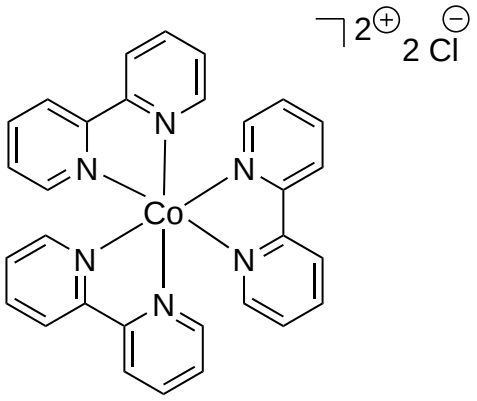

Co1

MS-ESI (pos): m/z 441.01 $[M\text{-}bpy+2Cl]^+$; 406.04 $[M\text{-}bpy+Cl]^+$; 249.97 $[M\text{-}2bpy+Cl]^+$; 185.54 $[M\text{-}bpy]]^+$.

Elemental analysis: calcd. for $C_{30}H_{24}N_6CoCl_2$: C, 60.22; H, 4.04; N, 14.04. found: C, 55.77; H, 4.80; N, 12.92.

Synthesis of Co2

0.29 g (1.2 mmol, 1 eq) $CoCl_2 \cdot 6\ H_2O$ and 0.6 g (3.9 mmol, 3.2 eq) 2,2'-bipyridine were mixed together and dissolved in 18 mL ethanol. The solution was refluxed overnight. Afterward the solvent was added to 110 mL Et_2O and a pale rose solid precipitated. The obtained solid was dried in vacuum.

Yield: 0.39 (73.5 %)

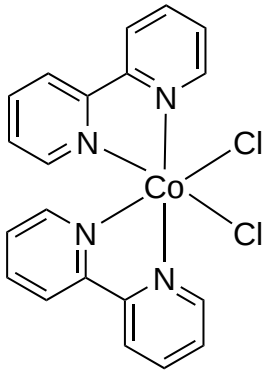

Co2

MS-ESI (pos): m/z 406.04 $[M\text{-}Cl]^+$; 371.07 $[M\text{-}2Cl]^+$; 185.54 $[M\text{-}bpy]]^+$.

Synthesis of Co3-1[194]

1.04 g (4.2 mmol, 1 eq) $CoCl_2 \cdot 6\ H_2O$ and 0.98 g (8.4 mmol, 2 eq) dimethylglyoxime were dissolved in 30 mL acetone, which resulted in a violet solution. The mixture was stirred for 10 min. Undissolved material was filtered off and the blue/violet solution was left standing overnight, during which green crystals grew. The crystals were filtered off and dried under vacuum. The substance was not characterized and directly used for the synthesis of **Co3** and the bimetallic systems.

Yield: 1.1 g (72.7 %)

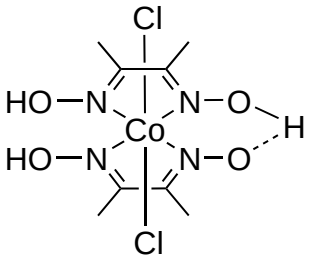

Co3-1

Synthesis of Co3[68]

0.40 g (1.1 mmol, 1 eq) $Co(dmgH)(dmgH)_2Cl_2$ was added to 40 mL methanol. During the addition of 0.15 mL (1.1 mmol, 1 eq) TEA, the color changed from dark

green to brown. 0.09 mL (1.1 mmol, 1 eq) pyridine was added, which resulted in a pale yellow precipitate. The reaction mixture was stirred for further 1.5 h and the precipitate was filtered off and washed with H_2O, EtOH and Et_2O. The solid was dried under vacuum.

Yield: 0.32 g (72.1 %)

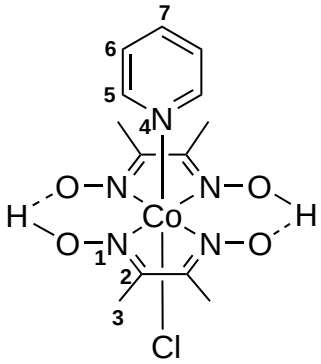

Co3

^{1}H NMR (500 MHz, $CDCl_3$): δ (ppm) 2.39 (s, 12H, H^3); 7.23 (dd, $^{3}J_{HH}$ = 6.85 Hz, 7.58 Hz, H^6); 7.70 (tt, $^{3}J_{HH}$ = 7.58 Hz, $^{4}J_{HH}$ = 1.42 Hz, 1H, H^7); 8.26 (dd, $^{3}J_{HH}$ = 6.85 Hz, $^{4}J_{HH}$ = 1.42 Hz, 2H, H^5).

^{13}C NMR (125 MHz, $CDCl_3$): δ (ppm) 13.3 (CH_3, C^3); 125.8 (CH, C^6); 139.1 (CH, C^7); 151.3 (CH, C^5); 152.8 (C_q, C^2).

^{15}N NMR (50.7 MHz, CD_2Cl_2): δ (ppm) 212.19 (s, N^4); 315.8 (s, N^1).

MS-ESI (pos): m/z 404.05 $[M]^+$; 368.08 $[M\text{-}Cl]^+$; 289.03 $[M\text{-}Py\text{-}Cl]^+$.

Elemental analysis: calcd. for $C_{13}H_{19}N_5O_4Co_2Cl$: C, 38.68; H, 4.74; N, 17.35. found: C, 38.51; H, 4.78; N, 17.23.

9.3.4 Bimetallic Complexes

Synthesis of [IrthCo]PF_6

0.031 g (0.08 mmol, 2 eq) Co(dmgH)(dmgH$_2$)Cl_2 was added to 10 mL methanol. 11.6 μL Et_3N (0.08 mmol, 2 eq) was added, which led to a brown solution. The solution was stirred at room temperature for 15 min. 0.051 g (0.042 mmol, 1 eq) **PS8** was dissolved in 5 mL CH_2Cl_2 and slowly added to the methanol solution. The

mixture was stirred at room temperature for 1 h 30 min. A stream of air was passed through the solution for 15 min. Afterward, the solution was added to cold Et_2O, which led to the precipitation of a yellow solid. The solid was filtered off, washed with Et_2O and dried under vacuum.

Yield: 0.064 g (90.1 %)

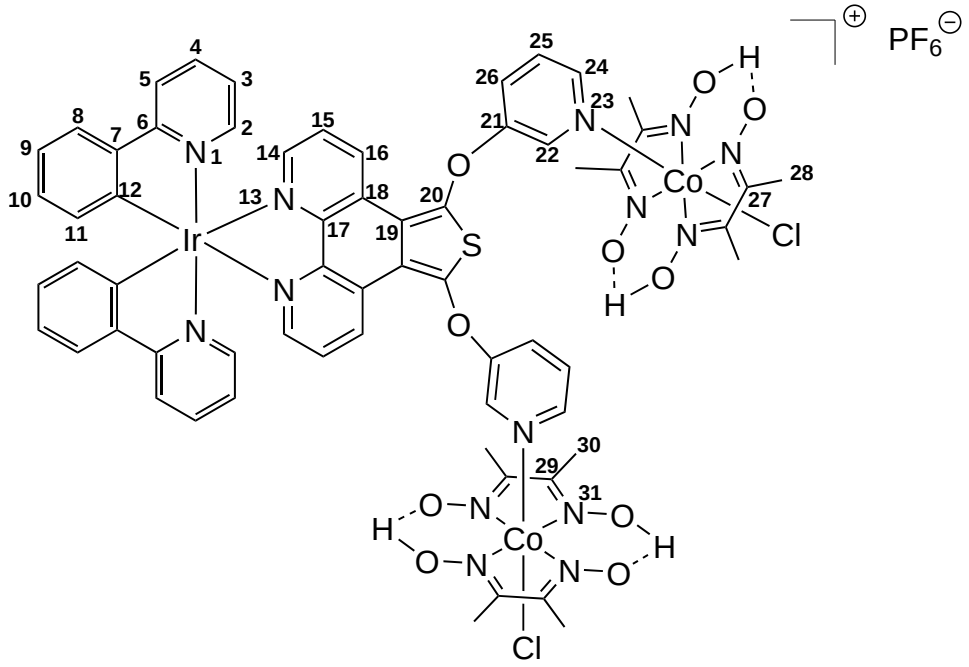

[IrOCo]PF_6

^{1}H NMR (700 MHz, CD_2Cl_2): δ (ppm) 2.37 (s, 12H, H^{32} or H^{34}); 2.38 (s, 12H, H^{32} or H^{34}); 6.37 (d, $^3J_{HH}$ = 7.5 Hz, 2H, H^{11}); 6.96–7.01 (m, 4H, H^3, H^{10}); 7.09 (ddd, $^3J_{HH}$ = 8.5 Hz, 7.3 Hz, $^4J_{HH}$ = 0.8 Hz, 2H, H^9); 7.31 (dd, $^3J_{HH}$ = 8.1 Hz, 5.9 Hz, 2H, H^{27}); 7.46 (d, $^3J_{HH}$ = 3.7 Hz, 2H, H^{23}); 7.49–7.53 (m, 4H, H^2, H^{15}); 7.55 (dd, $^3J_{HH}$ = 3.7 Hz, 2H, H^{22}); 7.77–7.81 (m, 4H, H^8, H^4); 7.98–8.00 (m, H^5, 4H, H^{26}); 8.13 (d, $^3J_{HH}$ = 5.9 Hz, 2H, H^{28}); 8.16 (dd, $^3J_{HH}$ = 5.2 Hz, $^4J_{HH}$ = 1.3 Hz, 2H, H^{14}); 8.54 (d, $^4J_{HH}$ = 1.7 Hz, 2H, H^{30}); 8.59 (dd, $^3J_{HH}$ = 8.5 Hz, $^4J_{HH}$ = 1.3 Hz, 2H, H^{16}).

^{13}C NMR (176 MHz, CD_2Cl_2): δ (ppm) 12.8 (CH_3, C^{31} or C^{33}); 119.9 (CH, C^5); 122.8 (CH, C^9); 123.4 (CH, C^3); 125.0 (CH, C^8); 127.2 (CH, C^{15} or C^{22}); 127.3 (CH, C^{15} or C^{22}); 126.0 (CH, C^{27}); 129.0 (C_q, C^{18}); 129.5 (C_q, C^{19}); 130.8 (CH, C^{10}); 131.7 (CH, C^{11}); 131.8 (C_q, C^{25}); 132.2 (CH, C^{23}); 132.6 (C_q, C^{21}); 134.1 (CH, C^{16}); 134.2 (C_q, C^{20}); 135.7 (CH, C^{26}); 138.3 (CH, C^4); 141.7 (CH, C^{24}); 143.7 (C_q, C^7); 147.7 (CH, C^{30}); 148.0 (C_q, C^{17}); 148.6 (CH, C^2); 149.8 (CH, C^{14}); 149.9 (C_q, C^{12}); 150.0 (CH, C^{28}); 152.9 (C_q, C^{31} or C^{33}); 152.9 (C_q, C^{31} or C^{33}); 167.8 (C_q, C^6).

^{15}N NMR (70.9 MHz, CD_2Cl_2): δ (ppm) 209.47 (s, N^{1}); 213.16 (s, N^{29}); 244.47 (s, N^{13}); 315.18 (s, N^{35}).

^{31}P NMR (202 MHz, CD_2Cl_2): δ (ppm) -144.53.

MS-ESI (pos): m/z 1703.18 $[M]^+$; 1379.17 $[M\text{-}Co(dmgH)_2Cl]^+$; 1055.17 $[M\text{-}2(Co(dmgH)_2Cl)]^+$; 528.09 $[M\text{-}2(Co(dmgH)_2Cl)]^{2+}$; 289.03 $[Co(dmgH)_2]^+$.

Elemental Analysis: calcd. for $C_{70}H_{62}N_{14}S_3O_8IrCo_2Cl_2PF_6$: C, 45.46; H, 3.38; N, 10.60; S, 5.20. found: C, 45.23; H, 3.67; N, 10.17; S, 4.75.

UV-Vis (CH_2Cl_2): λ_{abs} [nm] (ϵ \ $M^{-1}{\cdot}cm^{-1}$) 258 (12700), 268 (11560), 300 (70665), 333 (41108), 374 (26696), 468 (1652), 502 (992).

ATR-IR ($\tilde{\nu}$ [cm^{-1}]): 3078, 2355, 1605, 1562, 1478, 1446, 1423, 1369, 1317, 1240, 1161, 1093, 1062, 1035, 979, 840, 804, 758, 730, 693, 627, 557, 513, 416, 378, 276.

Synthesis of [IrOCo]PF_6

0.034 g (0.09 mmol, 2 eq) $Co(dmgH)(dmgH_2)Cl_2$ was added to 10.5 mL methanol. 13.1 μL Et_3N (0.09 mmol, 2 eq) was added, which led to a brown solution. The solution was stirred at room temperature for 15 min. 0.050 g (0.047 mmol, 1 eq) **IrO** was dissolved in 5 mL CH_2Cl_2 and slowly added to the methanol solution. The mixture was stirred at room temperature for 1 h 30 min. A stream of air was passed through the solution for 30 min. Afterward, the solution was added to cold Et_2O, which led to the precipitation of a yellow solid. The solid was filtered off, washed with Et_2O and dried under vacuum.

Yield: 0.062 g (76.8 %)

^{1}H NMR (700 MHz, CD_2Cl_2): δ (ppm) 2.17 (s, 12H, H^{28} or H^{30}); 2.27 (s, 12H, H^{28} or H^{30}); 6.39 (dd, $^{3}J_{HH}$ = 7.6 Hz, $^{4}J_{HH}$ = 0.7 Hz, 2H, H^{11}); 6.96–7.01 (m, 4H, H^{3}, H^{10}); 7.11 (ddd, $^{3}J_{HH}$ = 8.0 Hz, 7.5 Hz, $^{4}J_{HH}$ = 0.7 Hz, 2H, H^{9}); 7.30 (dd, $^{3}J_{HH}$ = 8.5 Hz, 5.6 Hz, 2H, H^{25}); 7.59 (dd, $^{3}J_{HH}$ = 8.4 Hz, 5.2 Hz, 2H, H^{15}); 7.73–7.81 (m, 8H, H^{2}, H^{4}, H^{8}, H^{26}); 7.96 (d, $^{3}J_{HH}$ = 7.9 Hz, 2H, H^{5}); 8.00 (d, $^{3}J_{HH}$ = 5.6 Hz, 2H, H^{24}); 8.09 (d, $^{4}J_{HH}$ = 2.5 Hz, 2H, H^{22}); 8.19 (dd, $^{4}J_{HH}$ = 5.2 Hz, $^{4}J_{HH}$ = 1.3 Hz, 2H, H^{14}); 8.71 (dd, $^{3}J_{HH}$ = 8.4 Hz, $^{4}J_{HH}$ = 1.3 Hz, 2H, H^{16}).

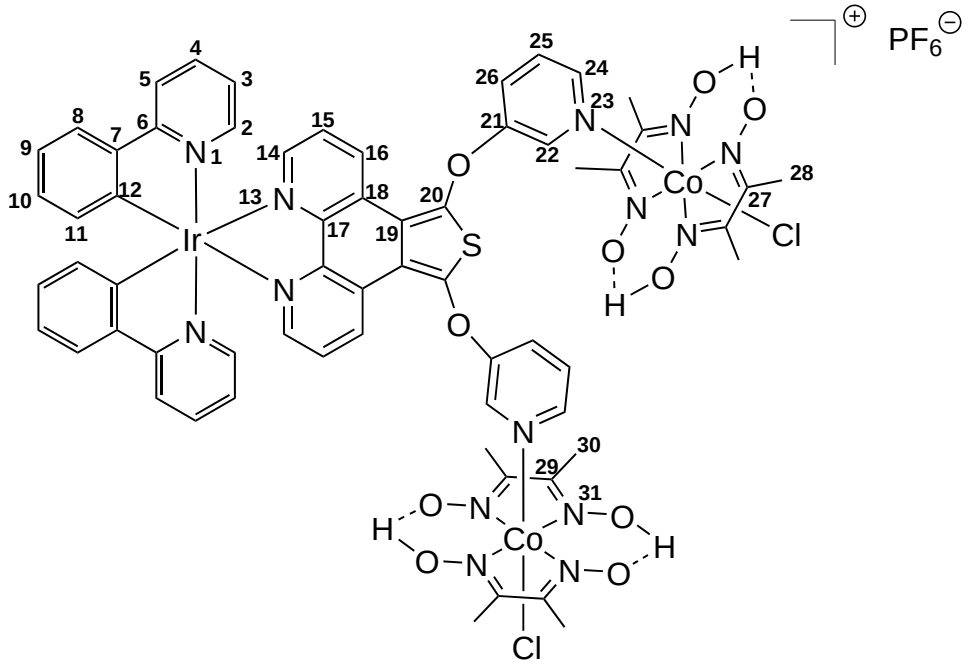

[IrOCo]PF_6

^{13}C NMR (176 MHz, CD_2Cl_2): δ (ppm) 13.0 (CH_3, C^{28} or C^{30}); 13.1 (CH_3, C^{28} or C^{30}); 119.4 (C_q, C^{19}); 120.1 (CH, C^5); 123.2 (CH, C^9); 124.3 (CH, C^3); 125.2 (CH, C^8); 127.2 (CH, C^{25}); 128.2 (C_q, C^{18}); 128.6 (CH, C^{15}); 131.1 (CH, C^{10}); 132.1 (CH, C^{11}); 135.4 (CH, C^{16}); 138.7 (CH, C^4); 140.6 (CH, C^{22}); 144.3 (C_q, C^7); 146.3 (C_q, C^{20}); 148.1 (CH, C^{24}); 149.0 (C_q, C^{17}); 149.7 (CH, C^2); 150.1 (C_q, C^{12}; 150.2 (CH, C^{14}); 153.1 (C_q, C^{27} or C^{29}); 153.3 (C_q, C^{27} or C^{29}); 154.6 (C_q, C^{21}); 167.8 (C_q, C^6).

^{15}N NMR (70.9 MHz, CD_2Cl_2): δ (ppm) 208.8 (s, N^1); 216.3 (s, N^{23}); 245.4 (s, N^{13}); 313.5 (s, N^{31}).

^{31}P NMR (202 MHz, CD_2Cl_2): δ (ppm) -144.7.

MS-ESI (pos): m/z 1571.18 $[M]^+$; 1247.18 $[M\text{-}Co(dmgH)_2Cl]^+$; 923.17 $[M\text{-}2(Co(dmgH)_2Cl)]^+$.

Elemental Analysis: calcd. for $C_{62}H_{58}N_{14}SO_{10}IrCo_2Cl_2PF_6$: C, 43.37; H, 3.40; N, 11.42; S, 1.87. found: C, 43.05; H, 3.62; N, 10.91; S, 1.75.

UV-Vis (CH_2Cl_2): λ_{abs} [nm] (ϵ \ $M^{-1}{\cdot}cm^{-1}$) 251(106944), 264 (117468), 273 (103097), 333 (25689), 376 (16997), 470 (1464), 512 (845).

ATR-IR ($\tilde{\nu}$ [cm^{-1}]): 3052, 2359, 2339, 1735, 1608, 1560, 1479, 1439, 1416, 1373, 1323, 1238, 1164, 1126, 1094, 1063, 1032, 982, 756, 730, 692, 556, 513, 419, 376 (Co-Cl), 284, 278.

Bibliography

[1] S. Rau, B. Schäfer, D. Gleich, E. Anders, M. Rudolph, M. Friedrich, H. Görls, W. Henry, J. G. Vos, *Angew. Chem.* **2006**, *118*, 6361–6364.

[2] A. T. Wagner, R. Zhou, K. S. Quinn, T. a. White, J. Wang, K. J. Brewer, *J. Phys. Chem. A* **2015**, *119*, 6781–6790.

[3] Z.-T. Yu, Y.-J. Yuan, X. Chen, J.-G. Cai, Z.-G. Zou, *Chem. - A Eur. J.* **2015**, *21*, 10003–10007.

[4] Y.-J. Yuan, Z.-T. Yu, H.-L. Gao, Z.-G. Zou, C. Zheng, W. Huang, *Chem. - A Eur. J.* **2013**, *19*, 6340–6349.

[5] K. Sakai, H. Ozawa, *Coord. Chem. Rev.* **2007**, *251*, 2753–2766.

[6] E. D. Cline, S. E. Adamson, S. Bernhard, *Inorg. Chem.* **2008**, *47*, 10378–10388.

[7] M. Elvington, J. Brown, S. M. Arachchige, K. J. Brewer, *J. Am. Chem. Soc.* **2007**, *129*, 10644–10645.

[8] H. Wales, T. Juniper, E. Shuckburgh, *Climate Change (A Ladybird Expert Book)*, Penguin Books Limited, **2017**.

[9] H. J. Rockström, J., Gaffney, O., Rogelj, J., Meinshausen, M., Nakicenovic, N., & Schellnhuber, *Science* **2017**, *355*, 1269–1271.

[10] A. Boddien, B. Loges, F. Gärtner, C. Torborg, K. Fumino, H. Junge, R. Ludwig, M. Beller, *J. Am. Chem. Soc.* **2010**, *132*, 8924–8934.

[11] F. Joó, *ChemSusChem* **2008**, *1*, 805–808.

[12] British Petroleum (BP) Public Limited Company, BP Statistical Review of World Energy June 2016, London, **2016**.

[13] *CO_2 Emissions from Fuel Combustion 2017*, OECD, **2017**.

[14] F. Armstrong, K. Blundell, *Energy... beyond oil*, OUP Oxford, **2007**.

[15] R. J. Nicholls, *GeoJournal* **1995**, *37*, 369–379.

[16] L. Tosi, L. Carbognin, *Geophys. Res. Lett.* **2002**, *29*, 1562–1566.

[17] D. Coumou, S. Rahmstorf, *Nat. Clim. Chang.* **2012**, *2*, 491–496.

[18] M. K. Van Aalst, *Disasters* **2006**, *30*, 5–18.

[19] N. W. Arnell, J. A. Lowe, B. Lloyd-Hughes, T. J. Osborn, *Clim. Change* **2018**, *147*, 61–76.

[20] C. P. Morice, J. J. Kennedy, N. A. Rayner, P. D. Jones, *J. Geophys. Res. Atmos.* **2012**, *117*, 1–58.

[21] T. Boden, G. Marland, R. Andres, Global, Regional, and National Fossil-Fuel CO_2 Emissions, Carbon Dioxide Information Analysis Center, Oak Ridge National Laboratory, **2010**.

[22] Umweltbundesamt, Erneuerbare Energien in Deutschland, tech. rep., Dessau-Roßlau, **2017**, pp. 6–23.

[23] E. Hau, *Windkraftanlagen: Grundlagen. Technik. Einsatz. Wirtschaftlichkeit*, Springer Berlin Heidelberg, **2017**.

[24] S. Geitmann, *Erneuerbare Energien und alternative Kraftstoffe: Mit neuer Energie in die Zukunft*, Books on Demand, **2005**.

[25] International Energy Agency, Hydrogen Production and Storage. R&D Priorities and Gaps, tech. rep., **2006**, pp. 1–33.

[26] M. Peukert, R. Diercks, F. O. Fischer, T. Rappuhn, J. Stachel, B. Albert, G. Romanowski, *Von Kohlehalden und Wasserstoff*, German Bunsen Society for Physical Chemistry, Frankfurt am Main, **2013**, pp. 1–69.

[27] Erstflug für viersitziges Wasserstoff-Flugzeug, http://www.scinexx.de/wissen-aktuell-20678-2016-09-30.html, Accessed: 2018-07-17, **2016**.

[28] Hier fährt der Wasserstoff-Zug, http://www.faz.net/aktuell/wirtschaft/erster-wasserstoff-zug-hessens-gestartet-15540616.html, Accessed: 2018-07-17, **2018**.

[29] D. Stolten, *Hydrogen and Fuel Cells: Fundamentals, Technologies and Applications*, John Wiley & Sons, **2010**.

[30] J. Töpler, J. Lehmann, *Wasserstoff und Brennstoffzelle*, Springer Berlin Heidelberg, Berlin, Heidelberg, **2017**.

[31] S. Colombaroli, C. E. Tuna, F. Henrique, M. D. Araujo, L. Silveira, L. F. Vane, D. T. Pedroso, *Sustainable Hydrogen Production Processes*, Springer International Publishing, Cham, **2017**.

[32] S. Geitmann, *Wasserstoff & Brennstoffzellen: Die Technik von morgen!*, Hydrogeit, **2013**.

[33] M. Carmo, D. L. Fritz, J. Mergel, D. Stolten, *Int. J. Hydrog. Energy* **2013**, *38*, 4901–4934.

[34] S. Paddison, K. Promislow, *Device and Materials Modeling in PEM Fuel Cells*, Springer New York, **2008**.

[35] I. Akkerman, M. Janssen, J. Rocha, R. H. Wijffels, *Int. J. Hydrog. Energy* **2002**, *27*, 1195–1208.

[36] C. Acar, I. Dincer, C. Zamfirescu, *Int. J. Energy Res.* **2014**, *38*, 1903–1920.

[37] T. Jafari, E. Moharreri, A. S. Amin, R. Miao, W. Song, S. L. Suib, *Molecules* **2016**, *21*, 1–29.

[38] I. Dincer, *Comprehensive Energy Systems*, Elsevier Science, **2018**.

[39] T. Bak, J. Nowotny, M. Rekas, C. Sorrell, *Int. J. Hydrog. Energy* **2002**, *27*, 991–1022.

[40] S. Giménez, J. Bisquert, *Photoelectrochemical Solar Fuel Production: From Basic Principles to Advanced Devices*, Springer, **2016**.

[41] H.-Z. B. für Materialien und Energie, Young Investigator Group Operando Characterization of Solar Fuel Materials.

[42] L. Yuan, C. Han, M.-Q. Yang, Y.-J. Xu, *Int. Rev. Phys. Chem.* **2016**, *35*, 1–36.

[43] L. L. Tinker, S. Bernhard, *Inorg. Chem.* **2009**, *48*, 10507–10511.

[44] P. Du, R. Eisenberg, *Energy Environ. Sci.* **2012**, *5*, 6012–6021.

[45] H. Ozawa, M.-a. Haga, K. Sakai, *J. Am. Chem. Soc.* **2006**, *128*, 4926–4927.

[46] H. Ozawa, K. Sakai, *Chem. Commun.* **2011**, *47*, 2227–2242.

[47] E. Amouyal, *Sol. Energy Mater. Sol. Cells* **1995**, *38*, 249–276.

[48] J. Hawecker, J.-M. Lehn, R. Ziessel, *Nouv. J. Chem.* **1983**, *14*.

[49] G. M. Brown, B. S. Brunschwig, C. Creutz, J. F. Endicott, N. Sutin, *J. Am. Chem. Soc.* **1979**, *101*, 1298–1300.

[50] J. R. Fisher, D. J. Cole-Hamilton, *J. Chem. Soc. Dalt. Trans.* **1984**, 809–813.

[51] H.-h. Cui, M.-q. Hu, H.-m. Wen, G.-l. Chai, C.-b. Ma, H. Chen, C.-n. Chen, *Dalt. Trans.* **2012**, *41*, 13899–13907.

[52] P. Zhang, M. Wang, X. Li, H. Cui, J. Dong, L. Sun, *Sci. China Chem.* **2012**, *55*, 1274–1282.

[53] A. Fihri, V. Artero, M. Razavet, C. Baffert, W. Leibl, M. Fontecave, *Angew. Chem.* **2008**, *120*, 574–577.

[54] K. L. Mulfort, *Comptes Rendus Chim.* **2017**, *20*, 221–229.

[55] S. E. Canton et al., *J. Phys. Chem. Lett.* **2013**, *4*, 1972–1976.

[56] S. Jasimuddin, T. Yamada, K. Fukuju, J. Otsuki, K. Sakai, *Chem. Commun.* **2010**, *46*, 8466–8468.

[57] T. Lazarides, M. Delor, I. V. Sazanovich, T. M. McCormick, I. Georgakaki, G. Charalambidis, J. A. Weinstein, A. G. Coutsolelos, *Chem. Commun.* **2014**, *50*, 521–523.

[58] S. Tschierlei et al., *Chem. - A Eur. J.* **2009**, *15*, 7678–7688.

[59] F. Gärtner, A. Boddien, E. Barsch, K. Fumino, S. Losse, H. Junge, D. Hollmann, A. Brückner, R. Ludwig, M. Beller, *Chem. - A Eur. J.* **2011**, *17*, 6425–6436.

[60] J. I. Goldsmith, W. R. Hudson, M. S. Lowry, T. H. Anderson, S. Bernhard, *J. Am. Chem. Soc.* **2005**, *127*, 7502–7510.

[61] M. Raynal, P. Ballester, A. Vidal-Ferran, P. W.N. M. van Leeuwen, *Chem. Soc. Rev.* **2014**, *43*, 1660–1733.

[62] Y. Pellegrin, F. Odobel, *Comptes Rendus Chim.* **2017**, *20*, 283–295.

[63] P. J. DeLaive, T. K. Foreman, C. Giannotti, D. G. Whitten, *J. Am. Chem. Soc.* **1980**, *102*, 5627–5631.

[64] M. Wang, Y. Na, M. Gorlov, L. Sun, *Dalt. Trans.* **2009**, 6458–6467.

[65] A. J. Esswein, D. G. Nocera, *Chem. Rev.* **2007**, *107*, 4022–4047.

[66] J. Lakowicz, *Principles of Fluorescence Spectroscopy*, Springer, **2013**.

[67] J. Lindon, G. Tranter, D. Koppenaal, *Encyclopedia of Spectroscopy and Spectrometry*, Elsevier Science, **2016**.

[68] P. Du, J. Schneider, G. Luo, W. W. Brennessel, R. Eisenberg, *Inorg. Chem.* **2009**, *48*, 4952–4962.

[69] M. Freitag, F. Giordano, W. Yang, M. Pazoki, Y. Hao, B. Zietz, M. Grätzel, A. Hagfeldt, G. Boschloo, *J. Phys. Chem. C* **2016**, *120*, 9595–9603.

[70] B. Valeur, M. Berberan-Santos, *Molecular Fluorescence: Principles and Applications*, Wiley-VCH, **2002**, pp. 77–89.

[71] A. Holleman, E. Wiberg, N. Wiberg, *Lehrbuch der anorganischen Chemie*, de Gruyter, **2007**.

[72] G. Wang, M. Zhou, J. T. Goettel, G. J. Schrobilgen, J. Su, J. Li, T. Schlöder, S. Riedel, *Nature* **2014**, *514*, 475–477.

[73] K.-i. Fujita, Y. Tanaka, M. Kobayashi, R. Yamaguchi, *J. Am. Chem. Soc.* **2014**, *136*, 4829–4832.

[74] N. Onishi, S. Xu, Y. Manaka, Y. Suna, W.-H. Wang, J. T. Muckerman, E. Fujita, Y. Himeda, *Inorg. Chem.* **2015**, *54*, 5114–5123.

[75] J. M. Thomsen, S. W. Sheehan, S. M. Hashmi, J. Campos, U. Hintermair, R. H. Crabtree, G. W. Brudvig, *J. Am. Chem. Soc.* **2014**, *136*, 13826–13834.

[76] A. J. Howarth, D. L. Davies, F. Lelj, M. O. Wolf, B. O. Patrick, *Inorg. Chem.* **2014**, *53*, 11882–11889.

[77] J. Liu, Y. Liu, Q. Liu, C. Li, L. Sun, F. Li, *J. Am. Chem. Soc.* **2011**, *133*, 15276–15279.

[78] Y. Tang, H.-R. Yang, H.-B. Sun, S.-J. Liu, J.-X. Wang, Q. Zhao, X.-M. Liu, W.-J. Xu, S.-B. Li, W. Huang, *Chem. - A Eur. J.* **2013**, *19*, 1311–1319.

[79] S. Okada et al., *Dalt. Trans.* **2005**, 1583–1590.

[80] A. F. Henwood, A. K. Bansal, D. B. Cordes, A. M. Z. Slawin, I. D. W. Samuel, E. Zysman-Colman, *J. Mater. Chem. C* **2016**, *4*, 3726–3737.

[81] K. Hasan, A. K. Bansal, I. D. Samuel, C. Roldán-Carmona, H. J. Bolink, E. Zysman-Colman, *Sci. Rep.* **2015**, *5*, 12325–12341.

[82] J. F. Hull, D. Balcells, J. D. Blakemore, C. D. Incarvito, O. Eisenstein, G. W. Brudvig, R. H. Crabtree, *J. Am. Chem. Soc.* **2009**, *131*, 8730–8731.

[83] R. Lalrempuia, N. D. McDaniel, H. Müller-Bunz, S. Bernhard, M. Albrecht, *Angew. Chem. Int. Ed.* **2010**, *49*, 9765–9768.

[84] G. Menendez Rodriguez, G. Gatto, C. Zuccaccia, A. Macchioni, *ChemSusChem* **2017**, *10*, 4503–4509.

[85] N. D. McDaniel, F. J. Coughlin, L. L. Tinker, S. Bernhard, *J. Am. Chem. Soc.* **2008**, *130*, 210–217.

[86] S.-y. Takizawa, C. Pérez-Bolívar, P. Anzenbacher, S. Murata, *Eur. J. Inorg. Chem.* **2012**, 3975–3979.

[87] S. Fan, X. Zong, P. E. Shaw, X. Wang, Y. Geng, A. R. G. Smith, P. L. Burn, L. Wang, S.-C. Lo, *Phys. Chem. Chem. Phys.* **2014**, *16*, 21577–21585.

[88] I. N. Mills, J. A. Porras, S. Bernhard, *Acc. Chem. Res.* **2018**, *51*, 352–364.

[89] M. Kirch, J.-M. Lehn, J.-P. Sauvage, *Helv. Chim. Acta* **1979**, *62*, 1345–1384.

[90] X. W. Song, Y. Meng, C. L. Zhang, C. B. Ma, C. N. Chen, *Inorg. Chem. Commun.* **2017**, *76*, 52–54.

[91] O. Bokareva, T. Möhle, A. Neubauer, S. Bokarev, S. Lochbrunner, O. Kühn, *Inorganics* **2017**, *5*, 23.

[92] D. R. Whang, K. Sakai, S. Y. Park, *Angew. Chem. Int. Ed.* **2013**, *52*, 11612–11615.

[93] F. Gärtner, B. Sundararaju, A.-E. Surkus, A. Boddien, B. Loges, H. Junge, P. H. Dixneuf, M. Beller, *Angew. Chem. Int. Ed.* **2009**, *48*, 9962–9965.

[94] Y. J. Yuan, Z. T. Yu, X. Y. Chen, J. Y. Zhang, Z. G. Zou, *Chem. - A Eur. J.* **2011**, *17*, 12891–12895.

[95] Z. T. Yu, Y. J. Yuan, J. G. Cai, Z. G. Zou, *Chem. - A Eur. J.* **2013**, *19*, 1303–1310.

[96] K. Kitamoto, K. Sakai, *Chem. - A Eur. J.* **2016**, *22*, 12381–12390.

[97] L. Petermann, R. Staehle, M. Pfeifer, C. Reichardt, D. Sorsche, M. Wächtler, J. Popp, B. Dietzek, S. Rau, *Chem. - A Eur. J.* **2016**, *22*, 8240–8253.

[98] L. Troian-Gautier, C. Moucheron, *Molecules* **2014**, *19*, 5028–5087.

[99] M. S. Lowry, S. Bernhard, *Chem. Eur. J.* **2006**, *12*, 7970–7977.

[100] I. Tavernelli, B. F. Curchod, U. Rothlisberger, *Chem. Phys.* **2011**, *391*, 101–109.

[101] C. E. Welby, L. Gilmartin, R. R. Marriott, A. Zahid, C. R. Rice, E. A. Gibson, P. I. P. Elliott, *Dalt. Trans.* **2013**, *42*, 13527–13536.

[102] R. A. Kirgan, B. P. Sullivan, D. P. Rillema in *Photochem. Photophysics Coord. Compd. II*, *Vol. 281*, Springer, Berlin, Heidelberg, **2007**, pp. 45–100.

[103] M. S. Lowry, W. R. Hudson, R. a. Pascal, S. Bernhard, *J. Am. Chem. Soc.* **2004**, *126*, 14129–14135.

[104] A. B. Tamayo, S. Garon, T. Sajoto, P. I. Djurovich, I. M. Tsyba, R. Bau, M. E. Thompson, *Inorg. Chem.* **2005**, *44*, 8723–8732.

[105] S. Lamansky, P. Djurovich, D. Murphy, F. Abdel-Razzaq, H. E. Lee, C. Adachi, P. E. Burrows, S. R. Forrest, M. E. Thompson, *J. Am. Chem. Soc.* **2001**, *123*, 4304–4312.

[106] M. S. Lowry, J. I. Goldsmith, J. D. Slinker, R. Rohl, R. A. Pascal, G. G. Malliaras, S. Bernhard, *Chem. Mater.* **2005**, *17*, 5712–5719.

[107] E. D. Cline, S. Bernhard, *Chim. Int. J. Chem.* **2009**, *63*, 709–713.

[108] B. F. DiSalle, S. Bernhard, *J. Am. Chem. Soc.* **2011**, *133*, 11819–11821.

[109] H. N. Kagalwala, D. N. Chirdon, S. Bernhard, *Solar Fuel Generation*, Wiley, Chichester, **2017**, Chapter 12, pp. 583–615.

[110] R. Marusak, K. Doan, S. Cummings, *Integrated Approach to Coordination Chemistry: An Inorganic Laboratory Guide*, Wiley, **2007**, pp. 193–214.

[111] K. Kalyanasundaram, M. Grätzel, *Photosensitization and Photocatalysis Using Inorganic and Organometallic Compounds*, Springer Science & Business Media, **2013**, pp. 124–126.

[112] Y. L. Chow, W. C. Danen, S. F. Nelsen, D. H. Rosenblatt, *Chem. Rev.* **1978**, *78*, 243–274.

[113] P. D. Frischmann, K. Mahata, F. Würthner, *Chem. Soc. Rev.* **2013**, *42*, 1847–1870.

[114] S.-C. Yang, G. Chang, G.-J. Yang, Y.-J. Wang, B. Fang, *Catal. Sci. Technol.* **2015**, *5*, 228–233.

[115] S. Metz, S. Bernhard, *Chem. Commun.* **2010**, *46*, 7551–7553.

[116] I. N. Mills, H. N. Kagalwala, D. N. Chirdon, A. C. Brooks, S. Bernhard, *Polyhedron* **2014**, *82*, 104–108.

[117] L. Tschugaeff, *Berichte der Dtsch. Chem. Gesellschaft* **1907**, *40*, 3498–3504.

[118] G. N. Schrauzer, J. Kohnle, *Chem. Ber.* **1964**, *97*, 3056–3064.

[119] G. N. Schrauzer, *Acc. Chem. Res.* **1968**, *1*, 97–103.

[120] G. N. Schrauzer, G. W. Parshall, E. R. Wonchoba, *Bis(Dimethylglyoximato)Cobalt Complexes: ("Cobaloximes")*, Wiley-Blackwell, **1968**, pp. 61–70.

[121] T.-H. Chao, J. H. Espenson, *J. Am. Chem. Soc.* **1978**, *100*, 129–133.

[122] X. Hu, B. S. Brunschwig, J. C. Peters, *J. Am. Chem. Soc.* **2007**, *129*, 8988–8998.

[123] J. L. Dempsey, B. S. Brunschwig, J. R. Winkler, H. B. Gray, *Acc. Chem. Res.* **2009**, *42*, 1995–2004.

[124] P. Connolly, J. H. Espenson, *Inorg. Chem.* **1986**, *25*, 2684–2688.

[125] M. Razavet, V. Artero, M. Fontecave, *Inorg. Chem.* **2005**, *44*, 4786–4795.

[126] T. Lazarides, T. McCormick, P. Du, G. Luo, B. Lindley, R. Eisenberg, *J. Am. Chem. Soc.* **2009**, *131*, 9192–9194.

[127] A. Fihri, V. Artero, A. Pereira, M. Fontecave, *Dalton Trans.* **2008**, 5567–5569.

[128] P. Zhang, M. Wang, C. Li, X. Li, J. Dong, L. Sun, *Chem. Commun.* **2010**, *46*, 8806–8808.

[129] C. Li, M. Wang, J. Pan, P. Zhang, R. Zhang, L. Sun, *J. Organomet. Chem.* **2009**, *694*, 2814–2819.

[130] C. Baffert, V. Artero, M. Fontecave, *Inorg. Chem.* **2007**, *46*, 1817–1824.

[131] A. Jacques, O. Schott, K. Robeyns, G. S. Hanan, B. Elias, *Eur. J. Inorg. Chem.* **2016**, *2016*, 1779–1783.

[132] C. Lentz, O. Schott, T. Auvray, G. Hanan, B. Elias, *Inorg. Chem.* **2017**, *56*, 10875–10881.

[133] T. M. McCormick, Z. Han, D. J. Weinberg, W. W. Brennessel, P. L. Holland, R. Eisenberg, *Inorg. Chem.* **2011**, *50*, 10660–10666.

[134] W. T. Eckenhoff, W. R. McNamara, P. Du, R. Eisenberg, *Biochim. Biophys. Acta* **2013**, *1827*, 958–973.

[135] S. Hansen, M. Klahn, T. Beweries, U. Rosenthal, *ChemSusChem* **2012**, *5*, 656–660.

[136] S. Fukuzumi, T. Kobayashi, T. Suenobu, *Angew. Chem. Int. Ed.* **2011**, *50*, 728–731.

[137] L. Sun, L. Hammarström, B. Åkermark, S. Styring, *Chem. Soc. Rev.* **2001**, *30*, 36–49.

[138] M. Karnahl, C. Kuhnt, F. Ma, A. Yartsev, M. Schmitt, B. Dietzek, S. Rau, J. Popp, *ChemPhysChem* **2011**, *12*, 2101–2109.

[139] M. G. Pfeffer et al., *Angew. Chem. Int. Ed.* **2015**, *54*, 5044–5048.

[140] G. Turkoglu, M. E. Cinar, T. Ozturk, *Top. Curr. Chem.* **2017**, *375*, 2–45.

[141] B. S. Ong, Y. Wu, Y. Li, P. Liu, H. Pan, *Chem. - A Eur. J.* **2008**, *14*, 4766–4778.

[142] X. Wang, Z.-G. Zhang, H. Luo, S. Chen, S. Yu, H. Wang, X. Li, G. Yu, Y. Li, *Polym. Chem.* **2014**, *5*, 502–511.

[143] X. Gao, Z. Zhao, *Sci. China Chem.* **2015**, *58*, 947–968.

[144] K. Takimiya, I. Osaka, T. Mori, M. Nakano, *Acc. Chem. Res.* **2014**, *47*, 1493–1502.

[145] A. C. Benniston, A. Harriman, *Coord. Chem. Rev.* **2008**, *252*, 2528–2539.

[146] L. Venkataraman, J. E. Klare, C. Nuckolls, M. S. Hybertsen, M. L. Steigerwald, *Nature* **2006**, *442*, 904–907.

[147] C. Liang, M. D. Newton, *J. Phys. Chem.* **1992**, *96*, 2855–2866.

[148] S. Woitellier, J. P. Launay, C. Joachim, *Chem. Phys.* **1989**, *131*, 481–488.

[149] H. Wynberg, H. J. Kooreman, *J. Am. Chem. Soc.* **1965**, *87*, 1739–1742.

[150] P. Anastas, J. Warner, *Green Chemistry: Theory and Practice*, Oxford University Press, **2000**.

[151] G. E. Collis, A. K. Burrell, S. M. Scott, D. L. Officer, *J. Org. Chem.* **2003**, *68*, 8974–8983.

[152] P. A. Chaloner, S. R. Gunatunga, P. B. Hitchcock, *J. Chem. Soc. Perkin Trans. 2* **1997**, 1597–1604.

[153] J. Linshoeft, C. Näther, A. Staubitz, *Acta Cryst. E* **2014**, *70*, o1133–o1134.

[154] C. Zhang, Y. Zang, E. Gann, C. R. McNeill, X. Zhu, C.-a. Di, D. Zhu, *J. Am. Chem. Soc.* **2014**, *136*, 16176–16184.

[155] N. Armaroli, L. De Cola, V. Balzani, J.-P. Sauvage, C. O. Dietrich-Buchecker, J.-M. Kern, *J. Chem. Soc. Faraday Trans.* **1992**, *88*, 553.

[156] Y. You, W. Nam, *Chem. Soc. Rev.* **2012**, *41*, 7061.

[157] M. Y. Wong, G. Xie, C. Tourbillon, M. Sandroni, D. B. Cordes, A. M. Z. Slawin, I. D. W. Samuel, E. Zysman-Colman, *Dalt. Trans.* **2015**, *44*, 8419–8432.

[158] X. Xuan, J. Wang, H. Wang, *Electrochim. Acta* **2005**, *50*, 4196–4201.

[159] J. Lambert, H. Marsmann, *Spektroskopie: Strukturaufklärung in der Organischen Chemie*, Pearson, **2012**.

[160] L.-P. Han, B. Li, J. Ying, *Acta Cryst. E* **2007**, *63*, m3133–m3133.

[161] L. Li, S. Zhang, L. Xu, J. Wang, L.-X. Shi, Z.-N. Chen, M. Hong, J. Luo, *Chem. Sci.* **2014**, *5*, 3808–3813.

[162] C. Wang, D. Liu, Z. Xie, W. Lin, *Inorg. Chem.* **2014**, *53*, 1331–1338.

[163] L. Li, S. Zhang, L. Xu, L. Han, Z.-N. Chen, J. Luo, *Inorg. Chem.* **2013**, *52*, 12323–12325.

[164] M.-L. Ho, Y.-A. Chen, T.-C. Chen, P.-J. Chang, Y.-P. Yu, K.-Y. Cheng, C.-H. Shih, G.-H. Lee, H.-S. Sheu, *Dalt. Trans.* **2012**, *41*, 2592–2600.

[165] K. K. W. Lo, C. K. Chung, T. K. M. Lee, L. H. Lui, K. H. K. Tsang, N. Zhu, *Inorg. Chem.* **2003**, *42*, 6886–6897.

[166] S. J. Liu, Q. Zhao, Q. L. Fan, W. Huang, *Eur. J. Inorg. Chem.* **2008**, 2177–2185.

[167] F.-X. Wang, M.-H. Chen, X.-Y. Hu, R.-R. Ye, C.-P. Tan, L.-N. Ji, Z.-W. Mao, *Sci. Rep.* **2016**, *6*, 38954.

[168] T. W. Hesterberg, X. Yang, B. J. Holliday, *Polyhedron* **2010**, *29*, 110–115.

[169] R. D. Costa, E. OrtÃ, H. J. Bolink, S. Graber, S. Schaffner, M. Neuburger, C. E. Housecroft, E. C. Constable, *Adv. Funct. Mater.* **2009**, *19*, 3456–3463.

[170] H. Yao, L. Zhang, Y. Peng, P. J. Carroll, L. Gong, E. Meggers, *Inorganica Chim. Acta* **2014**, *421*, 489–495.

[171] A. Bossi, A. F. Rausch, M. J. Leitl, R. Czerwieniec, M. T. Whited, P. I. Djurovich, H. Yersin, M. E. Thompson, *Inorg. Chem.* **2013**, *52*, 12403–12415.

[172] R. V. Kiran, C. F. Hogan, B. D. James, D. J. D. Wilson, *Eur. J. Inorg. Chem.* **2011**, *2011*, 4816–4825.

[173] S. Fery-Forgues, D. Lavabre, *J. Chem. Educ.* **1999**, *76*, 1260–1264.

[174] A. T. R. Williams, S. A. Winfield, J. N. Miller, *Analyst* **1983**, *108*, 1067–1071.

[175] C. Dragonetti et al., *Inorg. Chem.* **2007**, *46*, 8533–8547.

[176] H. Scientific, *DAS6 Operating Manual*, Horiba Scientific, New Jersey, **2017**, pp. 1–117.

[177] Y.-J. Yuan, J.-Y. Zhang, Z.-T. Yu, J.-Y. Feng, W.-J. Luo, J.-H. Ye, Z.-G. Zou, *Inorg. Chem.* **2012**, *51*, 4123–4133.

[178] P. N. Curtin, L. L. Tinker, C. M. Burgess, E. D. Cline, S. Bernhard, *Inorg. Chem.* **2009**, *48*, 10498–10506.

[179] K. P. S. Zanoni, B. K. Kariyazaki, A. Ito, M. K. Brennaman, T. J. Meyer, N. Y. Murakami Iha, *Inorg. Chem.* **2014**, *53*, 4089–4099.

[180] J. Sun, W. Wu, H. Guo, J. Zhao, *Eur. J. Inorg. Chem.* **2011**, 3165–3173.

[181] G. Calogero, G. Giuffrida, S. Serroni, V. Ricevuto, S. Campagna, *Inorg. Chem.* **1995**, *34*, 541–545.

[182] X. Zeng, M. Tavasli, I. F. Perepichka, A. S. Batsanov, M. R. Bryce, C.-J. Chiang, C. Rothe, A. P. Monkman, *Chem. - A Eur. J.* **2008**, *14*, 933–943.

[183] M. Bandini, M. Bianchi, G. Valenti, F. Piccinelli, F. Paolucci, M. Monari, A. Umani-Ronchi, M. Marcaccio, *Inorg. Chem.* **2010**, *49*, 1439–1448.

[184] H. Lin, M. E. Cinar, M. Schmittel, *Dalt. Trans.* **2010**, *39*, 5130–5138.

[185] J. I. Kim, I.-S. Shin, H. Kim, J.-K. Lee, *J. Am. Chem. Soc.* **2005**, *127*, 1614–1615.

[186] L. He, L. Duan, J. Qiao, R. Wang, P. Wei, L. Wang, Y. Qiu, *Adv. Funct. Mater.* **2008**, *18*, 2123–2131.

[187] S.-y. Takizawa, K. Shimada, Y. Sato, S. Murata, *Inorg. Chem.* **2014**, *53*, 2983–2995.

[188] W. Y. Wong, G. J. Zhou, X. M. Yu, H. S. Kwok, Z. Lin, *Adv. Funct. Mater.* **2007**, *17*, 315–323.

[189] P.Rehsies, Bachelor thesis, Paderborn, **2016**.

[190] P. Pellon, *Tetrahedron Lett.* **1992**, *33*, 4451–4452.

[191] A. Staubitz, A. P. M. Robertson, M. E. Sloan, I. Manners, *Chem. Rev.* **2010**, *110*, 4023–4078.

[192] C. V. Krishnan, B. S. Brunschwig, C. Creutz, N. Sutin, *J. Am. Chem. Soc.* **1985**, *107*, 2005–2015.

[193] T. Krämer, J. Strähle, *Zeitschrift fur Naturforsch. - Sect. B J. Chem. Sci.* **1986**, *41b*, 692–696.

[194] W. Trogler, R. C. Stewart, L. A. Epps, L. G. Marzilli, *Inorg. Chem.* **1974**, *13*, 1564–1570.

[195] D. J. Szalda, C. Creutz, D. Mahajan, N. Sutin, *Inorg. Chem.* **1983**, *22*, 2372–2379.

[196] Q. Huang, L. Diao, C. Zhang, F. Lei, *Molecules* **2011**, *16*, 2871–2883.

[197] K. Arun Kumar, M. Amuthaselvi, A. Dayalan, *Acta Crystallogr. Sect. E Struct. Reports Online* **2011**, *67*, m468.

[198] E. Ngameni, J. Ngoune, A. Nassi, M. Belombe, R. Roux, *Electrochim. Acta* **1996**, *41*, 2571–2577.

[199] D. W. Wakerley, E. Reisner, *Phys. Chem. Chem. Phys.* **2014**, *16*, 5739–5746.

[200] A. Kahnt, K. Peuntinger, C. Dammann, T. Drewello, R. Hermann, S. Naumov, B. Abel, D. M. Guldi, *J. Phys. Chem. A* **2014**, *118*, 4382–4391.

[201] J. Wang, C. Li, Q. Zhou, W. Wang, Y. Hou, B. Zhang, X. Wang, *Dalt. Trans.* **2015**, *44*, 17704–17711.

[202] A. Panagiotopoulos, K. Ladomenou, D. Sun, V. Artero, A. G. Coutsolelos, *Dalt. Trans.* **2016**, *45*, 6732–6738.

[203] P.-A. Jacques, V. Artero, J. Pecaut, M. Fontecave, *Proc. Natl. Acad. Sci.* **2009**, *106*, 20627–20632.

[204] L. L. Tinker, N. D. McDaniel, P. N. Curtin, C. K. Smith, M. J. Ireland, S. Bernhard, *Chem. Eur. J.* **2007**, *13*, 8726–8732.

[205] P. Zhang, P. A. Jacques, M. Chavarot-Kerlidou, M. Wang, L. Sun, M. Fontecave, V. Artero, *Inorg. Chem.* **2012**, *51*, 2115–2120.

[206] C. F. Leung, Y. Z. Chen, H. Q. Yu, S. M. Yiu, C. C. Ko, T. C. Lau, *Int. J. Hydrog. Energy* **2011**, *36*, 11640–11645.

[207] P. Du, K. Knowles, R. Eisenberg, *J. Am. Chem. Soc.* **2008**, *130*, 12576–12577.

[208] L. I. Simándi, Z. Szeverényi, É Budó-Záhonyi, *Inorg. Nucl. Chem. Lett.* **1975**, *11*, 773–777.

[209] A. Bakac, J. H. Espenson, *J. Am. Chem. Soc.* **1984**, *106*, 5197–5202.

[210] V. Artero, M. Chavarot-Kerlidou, M. Fontecave, *Angew. Chem. Int. Ed.* **2011**, *50*, 7238–7266.

[211] T. Banerjee, F. Haase, G. Savasci, K. Gottschling, C. Ochsenfeld, B. V. Lotsch, *J. Am. Chem. Soc.* **2017**, *139*, 16228–16234.

[212] C. C. L. McCrory, C. Uyeda, J. C. Peters, *J. Am. Chem. Soc.* **2012**, *134*, 3164–3170.

[213] T. Li, Y. Chen, W.-F. Fu, *Catal. Commun.* **2014**, *45*, 91–94.

[214] O. Pantani, E. Anxolabéhère-Mallart, A. Aukauloo, P. Millet, *Electrochem. Commun.* **2007**, *9*, 54–58.

[215] T. Matsuo, K. Komatsuzaki, T. Tsuji, T. Hayashi, *J. Porphyr. Phthalocyanines* **2012**, *16*, 616–625.

[216] Y. Mulyana, K. G. Alley, K. M. Davies, B. F. Abrahams, B. Moubaraki, K. S. Murray, C. Boskovic, *Dalt. Trans.* **2014**, *43*, 2499–2511.

[217] E. S. Andreiadis, M. Chavarot-Kerlidou, M. Fontecave, V. Artero, *Photochem. Photobiol.* **2011**, *87*, 946–964.

[218] N. Turro, V. Ramamurthy, J. Scaiano, *Modern Molecular Photochemistry of Organic Molecules*, University Science Books, **2010**.

[219] K. Kalyanasundaram, J. Kiwi, M. Gratzel, *Helv. Chim. Acta* **1978**, *61*, 2720–2730.

[220] E. S. Andreiadis et al., *Nat. Chem.* **2013**, *5*, 48–53.

[221] R. S. Drago, *J. Organomet. Chem.* **1996**, *512*, 61–68.

[222] S. D. Cummings, R. Eisenberg, *J. Am. Chem. Soc.* **1996**, *118*, 1949–1960.

[223] L.-C. Song, M.-Y. Tang, F.-H. Su, Q.-M. Hu, *Angew. Chem. Int. Ed.* **2006**, *45*, 1130–1133.

[224] L.-C. Song, M.-Y. Tang, S.-Z. Mei, J.-H. Huang, Q.-M. Hu, *Organometallics* **2007**, *26*, 1575–1577.

[225] G.-G. Luo, K. Fang, J.-H. Wu, J.-C. Dai, Q.-H. Zhao, *Phys. Chem. Chem. Phys.* **2014**, *16*, 23884–23894.

[226] L.-J. Liu, L. Lu, H.-J. Zhong, B. He, D. W. J. Kwong, D.-L. Ma, C.-H. Leung, *J. Med. Chem.* **2015**, *58*, 6697–6703.

[227] O. Johansson, M. Borgström, R. Lomoth, M. Palmblad, J. Bergquist, L. Hammarström, L. Sun, B. Åkermark, *Inorg. Chem.* **2003**, *42*, 2908–2918.

[228] J. Liu, W. Jiang, *Dalt. Trans.* **2012**, *41*, 9700–9707.

[229] J. N. Roy, D. N. Bose, *Photovoltaic Science and Technology*, Cambridge University Press, **2017**.

[230] H. Wagemann, H. Eschrich, *Photovoltaik: Solarstrahlung und Halbleitereigenschaften, Solarzellenkonzepte und Aufgaben*, Vieweg+Teubner, **2010**.

[231] M. A. Gross, A. Reynal, J. R. Durrant, E. Reisner, *J. Am. Chem. Soc.* **2014**, *136*, 356–366.

[232] Y. Na, M. Wang, J. Pan, P. Zhang, B. Åkermark, L. Sun, *Inorg. Chem.* **2008**, *47*, 2805–2810.

[233] B. van den Bosch, H.-C. Chen, J. I. van der Vlugt, A. M. Brouwer, J. N. H. Reek, *ChemSusChem* **2013**, *6*, 790–793.

[234] P. Zhang, M. Wang, J. Dong, X. Li, F. Wang, L. Wu, L. Sun, *J. Phys. Chem. C* **2010**, *114*, 15868–15874.

[235] F. Gärtner et al., *Chem. - A Eur. J.* **2012**, *18*, 3220–3225.

[236] B. Probst, M. Guttentag, A. Rodenberg, P. Hamm, R. Alberto, *Inorg. Chem.* **2011**, *50*, 3404–3412.

[237] M. Natali, R. Argazzi, C. Chiorboli, E. Iengo, F. Scandola, *Chem. - A Eur. J.* **2013**, *19*, 9261–9271.

[238] B. Probst, C. Kolano, P. Hamm, R. Alberto, *Inorg. Chem.* **2009**, *48*, 1836–1843.

[239] P. Lei, M. Hedlund, R. Lomoth, H. Rensmo, O. Johansson, L. Hammarström, *J. Am. Chem. Soc.* **2008**, *130*, 26–27.

[240] B. L. Wadsworth, A. M. Beiler, D. Khusnutdinova, S. I. Jacob, G. F. Moore, *ACS Catal.* **2016**, *6*, 8048–8057.

[241] R. Meinhardt, PhD thesis, Paderborn, **2018**.

[242] J.-S. Lee, Compound and organic light-emitting device including the same, **2015**.

[243] J. M. Villegas, S. R. Stoyanov, D. P. Rillema, *Inorg. Chem.* **2002**, *41*, 6688–6694.

[244] F. Neese, *WIREs Comput Mol Sci* **2012**, *2*, 73–78.

[245] S. Grimme, J. G. Brandenburg, C. Bannwarth, A. Hansen, *J. Chem. Phys.* **2015**, *143*, 1–19.

[246] D. A. Pantazis, X.-Y. Chen, C. R. Landis, F. Neese, *J. Chem. Theory Comput.* **2008**, *4*, 908–919.

[247] C. Van Wüllen, *J. Chem. Phys.* **1998**, *109*, 392–399.

[248] M. Chiba, T. Tsuneda, K. Hirao, *J. Chem. Phys.* **2006**, *124*, 144106/1–11.

[249] H. Iikura, T. Tsuneda, T. Yanai, K. Hirao, *J. Chem. Phys.* **2001**, *115*, 3540–3544.

[250] Y. Tawada, T. Tsuneda, S. Yanagisawa, T. Yanai, K. Hirao, *J. Chem. Phys.* **2004**, *120*, 8425–8433.

[251] Bruker AXS Inc. SMART (Version 5.63), SAINT (Version 6.02), SHELXTL (Version 6.10), and SADABS (Version 2.03), Madison, Wisconcin, USA, **2002**.

[252] PLATON: A Multipurpose Crystallographic Tool; University of Utrecht: Utrecht, The Netherlands, **2003**.

[253] A. L. Spek, *J. Appl. Cryst.* **2003**, *36*, 7–13.

[254] A. S. Denisova, M. B. Degtyareva, E. M. Dem'yanchuk, A. A. Simanova, *Russ. J. Org. Chem.* **2005**, *41*, 1690–1693.

[255] L. K. Povlich, J. C. Cho, M. K. Leach, J. M. Corey, J. Kim, D. C. Martin, *Biochim. Biophys. Acta* **2013**, *1830*, 4288–4293.

[256] S. P. Mee, V. Lee, J. E. Baldwin, *Angew. Chem. Int. Ed.* **2004**, *43*, 1132–1136.

[257] M. Nonoyama, *Bull. Chem. Soc. Jpn.* **1974**, *47*, 767–768.

Scientific Contributions

Publications

M. Tünnermann, P. Rehsies, U. Flörke M. Bauer "A straightforward synthesis to novel 1,10-phenanthrolines with fused thiophene structure", Synlett, submitted.

M. Tünnermann, P. Rehsies, P. Müller, U. Flörke, A. Neuba, M. Bauer "Impact of diimine ligand modification on iridium complexes for the application in photocatalytic water reduction", in preparation.

M. Tünnermann, P. Rehsies, P. Müller, A. Neuba, M. Bauer "Systematic investigation of new iridium-cobalt dyads for photocatalytic proton reduction", in preparation.

Conference Contributions

"Photokatalytische Wasserreduktion mit Iridium-Cobalt-Systemen", (Photocatalytic water reduction with iridium-cobalt-systems), DBU Stipendiatenseminar, Frenswegen, Germany, **April 2018**, Oral Presentation.

"Photokatalytische Wasserreduktion mit Iridium Cobalt Systemen" (Photocatalytic water reduction with iridium cobalt systems), Koordinationschemikertreffen, Heidelberg, Germany, **February 2018**, Oral Presentation.

"Photokatalytische Wasserreduktion mit Ein- und Mehrkomponentensystemen" (Photocatalytic water reduction with one- and multi-component systems), DBU Stipendiatenseminar, Papenburg, Germany, **November 2017**, Oral Presentation.

"Neue eisenbasierte Dyaden zur nachhaltigen photokatalytischen Wasserreduktion" (New iron-based dyads for sustainable photocatalytic water reduction), DBU Stipendiatenseminar, Lenzen, Germany, **September 2016**, Oral Presentation.

"Photocatalytic water reduction with an iron pincer complex", Ferrocene Colloquium, Mainz, Germany, **February 2018**, Poster Presentation.

Koordinationschemietreffen, Paderborn, **March 2015**.

International Symposium on Green Chemistry, La Rochelle, France, **May 2015**.

Appendix

Crystal Structures

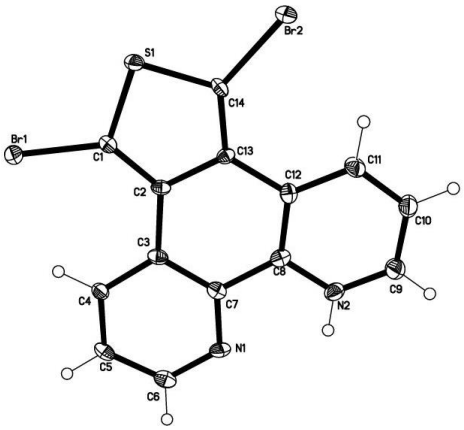

Table 1. Crystal data and structure refinement for a2485.

Identification code	a2485	
Empirical formula	C14 H7 Br3 N2 S	
Formula weight	475.01	
Temperature	130(2) K	
Wavelength	0.71073 Å	
Crystal system	Monoclinic	
Space group	Cc	
Unit cell dimensions	a = 10.8787(19) Å	α= 90°.
	b = 21.196(4) Å	β= 114.846(3)°.
	c = 7.2144(12) Å	γ = 90°.
Volume	1509.6(4) $Å^3$	
Z	4	
Density (calculated)	2.090 Mg/m^3	
Absorption coefficient	8.144 mm^{-1}	
F(000)	904	
Crystal size	0.27 x 0.11 x 0.06 mm^3	
Theta range for data collection	1.92 to 27.87°.	
Index ranges	-14<=h<=14, -27<=k<=25, -9<=l<=9	
Reflections collected	7062	
Independent reflections	3552 [R(int) = 0.0277]	
Completeness to theta = 27.87°	99.9 %	
Absorption correction	Semi-empirical from equivalents	
Max. and min. transmission	0.6407 and 0.2171	
Refinement method	Full-matrix least-squares on F^2	
Data / restraints / parameters	3552 / 2 / 192	
Goodness-of-fit on F^2	1.010	
Final R indices [I>2sigma(I)]	R1 = 0.0335, wR2 = 0.0765	
R indices (all data)	R1 = 0.0366, wR2 = 0.0776	
Absolute structure parameter	0.074(11)	
Largest diff. peak and hole	0.740 and -0.676 e.$Å^{-3}$	

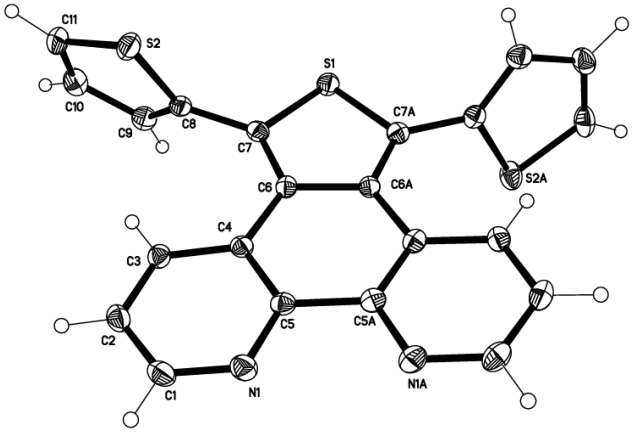

Table 1. Crystal data and structure refinement for a2720.

Identification code	a2720	
Empirical formula	C22 H12 N2 S3	
Formula weight	400.52	
Temperature	130(2) K	
Wavelength	0.71073 Å	
Crystal system	Monoclinic	
Space group	C 2/c	
Unit cell dimensions	a = 18.681(6) Å	α= 90°.
	b = 9.750(3) Å	β= 102.248(11)°.
	c = 9.655(3) Å	γ = 90°.
Volume	1718.7(9) $Å^3$	
Z	4	
Density (calculated)	1.548 Mg/m^3	
Absorption coefficient	0.441 mm^{-1}	
F(000)	824	
Crystal size	0.390 x 0.100 x 0.090 mm^3	
Theta range for data collection	2.231 to 27.873°.	
Index ranges	-24<=h<=24, -12<=k<=12, -12<=l<=12	
Reflections collected	7910	
Independent reflections	2046 [R(int) = 0.0592]	
Completeness to theta = 25.242°	100.0 %	
Absorption correction	Semi-empirical from equivalents	
Max. and min. transmission	1.0000 and 0.6372	
Refinement method	Full-matrix least-squares on F^2	
Data / restraints / parameters	2046 / 0 / 123	
Goodness-of-fit on F^2	1.062	
Final R indices [I>2sigma(I)]	R1 = 0.0467, wR2 = 0.1046	
R indices (all data)	R1 = 0.0673, wR2 = 0.1166	
Extinction coefficient	n/a	
Largest diff. peak and hole	0.497 and -0.299 $e.Å^{-3}$	

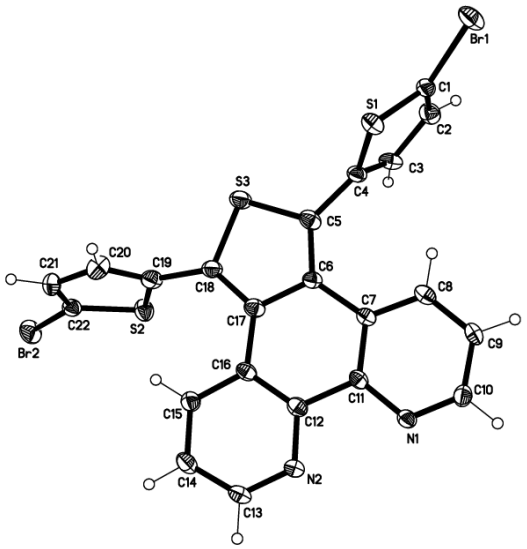

Table 1. Crystal data and structure refinement for a2715.

Identification code	a2715	
Empirical formula	C23 H11 Br2 Cl3 N2 S3	
Formula weight	677.69	
Temperature	130(2) K	
Wavelength	0.71073 Å	
Crystal system	Monoclinic	
Space group	P 21/c	
Unit cell dimensions	a = 11.256(2) Å	α= 90°.
	b = 14.702(3) Å	β= 107.119(6)°.
	c = 15.405(4) Å	γ = 90°.
Volume	2436.2(9) $Å^3$	
Z	4	
Density (calculated)	1.848 Mg/m^3	
Absorption coefficient	3.931 mm^{-1}	
F(000)	1328	
Crystal size	0.230 x 0.110 x 0.100 mm^3	
Theta range for data collection	1.893 to 27.872°.	
Index ranges	-14<=h<=13, -18<=k<=19, -20<=l<=20	
Reflections collected	22900	
Independent reflections	5807 [R(int) = 0.0910]	
Completeness to theta = 25.242°	100.0 %	
Absorption correction	Semi-empirical from equivalents	
Max. and min. transmission	1.0000 and 0.7291	
Refinement method	Full-matrix least-squares on F^2	
Data / restraints / parameters	5807 / 0 / 298	
Goodness-of-fit on F^2	0.995	
Final R indices [I>2sigma(I)]	R1 = 0.0541, wR2 = 0.0990	
R indices (all data)	R1 = 0.1026, wR2 = 0.1175	
Extinction coefficient	n/a	
Largest diff. peak and hole	0.636 and -0.474 e.$Å^{-3}$	

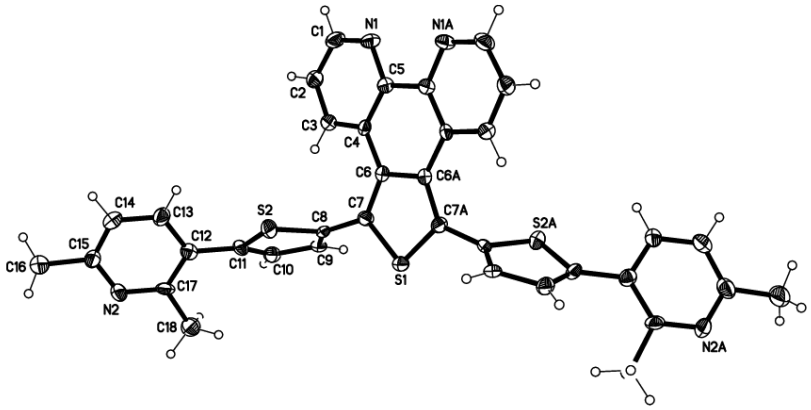

Table 1. Crystal data and structure refinement for t2864.

Identification code	t2864	
Empirical formula	C36 H26 N4 S3	
Formula weight	610.79	
Temperature	130(2) K	
Wavelength	0.71073 Å	
Crystal system	Monoclinic	
Space group	C 2/c	
Unit cell dimensions	a = 30.67(2) Å	α= 90°.
	b = 9.577(8) Å	β= 96.223(19)°.
	c = 9.824(8) Å	γ = 90°.
Volume	2869(4) $Å^3$	
Z	4	
Density (calculated)	1.414 Mg/m^3	
Absorption coefficient	0.293 mm^{-1}	
F(000)	1272	
Crystal size	0.480 x 0.040 x 0.030 mm^3	
Theta range for data collection	2.229 to 27.867°.	
Index ranges	-40<=h<=40, -12<=k<=12, -12<=l<=12	
Reflections collected	13150	
Independent reflections	3418 [R(int) = 0.3194]	
Completeness to theta = 25.242°	99.9 %	
Absorption correction	Semi-empirical from equivalents	
Max. and min. transmission	1.0000 and 0.2162	
Refinement method	Full-matrix least-squares on F^2	
Data / restraints / parameters	3418 / 0 / 197	
Goodness-of-fit on F^2	0.811	
Final R indices [I>2sigma(I)]	R1 = 0.0803, wR2 = 0.1112	
R indices (all data)	R1 = 0.2682, wR2 = 0.1730	
Extinction coefficient	n/a	
Largest diff. peak and hole	0.336 and -0.323 e.$Å^{-3}$	

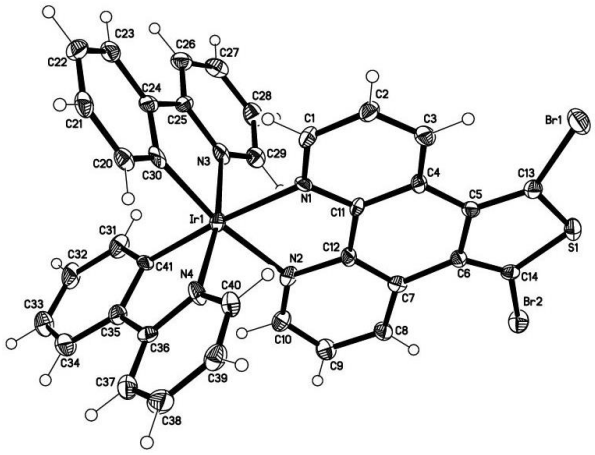

Table 1. Crystal data and structure refinement for a2488.

Identification code	a2488	
Empirical formula	C40.92 H33.83 Br2 Cl1.83 F6 Ir N4 O P S	
Formula weight	1191.54	
Temperature	130(2) K	
Wavelength	0.71073 Å	
Crystal system	Monoclinic	
Space group	P2(1)/n	
Unit cell dimensions	a = 13.707(2) Å	α= 90°.
	b = 13.842(2) Å	β= 98.492(3)°.
	c = 20.726(3) Å	γ = 90°.
Volume	3889.5(11) Å^3	
Z	4	
Density (calculated)	2.035 Mg/m^3	
Absorption coefficient	5.779 mm^{-1}	
F(000)	2314	
Crystal size	0.43 x 0.40 x 0.04 mm^3	
Theta range for data collection	1.67 to 27.88°.	
Index ranges	-18<=h<=18, -18<=k<=17, -27<=l<=19	
Reflections collected	35281	
Independent reflections	9280 [R(int) = 0.1033]	
Completeness to theta = 27.88°	99.9 %	
Absorption correction	Semi-empirical from equivalents	
Max. and min. transmission	0.8018 and 0.1901	
Refinement method	Full-matrix least-squares on F^2	
Data / restraints / parameters	9280 / 1 / 492	
Goodness-of-fit on F^2	0.860	
Final R indices [I>2sigma(I)]	R1 = 0.0438, wR2 = 0.0847	
R indices (all data)	R1 = 0.0766, wR2 = 0.0900	
Extinction coefficient	0.00020(5)	
Largest diff. peak and hole	2.299 and -1.392 e.Å^{-3}	

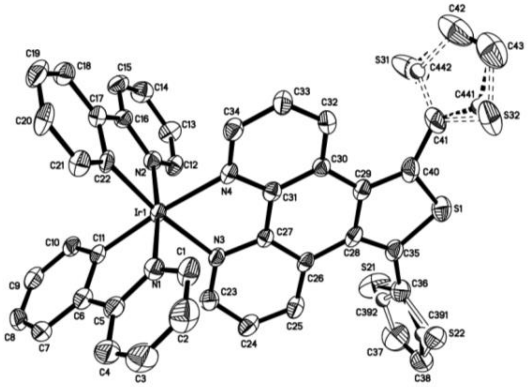

Table 1. Crystal data and structure refinement for a2569.

Identification code	a2569	
Empirical formula	C50 H40 F6 Ir N4 O2 P S3	
Formula weight	1162.21	
Temperature	130(2) K	
Wavelength	0.71073 Å	
Crystal system	Orthorhombic	
Space group	P2(1)2(1)2(1)	
Unit cell dimensions	a = 10.0309(8) Å	α= 90°.
	b = 19.0896(14) Å	β= 90°.
	c = 24.0712(18) Å	γ = 90°.
Volume	4609.3(6) $Å^3$	
Z	4	
Density (calculated)	1.675 Mg/m^3	
Absorption coefficient	3.138 mm^{-1}	
F(000)	2312	
Crystal size	0.45 x 0.20 x 0.18 mm^3	
Theta range for data collection	1.36 to 27.88°.	
Index ranges	-13<=h<=13, -25<=k<=25, -31<=l<=31	
Reflections collected	43750	
Independent reflections	10998 [R(int) = 0.0466]	
Completeness to theta = 27.88°	100.0 %	
Absorption correction	Semi-empirical from equivalents	
Max. and min. transmission	0.6020 and 0.3325	
Refinement method	Full-matrix least-squares on F^2	
Data / restraints / parameters	10998 / 3 / 589	
Goodness-of-fit on F^2	1.016	
Final R indices [I>2sigma(I)]	R1 = 0.0318, wR2 = 0.0647	
R indices (all data)	R1 = 0.0365, wR2 = 0.0659	
Absolute structure parameter	0.031(5)	
Largest diff. peak and hole	2.458 and -0.546 $e.Å^{-3}$	

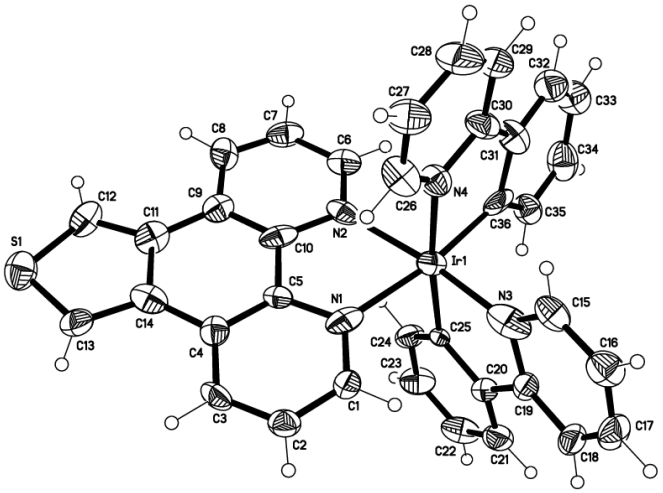

Table 1. Crystal data and structure refinement for t2944.

Identification code	t2944	
Empirical formula	C41 H36 Cl2 F6 Ir N4 O P S	
Formula weight	1040.87	
Temperature	130(2) K	
Wavelength	0.71073 Å	
Crystal system	Triclinic	
Space group	P -1	
Unit cell dimensions	a = 9.839(3) Å	α= 85.054(7)°.
	b = 12.049(4) Å	β= 76.424(7)°.
	c = 16.490(5) Å	γ = 77.845(7)°.
Volume	1856.4(10) Å^3	
Z	2	
Density (calculated)	1.862 Mg/m^3	
Absorption coefficient	3.912 mm^{-1}	
F(000)	1028	
Crystal size	0.480 x 0.140 x 0.090 mm^3	
Theta range for data collection	1.271 to 27.873°.	
Index ranges	-12<=h<=12, -15<=k<=15, -21<=l<=21	
Reflections collected	17389	
Independent reflections	8795 [R(int) = 0.1078]	
Completeness to theta = 25.242°	99.9 %	
Absorption correction	Semi-empirical from equivalents	
Max. and min. transmission	1.0000 and 0.3542	
Refinement method	Full-matrix least-squares on F^2	
Data / restraints / parameters	8795 / 0 / 442	
Goodness-of-fit on F^2	0.902	
Final R indices [I>2sigma(I)]	R1 = 0.0828, wR2 = 0.1685	
R indices (all data)	R1 = 0.1570, wR2 = 0.1946	
Extinction coefficient	n/a	
Largest diff. peak and hole	2.510 and -2.100 e.Å^{-3}	

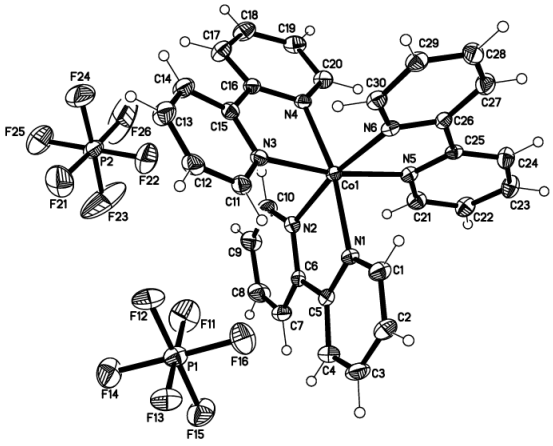

Table 1. Crystal data and structure refinement for a2714.

Identification code	a2714	
Empirical formula	C30 H24 Co F12 N6 P2	
Formula weight	817.42	
Temperature	130(2) K	
Wavelength	0.71073 Å	
Crystal system	Trigonal	
Space group	P 31	
Unit cell dimensions	a = 10.3453(4) Å	α= 90°.
	b = 10.3453(4) Å	β= 90°.
	c = 26.126(2) Å	γ = 120°.
Volume	2421.5(3) $Å^3$	
Z	3	
Density (calculated)	1.682 Mg/m^3	
Absorption coefficient	0.734 mm^{-1}	
F(000)	1233	
Crystal size	0.490 x 0.200 x 0.190 mm^3	
Theta range for data collection	2.273 to 27.875°.	
Index ranges	-13<=h<=13, -13<=k<=13, -34<=l<=34	
Reflections collected	23112	
Independent reflections	7685 [R(int) = 0.0360]	
Completeness to theta = 25.242°	100.0 %	
Absorption correction	Semi-empirical from equivalents	
Max. and min. transmission	1.0000 and 0.5699	
Refinement method	Full-matrix least-squares on F^2	
Data / restraints / parameters	7685 / 1 / 461	
Goodness-of-fit on F^2	1.055	
Final R indices [I>2sigma(I)]	R1 = 0.0494, wR2 = 0.1214	
R indices (all data)	R1 = 0.0544, wR2 = 0.1255	
Absolute structure parameter	0.990(19)	
Extinction coefficient	n/a	
Largest diff. peak and hole	0.512 and -0.352 e.$Å^{-3}$	

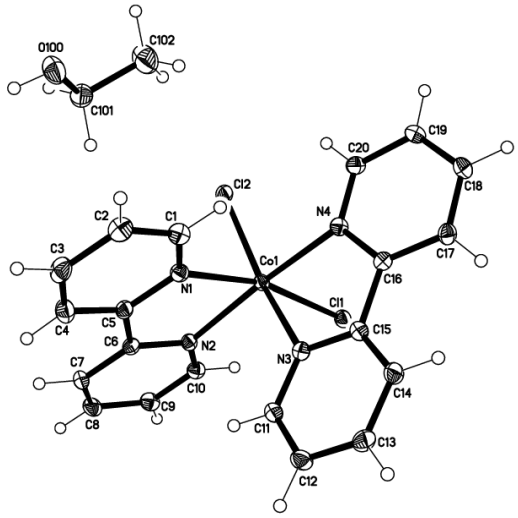

Table 1. Crystal data and structure refinement for a2693.

Identification code	a2693	
Empirical formula	C22 H22 Cl2 Co N4 O	
Formula weight	488.27	
Temperature	130(2) K	
Wavelength	0.71073 Å	
Crystal system	Monoclinic	
Space group	P2(1)/c	
Unit cell dimensions	a = 9.8892(19) Å	α= 90°.
	b = 14.155(3) Å	β= 99.977(5)°.
	c = 15.429(3) Å	γ = 90°.
Volume	2127.1(7) $Å^3$	
Z	4	
Density (calculated)	1.525 Mg/m^3	
Absorption coefficient	1.080 mm^{-1}	
F(000)	1004	
Crystal size	0.23 x 0.21 x 0.20 mm^3	
Theta range for data collection	1.97 to 27.87°.	
Index ranges	-13<=h<=12, -18<=k<=15, -20<=l<=20	
Reflections collected	19913	
Independent reflections	5068 [R(int) = 0.0590]	
Completeness to theta = 27.87°	100.0 %	
Absorption correction	Semi-empirical from equivalents	
Max. and min. transmission	0.8130 and 0.7893	
Refinement method	Full-matrix least-squares on F^2	
Data / restraints / parameters	5068 / 0 / 273	
Goodness-of-fit on F^2	1.066	
Final R indices [I>2sigma(I)]	R1 = 0.0405, wR2 = 0.0845	
R indices (all data)	R1 = 0.0582, wR2 = 0.0931	
Largest diff. peak and hole	0.418 and -0.337 $e.Å^{-3}$	

NMR spectra

NMR data of L2

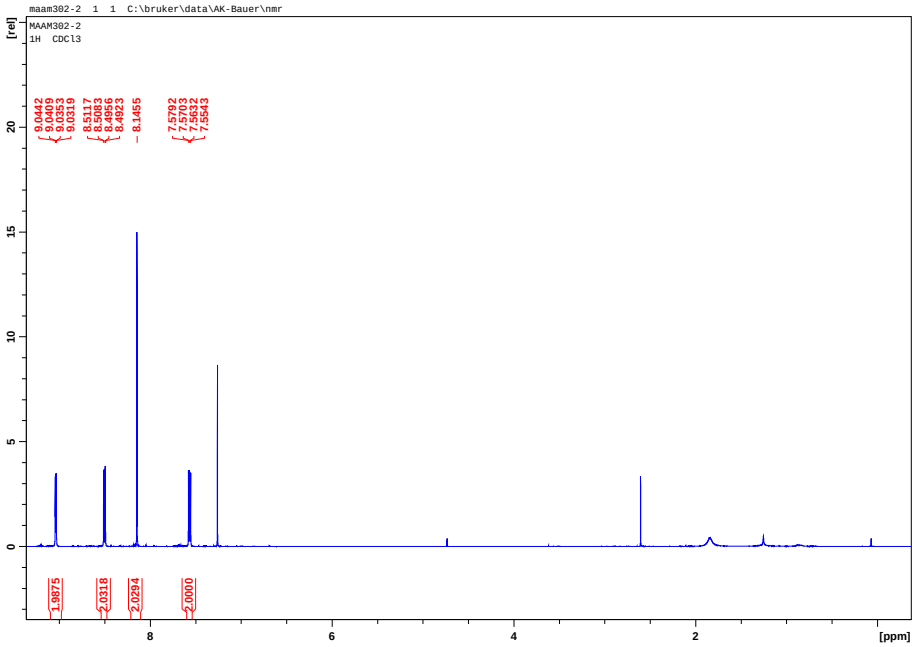

Figure 9.1: ^{1}H NMR spectra of **L2** in $CDCl_3$. Best viewed digitally.

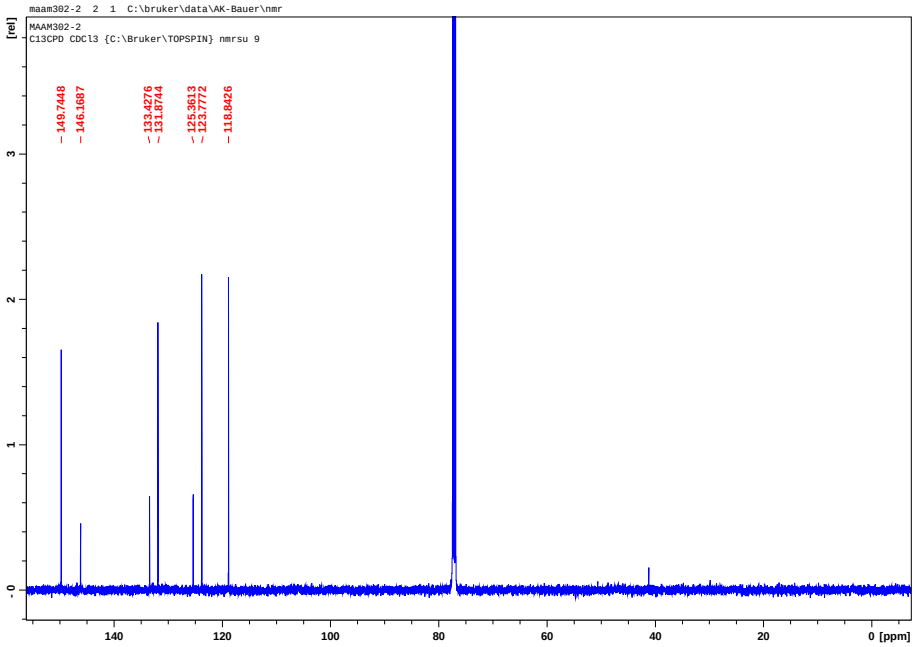

Figure 9.2: ^{13}C NMR spectra of **L2** in $CDCl_3$. Best viewed digitally.

NMR data of L3

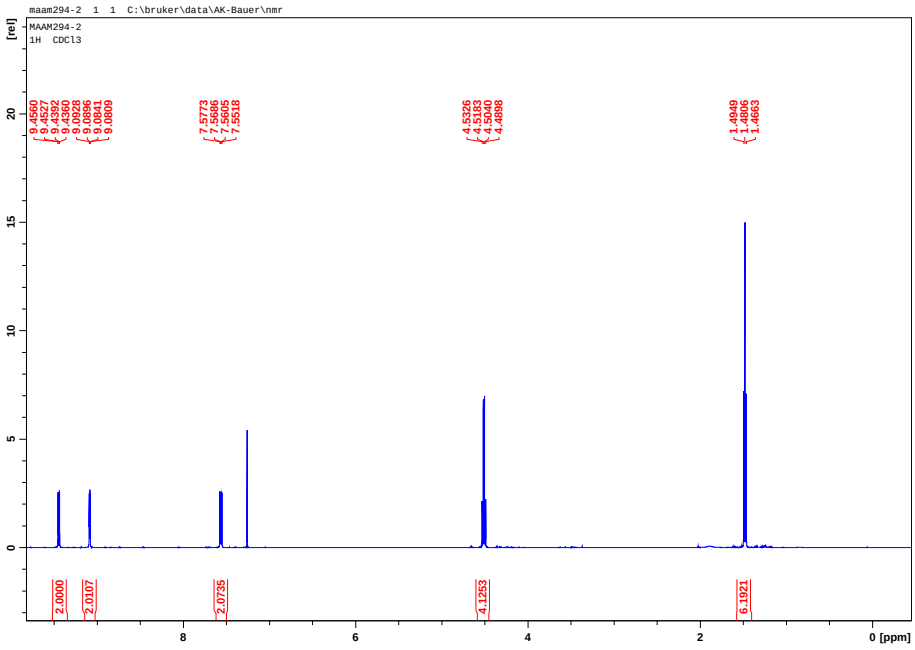

Figure 9.3: ^{1}H NMR spectra of **L3** in $CDCl_3$. Best viewed digitally.

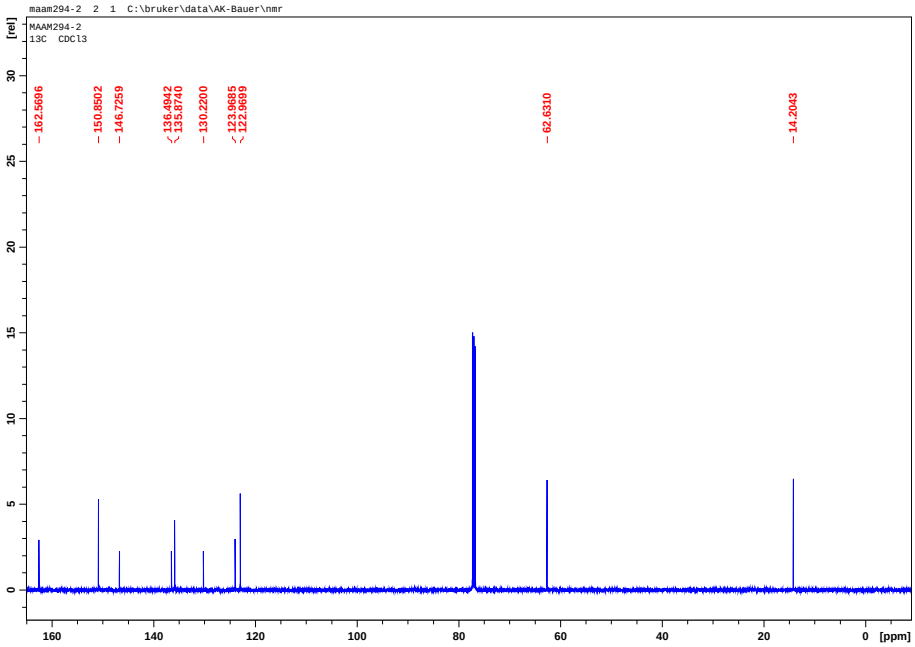

Figure 9.4: ^{13}C NMR spectra of **L3** in $CDCl_3$. Best viewed digitally.

NMR data of L5

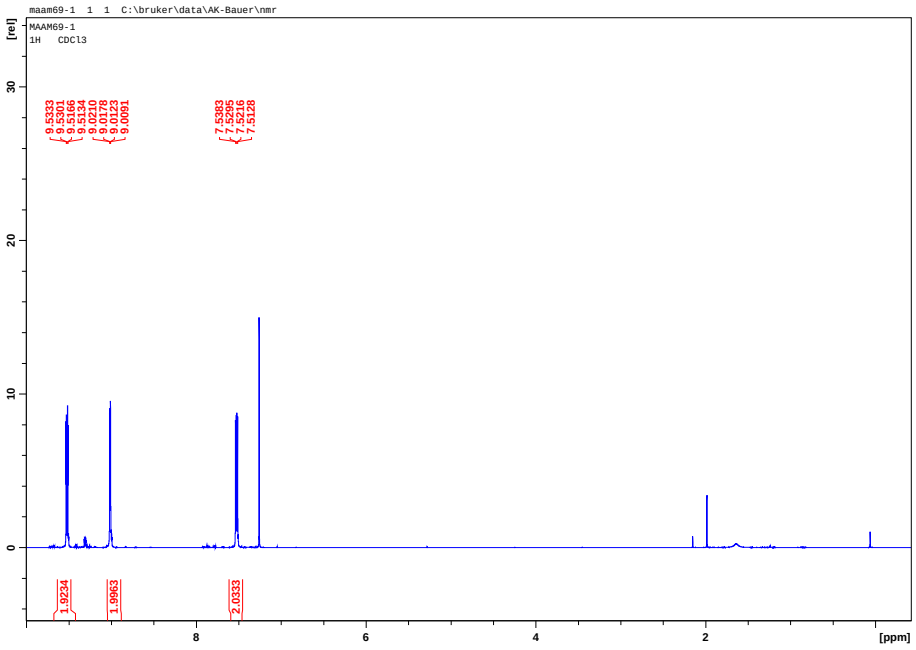

Figure 9.5: ^{1}H NMR spectra of **L5** in $CDCl_3$. Best viewed digitally.

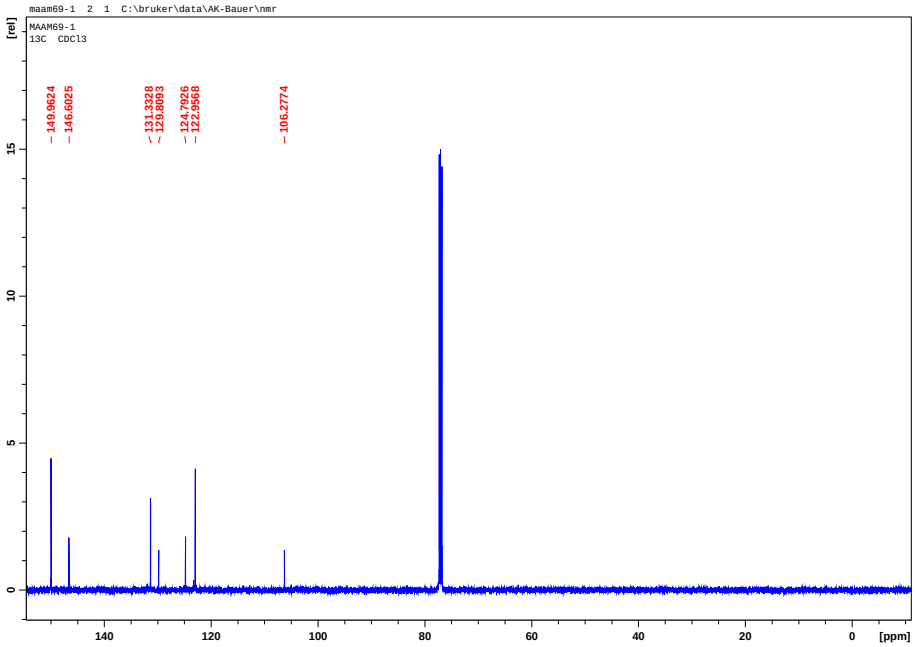

Figure 9.6: ^{13}C NMR spectra of **L5** in $CDCl_3$. Best viewed digitally.

NMR data of L6

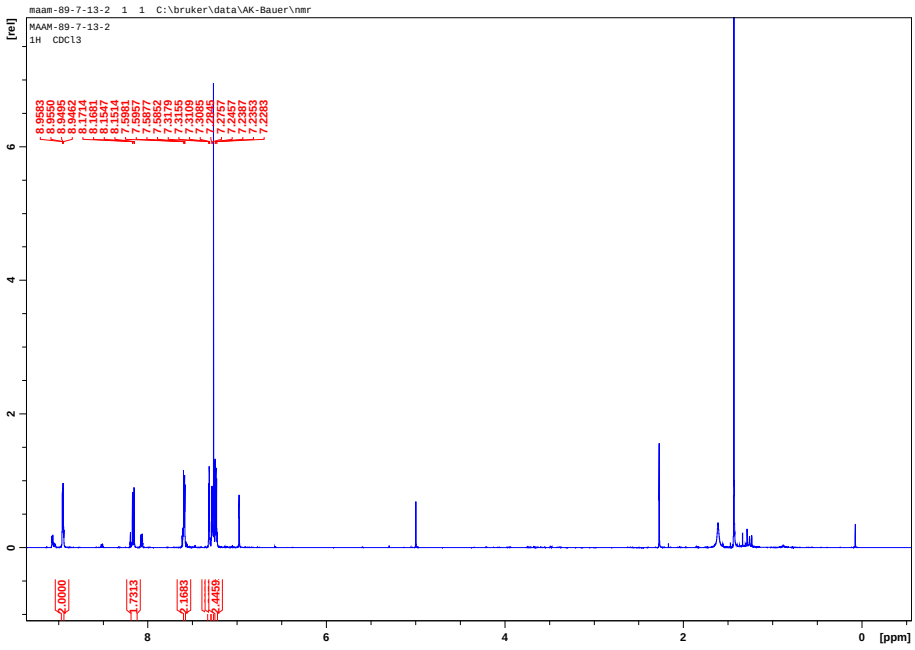

Figure 9.7: ^{1}H NMR spectra of **L6** in $CDCl_3$. Best viewed digitally.

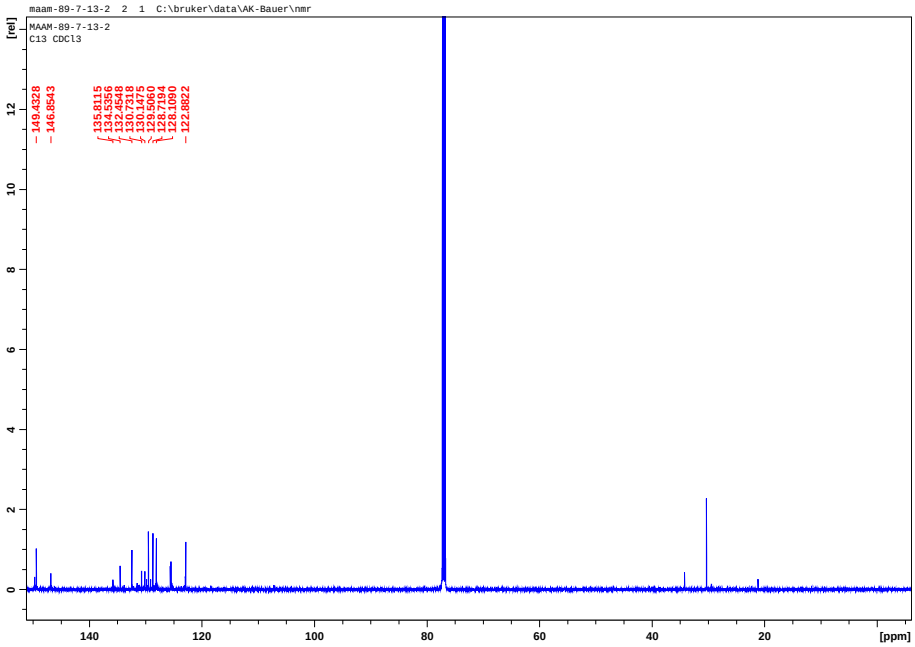

Figure 9.8: ^{13}C NMR spectra of **L6** in $CDCl_3$. Best viewed digitally.

NMR data of L7

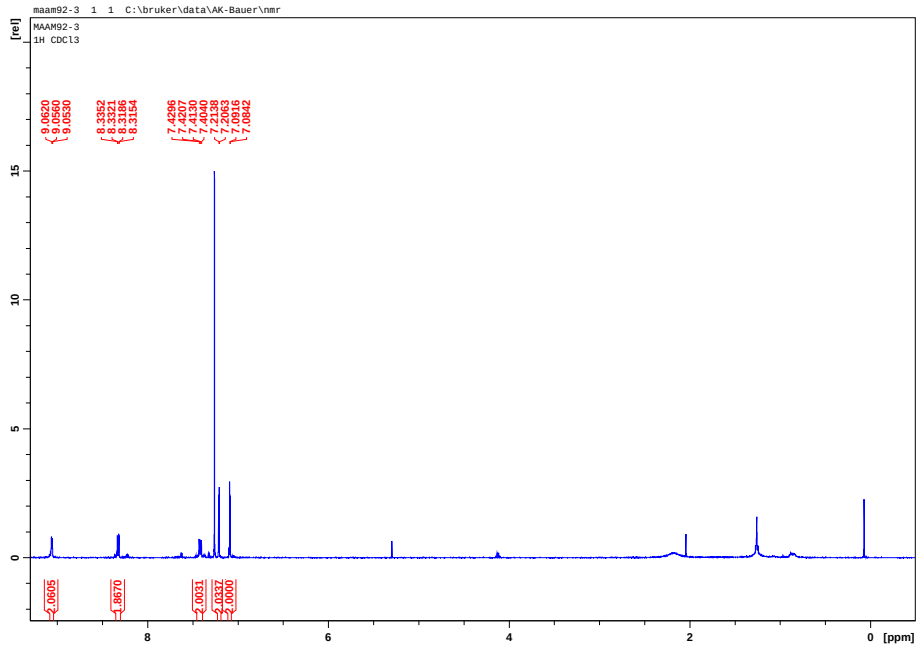

Figure 9.9: ^{1}H NMR spectra of **L7** in $CDCl_3$. Best viewed digitally.

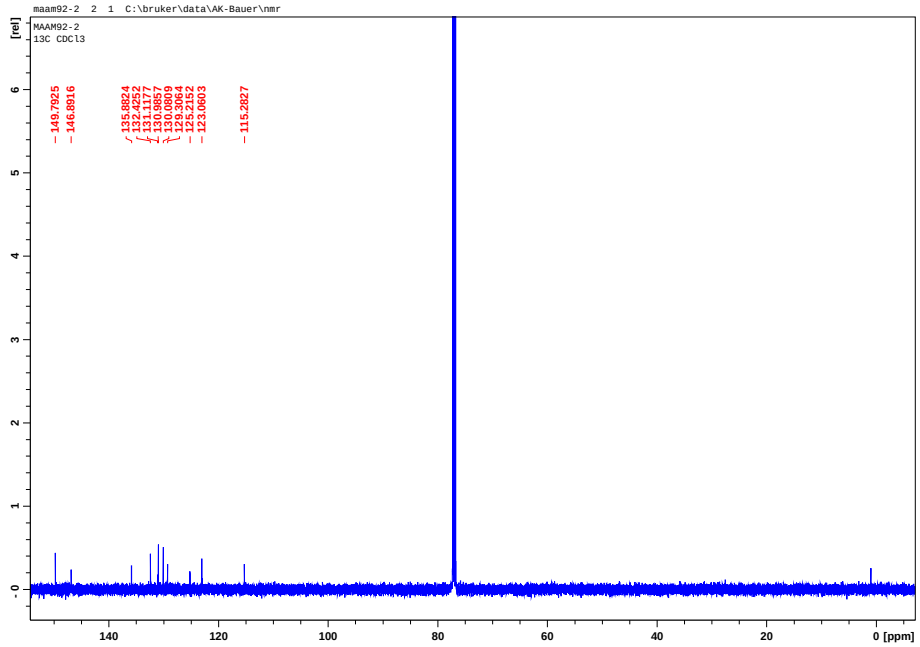

Figure 9.10: ^{13}C NMR spectra of **L7** in $CDCl_3$. Best viewed digitally.

NMR data of L8

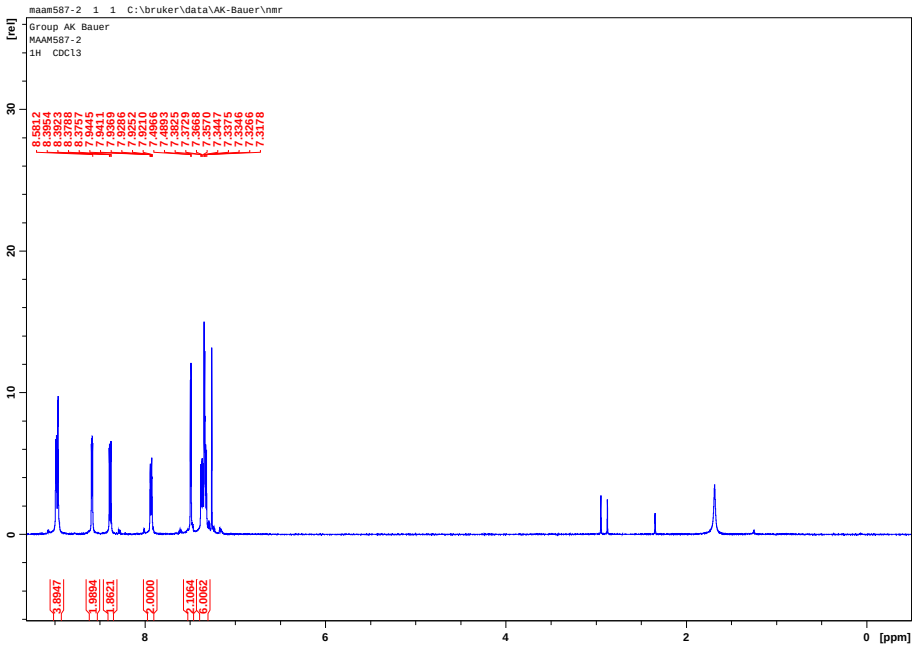

Figure 9.11: ^{1}H NMR spectra of **L8** in $CDCl_3$. Best viewed digitally.

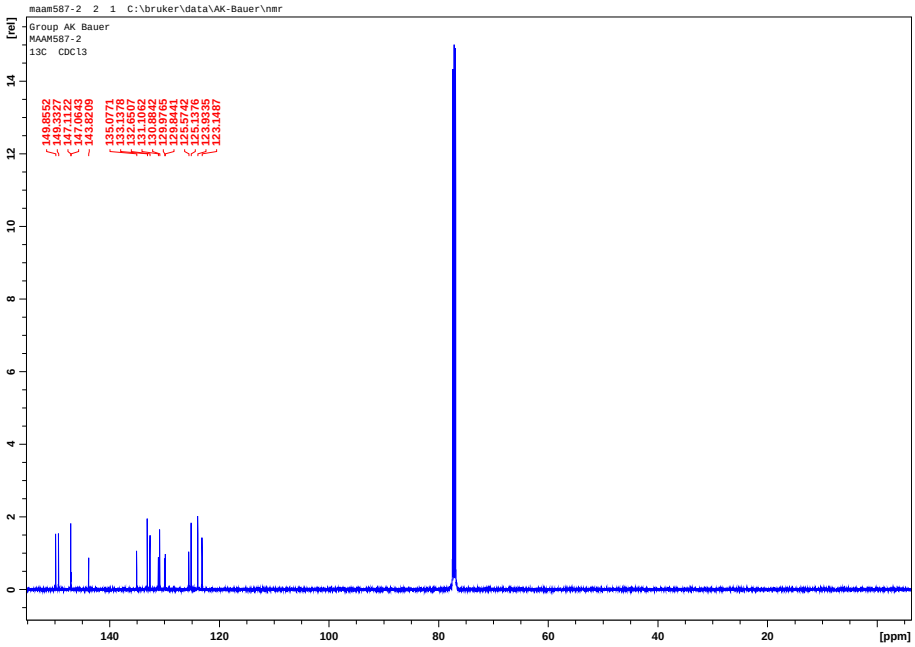

Figure 9.12: ^{13}C NMR spectra of **L8** in $CDCl_3$. Best viewed digitally.

NMR data of L9

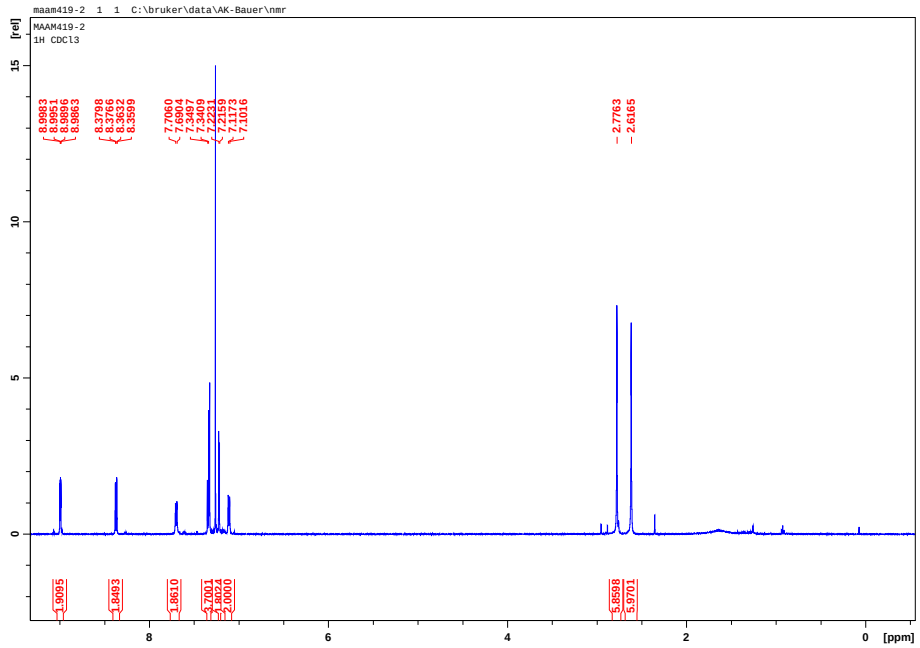

Figure 9.13: ^{1}H NMR spectra of **L9** in $CDCl_3$. Best viewed digitally.

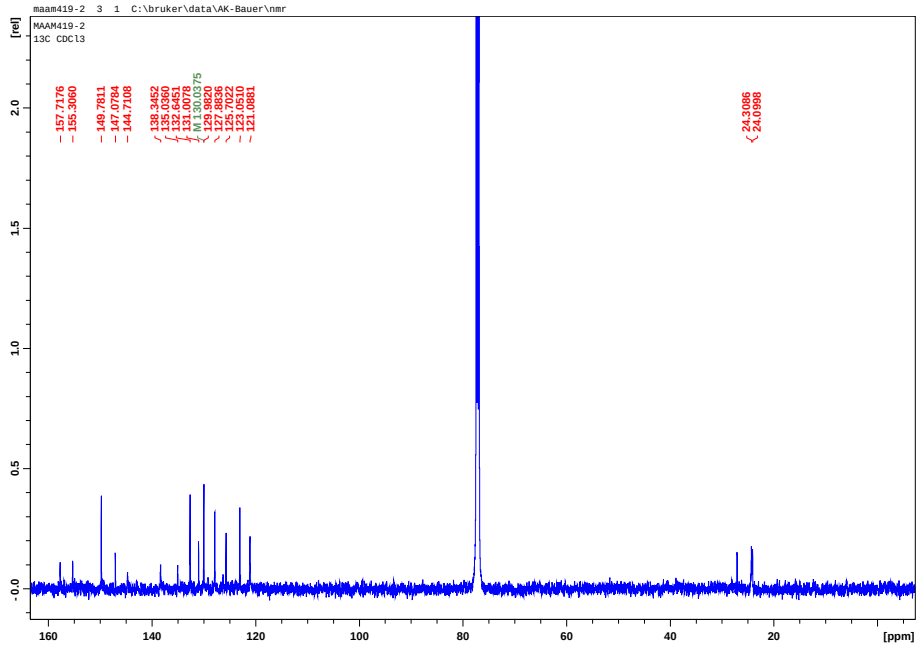

Figure 9.14: ^{13}C NMR spectra of **L9** in $CDCl_3$. Best viewed digitally.

NMR data of PS2

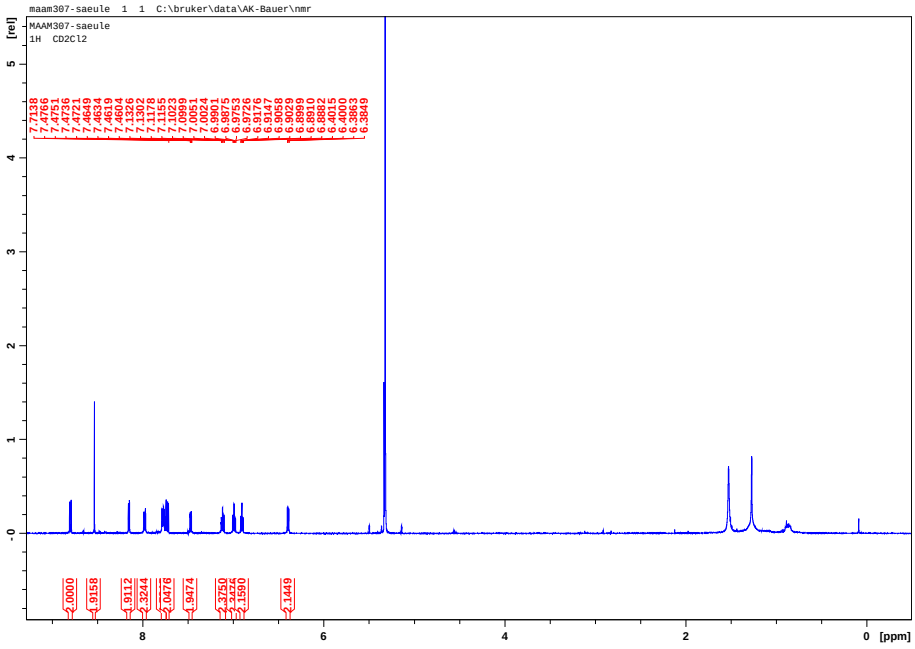

Figure 9.15: ^{1}H NMR spectra of **PS2** in CD_2Cl_3. Best viewed digitally.

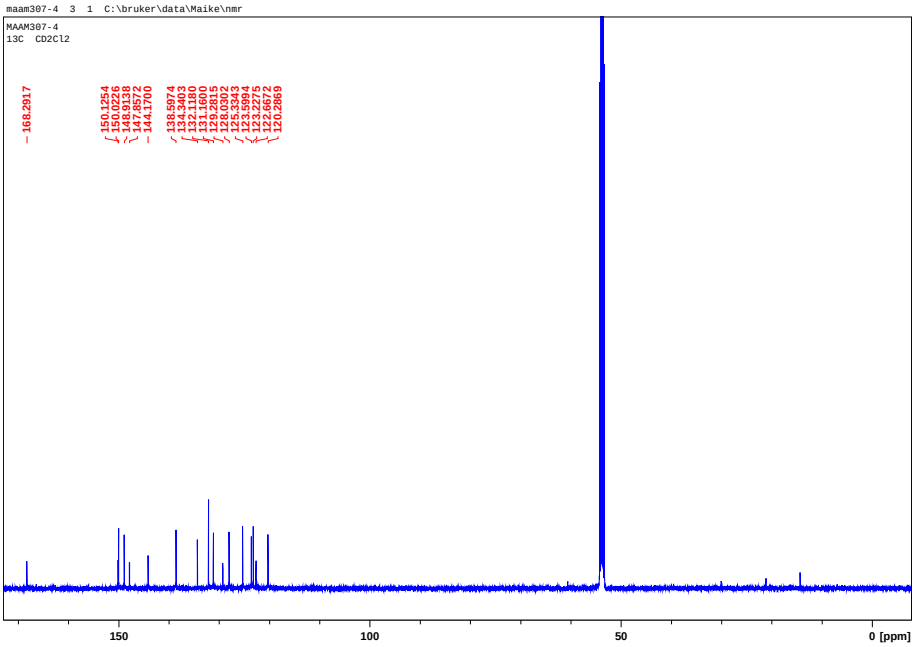

Figure 9.16: ^{13}C NMR spectra of **PS2** in CD_2Cl_3. Best viewed digitally.

NMR data of PS3

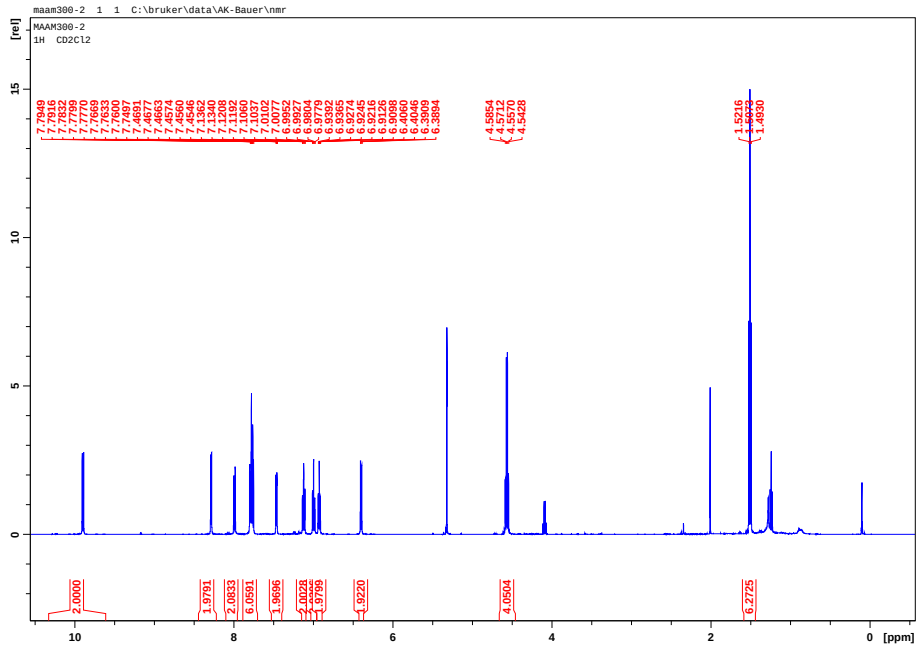

Figure 9.17: ^{1}H NMR spectra of **PS3** in CD_2Cl_3. Best viewed digitally.

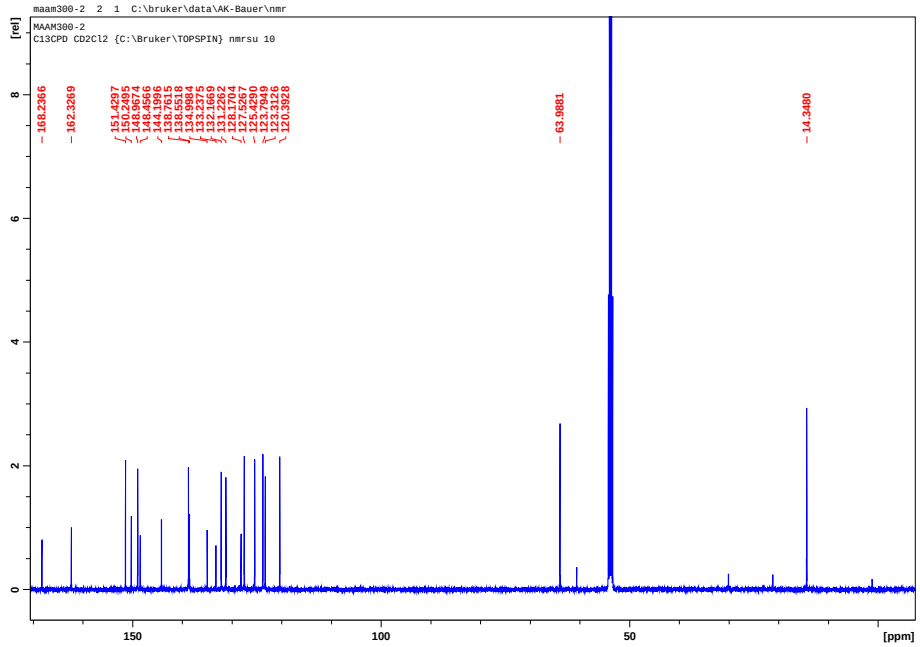

Figure 9.18: ^{13}C NMR spectra of **PS3** in CD_2Cl_3. Best viewed digitally.

NMR data of PS5

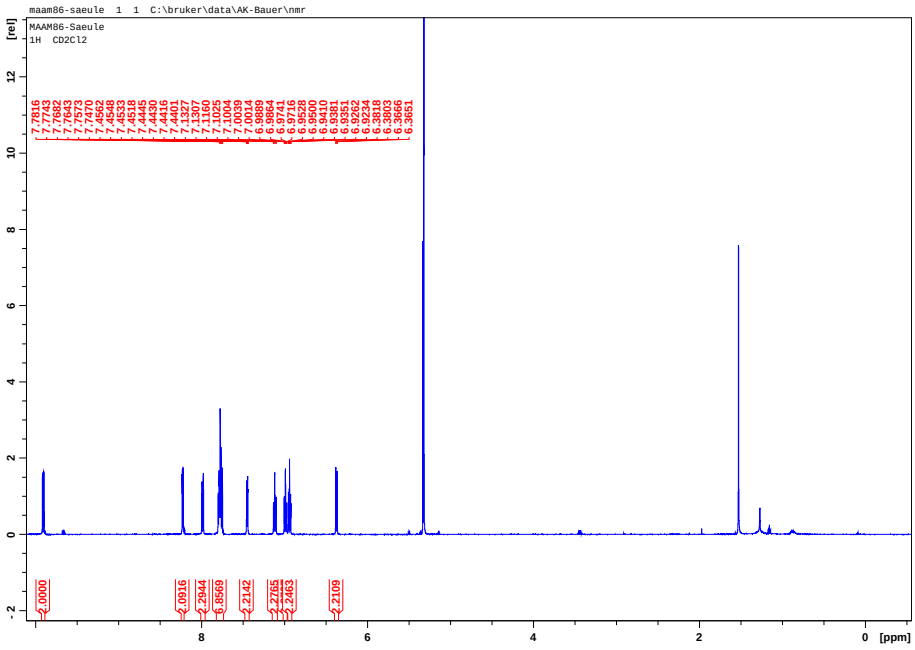

Figure 9.19: ^{1}H NMR spectra of **PS5** in CD_2Cl_3. Best viewed digitally.

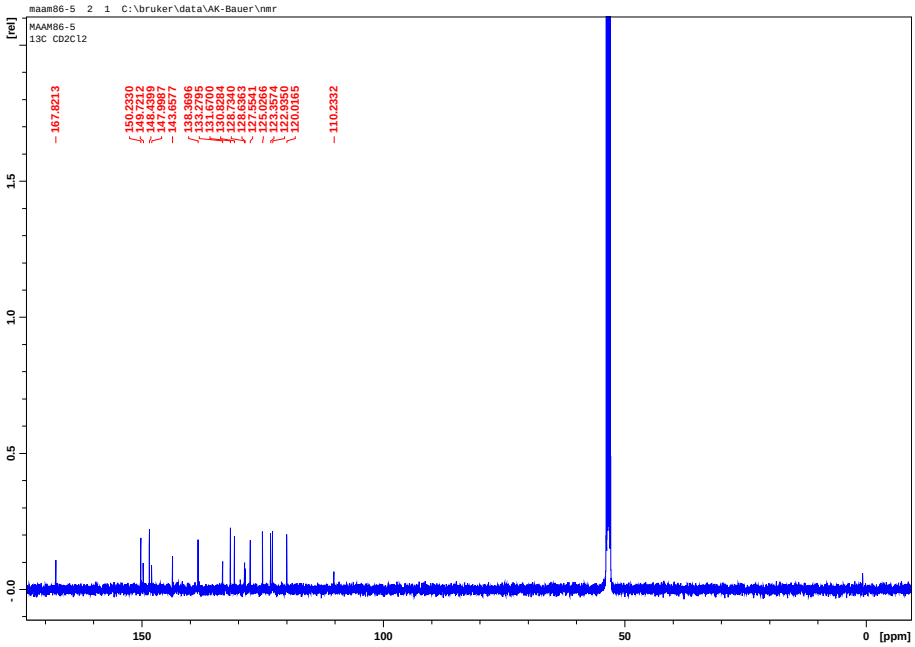

Figure 9.20: ^{13}C NMR spectra of **PS5** in CD_2Cl_3. Best viewed digitally.

NMR data of PS6

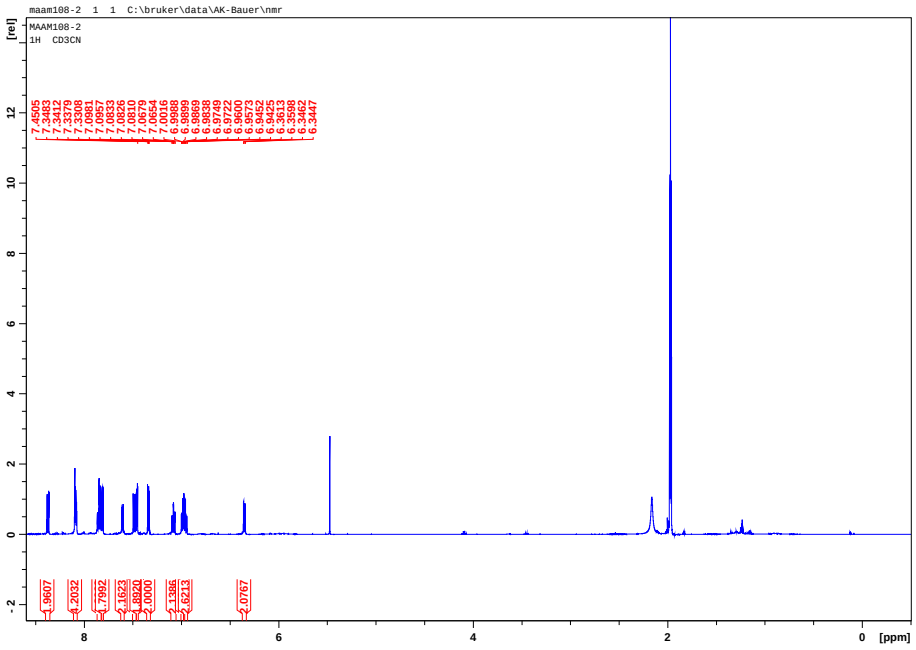

Figure 9.21: ^{1}H NMR spectra of **PS6** in CD_3CN. Best viewed digitally.

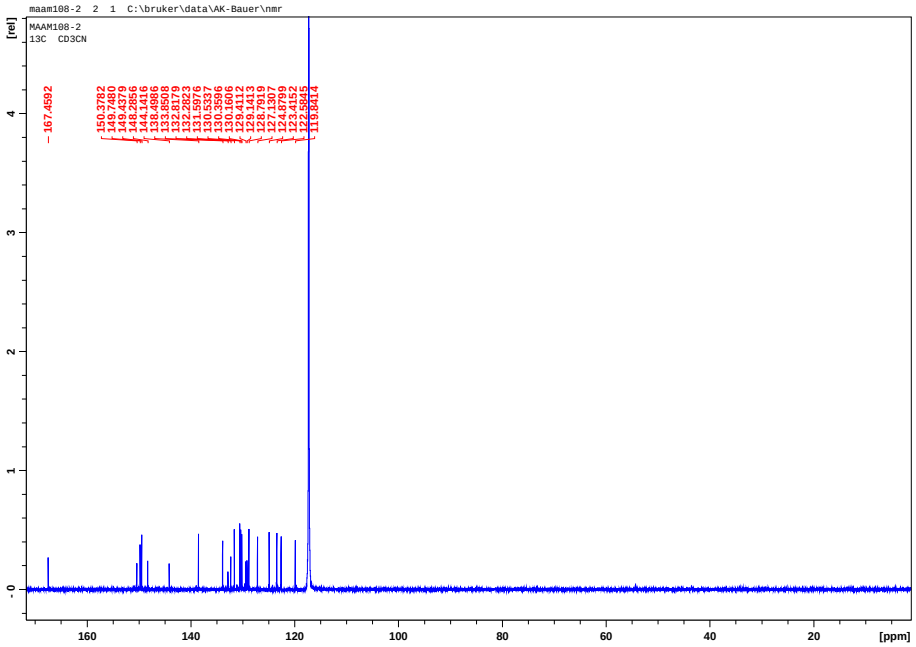

Figure 9.22: ^{13}C NMR spectra of **PS6**.in CD_3CN. Best viewed digitally.

NMR data of PS7

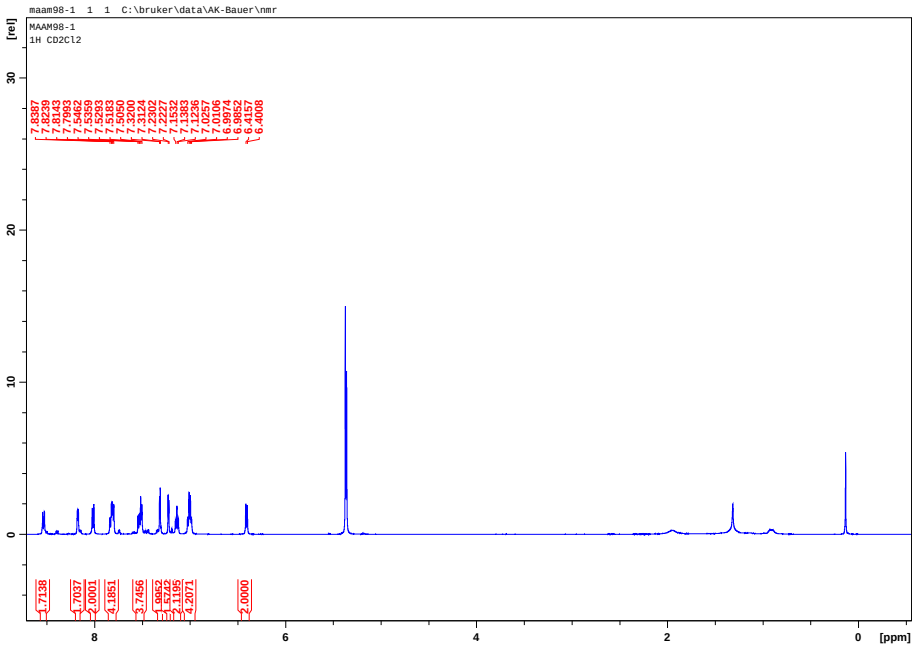

Figure 9.23: ^{1}H NMR spectra of **PS7** in CD_2Cl_3. Best viewed digitally.

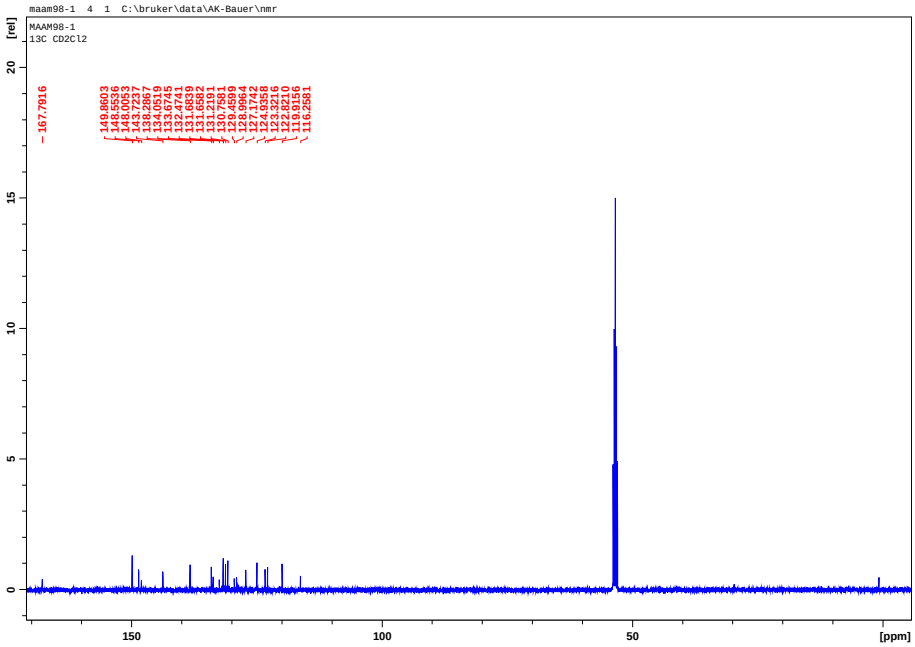

Figure 9.24: ^{13}C NMR spectra of **PS7** in CD_2Cl_3. Best viewed digitally.

NMR data of PS8

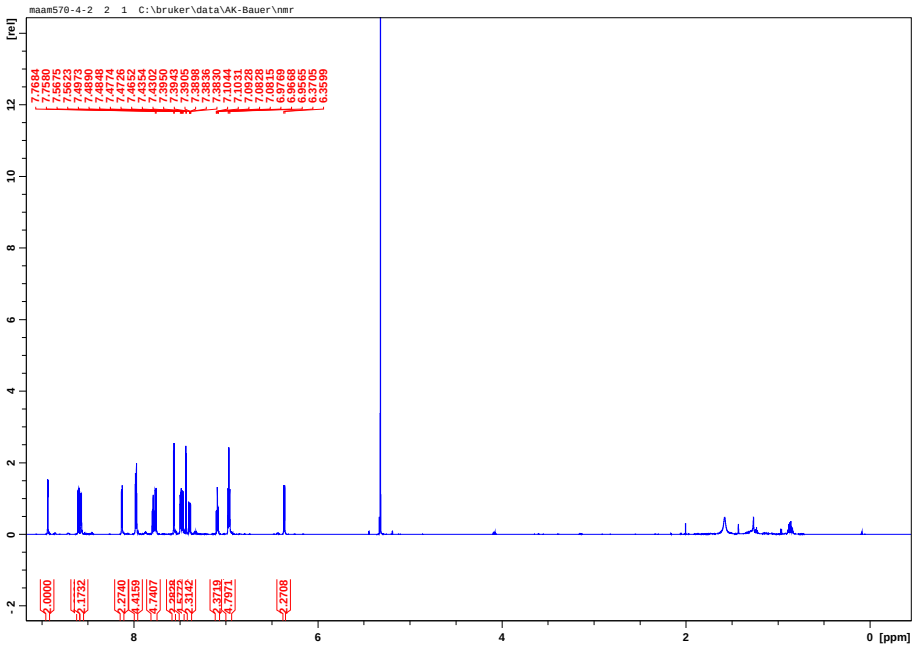

Figure 9.25: ^{1}H NMR spectra of **PS8** in CD_2Cl_3. Best viewed digitally.

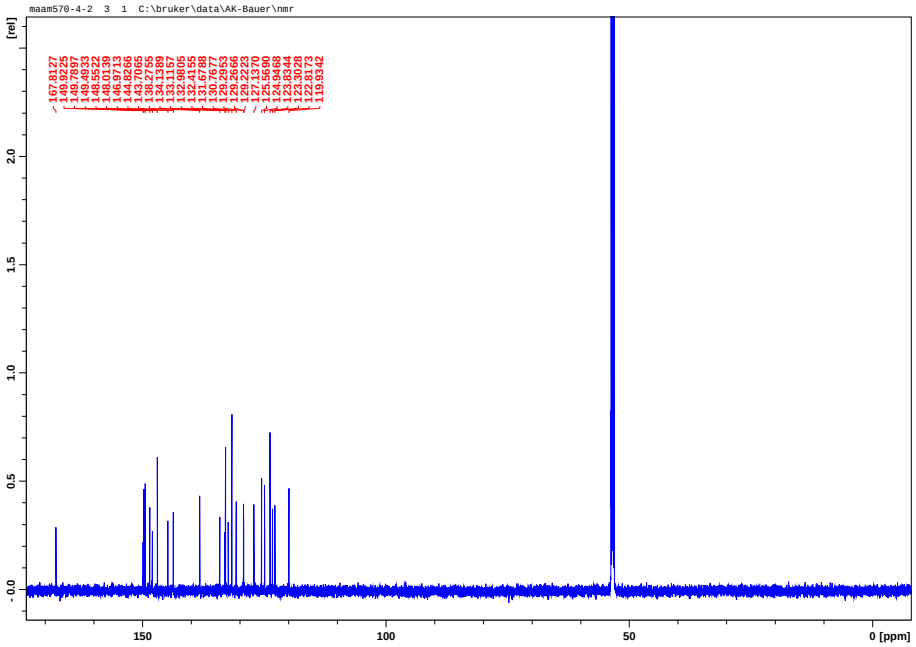

Figure 9.26: ^{13}C NMR spectra of **PS8** in CD_2Cl_3. Best viewed digitally.

NMR data of PS9

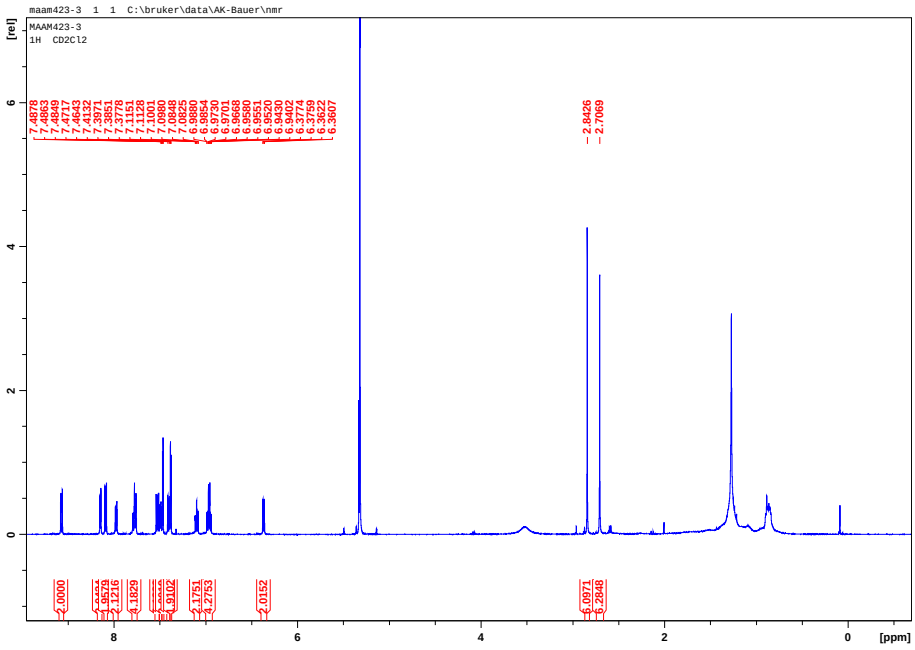

Figure 9.27: ^{1}H NMR spectra of **PS9** in CD_2Cl_3. Best viewed digitally.

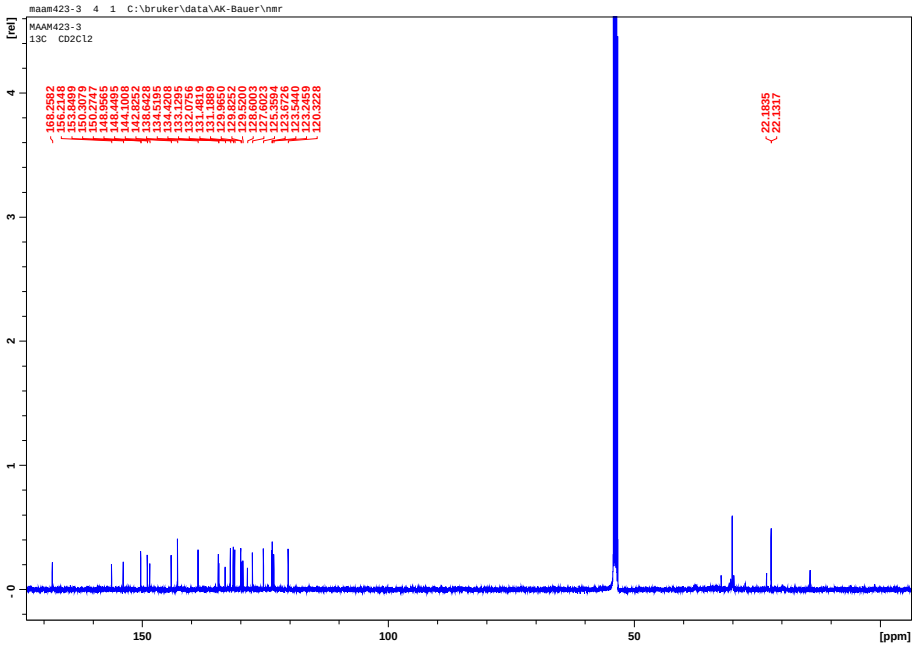

Figure 9.28: ^{13}C NMR spectra of **PS9** in CD_2Cl_3. Best viewed digitally.

NMR data of IrO

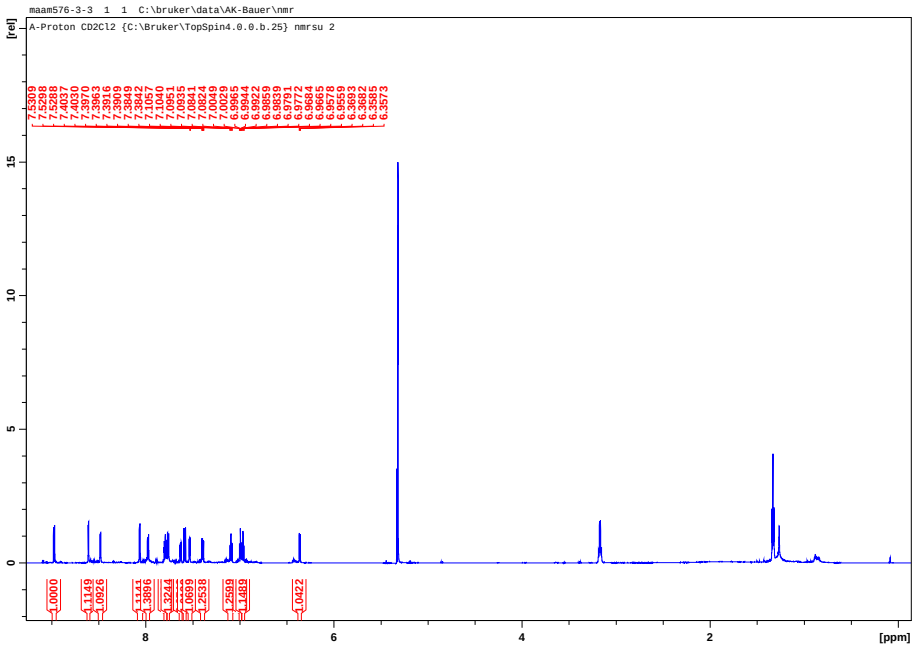

Figure 9.29: ^{1}H NMR spectra of **IrO** in CD_2Cl_3. Best viewed digitally.

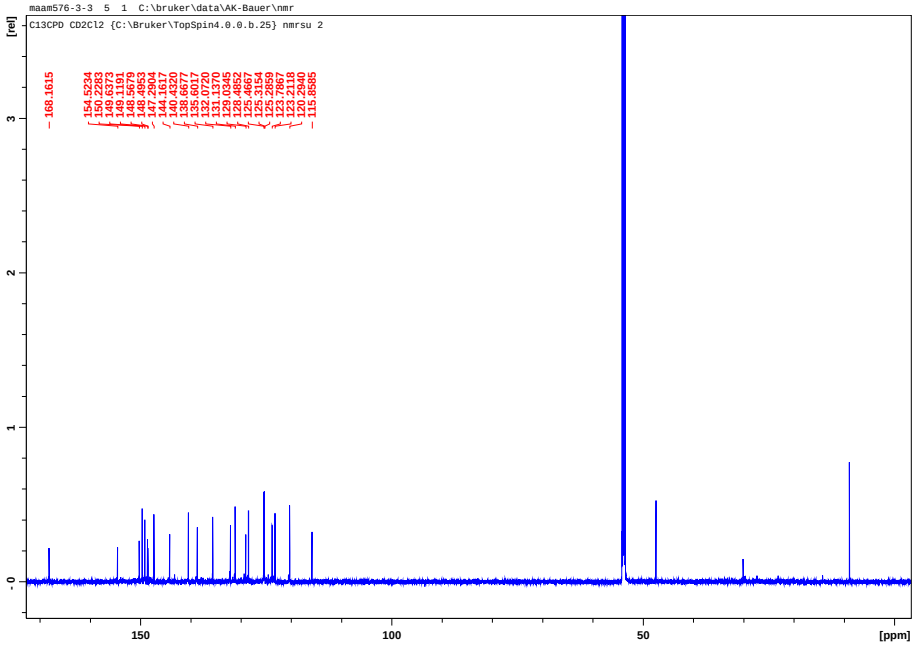

Figure 9.30: ^{13}C NMR spectra of **IrO** in CD_2Cl_3. Best viewed digitally.

NMR data of IrthCo

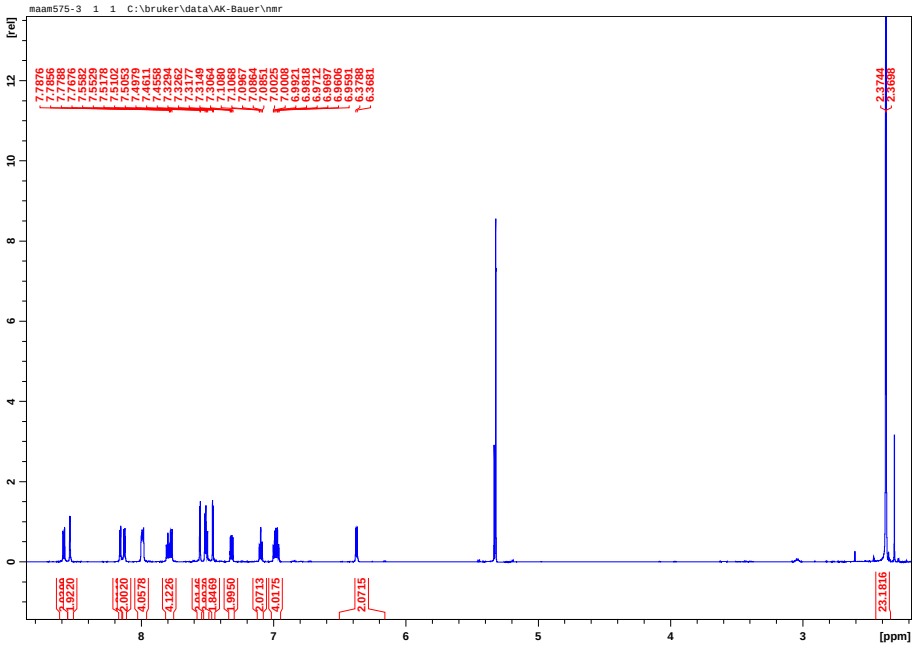

Figure 9.31: ^{1}H NMR spectra of **IrthCo** in CD_2Cl_3. Best viewed digitally.

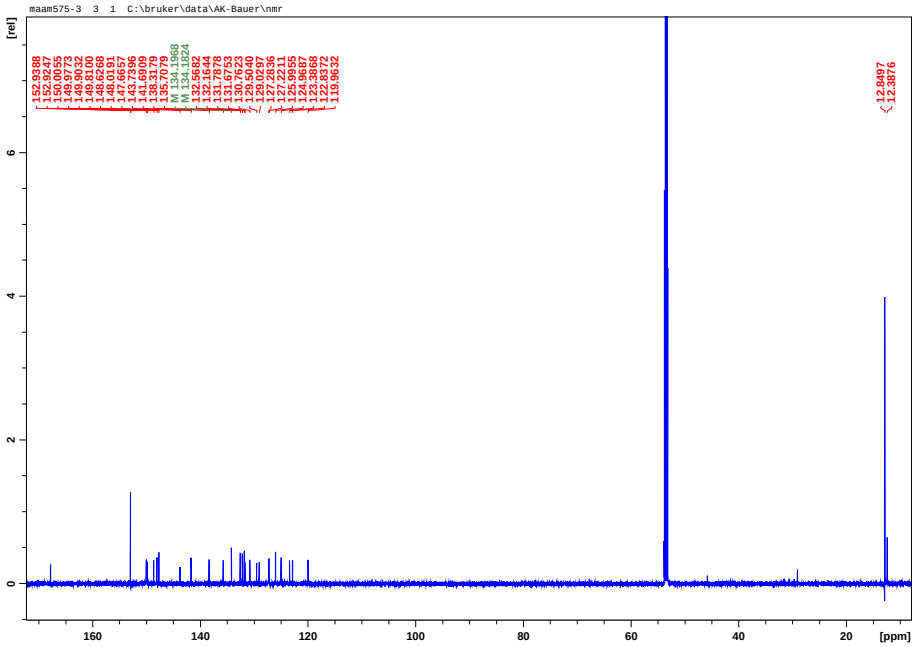

Figure 9.32: ^{13}C NMR spectra of **IrthCo** in CD_2Cl_3. Best viewed digitally.

NMR data of IrOCo

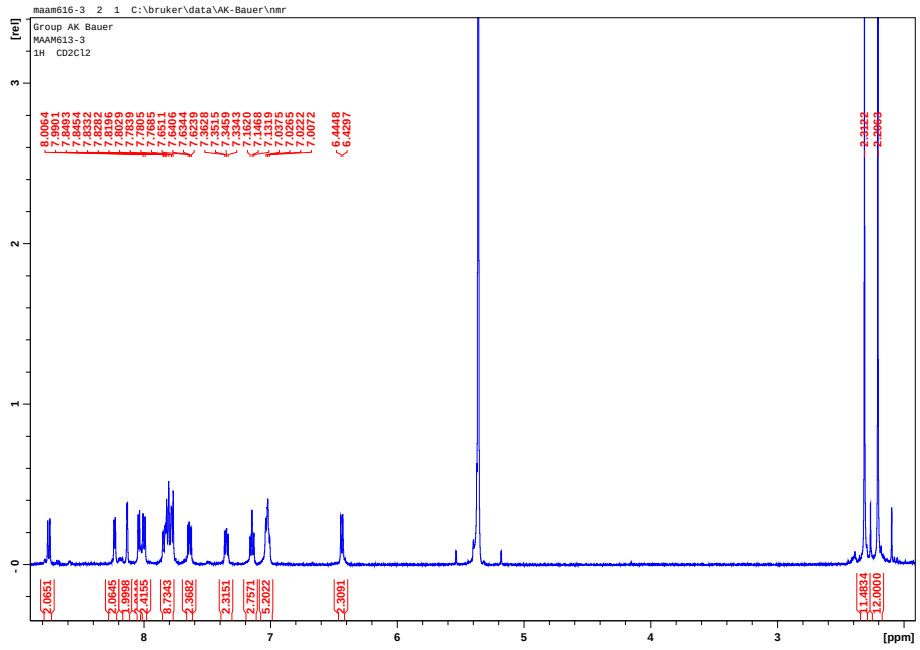

Figure 9.33: ^{1}H NMR spectra of **IrOCo** in CD_2Cl_3. Best viewed digitally.

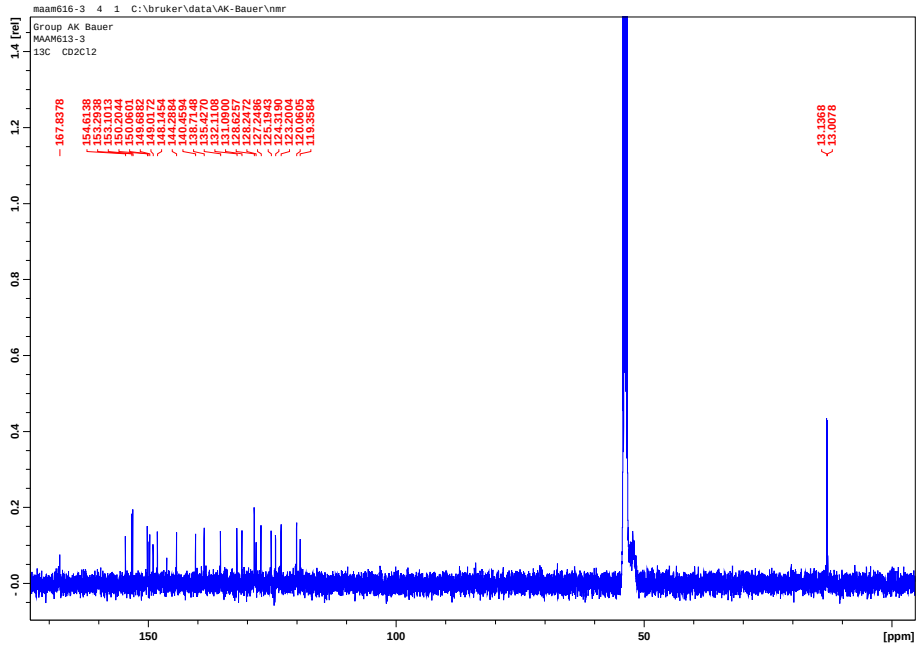

Figure 9.34: ^{13}C NMR spectra of **IrOCo** in CD_2Cl_3. Best viewed digitally.

List of Figures

List of Tables

List of Schemes

Declaration

I hereby declare that this thesis was written independently and without the use of any other means indicated in the work. Furthermore, I assure that the work has not been submitted to another examination authority either in Germany or abroad in the same or similar form. I also confirm that I did not apply for a doctorate at another university or faculty earlier or at the same time.

Paderborn, September, 2018

Maike Tünnermann